

**EFFECT OF SINTERING PARAMETERS ON THE
MECHANICAL AND PHYSICAL PROPERTIES
OF SINTER FORMED MATERIALS**

BY

AHMAD AL-TOUNSI

(B.Eng, M.Eng)

**This thesis is submitted as the fulfilment of the requirement
for the award of Doctor of Philosophy to :**

DUBLIN CITY UNIVERSITY

Sponsoring Establishment:

**Scientific Studies and Research Center
DAMASCUS - SYRIA**

Collaborating Establishment:

**Harris Ireland
DUNDALK - IRELAND**

AUGUST 1992

بِسْمِ اللَّهِ الرَّحْمَنِ الرَّحِيمِ

IN THE NAME OF ALLAH,
MOST GRACIOUS,
MOST MERCIFUL.

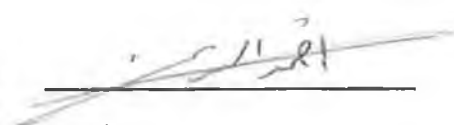
To
My Parents

DECLARATION

I here declare that all the work reported in this thesis was carried out by me at Dublin City University and Harris Ireland during the period of October 1989 to August 1992.

To the best of my knowledge, the results presented in this thesis are originated from the present study, except where references have been made. This thesis has not been submitted for any other degree award at this or any other institute.

Signed:

A handwritten signature in dark ink, appearing to read 'Ahmad AL-TOUNSI', is written over a horizontal line. The signature is somewhat stylized and includes a flourish at the end.

Ahmad AL-TOUNSI

ACKNOWLEDGEMENT

The author wishes to express his appreciation to Prof. M.S.J. Hashmi, Head of School of Mechanical and Manufacturing Engineering for his supervision, guidance and his constructive suggestions and comments during the course of this project.

The author would also like to express his gratitude to Dr. R. Puyane, from Harris Ireland, for his resourcefulness, advice, dedication and endurance to the end.

Special thanks to Mrs. A. Hopper, from Harris Ireland, for her help and advice in using the equipment at Harris Ireland and in the SEM photographs.

Thanks also extend to the SSRC, Damascus, SYRIA for their financial support during the course of this work.

Thanks are also extended to everyone who have supported and contributed to this work at every stage and level in Harris Ireland and Dublin City University.

**EFFECT OF SINTERING PARAMETERS ON THE
MECHANICAL AND PHYSICAL PROPERTIES
OF SINTER FORMED MATERIALS**

ABSTRACT:

Sinter formed materials have been studied in this project. The powders used were stainless steel powders and zinc oxide powders.

Three stainless steel powders were studied to evaluate the compressibility, shrinkage and densification during sintering and strength behaviour. The effect of sintering temperature on the high strain rate behaviour of stainless steel powder compacts has been investigated. A dynamic constitutive equation, which describes the material behaviour under dynamic loading, has been established. This equation takes into account the density of the compact.

Regarding ceramic powders, the compressibility of four zinc oxide varistor powders have been studied taking into account the particle size, binder content, binder type and lubricant. The green and sintered strength of ceramic compacts have been assessed in relation to the above mentioned parameters.

As for sintering, it was required to optimize the temperature profile of the sintering process. To accomplish this, two instruments were developed. The first one was used to monitor and control the weight loss, due to the binder burn out, at a constant rate. The second instrument was developed to monitor and control the shrinkage during sintering. The optimized temperature profile during binder burn out was checked for verification and it has proved reliable.

A brief look at the grain growth during sintering was carried out to see the effect of heating rate and soaking time on the grain growth since this is a critical material property influencing the electrical characteristics of zinc oxide varistors.

TABLE OF CONTENTS

DECLARATION	I
ACKNOWLEDGEMENT	II
ABSTRACT	III
TABLE OF CONTENTS	IV
CHAPTER ONE: INTRODUCTION	1
1.1 INTRODUCTION TO POWDER METALLURGY	1
1.2 LITERATURE SURVEY ON METAL POWDERS	4
1.2.1 P/M STAINLESS STEEL	8
1.2.2 DYNAMIC BEHAVIOUR OF SINTERED COMPACTS	11
1.3 LITERATURE SURVEY ON CERAMIC POWDERS	13
1.3.1 COMPACTION AND STRENGTH	17
1.3.2 CERAMIC SINTERING	21
1.4 PRESENT WORK AND ITS OBJECTIVES	26
1.4.1 METAL POWDER COMPACTS	26
1.4.2 CERAMIC POWDER COMPACTS	27
CHAPTER TWO: MATERIAL, EQUIPMENT, AND TEST PIECE PREPARATION	30
2.1 MATERIALS	30
2.1.1 POWDERS	30
2.1.2 LUBRICANT	32
2.2 TOOLS	33
2.2.1 POWDER MIXING TOOL	33
2.2.2 POWDER COMPACTION TOOLS	33
2.3 EQUIPMENT	34

2.3.1	COMPACTION RIG	34
2.3.2	SINTERING UNIT	35
2.3.3	COMPRESSION TESTING MACHINE	36
2.3.4	BALLISTIC TESTING APPARATUS	37
2.3.5	WEIGHT LOSS EQUIPMENT	38
2.3.6	SHRINKAGE EQUIPMENT	40
2.4	MEASUREMENTS	41
2.5	TEST-PIECE PREPARATION	42
2.5.1	POWDER MIXING	42
2.5.2	POWDER COMPACTION	42
2.5.3	SINTERING	44
2.5.4	MACHINING	46
CHAPTER THREE: TEST PROCEDURE AND RESULTS		70
3.1	INTRODUCTION	70
3.2	STATIC TEST PROCEDURE	71
3.2.1	RESULTS	71
3.2.2	DISCUSSION	72
3.3	BALLISTIC TEST PROCEDURE	75
3.3.1	RESULTS	76
3.3.2	DISCUSSION	77
CHAPTER FOUR: SIMULATION OF DYNAMIC BEHAVIOUR USING FINITE DIFFERENCE NUMERICAL TECHNIQUE		90
4.1	INTRODUCTION	90
4.2	THE MATHEMATICAL MODEL	92
4.3	FORMULATION OF EQUATIONS	94
4.4	SIMULATION	101

4.5 RESULTS AND DISCUSSION	104
CHAPTER FIVE: CERAMIC COMPACTION AND STRENGTH	126
5.1 COMPACTION	126
5.1.1 EXPERIMENTAL PROCEDURE	126
5.1.2 RESULTS AND DISCUSSION	128
5.2 CERAMIC STRENGTH	130
5.2.1 FRACTURE THEORY	131
5.2.2 RESULTS AND DISCUSSION	135
CHAPTER SIX: SINTERING	154
6.1 WEIGHT LOSS	154
6.1.1 MANUALLY CONTROLLED WEIGHT LOSS	154
6.1.1.1 EXPERIMENTAL SET UP	155
6.1.1.2 RESULTS AND DISCUSSION	156
6.1.2 COMPUTER CONTROLLED WEIGHT LOSS	161
6.1.2.1 EXPERIMENTAL SET UP	162
6.1.2.2 RESULTS AND DISCUSSION	163
6.1.3 TEMPERATURE GRADIENT	167
6.2 SHRINKAGE	170
6.2.1 EXPERIMENTAL SET UP	172
6.2.2 RESULTS AND DISCUSSION	174
6.3 GRAIN SIZE	180
6.4 VARISTOR TESTING	183
CHAPTER SEVEN: CONCLUSIONS AND RECOMMENDATIONS	232
7.1 CONCLUSIONS	232
7.1.1 STAINLESS STEEL	232

7.1.2 CERAMIC	233
7.2 RECOMMENDATION	235
7.2.1 STAINLESS STEEL	235
7.2.2 CERAMIC	236
REFERENCES	238
APPENDIX A	A1
APPENDIX B	B1
APPENDIX C	C1
APPENDIX D: PUBLICATIONS	D1

CHAPTER ONE

1.1 INTRODUCTION TO POWDER METALLURGY

Powder metallurgy is one of the most diverse manufacturing approach among the various metalworking technologies. It simply consists of pressing the powder in a shaped die to produce a green compact, and then sintering the compact at an elevated temperature in a furnace under a protective atmosphere. During sintering the compact becomes consolidated and strengthened.

The advantages and attractions of powder metallurgy originate from several attributes. One of the major attractions is the ability to shape powders directly into a final component with high quality, complex shape and close tolerances in an economical manner. Other advantages of powder metallurgy can be summed by:

- 1 - High volume production of precise, high quality structural parts, typically from ferrous based alloys.
- 2 - Difficult-to-process materials, where fully dense high performance alloys can be fabricated with uniform microstructures.

3 - Specialty alloys, typically composites containing mixed phases.

4 - The complex parts possessing unique and uncommon shapes or ingredients.

Part fabrication using powder metallurgy consists of different stages which can simply be summed by powder production, compaction and sintering. This may be followed by repressing and re-sintering to further increase the strength and reduce the porosity of the compact.

There are different methods of metal powder production⁽¹⁾ which influence the size, shape, microstructure, chemistry and cost. Powder can be produced by:

- Mechanical Techniques which includes machining, milling and mechanical alloying⁽²⁾.

- Electrolytic Technique where a powder is precipitated at the cathode of an electrolytic cell under certain operating condition.

- Chemical Techniques where a powder is formed by decomposition of a solid by a gas or by precipitation from a liquid or gas.

- Atomization Techniques which is the most common technique in powder fabrication. It involves the formation of powder from molten metal using a spray of droplets. The spraying medium can be gas or water^(3,4).

In compaction, pressure is used to form powders into

engineered shapes with close dimensional control. This compaction process involves both rearrangement and deformation of the particles, leading to the development of interparticle bonds. Compaction can be carried out by various methods depending on the shape and the future use of the component. It can be carried out in a die with single or multiple punch, or by extruding a canned powder, or forming it into a sheet by rolling. Depending on the compaction technique employed and the pressure and temperature applied, the mechanical properties of the component will vary. Die compaction is the most common method of shaping powders. In die compaction the die cavity is filled with the powder and an external pressure is applied on the powder via the punches. During compaction, powder consolidation takes place in a number of stages and in each stage a particular mechanism is dominant. A detailed discussion of the mechanisms governing powder compaction can be found in reference⁽⁵⁾.

The next stage after compaction is sintering where the compacted parts are put in a furnace and heated to a high temperature below the melting point and left to soak for specific period of time. This stage provides the thermal energy needed to initiate interparticle welds and improve the mechanical properties of the component. In the sintering process cohesion takes place as necks grow at the points of particle contact. This growth of necks causes all the changes of the properties of the component. The sintering time and temperature have a considerable effect on the mechanical

properties of the sintered part.

After sintering a finished component with fairly good mechanical properties is produced. However, because of the presence of porosity the mechanical properties of the sintered components are lower than their counterparts in wrought material. Therefore, a forging process becomes essential when full density is required. In this process the material is allowed to deform in order to densify and at the same time fill the die cavity and consequently it work hardens as well. But the successful forging process is the one which allows the compact to fill the die cavity without cracking and reach full density without excessive load⁽⁶⁾.

1.2 LITERATURE SURVEY ON METAL POWDERS:

The subject of powder metallurgy has been given extensive consideration in recent years, and much effort has been directed to the study of a wide range of processes and manufacturing techniques such as powder production, powder compaction, sintering process, forging and heat treatment of the sintered compacts.

The first aim of this review is to gather up to date information on the mechanical properties of sintered compacts and how these properties vary with the variation of the process parameters. Another objective is to have a good background about the subject of powder metallurgy.

As mentioned earlier, powder compacts are widely manufactured using die compaction. Donachie and Burr⁽⁷⁾ indicate that the mechanism of powder compaction takes place in three stages. The first stage of compaction is attributed to particles flowing past one another usually referred to as transitional restacking. In the second stage, compaction is attributed to the localized plastic deformation of particles and in the third stage to cold working of the compact.

Lubrication plays a major part in the compaction process. The lubricant is added to powders to reduce the friction between powder particles and the die wall during pressing and ejection. It also improves the compressibility of powders and extends the tool life. Different kinds of lubricants are employed in different ways, either by mixing them with the powder or by diluting them in a liquid and spraying them on the die walls. Kao and Koczak⁽⁸⁾ studied the effect of three types of lubricants (Acrawax C, Lithium stearate and Zinc stearate) added to atomized steel (Ancorsteel 1000) and prealloyed 316L stainless steel and they concluded that zinc stearate addition provides higher apparent densities and improved flow in them. They also indicated that the green strength decreases with increasing lubricant additions in steel powders and appears independent of the lubricant type in the stainless steel powders.

Regarding the compaction process, the major effect of increasing compacting pressure is the enhancement of the density of the compact and a parallel reduction in porosity.

Wheatley and Smith⁽⁹⁾ working with electrolytic iron powder found that increasing the compacting pressure resulted in smaller pore size and the structure displayed a more coherent appearance after sintering at 1050 C. Clyens⁽¹⁰⁾ Considered the compaction process to be dynamic if it is carried out at strain rates greater than 10 per second. He suggested that increasing the rate of compaction results in a more uniform density distribution, improved green strength and lower ejection forces. Page and Killen⁽¹¹⁾ made a comparison between powder flow in quasistatic and dynamic compactions. They produced compacts of the same average density in both methods and they concluded that compacts made using dynamic compaction had a more uniform density distribution and greater hardness than those made using quasistatic compaction method.

Particle shape, particle size and particle size distribution have an effect on the packing of the powders during the compaction process and the resulting mechanical properties of the finished compacts. German⁽¹²⁾ has found significant dependence of particle size on the tensile stress of compacts made from spherical aluminium and copper powders. He found that the smaller the particle size the higher the tensile stress. Honda⁽¹³⁾ observed the same effect on fatigue strength using iron powder compacts. This was attributed to the variation in the stress concentration factor with particle size. Also Duffield and Grootenhuis⁽¹⁴⁾ concluded earlier that the optimum strength necessitates use of fine powders with narrow size distribution.

As known, most metals oxidise when heated in air, so the sintering atmosphere is important to the sintering process and it affects the properties of the sintered product. There are different sintering atmospheres used. However, the choice of the correct atmosphere for sintering is important in relation to the strength of the compacts. Wiest⁽¹⁵⁾ reported that iron compacts sintered in hydrogen were stronger and tougher than those sintered in vacuum but their fatigue strength did not differ significantly. However, Wheatley and Smith⁽⁹⁾ found that the fatigue strength did not differ when iron compacts were sintered in vacuum or nitrogen.

In respect to the sintering process, a large amount of work has been concentrated on the effect of sintering parameters on the mechanical properties of the sintered compact. These parameters include sintering time and temperature and sintering atmosphere. During sintering a number of events take place depending on the sintering time and temperature employed during the process. Powder particles start to weld together by forming necks between them. These necks grow at the points of particle contact and the neck size ratio increases with sintering time. Moreover, the compacted powder has a large surface area which corresponds to a large surface energy, so that at high temperatures, diffusion takes place due to the excess energy. This is to reduce the surface area and consequently to reduce the net surface energy. At later stages of sintering the grains start to grow and the pores become spherical and isolated and the small pores are eliminated⁽¹⁾.

1.2.1 P/M OF STAINLESS STEEL

Sintered stainless steel parts are gaining greater significance in high technological areas like nuclear and aerospace applications⁽¹⁶⁾. There are many reasons for choosing stainless steel parts produced through powder metallurgy route because of the wide variety of features stainless steel possesses such as, corrosion and oxidation resistance, good mechanical properties, wear resistance and magnetic and nonmagnetic properties.

Compaction pressure affects the green density of stainless steel powder. Row and Klar⁽¹⁷⁾ reported this in the range of 270 to 820 MPa for 316L stainless steel. The densities obtainable were in the range of 6.2 to 6.9 g/cc. They also reported that all properties of sintered 316L stainless steel increase with higher densities.

Design and processing of stainless steel sinterformed parts are subject to the same basic consideration as are other sinterformed materials. However, sintering is the most important and critical step in the processing of sintered stainless steel parts. Although sintering characteristics of different grades of stainless steel are similar, the sintering rate is faster for ferritic stainless steel as compared to austenitic stainless steel as mentioned by Mukhevjee & Upadhyaya⁽¹⁸⁾. They related their observation to the close-packed face centred cubic structure of austenitic stainless steel.

Moyer⁽¹⁹⁾ stated that addition of 0.5 to 1 % lubricant to 316L stainless steel powder is good practice in order to give the compact enough strength for handling and to lubricate the die walls to facilitate pressing as well as ejecting the compacted part. However, the presence of lubricant in the finished part is not desirable, hence it should be burnt off before sintering takes place. The burnt off temperature for lubricant is between 430 to 540 C depending on the lubricant type and sintering atmosphere⁽¹⁶⁾.

In regard to the sintering process, a number of events take place like densification which is due to shrinkage. German⁽²⁰⁾ examined the shrinkage kinetics of 304L stainless steel powder. He observed that initial densification is controlled by strain assisted volume diffusion mechanism. He also noticed that grain growth reduces the shrinkage rate at temperatures above 1330 K.

Dyke and Ambs⁽²¹⁾ reported an increase in the ultimate tensile strength and percentage elongation with increasing sintering temperature whereas the yield strength and hardness showed a decreasing trend. Lal and Upadhyaya⁽²²⁾ stated that the ultimate tensile strength and elongation were increased to an optimum at 1% phosphorus and 4% silicon addition to 316L stainless steel.

After sintering the compacts should be cooled as fast as possible without deforming their shape to prevent nitrogen absorption and its subsequent precipitation as Cr_2N along the

grain boundaries. Stosuy and Holmes⁽²³⁾ carried out sintering tests on 316L stainless steel. They observed that regardless of the atmosphere, the rate of cooling from the sintering temperature affects the properties of sintered 316L stainless steel. They also observed that with slow cooling rate chromium carbides and nitrides tend to precipitate as fine particles along the grain boundaries. Moreover they found that a cooling rate of about 63°C/min from sintering temperature gave the best combination of tensile strength and percentage elongation for 316L stainless steel after sintering in dissociated ammonia or argon.

Regarding sintering time, Stosuy⁽²⁴⁾ reported an increase in tensile and yield strengths of sintered 316L stainless steel with the increase in sintering time from 30 minutes to 3 hours. Stosuy and holmes⁽²³⁾ also found an increase in ductility and shrinkage with increasing sintering time. French and Mardon⁽²⁵⁾ reported that sintered density of 316L stainless steel increased as the sintering time was increased upto 6 hours, when it approached the theoretical density.

In respect to the effect of alloying elements Lal and Upadhyaya⁽²²⁾ studied the effect of phosphorus (up to 2%) and silicon (up to 5%) additions to 316L stainless steel containing 4% yttria. The compacts were sintered at 1100°C and 1300°C for 1 hour in hydrogen. They found that greater improvement in densification behaviour was noticed for phosphorus addition than for silicon addition after sintering at 1300°C. However, better corrosion resistance was noticed

after silicon addition than phosphorus addition.

1.2.2 DYNAMIC BEHAVIOUR OF SINTERED COMPACTS:

The dynamic behaviour of metals during high strain rate loading has been studied extensively. However, little work has been carried out regarding sinterformed metals. In the literature, the dynamic behaviour of metals has been introduced as a guide line for the understanding of this kind of behaviour.

The response of metals to dynamic loading may be dependent upon the rate at which the load is applied. Between the two extremes of loading rates, the static loading and impact loading in which the stress propagates through the metal as a uniaxial strain shock wave, there is a wide range of situations characterised by diverse responses. The loading rates providing strain rates above 10^2 sec^{-1} are considered to be high strain rates⁽²⁶⁾.

Hopkinson^(27,28) investigated the effect of a blow delivered by a falling weight on an iron wire. His results demonstrated that the tensile strength of iron is greater at high rates of loading than under static loading and he confirmed his analytical conclusion, based on an analysis of wave motion that the ability of a blow to rupture a wire is determined by the velocity with which it is delivered rather than by its energy or its momentum.

The influence of speed of testing on material properties has been the subject of numerous investigations. In the past, strain-rate has generally been measured by dividing the rate of head motion by the initial gauge length or height of specimen. Hennecke⁽²⁹⁾ presented his results in the form of static and dynamic deformation because he had no facilities for direct or indirect measurements of strain rate. Pugh and Watkins⁽³⁰⁾ determined the average rate of strain as $v_0/2H_0$ where H_0 is the initial specimen height and v_0 is the striking velocity of the tup. Harding⁽³¹⁾ stated that most metals and alloys exhibit some increase in strength with increasing strain rate. He included a complete review on the effect of strain rate on the mechanical properties of metals and alloys.

As for sinterformed metals, Honda⁽³²⁾ carried out tensile tests on iron powder compacts at different slow strain rates of between 10^{-4} to 10^{-1} per second and he reported that tensile strength is almost constant at these rates which corresponds in general with the results of Campbell and Ferguson⁽³³⁾ in their work on mild steel wrought metal. He also noted⁽³²⁾ that elongation is decreased with the increase in strain rate. Clyens and Johnson⁽³⁴⁾ developed a shear cell to determine the dynamic shear strength of metal powders. They used copper powder in their test and found that the shear strength of copper powder is sensitive to the rate at which the powder is deformed. This behaviour is also similar to the strain rate sensitivity exhibited by many solids. Bose et.al.⁽³⁵⁾ studied the influence of the test temperature and

strain rate sensitivity on the strength of 90W-7Ni-3Fe tungsten alloy in as-sintered condition. Their experiments were in the range of 10^{-3} to 10^3 and they found that the strength increases slightly with strain rate while ductility decreases.

The author⁽³⁶⁾ studied the effect of sintering temperature on the strain rate sensitivity of iron powder compacts and wrought mild steel for comparison. The results showed that sintering temperature affects the strain rate sensitivity. By comparing these results with the mild steel results, it was shown that the wrought steel has a higher strain rate sensitivity than sintered iron compacts.

1.3 LITERATURE SURVEY ON CERAMIC POWDERS:

This work is related to the production of metal oxide varistors based on doped zinc oxide used as transient over voltage suppression devices. These devices are used to protect electrical and electronic systems from power surges and lightning strikes.

There are two major categories of transient overvoltage suppression devices which can be considered for the protection of electrical and electronic equipment: one is based on the principle of attenuating the transient and the other diverting the overvoltage transient from the sensitive load in order to limit the residual voltage. In the first category, devices such as series filters can be considered.

They are inserted in the circuit, usually a low-pass type, which attenuates the transient (high frequency pulse) letting the signal or power (low frequency component) flow undisturbed. Examples of the second category are 'crowbars' and voltage clamping devices. These having a variable impedance depending on the current flowing through the device. An important advantage of this type of device is that the functional characteristics of an electronic or electrical circuit are not affected by the insertion of such a device either before or after the transient for any steady-state voltage below the maximum clamping voltage of the device. Voltage clamping devices are Selenium cells, Zener diodes and varistors which are either silicon carbide or metal oxide.

The present work is geared essentially to the production of ZnO varistors for high voltage, high energy applications.

Zinc oxide varistors are ceramic, semiconducting, N-type elements characterised by an extremely non-linear current voltage behaviour⁽³⁷⁾, as shown in the typical I-V curve in figure(1-1). The voltage-current function in the normal varistor operation range (the non-ohmic region) may be mathematically described by an exponential function such as:

$$I=k \cdot V^\alpha \quad (1.1)$$

where:

$$\alpha = \frac{\log I_2 - \log I_1}{\log V_2 - \log V_1} \quad (1.2)$$

and k is a proportional constant related to the non-ohmical

behaviour.

brittleness and this is demonstrated by the behaviour of
this curve shows the leakage, nominal varistor's
operation and upturn regions. Additives such as Bi_2O_3 , Co_2O_3 ,
 MnO , Sb_2O_3 and others are required to optimize the non-linear
characteristics of ZnO varistors, and by varying the overall
chemical composition and the processing conditions during
manufacturing of the varistors, this V-I curve can be shifted
up, down or to the left or right and the value of α may be
changed.

The term 'Ceramics' includes a very wide range of
materials like heavy clayware, refractories, cement and
abrasives, pure oxides, etc. Oxides are the largest group of
ceramics. These include the majority of the traditional
materials which are generally based on silica, alumina
magnesia or two or more of these.

Ceramic materials possess many attractive properties
including chemical inertness, refractoriness, low thermal and
electrical conductivities and they are usually cheap. The
most characteristic mechanical property of ceramics is

iece aceramic like a cup when ropped onto a hard floor.
This represents a serious limitation to the use of ceramics
under conditions of load or shock, and since this covers most
applications a study of mechanical properties plays a central
role in the science of ceramics.

The mechanical properties of ceramics, like those of all materials are determined by their structure. The structure of oxide ceramics are extremely varied and range from those of glasses to those of bricks. The degree of understanding naturally depends on the complexity of the material, but work on simple systems such as glasses, single crystals, pure polycrystals and various model systems has led to a good appreciation of the basic principles determining mechanical behaviour.

Ceramics are brittle because they can not undergo significant amounts of plastic deformation at ambient temperatures. The stress-strain behaviour is thus elastic in nature, stress rising linearly with strain up to the fracture stress, whereupon catastrophic failure usually follows. At high temperatures several mechanisms involving plastic flow become important and these militate against brittleness, generally at the expense of a reduction in strength. However, there is large volume of experimental data for materials tested at high temperatures, and fundamental understanding decreases as the temperature and complexity of the deformation process increase.

The fabrication of ceramics generally involves the consolidation and shaping of a fine powder, followed by a sintering process to achieve the required microstructure and properties. One of the most popular methods for achieving these steps in the manufacturing of ceramics is dry pressing. Dry pressing may be defined as the uniaxial compaction and

shaping of a granular powder with small amounts of moisture and organic binders during confined compression in a die. Since the compaction pressure controls the density and the resulting mechanical properties of the final product, a knowledge of the relationship between the compaction pressure and the material properties is very important.

1.3.1 COMPACTION AND STRENGTH:

The compaction process demands two mechanical properties of raw powders: superior compactibility or plasticity during pressing and sufficient strength of the compact to bear the subsequent handling during manufacturing. These properties are controlled by the incorporation of the so-called additives⁽³⁸⁾. The additive system consists of binders which enhance the interparticle cohesive force, plasticizers which give flexibility to the binder phase and lubricants which reduce the frictional force between the particles and the die wall⁽³⁹⁾. Levine⁽⁴⁰⁾ lists the types of binders available for ceramics.

Van Der Zwan and Siskens⁽⁴¹⁾ stated that the compaction of agglomerated materials consists of four stages: the first stage is the filling of the holes between the agglomerates, the second stage is the fragmentation and plastic deformation of the granules, the third stage is the filling of the holes between the primary particles and the fourth stage is the fragmentation and plastic deformation of the primary particles. Dynys and Halloran⁽⁴²⁾ studied the behaviour of

aggregated alumina powders during compaction using aggregates with different size distribution. They found that the aggregates were crushed during compaction and the size distribution shifts to lower sizes at higher compaction pressures. Moreover, these changes in the aggregate size distribution are reflected in the size distribution of open porosity of the pressed compacts, so that there is a decrease in the pore volume with the increase in the compacting pressure and this corresponds to an increase in the green density of the compact. Frey and Halloran⁽⁴³⁾ concluded that compaction of spray-dried alumina is very sensitive to the volume fraction of the binder and moisture content. They found that the density of the green compact increases with the decrease in the binder content, whereas it increases with the increase in the moisture content. They also found that the granule size has little effect on the compaction process.

Dimila and Reed⁽⁴⁴⁾ investigated the stress transmission through the compact during the compaction of a spray dried alumina powder containing polyvinyl alcohol binder stored at different relative humidities. They found that stress transmission was enhanced by lubricating the die and decreasing the thickness/diameter ratio. They also found that radial/axial stress ratio was decreased with lubrication of the die and the storage of the granulated powder at higher relative percent humidity. Strijbos⁽⁴⁵⁾ studied the friction between ferric oxide powders and cemented tungsten carbide walls. This was done by using a die with polished, spark-eroded and ground walls. He concluded that powder-wall

friction can be reduced by grinding die walls in the axial direction and by the application of lubricant film with thickness much larger than the particle size. Cooper and Eaton⁽⁴⁶⁾ studied the compaction behaviour of four ceramic powders of widely different hardness but of the same particle size fraction. They concluded that the softer powders yielded greater fractional volume compaction at a given pressure.

In studying the strength of brittle materials, conventional tests present difficulty both in specimen preparation and in alignment during the test. As an alternative, bending tests are often used, but in addition, a large number of less conventional specimens have been proposed for the measurement of tensile strength as reported by Marchall and Rudnick⁽⁴⁷⁾. One of the more interesting of these tests is the diametral compression of a solid disc. the beauty of this test is that the specimen is simple to prepare and load. This test was proposed by Carniero and Barcellos⁽⁴⁸⁾. In this test there is an extensive region along the axis of loading in the specimen where the stress transverse to the loading axis is tensile and constant with magnitude about one-third of the compressive stress in the loading direction⁽⁴⁹⁾.

Nies and Messing⁽⁵⁰⁾ studied the effect of varying the ratios of binder(PVA) and plasticizer(PEG) on the green density and the green strength of ceramic compacts. They found that the green density of the compact decreases with the increase in PVA ratio in the binder system. However, the

green strength increases with the increase in the PVA ratio in the binder system. Harvey and Johnson⁽⁵¹⁾ stated that for maximum green strength, there is an upper limit of binder concentration. They reported that a high agglomerate strength from high concentration of binders may not allow extensive bonding in a compact and will cause low strength except at high compaction pressures.

A fundamental distinction between the mechanical strength characteristics of ductile and brittle materials is the unusually high degree of variability exhibited by brittle materials.

Test results for identical steel specimens will seldom differ from specimen to specimen by more than 5%. The minimum value can be specified for a particular property and this is a satisfactory value for design. However, with similar specimens of a brittle material a particular strength property may show variations of 100% or more⁽⁵²⁾.

A statistical basis widely used for the interpretation of test data and for failure prediction in brittle materials is that of Weibull⁽⁵³⁾. Davies⁽⁵⁴⁾ has discussed the physical basis and implication of Weibull theory and has illustrated its use in analysing and correlating test data. Williams and Swank⁽⁵⁵⁾ carried out rotational fast fracture, modulus-of-rupture and ball-on-ring tests and the measurements were correlated using Weibull statistics and finite element techniques. They concluded that the agreement between the

predicted and observed values demonstrates the applicability of the Weibull equation.

1.3.2 SINTERING:

The firing process is used to give the green compact the required final properties. To reach the firing temperature the green compacts have to go through different stages before reaching the peak firing temperature. These stages are: weight loss where the binder is eliminated from the compact and shrinkage where the densification takes place. Different ramps and dwells in the temperature profile are used to control these two events (weight loss and shrinkage). These ramps and dwells are developed on historical trial and error basis⁽⁵⁶⁾.

As mentioned earlier, binders are added to ceramic powders to improve the mechanical properties of the green compact. These binders are organic compounds which will burn out during the firing process. In choosing the binder type, account has to be taken of its burning temperature which should be less than the temperature at which the compact shrinkage starts. This is to prevent some of the binder being kept inside the compact when shrinkage takes place.

Weight loss is caused by the evaporation of moisture and the added binders which are burned during the firing process. If the binder burns at an inconsistent rate it can adversely affect the quality of the finished ceramic component due to

the creation of micro cracks which will develop into bigger cracks at a later stage of the firing process, or other defects such as explosive spalling or bubble formation⁽⁵⁷⁾.

Tsurumi and Bowen⁽⁵⁸⁾ stated that in the binder burn out process, if the heating rate is too rapid, failure may occur through cracking and even explosive spalling or defects such as void and pores may be produced in the final product. They suggested that a possible source of these failures or defects is bubble formation. Verweij and Bruggink⁽⁵⁹⁾ reported that the rate of temperature increase should be kept very low during the binder burn out to avoid the formation of cracks, blisters and bubbles and the occurrence of delamination.

Johnsson et al⁽⁶⁰⁾ developed a system for binder removal for injection-molded compacts called Rate-Controlled Extraction (RCE). They used compacts of different geometries and sizes in this system for binder extraction. Their results show almost linear weight loss of the organic binder with time and no damage in the green compact was observed after the process. Carlstrom et al⁽⁶¹⁾ studied the binder removal from injection moulded turbocharger rotors. They reported that binder removal was accomplished using a proportional control to the heating rate instead of heating the pieces at a constant heating rate until a preprogrammed weight loss rate was reached and above this rate the temperature was decreased. They stated that the proportional control method produces defect free bodies compared to the previous method which produced cracks due to the complexity of the part which

has thin and thick sections.

Lackey et al⁽⁶²⁾ studied the control of ceramic drying and calcining operation. They carried out their test using thermogravimetric analysis apparatus and used the output signal coming from it as an input signal to a computer system which varied the temperature as required to cause mass loss to follow a preselected rate. They stated that using this procedure, materials were prepared crack-free.

Cima et al,⁽⁶³⁾ stated that capillary forces were shown to influence the distribution of binder within the ceramic green bodies during binder burnout. They used tape-cast sheets of alumina in their experiments and observed that the early stage of binder removal was found to be similar to the drying of particle beds in which capillary forces draw liquid into the smaller pores at the surface.

Ceramics based on zinc oxide doped with metal oxides are the common materials for varistors. High temperature firing is the most important stage in their manufacturing. This produces the phases and the granular structure required which give rise at the grain boundaries to potential barriers that are responsible for the nonlinear electrical behaviour.

During firing densification takes place and the density of the fired compact could reach the solid density depending on several parameters, one of which is the metal oxide additives which can be one or several of oxides of Bi, Co,

Mn, Cr, Sb, Ti or Li. Trontelj and Kojar⁽⁶⁴⁾ studied the sintering of ZnO-based ceramics. They found that the addition of 0.5% Li₂O to ZnO shifts the onset of sintering towards 600°C, where the shrinkage starts; and the addition of Sb₂O₃ to ZnO shifts the onset of sintering to higher temperatures (1000°C). This was also observed by Marshall et al.⁽⁶⁵⁾. Asokan et al.⁽⁶⁶⁾ investigated the effect of metal oxide additions to ZnO on the microstructure and density of the sintered compacts. They used Sb₂O₃ and Bi₂O₃ additives of up to 5% and sintering was carried out at 1100, 1200 and 1300°C. They found that additions of Sb₂O₃ to ZnO decreases the bulk density and grain size at all temperatures. They indicated that Sb₂O₃ inhibits the grain growth and this was supported by scanning electron micrographs. However, additions of Bi₂O₃ increases the grain size at all sintering temperatures. As for the density, it was increased when sintering was carried out at 1100°C, but it was decreased at the other sintering temperatures.

Chu et al⁽⁶⁷⁾ studied the effect of heating rate on the densification of ZnO powder compacts using samples with the same initial relative density (50%). The heating rates used were 0.5, 2, 5, 10 and 15°C/min. They carried out the tests using a dilatometer by heating the sample to 500°C at 10°C/min then using one of the above heating rates up to 1000°C. They found that the higher the heating rate the higher the temperature at which densification starts. They also noted that the final densities obtained were independent on the heating rate. Lange⁽⁶⁸⁾, also studied the sintering of

Al_2O_3 powder compacts with the same initial relative density at constant heating rates. They found that for each heating rate the shrinkage strain rate is increased to a maximum and then decreased. The maximum densification strain rate occurred at approximately the same relative density of 0.77 for each heating rate. Lange suggested that sintering kinetics dominated the densification process up to a relative density of 0.77 after which coarsening kinetics are dominant.

Huckabee and Palmour III⁽⁶⁹⁾ studied the rate controlled sintering of Al_2O_3 containing 0.1% MgO. They reported that the conventional standard firing curves do not represent an optimum for Al_2O_3 because its earlier densification rates are excessive which create trapped pores. They also reported that the constant heating rate firing curves also produce rapid initial densification, pore entrapment and excessive grain growth. They concluded that the linear-linear-logarithmic decreasing densification rate regime produces near optimum firing conditions with an average grain size of $1\mu\text{m}$.

Kaysser and Lenhart⁽⁷⁰⁾ studied the sintering of agglomerated ZnO at 1360°C in O_2 . They found that the directly heated samples showed large residual pores after sintering whereas the presintered samples at 1000°C reached full density. They related the occurrence of these pores to particle rearrangement processes due to the density gradient of the initial agglomerates.

Sintering atmosphere has an effect on the pore size

evolution during sintering. Varela and Whittemore⁽⁷¹⁾ reported that during sintering of MgO in a inert atmosphere, like argon, pores shrink in the first minutes of sintering. They related that to rearrangement and other densifying mechanisms. In contrast, during sintering of ZnO in dry argon at low temperatures, there is a slight widening of pores with no grain growth due to surface diffusion.

1.4 PRESENT WORK AND ITS OBJECTIVES

The present work involves the study effect of sintering parameters on metallic and ceramic powder compacts.

1.4.1 METAL POWDER COMPACTS

The part of the work is geared towards the study of the dynamic behaviour of metal powder compacts. Three types of stainless steel powders series 300 were used in this work. The main objective of this work is to establish a constitutive equation which describes the dynamic behaviour of sintered stainless steel compacts and to determine the effect of sintering temperature on such behaviour. Some focus has been given to the process (compaction, densification and shrinkage) which will assist in establishing the above mentioned equation.

To reach these objectives, compacts were produced and sintered at different sintering temperatures as described in chapter two, which contains the details of the materials and

equipment used to carry out the work. Chapter three gives the results of the static and dynamic tests which were carried out on the sintered compacts. Chapter four fully describes a technique based on finite difference numerical analysis which was used to simulate the deformation behaviour under dynamic loading and to establish a constitutive equation for describing the dynamic behaviour in terms of the strain rate and the current density of the deformed compact.

1.4.2 CERAMIC POWDER COMPACTS:

This work is related to the production of zinc oxide varistors which are used to protect electronic equipment from power surges and lightning.

The work is divided into two parts:

- Compaction.
- Sintering

The main objective of the first part is to study the compaction behaviour of agglomerated zinc oxide ceramic powders, and the effect of powder characteristics on their compressibility. These powder characteristics include agglomerate particle size, type and amount of binder and amount of lubricant. Another objective is to study the green and fired strength of compacts made from these powders.

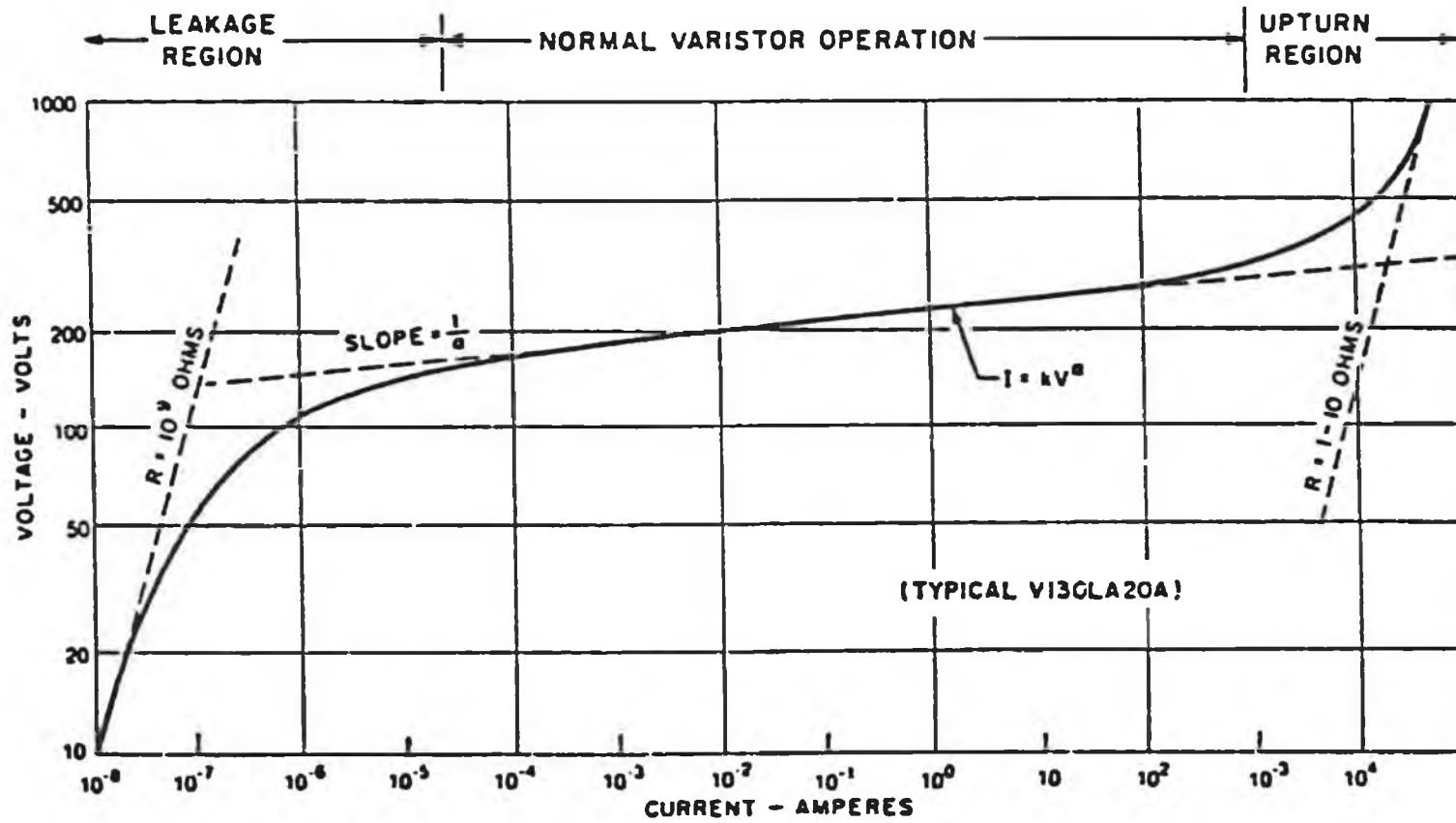
Regarding the second part (sintering), the idea is to

establish a system which takes into account all the parameters which affect the sintering process, such as compact weight, compact temperature profile, evolved gas composition, shrinkage, etc., to produce an improved ceramic part with minimal or no defects.

At the moment, the objective is to optimize the temperature profile for the firing process through monitoring and controlling two process parameters. These parameters include weight loss and shrinkage. Then, the generation of temperature gradient within the compact will also be studied.

To reach these objectives, two instruments have been constructed. The first instrument controls the binder burn out at a certain rate, while the other controls the shrinkage during sintering at a certain rate. These instruments were specially built for this work and they are fully described in chapter six along with the results from these instruments.

Figure 1-1 Typical V-I curve.



CHAPTER TWO

MATERIALS, EQUIPMENT AND TEST-PIECE PREPARATION

2.1 MATERIALS:

2.1.1 Powders:

Three kinds of stainless steel powders were used in this work. Their grades are: AISI 304L, AISI 316L and AISI 347. These powders were prealloyed and no other alloying elements have been added. The chemical composition of these powders are shown in table (2.1). The powders were atomized with mean particle size of $45\mu\text{m}$ as specified by the manufacturers. However, these powders were analyzed and it was found that the average particle size is around $23\mu\text{m}$. Analysis sheets (1), (2) and (3) show the particle size distribution curves for 304L, 316L and 347 respectively. These sheets show that the particle size distribution curves for 304L and 347 seem to be similar, whereas the particle size distribution curve for 316L show two distribution peaks with the same average particle size. This may imply that powder type 316 may densify better during the compaction process due to the two peak distribution where the small particles fill the voids between the large particles.

Table 2.1 Chemical analysis of the powders.

POWDER	C	Si	Ni	Cr	Mo	Mn	Nb	Fe
AISI 304L	.019	.69	10.2	18.3	-	-	-	BAL
AISI 316L	.022	.64	12.5	17.2	2.13	-	-	BAL
AISI 347	.015	.66	10.2	18.5	-	1.84	0.12	BAL

Regarding ceramic powders, four different spray dried powders of zinc oxide and additives have been prepared for this work. These powders were calcined and spray dried. Their characteristics are shown in table (2.2).

Table 2.2 Ceramic powder Characteristics.

Powder Type	Average Particle Size μm	Bulk Density g/cc	Tap Density g/cc	Binder Content g/kg	Moisture Content g/kg	Binder Type
D503	47	1.738	2.062	15	0.73	A
D504	47	1.716	2.073	13.3	0.78	A
D505	48	1.785	2.158	16.5	0.90	B
D506	47.5	1.688	2.088	24.14	0.74	B+C

The powders were chosen in such a way that the first two powders D503 and D504 have the same type of binder (type A) but they were sprayed with different nozzles to study the effect of particle size on the compressibility of powders. However, upon powder characterization it was found that both powders have the same average particle size. The results of powder characterization are shown in the sieve analysis graph sheets numbered 4 to 7 for the four powders respectively.

Regarding the effect of binder type on the compressibility of powders, powders type D503 and D505 were used. These have different binder types with the same content

of binder. However, upon analysis it was found that they differ a little bit in the percentage. Moreover, their average particle size were nearly the same.

In respect to the binder content, powders type D505 and D506 were used. These have different binder contents to observe the effect of binder content on the compressibility behaviour of powders.

Powder characterization was carried out for these powders as mentioned above. The particle size distribution was determined using sieve analysis. The bulk density was measured by filling a cup of known volume with powder and weighing it. The tap density was measured using a tapping machine set for 1000 tap. The moisture and binder content were measured by weighing a sample of powder and putting it in a furnace for 1 hour at 120°C to evaporate the moisture and the sample is weighed again to calculate the moisture content. Then the sample was put in another furnace for 1 hour at 520°C to burnout the binder and the sample was weighed again to calculate the binder content.

2.1.2 Lubricant:

To aid the compact to be extracted from the die during ejection a lubricant had to be used. The lubricant was Zinc Stearate in a powder form which was added to the stainless steel and zinc oxide powder directly and then mixed together.

As for the quasi-static compression test and the dynamic test for stainless steel powder compacts, several types of lubricants were tried and it was found that the polyethylene sheets gave the lowest friction effect.

2.2 TOOLS:

2.2.1 Powder Mixing Tool:

A stainless steel V-shaped mixer of 1.25 ltr. capacity was used for mixing each stainless steel powder with Zinc Stearate. The rotating chuck of a lathe was used to hold the mixer and rotate it at a speed of 40 r.p.m. Plate (2.1) shows a photograph of the mixer.

A Turbula Shaker-Mixer was used to mix the ceramic powders with zinc stearate. The mixer was manufactured by Willy in Switzerland type T2C and it has a capacity of 10 kg load. This mixer gives a three dimensional movement which causes the material in any container to be swept into an intense turbulence which gives a good degree of homogeneity to the materials mixed. Plate (2.2) shows a photograph of the mixer.

2.2.2 Powder Compaction Tools:

Two compaction die sets were used for stainless steel compaction. The first die set was designed to produce cylindrical compacts of 10mm diameter while the second die

set produced cylindrical compacts of 5mm diameter. The dies were designed to work as a floating dies, thus producing a condition of double action pressing. The first set consisted of a die body, upper punch, lower punch and ejection tool as shown in figure (2.1). As for the second set a tray was added on the die body and a feeding ring was used to fill the die cavity as shown in figure (2.2) due to the difficulty in filling the die cavity manually. Plate (2.3) shows a photograph of the second die set.

Both dies were made from high carbon high chromium tool steel hardened and tempered to 60 Rockwell C.

As for ceramic compaction, one die set has been used. This die set was designed to produce cylindrical discs of 17 mm diameter with different thicknesses. The die set consisted of a base which held the lower punch and the guide rods, a die body and an upper punch. The punch tips and the die wall were made as inserts of tungsten carbide while the rest of the die parts were made from high carbon high chromium steel. The die was designed as a floating die set, where the die body was supported by springs, to produce double sided compression with an option for a single action pressing. Figure (2.3) shows an assembly drawing of the die set. Plate (2.4) shows a photograph of the die assembly.

2.3 EQUIPMENT:

2.3.1 Compaction Rig:

The compaction rig used in this project was an INSTRON

Testing Machine, which is described fully in section (2.3.3). This machine was used for the compaction of stainless steel and ceramic powders using the appropriate die set.

The die set was placed on the anvil and the force was applied via the upper ram. The machine has the capability of setting the limits for the ram movement and the applied load with a very good accuracy, so the compacts had the same height and density as required.

2.3.2 Sintering Unit:

A special tube furnace was used for the sintering of stainless steel powder compacts. This furnace was heated by means of four silicon-carbide heating elements positioned around and parallel to the central tube. The elements were connected in series and supplied with power from 240 Volt AC supply. The tube was closed at both ends by means of special plugs. Argon gas with 5% Hydrogen was used as a protective atmosphere. The gas was fed through a hole in one plug and the other plug was connected with a fine tube which led to a water jar. This technique was very effective in maintaining a controlled inert atmosphere inside the tube at a very small flow rate of the gas. After charging each batch of compacts to be sintered, the gas was allowed to pass at a high flow rate to replace the air inside the tube.

The furnace was calibrated to find the area where the temperature is constant along the tube. Figure(2.4) shows the

calibration curves for three temperatures. It can be seen that the actual temperature inside the furnace is less than the one which is measured by the furnace controller. This difference in temperature has been accounted for during sintering of the compacts. Moreover, it can be noticed that the length where the temperature is constant is about 6 cm and that length is used later to put the compacts in during sintering.

Plate (2.5) shows a photograph of the sintering unit. The furnace type was LENTON Tube Furnace with maximum operating temperature of 1400°C.

Regarding the sintering of ceramic powder compacts, a pot furnace was used for this process which is fully described in section (2.3.5).

2.3.3 Compression Testing Machine:

The compression testing machine was an INSTRON Universal testing Instrument Model 4204, which consists of a loading frame and a control console as a separate assembly accompanied with a plotter. The frame has a load capacity of up to 50 kN and is designed for testing materials in either tension or compression by changing the grips.

The basic operation of the instrument consists of selecting a load cell for a particular testing application, mounting the load cell in the moving cross head within the

loading frame, then setting a specimen in position so that the load applied can be measured. The specimen is held by grips for tension testing or is table-mounted for compression testing. The load cell which was used had a capacity of 50 kN. Refer to appendix A for the full specifications of the machine.

During a test, results are displayed as tracked values of load , extension and strain or, after a test as stored break and peak values of these parameters. The action of the moving cross head during a test - Stop, Return and cycle - may be controlled, to an accuracy of 0.01 mm., manually by push button switches or automatically by the functions provided in the limits panel. These functions may be based on the applied load, extension or strain or to a specimen break detection. Plate (2.6) shows a photograph of the machine.

2.3.4 Ballistic Testing Apparatus:

A ballistic testing apparatus had been designed, constructed and commissioned by Haque⁽⁷²⁾ to facilitate firing of cylindrical projectiles at speeds varying from 30 to 300 m/sec on a small cylindrical specimen placed on a rigid anvil. Figure (2.5) shows a schematic diagram of the apparatus, while plate (2.7) shows a photograph of the actual apparatus. Some modifications have been carried out on the apparatus to improve its operation. The ball valve was changed with a solenoid valve to improve the consistency of the speed of the projectile at a specific air pressure. This

adjustment made the projectile speed repeatable at a given pressure. The specimen is placed on a rigid anvil while the pressure chamber is filled with compressed air. The projectile is placed in its position. Just above the specimen a laser beam and a photo cell are placed opposite each other and the photo cell is connected to a timer. When the valve of the pressure chamber is opened the compressed air propels the projectile at high speed and it crosses the laser beam just before hitting the specimen. At this moment the timer will count the obstruction time which can be used to calculate the impact speed.

The projectile was a flat headed cylinder made of tool steel and was heat treated to induce a hardness of 800Hv. The height of the projectile was 19 mm. with a diameter of 9.5mm.

2.3.5 WEIGHT LOSS EQUIPMENT:

The equipment used to control the weight loss during binder burnout stage are:

- Balance (METTLER PM 6100) with option 016 for communication with a computer through an RS232 interface. The balance can weigh up to 6.1 kg with a resolution of 0.01 g.

- Pot furnace type(Surefire TS25, K+F) equipped with WEST 2054 controller programmer which is capable of programming the temperature profile for the firing cycle.

The controller is equipped with an option X02 for communication with a personal computer through an RS485 interface. The programmable controller has 8 temperature control modules and each module has 4 stages. Each stage consists of a ramp and dwell. The modules can be linked together to form a recipe which produces the desired temperature profile.

- Personal Computer (AMSTRAD 1512) equipped with a two port serial communication card SIO-2 for the communication with the balance and the furnace controller.

- RS232/RS485 signal converter to convert the signal from the computer to a suitable form for the controller and vice versa.

To monitor the temperature gradient within the disc during the binder burn out, an 8-channel thermocouple card (TIP-8) was used. This card was placed inside the personal computer. It has 8 channels which means that 8 thermocouples can be connected and temperatures can be measured using this card. This card works as follows: it takes the electrical signal from the thermocouple and converts this signal from analogue to digital signal. The digital signal is then compared with correction tables in the card to improve the accuracy. Then the corrected value is placed in an address in the computer to be read from.

The thermocouples used in conjunction with the card are thermocouples type K with maximum operation temperature of around 500°C.

2.3.6 SHRINKAGE EQUIPMENT:

A high temperature dilatometer was used to measure the shrinkage/expansion of a sample (NETZSCH Model 402 E). It consists of a small furnace with a displacement transducer sensing the sample through a ceramic rod in the furnace and thus measuring its expansion/shrinkage during the thermal cycle. The sample which can be loaded into the dilatometer is a cylindrical sample with 25 mm height and 5 mm diameter. Other parts are connected to the dilatometer e.g. a temperature programmer in which a temperature profile can be set to follow a certain path and a controller to make the temperature increase follow the pattern set in the programmer. Plate (2.8) shows a photograph of the dilatometer and its accessories.

The equipment used to control the shrinkage during the firing process are:

- Displacement transducer with spring return armature (LVDT type ACT/500/A, RDP Group) to measure the compact contraction during firing. The transducer can measure displacements of up to +/- 12.5 mm.

- Digital transducer indicator and conditioner (model

400/LVDT, RDP Group) for converting the electrical signal from the transducer from an analog signal to a digital signal suitable for the computer. The indicator has a resolution of $1\mu\text{m}$.

- Pot furnace type(Surefire TS25, K+F) as the one described earlier.

- Personal Computer (AMSTRAD 1512) the same as the one used for the weight loss control

- RS232/RS485 signal converter to convert the signal from the computer to make it suitable for the controller and vice versa.

2.4 MEASUREMENTS:

Generally all the dimensional measurements were taken using a micrometer with an accuracy of $1\mu\text{m}$. Weighing the powder samples for compaction was carried out using an analytical balance with an accuracy of 0.1mg. As for measuring the speed of the projectile a laser beam device and a photo cell were placed opposite to each other. The photo cell was connected to a timer. As the projectile was fired the laser beam was obstructed by the projectile for a period of time and that time was recorded on the time display. The timer accuracy was $0.1\mu\text{sec}$. From the known length of the projectile and the obstruction time, it was possible to calculate the speed of the projectile. It should be noted

that the acceleration just before impact is negligible as confirmed by Haque⁽⁷²⁾, so there is no need to use a second laser beam for determining the speed of the projectile.

2.5 TEST-PIECE PREPARATION:

2.5.1 Powder Mixing:

Powder mixing was carried out using the above mentioned V-shape mixer. Each powder sample was loaded separately into the mixer and zinc stearate was added in the ratio of 0.75% as a lubricant to reduce friction between the powder particles and the die wall during compaction and ejection. After loading the powders the mixer was positioned on a lathe to rotate at a speed of 40 r.p.m. for 1 hour. After mixing had been completed the mixed powder was unloaded and the mixer was cleaned thoroughly to prevent the other stainless steel powders from being contaminated.

The turbula shaker mixer was used for mixing the ceramic powder D503 with zinc stearate for studying the effect of lubricant addition on the compressibility. The powder was mixed with three different percentages of lubricant 0.1%, 0.25% and 0.5%.

2.5.2 Powder Compaction:

Stainless steel powder compaction was carried out using

the universal testing machine and a press. A predetermined amount of powders was weighed to an accuracy of 0.01 g and poured into the die cavity. The upper punch was inserted in the die cavity and the whole assembly was placed at the compression anvil of the machine. The compression load was applied gradually until the level of the required density was reached. This was accomplished by setting limits to the cross head to force it to stop after a certain displacement. Ejection was done by removing the upper punch and placing the ejection tool at the top of the die body and reapplying the load to eject the compact. All compacts of AISI 304L, AISI 316L and AISI 347 had an initial relative density of 80% of the full density.

Two sets of dies were used to produce the required compacts for this work. The first die set produced compacts of 10 mm diameter and 10 mm height for the static compression test, while the second die set produced compacts of 5 mm diameter and 6 mm height for the dynamic test.

Initial compaction tests were carried out before producing the compacts to find the compressibility curves of these powders. Figure (2.6) shows the compressibility curves for these three powder. It can be seen that the density of the compact increases rapidly at low compaction pressures. This is due to the initial transition with pressurisation from loose particles to a closer packing. As the pressure increases the contact points between the particles start to deform which makes the powder resist compaction as shown in

the curves where the slopes of the curves start to decrease. Furthermore, the figure shows a difference in compressibility where it can be seen that the compaction stress required to reach a given density is not the same and that AISI 304L shows the least compactibility while AISI 347 shows the highest compressibility. It should be mentioned that some difficulty in handling the compacts made from AISI 347 was observed. This is due to the relatively small compaction stress required to reach the 80% initial relative density.

2.5.3 Sintering:

Due to the small effective area in the tube furnace where the temperature is constant, the 10mm diameter compacts were sintered in batches of 5 at four different sintering temperatures, while the 5 mm diameter specimens were sintered in batches of 10. These sintering temperatures were 900, 1000, 1100 and 1200°C. The sintering atmosphere was Argon-5% Hydrogen. The compacts were inserted inside the tube and the gas was fed to the furnace at a high flow rate to remove all the air inside the tube, then the tube was sealed with a special seal having an orifice to let the gas out of the tube and the gas flow was reduced to a minimum. The sintering cycle was as follows: After the compacts were put inside the furnace the furnace was heated to 525°C and kept at this temperature for 30 minutes. This was to remove all the added lubricant and to ensure that the impurities were burnt. The furnace, then was heated to the sintering temperature and the compacts were left to soak for 1 hour at this temperature.

Cooling was carried out by switching the furnace off and leaving the compacts to cool inside the furnace to room temperature. It should be noted that the flow of Argon was maintained during the whole cycle of sintering.

During sintering a number of events take place, e.g. diffusion which takes place at the contact areas between powder particles which causes the diminution of the surface area of the compact. Additionally, there are pore rounding which depends on the sintering temperature, relief of internal stress caused during compaction process and grain growth. A degree of densification will also occur in a liquid phase sintering once a small amount of liquid is formed, its further formation becomes rapid as the surface tension forces cause rapid flow and wetting of all other surfaces.

After sintering, there was a change in the volume of the compacts. This change in volume was different for each sintering temperature. The linear shrinkage was measured for the sintered compacts and the results are shown in figure (2.7). This figure shows that the linear shrinkage increases with the increase in sintering temperature. However, the amount of shrinkage varies in each stainless steel compact, where it can be seen that the amount of linear shrinkage of AISI 304L and AISI 316L are close to each other, whereas the amount of shrinkage for AISI 347 is less at all sintering temperatures. Moreover, the figure shows that at 900°C, stainless steel type AISI 347 compacts did not shrink but they were swollen. This means that they were not sintered

properly. It can be concluded that the higher the sintering temperature the larger the shrinkage.

Shrinkage is accompanied by densification. A parameter which measures the amount of densification is called densification parameter Φ which is defined as the change in density from the green state divided by the maximum possible density change⁽¹⁾:

$$\Phi = \frac{\rho_s - \rho_g}{\rho_t - \rho_g} \quad (2.1)$$

where: ρ_t is the theoretical density of the material.

ρ_s is the sintered density.

ρ_g is the green density.

Figure (2.8) shows the densification curves for stainless steel powder compacts. It can be seen that there is minimal densification for the compacts sintered at 900°C which is due to the solid state sintering. As for the other sintering temperatures it can be seen that the material densifies as the temperature increases. However, the densification of AISI 347 is less than the amount of densification of AISI 304L and AISI 316L. This could be due to the presence of niobium in the alloy as discussed earlier.

2.5.4 Machining:

All the stainless steel compacts were ground on both sides to the required height. The 10 mm diameter compacts were ground to a height of 8 mm, while the 5 mm diameter compacts were ground to a height of 5 mm.

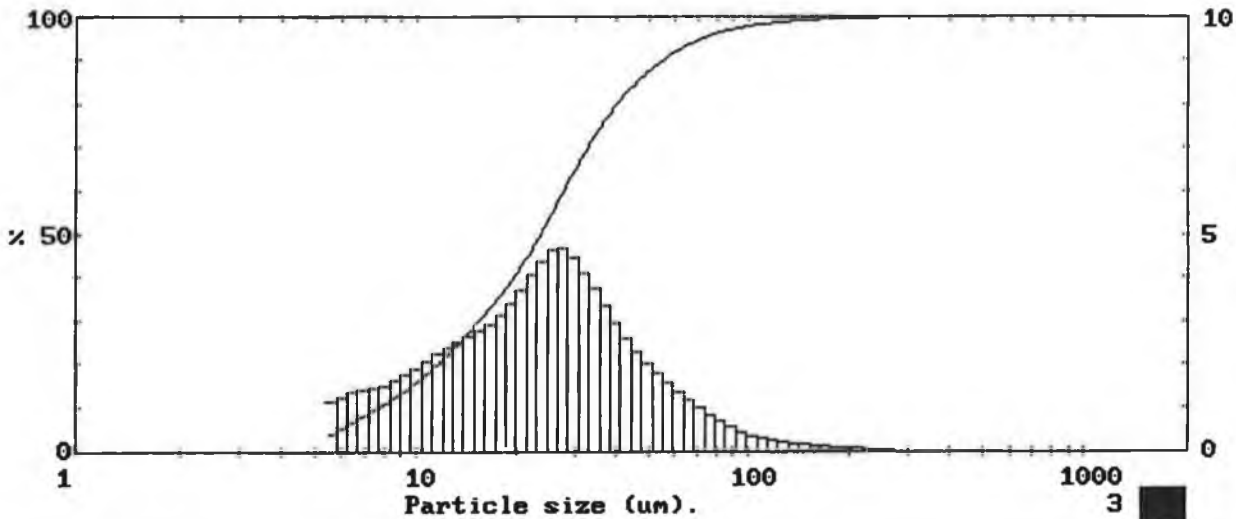
MALVERN Instruments SB.0B

stainless steel AISI 304L . 26-9-91. A.T.

00000650

1978 pil 1JP337

High Size	Under %	High Size	Under %	High Size	Under %	High Size	Under %	High Size	Under %	High Size	Under %	Span	
564	100	254	99.9	114	98.5	51.3	88.3	23.1	49.0	10.4	17.0	D[4,3]	
524	100	236	99.9	106	98.2	47.7	86.3	21.4	44.9	9.64	15.0	29.06 μ m	
488	100	219	99.8	98.6	97.8	44.4	84.0	19.9	41.2	8.97	13.3	D[3,2]	
454	100	204	99.7	91.7	97.4	41.2	81.4	18.5	37.8	8.34	11.7	15.20 μ m	
422	100	190	99.6	85.3	96.8	38.4	78.4	17.2	34.6	7.76	10.1	D[v,0.9]	
392	100	176	99.5	79.3	96.1	35.7	75.1	16.0	31.7	7.21	8.7	54.82 μ m	
365	100	164	99.4	73.8	95.3	33.2	71.3	14.9	28.9	6.71	7.2	D[v,0.1]	
339	100	153	99.3	68.6	94.3	30.8	67.2	13.9	26.3	6.24	5.9	7.71 μ m	
315	100	142	99.1	63.8	93.1	28.7	62.7	12.9	23.7	5.80	4.6	D[v,0.5]	
293	100	132	98.9	59.3	91.7	26.7	58.0	12.0	21.3			23.47 μ m	
273	100	123	98.7	55.2	90.1	24.8	53.4	11.2	19.1				
Source = Res.:steel		Beam length = 14.3 mm		Model indp		Record No. = 1		Log. Diff. = 3.338		Volume Conc. = 0.0064%		D[v,0.5]	
Focal length = 300 mm		Obscuration = 0.1647		Sp.S.A 0.3947 m ² /cc.		Presentation = pil		Volume distribution					



HARRIS IRELAND

Analysis sheet 1 Particle size results for AISI 304L.

MALVERN Instruments SB.0B

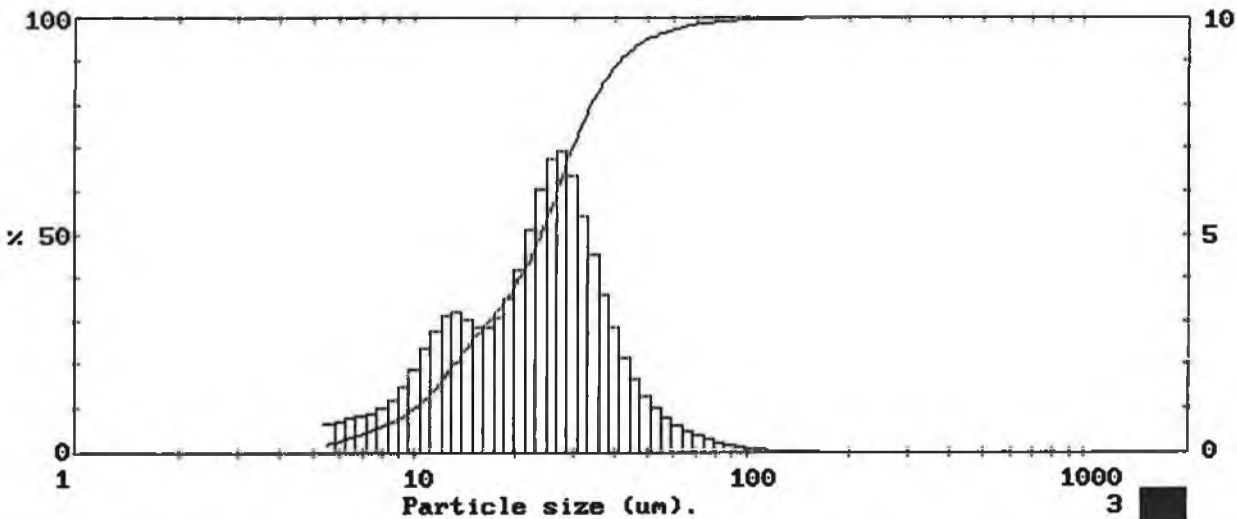
stainless steel AISI 316L . 26-9-91. A.T.
 ultra sonic bath with stir.
 dispersant Nopcosant K

000000651

000000654

1978 pil 1JP337

High Size	Under %	High Size	Under %	High Size	Under %	High Size	Under %	High Size	Under %	High Size	Under %	Span
564	100	254	100	114	99.7	51.3	95.4	23.1	47.6	10.4	11.1	D[4,3]
524	100	236	100	106	99.7	47.7	94.2	21.4	42.4	9.64	9.2	25.23 μ m
488	100	219	100	98.6	99.6	44.4	92.5	19.9	38.2	8.97	7.7	D[3,2]
454	100	204	100	91.7	99.4	41.2	90.3	18.5	34.7	8.34	6.5	17.14 μ m
422	100	190	100	85.3	99.3	38.4	87.4	17.2	31.6	7.76	5.5	D[v,0.9]
392	100	176	100	79.3	99.1	35.7	83.8	16.0	28.7	7.21	4.6	40.93 μ m
365	100	164	99.9	73.8	98.8	33.2	79.2	14.9	25.8	6.71	3.8	D[v,0.1]
339	100	153	99.9	68.6	98.4	30.8	73.8	13.9	22.7	6.24	3.0	9.95 μ m
315	100	142	99.9	63.8	97.9	28.7	67.4	12.9	19.5	5.80	2.3	D[v,0.5]
293	100	132	99.8	59.3	97.3	26.7	60.4	12.0	16.3			23.77 μ m
273	100	123	99.8	55.2	96.5	24.8	53.7	11.2	13.5			
Source = Res.:steel		Beam length = 14.3 mm		Model indp								
Record No. = 2		Log. Diff. = 3.478										
Focal length = 300 mm		Obscuration = 0.2438		Volume Conc. = 0.0112%								
Presentation = pil		Volume distribution		Sp.S.A 0.3501 m ² /cc.								



HARRIS IRELAND

Analysis sheet 2 Particle size results for AISI 316L.

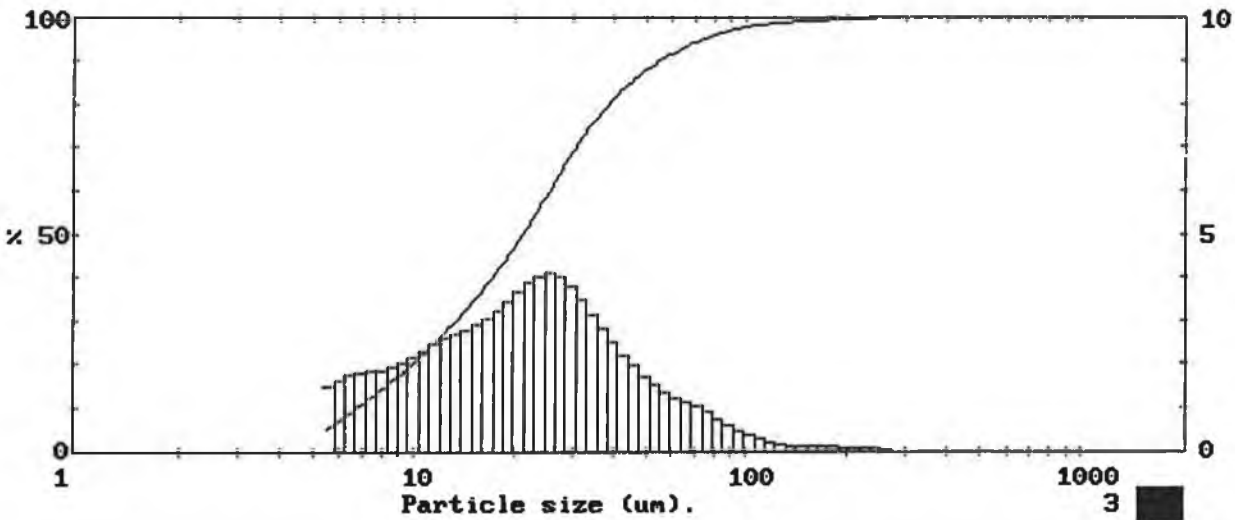
MALVERN Instruments SB.0B

stainless steel AISI 347 . 26-9-91. A.T.
 ultra sonic bath with stir.
 dispersant Nopcosant K

000000660

1978 pil 1JP337

High Size	Under %	High Size	Under %	High Size	Under %	High Size	Under %	High Size	Under %	High Size	Under %	Span
564	100	254	99.9	114	98.5	51.3	88.6	23.1	54.6	10.4	21.6	2.27
524	100	236	99.9	106	98.2	47.7	86.9	21.4	50.7	9.64	19.4	D[4,3]
488	100	219	99.8	98.6	97.8	44.4	84.9	19.9	47.1	8.97	17.3	27.59 μ m
454	100	204	99.7	91.7	97.3	41.2	82.7	18.5	43.6	8.34	15.4	D[3,2]
422	100	190	99.6	85.3	96.7	38.4	80.1	17.2	40.4	7.76	13.5	13.38 μ m
392	100	176	99.4	79.3	95.9	35.7	77.3	16.0	37.4	7.21	11.7	D[v,0.9]
365	100	164	99.3	73.8	95.0	33.2	74.1	14.9	34.5	6.71	9.8	54.65 μ m
339	100	153	99.2	68.6	94.0	30.8	70.6	13.9	31.7	6.24	8.1	D[v,0.1]
315	100	142	99.1	63.8	92.8	28.7	66.8	12.9	28.9	5.80	6.4	6.75 μ m
293	100	132	98.9	59.3	91.6	26.7	62.8	12.0	26.3			
273	100	123	98.7	55.2	90.2	24.8	58.7	11.2	23.9			
Source = Res.:steel		Beam length = 14.3 mm		Mode ¹ indp								D[v,0.5]
Record No. = 3		Log. Diff. = 2.853		Volume Conc. = 0.0024%								21.14 μ m
Focal length = 300 mm		Obscuration = 0.0736		Sp.S.A 0.4486 m ² /cc.								
Presentation = pil		Volume distribution										



HARRIS IRELAND

Analysis sheet 3 Particle size results for AISI 347.

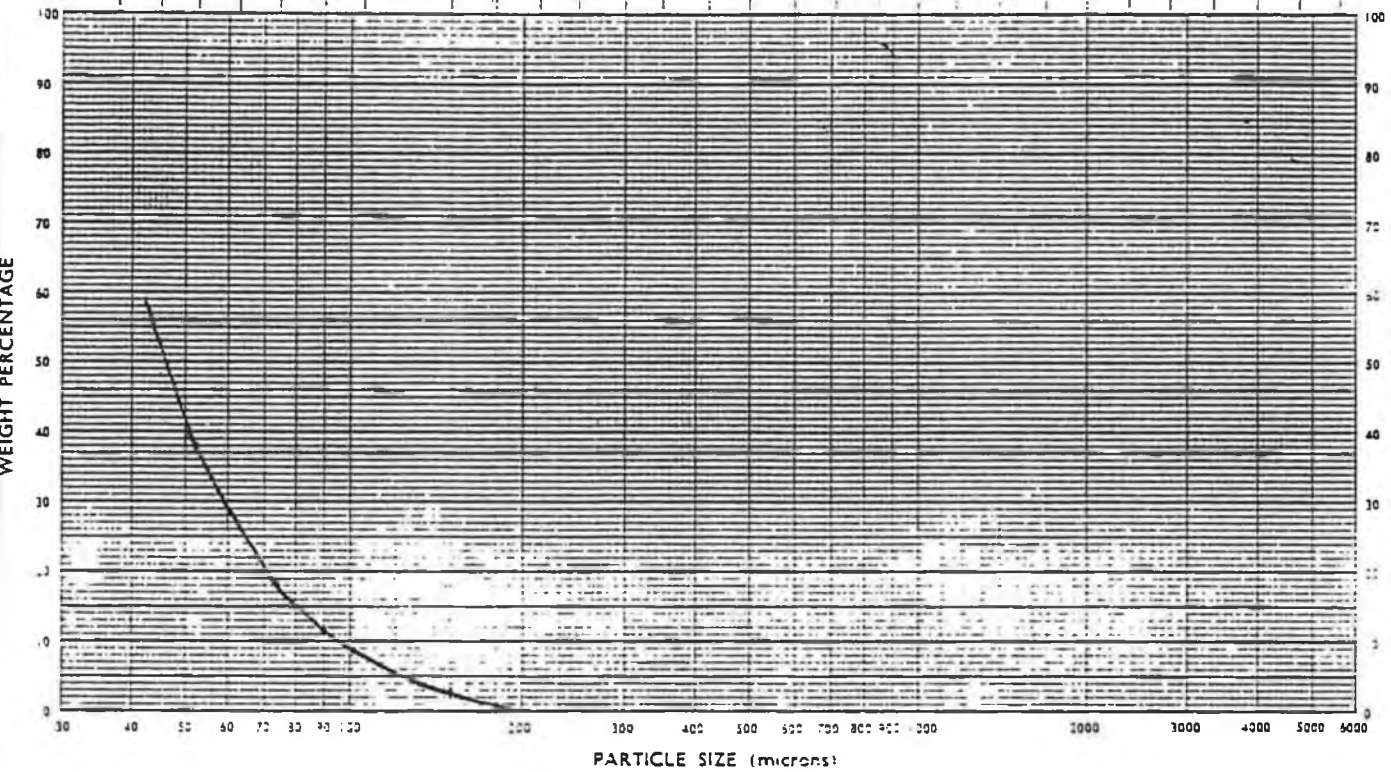
SIEVE ANALYSIS GRAPH SHEET

EQUIVALENT SIEVE MESH NUMBERS

B.S.	400	350	300	240	200	170	150	120	100	85	72	60	52	44	36	30	25	22	18	16	14	12	10	8	7	5	4	3	2	1	3/5	
A.S.T.M.	400	325	270	230	200	170	140	120	100	80	70	60	50	45	40	35	30	25	20	18	16	14	12	10	8	7	6	5	4	3	2	3/5

ISO SIEVE APERTURE SIZES (millimetres)

PRINCIPAL	0.038	0.045	0.053	0.063	0.075	0.090	0.106	0.125	0.150	0.180	0.212	0.250	0.300	0.355	0.425	0.500	0.600	0.710	0.850	1.00	1.18	1.40	1.75	2.00	2.36	2.80	3.35	4.75	SUPPLEMENTARY	5.60
-----------	-------	-------	-------	-------	-------	-------	-------	-------	-------	-------	-------	-------	-------	-------	-------	-------	-------	-------	-------	------	------	------	------	------	------	------	------	------	---------------	------



MESH No.	APERTURE SIZE millimetre micron	Weight (g)		PERCENTAGES		PERCENTAGES		PERCENTAGES	
		PERCENTAGES		PERCENTAGES		PERCENTAGES		PERCENTAGES	
		FRACTIONAL	CUMULATIVE	FRACTIONAL	CUMULATIVE	FRACTIONAL	CUMULATIVE	FRACTIONAL	CUMULATIVE
	180	0.0606		1.2	1.2				
	150	0.0875		1.8	3.0				
	90	0.4230		8.5	11.5				
	75	0.3354		6.7	18.2				
	53	0.9941		19.9	38.1				
	45	0.7282		14.6	52.7				
	PAN	2.9687		47.4	100.1				
	TOTAL	4.9985							

Lot # : D503

Date : 14/8/1991

Average Particle Size :

Binder Content : 15g/kg

Bulk Density : 1.738 g/cc

Moisture Content : 0.73 g/kg

Tap Density : 2.067 g/cc

Analysis sheet 4 Powder characteristics for D503.

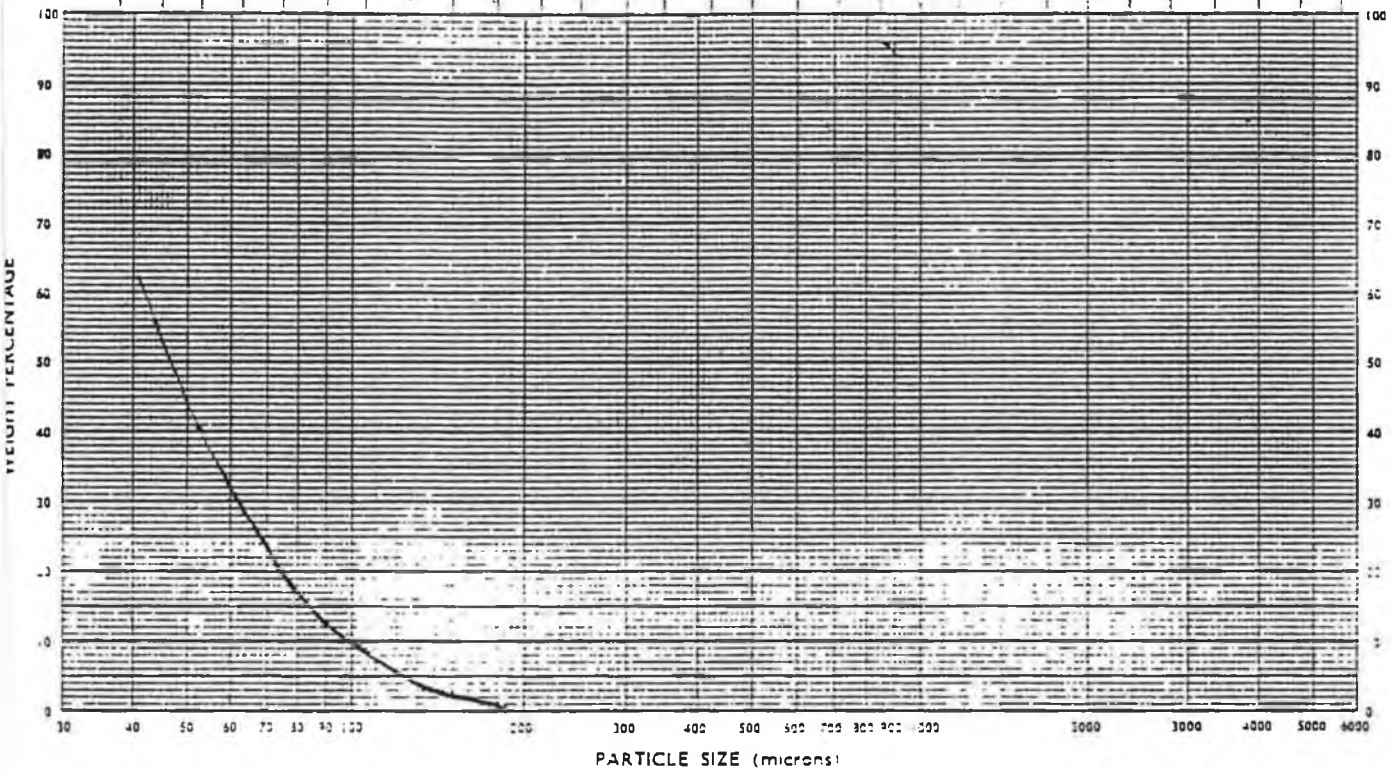
SIEVE ANALYSIS GRAPH SHEET

EQUIVALENT SIEVE MESH NUMBERS

B.S.	400	350	300	240	200	170	150	120	100	85	72	60	52	44	36	30	25	22	18	16	14	12	10	8	7	6	5	4	3	2	1
A.S.T.M.	400	325	270	230	200	170	140	120	100	80	70	60	50	45	40	35	30	25	20	18	16	14	12	10	8	7	6	5	4	3	2

ISO SIEVE APERTURE SIZES (millimetres)

PRINCIPAL	0.038	0.053	0.075	0.106	0.150	0.212	0.300	0.425	0.600	0.850	1.18	1.60	2.00	2.50	3.35	4.75	SUPPLEMENTARY
	0.045	0.063	0.090	0.125	0.180	0.250	0.355	0.500	0.710	1.00	1.40	2.00	2.80	4.00	5.60		



MESH No.	APERTURE SIZE millimetre micron	weight (g)		PERCENTAGES		PERCENTAGES		PERCENTAGES	
		PERCENTAGES		PERCENTAGES		PERCENTAGES		PERCENTAGES	
		FRACTIONAL	CUMULATIVE	FRACTIONAL	CUMULATIVE	FRACTIONAL	CUMULATIVE	FRACTIONAL	CUMULATIVE
	180	0.0438		0.9	0.9				
	150	0.0780		1.6	2.5				
	90	0.497		9.9	12.4				
	75	0.3914		7.8	20.2				
	53	1.0241		20.3	40.5				
	45	0.7405		14.7	55.2				
	PAN	2.2683		45.0	100.2				
	TOTAL	5.0431							

Lot # : D504

Date : 14/8/1991

Average Particle Size :

Binder Content : 13.3 g/kg

Bulk Density : 1.716 g/cc

Moisture Content : 0.78 g/kg

Tap Density : 2.073 g/cc

Analysis sheet 5 Powder characteristics for D504.

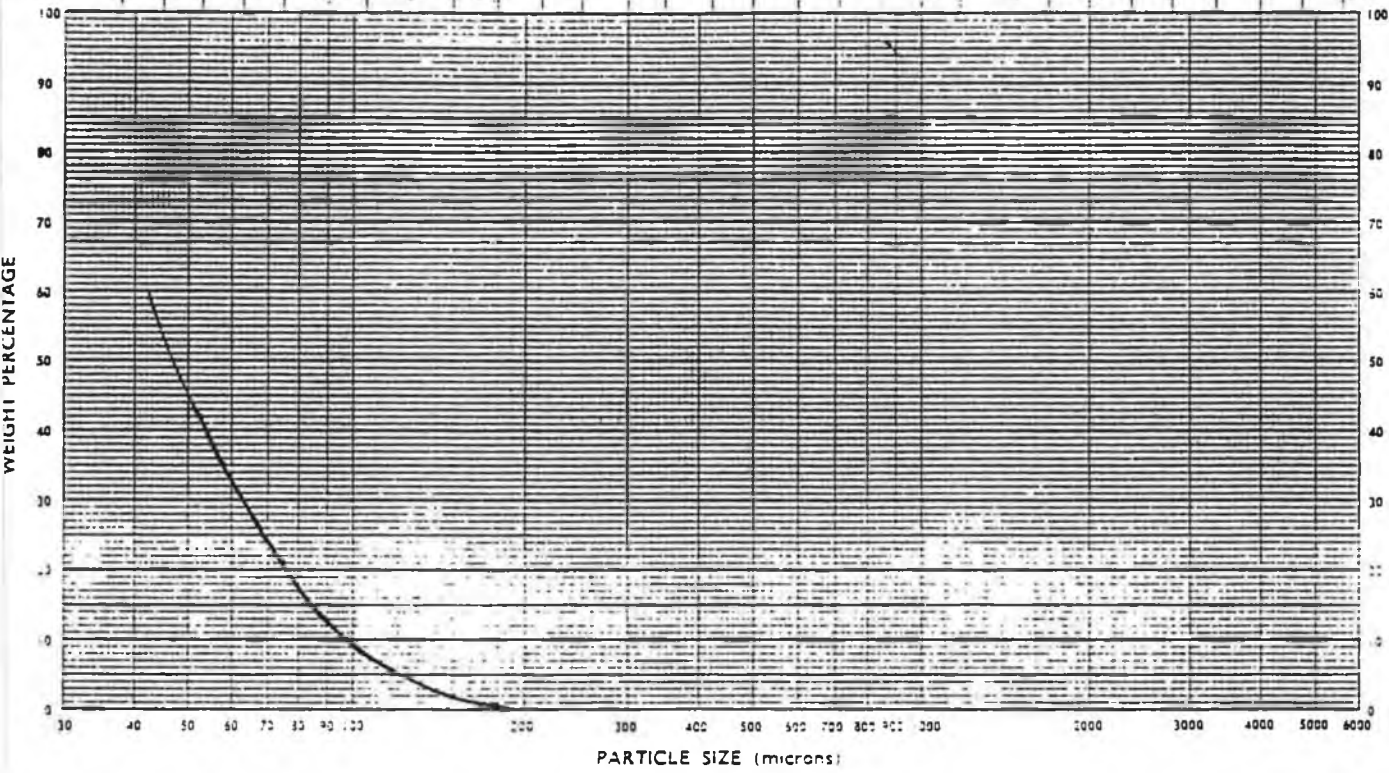
SIEVE ANALYSIS GRAPH SHEET

EQUIVALENT SIEVE MESH NUMBERS

B.S.	400	350	300	240	200	170	150	120	100	85	72	60	52	44	36	30	25	22	18	16	14	12	10	8	7	6	5	4	3	3.5	
A.S.T.M.	400	325	270	230	200	170	140	120	100	80	70	60	50	45	40	35	30	25	20	18	16	14	12	10	8	7	6	5	4	3	3.5

ISO SIEVE APERTURE SIZES (millimetres)

PRINCIPAL	0.038	0.045	0.053	0.063	0.075	0.106	0.150	0.212	0.300	0.425	0.600	0.850	1.18	1.60	2.00	2.50	3.15	4.75	SUPPLEMENTARY	5.60
-----------	-------	-------	-------	-------	-------	-------	-------	-------	-------	-------	-------	-------	------	------	------	------	------	------	---------------	------



MESH No.	APERTURE SIZE millimetre micron	PERCENTAGES		PERCENTAGES		PERCENTAGES		PERCENTAGES	
		FRACTIONAL	CUMULATIVE	FRACTIONAL	CUMULATIVE	FRACTIONAL	CUMULATIVE	FRACTIONAL	CUMULATIVE
	180	0.0367		0.73	0.73				
	150	0.0549		1.09	1.82				
	90	0.5685		11.29	13.11				
	75	0.4048		8.04	21.15				
	53	1.0531		20.92	42.07				
	45	0.6553		13.02	55.09				
	PAN	2.2612		44.91	100				
	TOTAL	5.0345							

Lot # : D505

Date : 14/8/1991

Average Particle Size :

Binder Content : 16.5 g/kg

Bulk Density : 1.7852 g/cc

Moisture Content : 0.9 g/kg

Tap Density : 2.1582 g/cc

Analysis sheet 6 Powder characteristics for D505.

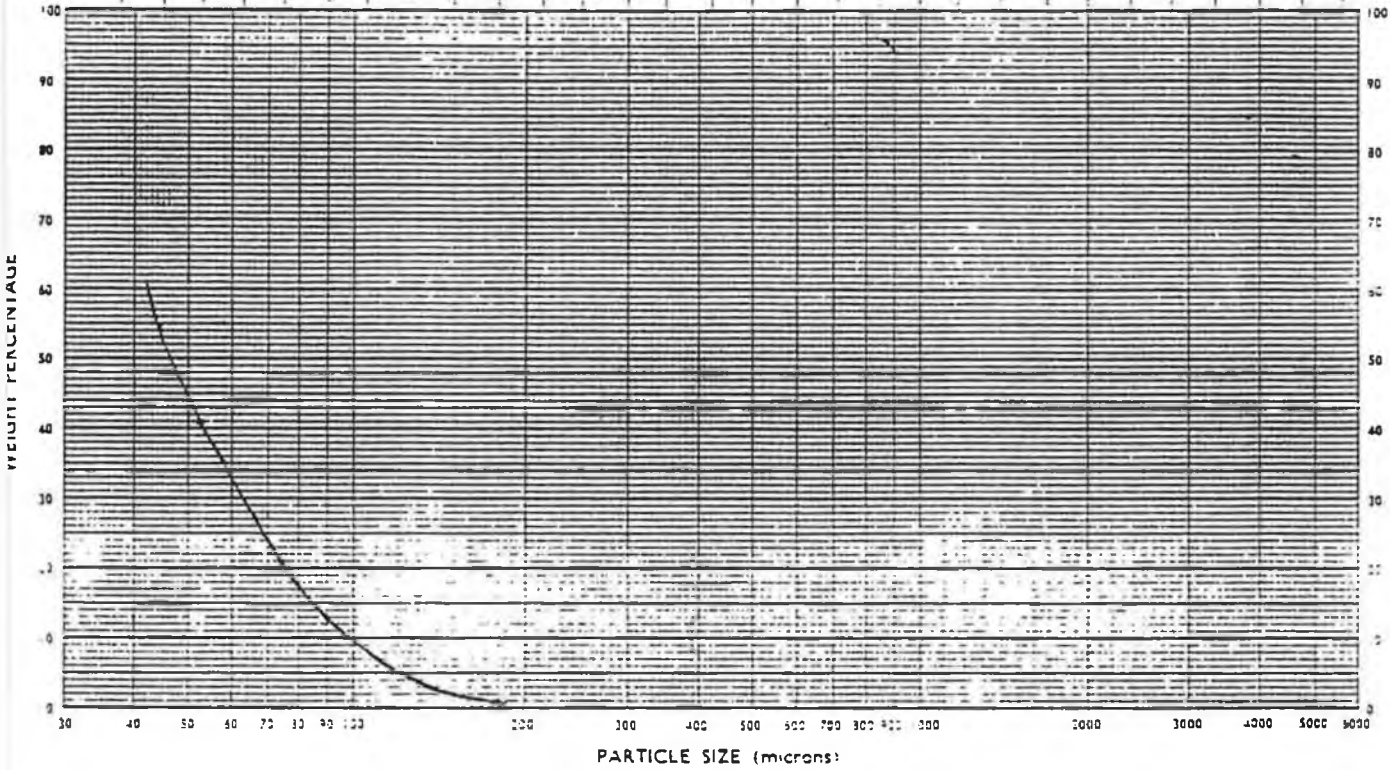
SIEVE ANALYSIS GRAPH SHEET

EQUIVALENT SIEVE MESH NUMBERS

B.S.	400	350	300	240	200	170	150	120	100	85	72	60	52	44	36	30	25	22	18	16	14	12	10	8	7	5	4	3	2	1	0.5	
A.S.T.M.	400	325	270	230	200	170	140	120	100	80	70	60	50	45	40	35	30	25	20	18	16	14	12	10	8	7	6	5	4	3	2	1

ISO SIEVE APERTURE SIZES (millimetres)

PRINCIPAL	0.038	0.045	0.053	0.063	0.075	0.090	0.106	0.125	0.150	0.180	0.212	0.250	0.300	0.355	0.425	0.500	0.600	0.710	0.850	1.00	1.18	1.40	1.75	2.00	2.36	2.80	3.35	4.00	4.75	SUPPLEMENTARY	5.60
-----------	-------	-------	-------	-------	-------	-------	-------	-------	-------	-------	-------	-------	-------	-------	-------	-------	-------	-------	-------	------	------	------	------	------	------	------	------	------	------	---------------	------



MESH No.	APERTURE SIZE millimetre micron	PERCENTAGES		PERCENTAGES		PERCENTAGES		PERCENTAGES	
		FRACTIONAL	CUMULATIVE	FRACTIONAL	CUMULATIVE	FRACTIONAL	CUMULATIVE	FRACTIONAL	CUMULATIVE
	180	0.0390		0.78	0.78				
	150	0.0529		1.06	1.84				
	90	0.5727		11.43	13.27				
	75	0.396		7.90	21.17				
	53	0.9986		19.93	41.1				
	45	0.6762		13.50	54.6				
	PAN	2.275		45.4	100				
	TOTAL	5.6104							

Lot # : D506

Date : 14/8/1991

Average Particle Size :

Binder Content : 24.14g/kg

Bulk Density : 1.688g/cc

Moisture Content : 0.74g/kg

Tap Density : 2.088g/cc

Analysis sheet 7 Powder characteristics for D506.



Plate 2.1 Photograph of the V-Mixer.



Plate 2.2 Photograph of the Turbula Shaker-Mixer.



Plate 2.3 Photograph of the 5 mm. diameter die set.

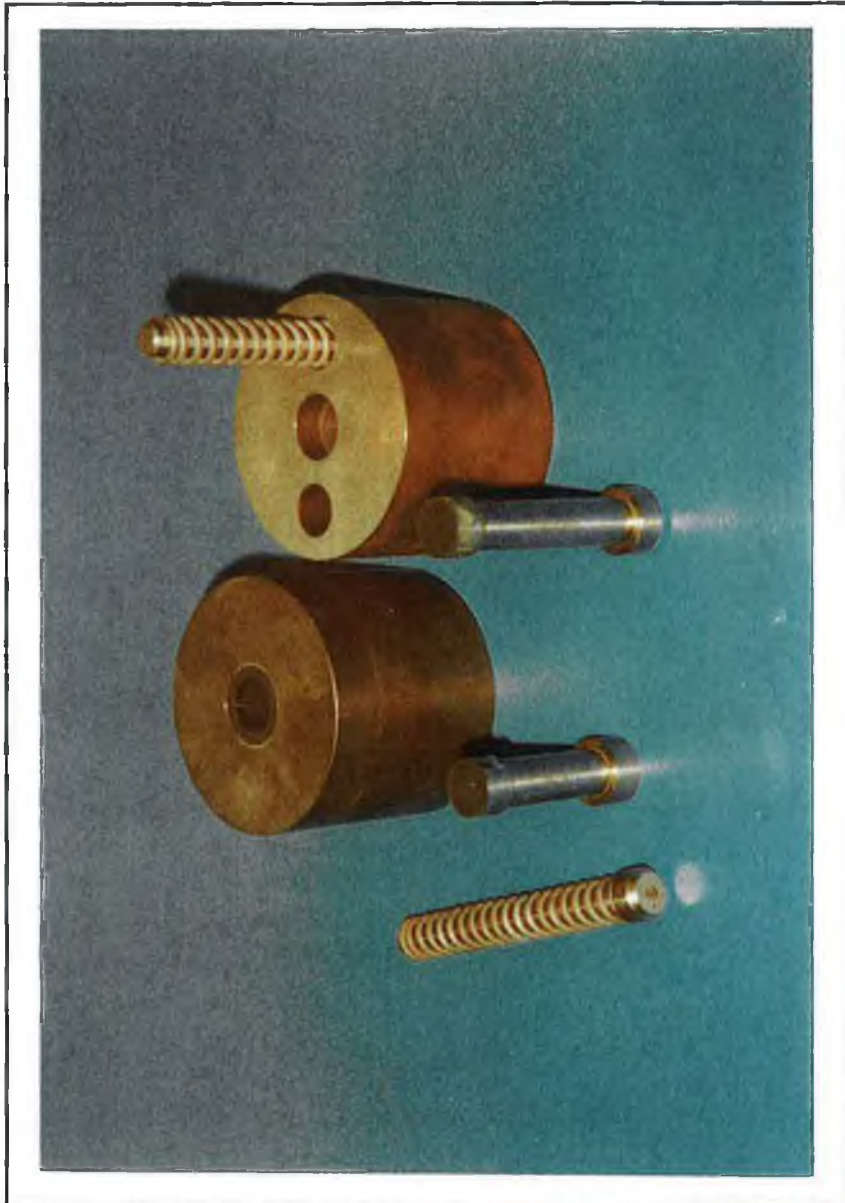


Plate 2.4 Photograph of the 17 mm. diameter die set.

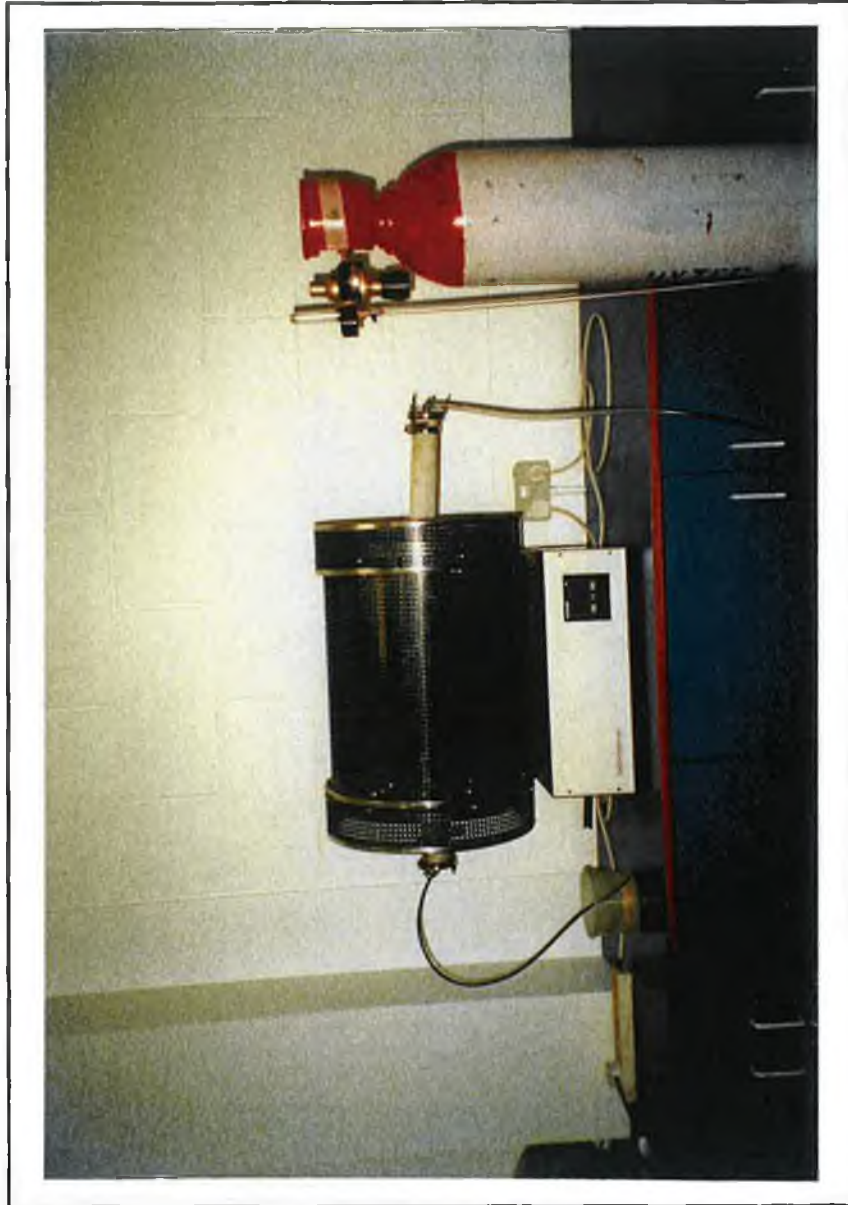


Plate 2.5 Photograph of the tube furnace.



Plate 2.6 Photograph of the Universal Testing Machine.



Plate 2.7 Photograph of the Ballistic Testing Machine.

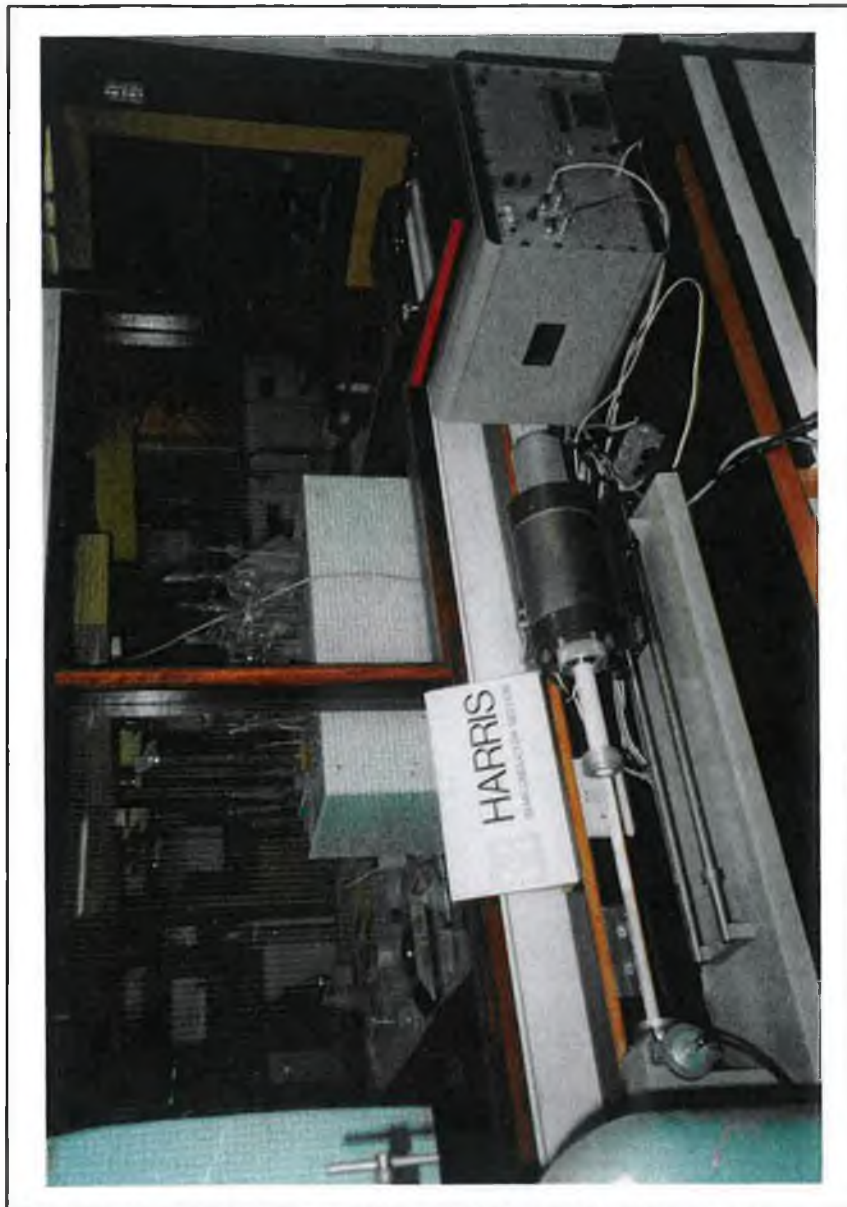


Plate 2.8 Photograph of the Dilatometer.

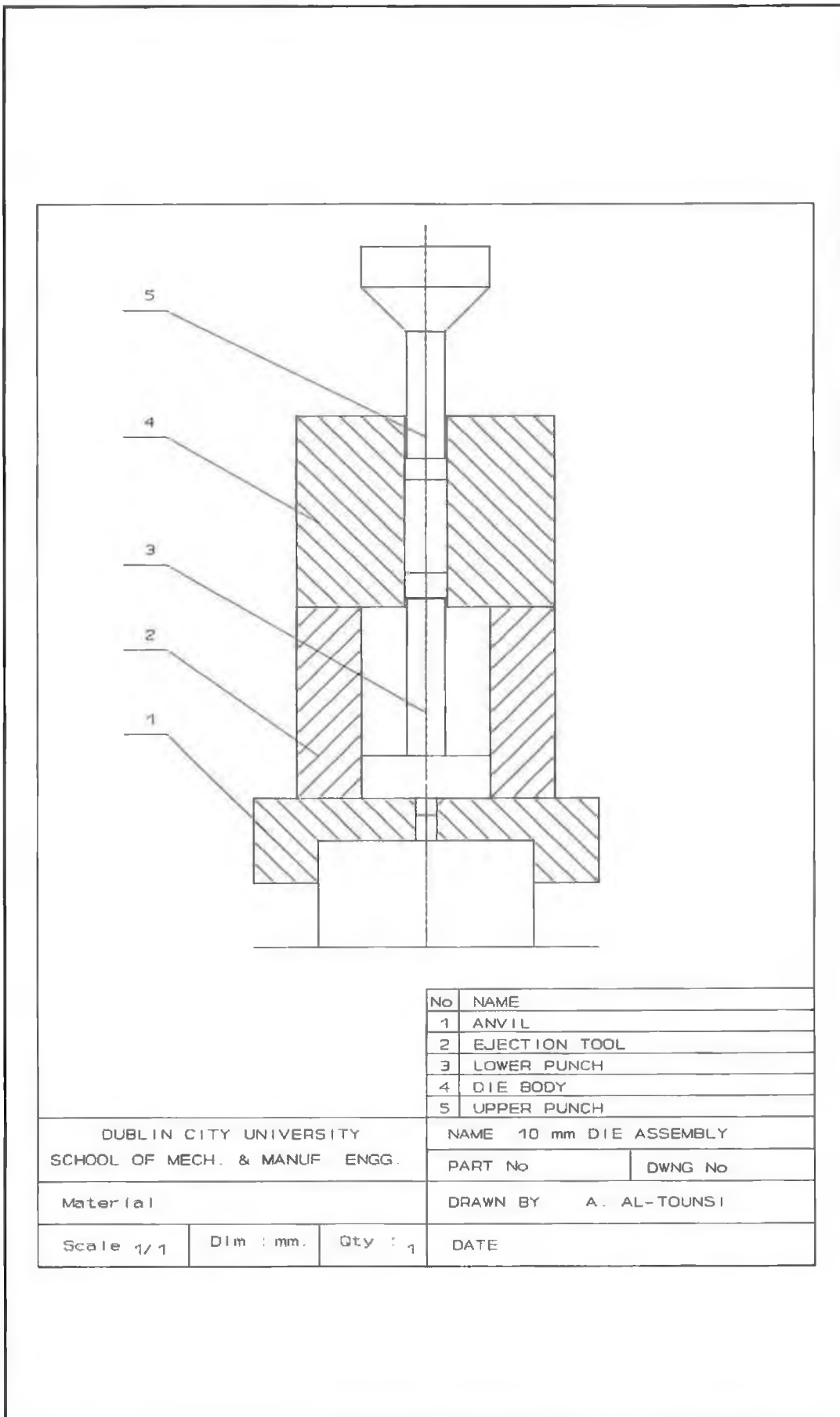
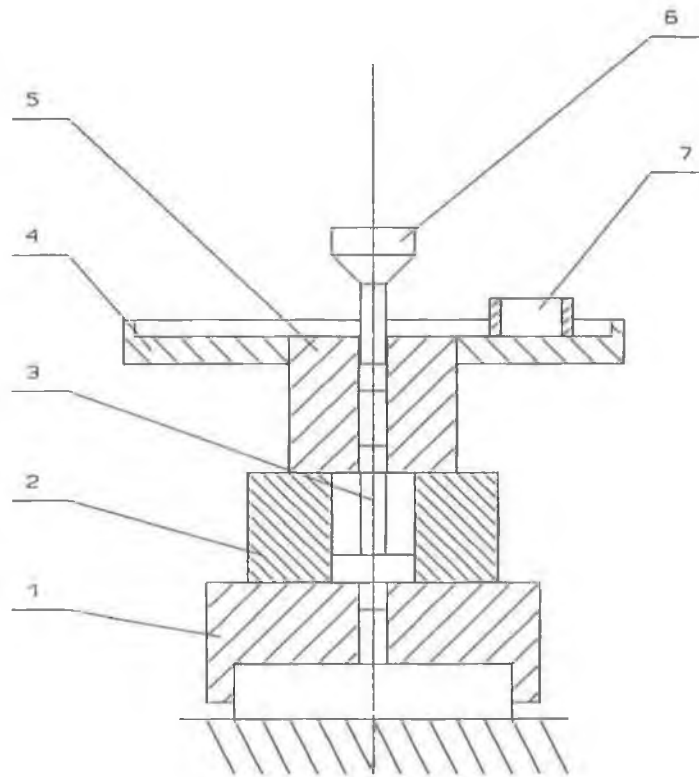


Figure 2.1 Assembly drawing of the 10 mm. die set.



No	NAME
1	ANVIL
2	EJECTION TOOL
3	LOWER PUNCH
4	TRAY
5	DIE BODY
6	UPPER PUNCH
7	FEEDING RING

DUBLIN CITY UNIVERSITY		NAME 5 mm DIE ASSEMBLY	
SCHOOL OF MECH. & MANUF. ENGG.		PART No	DWNG No
Material		DRAWN BY A. AL-TOUNSI	
Scale 1/1	Dim : mm.	Qty : 1	DATE

Figure 2.2 Assembly drawing of the 5mm. die set.

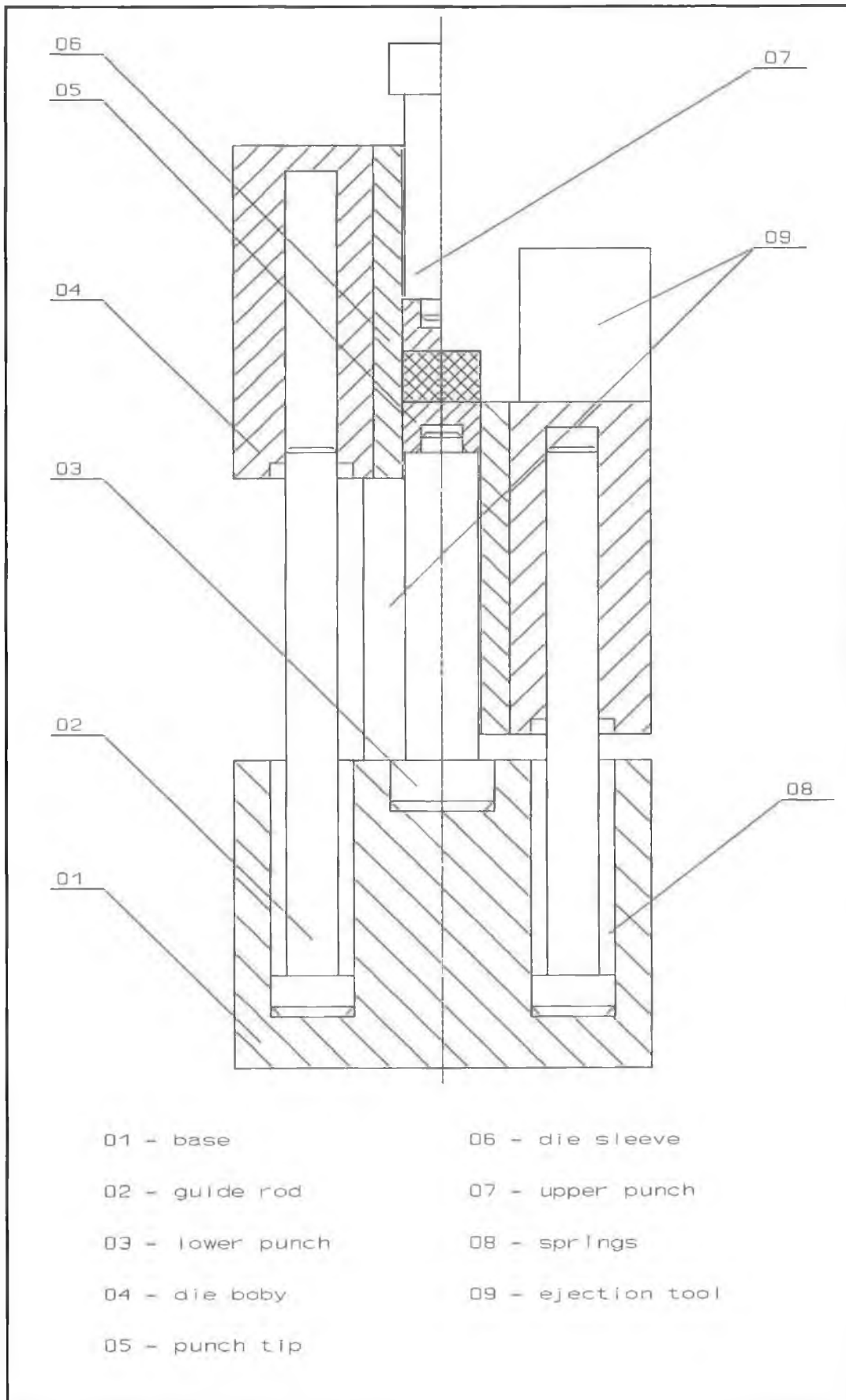
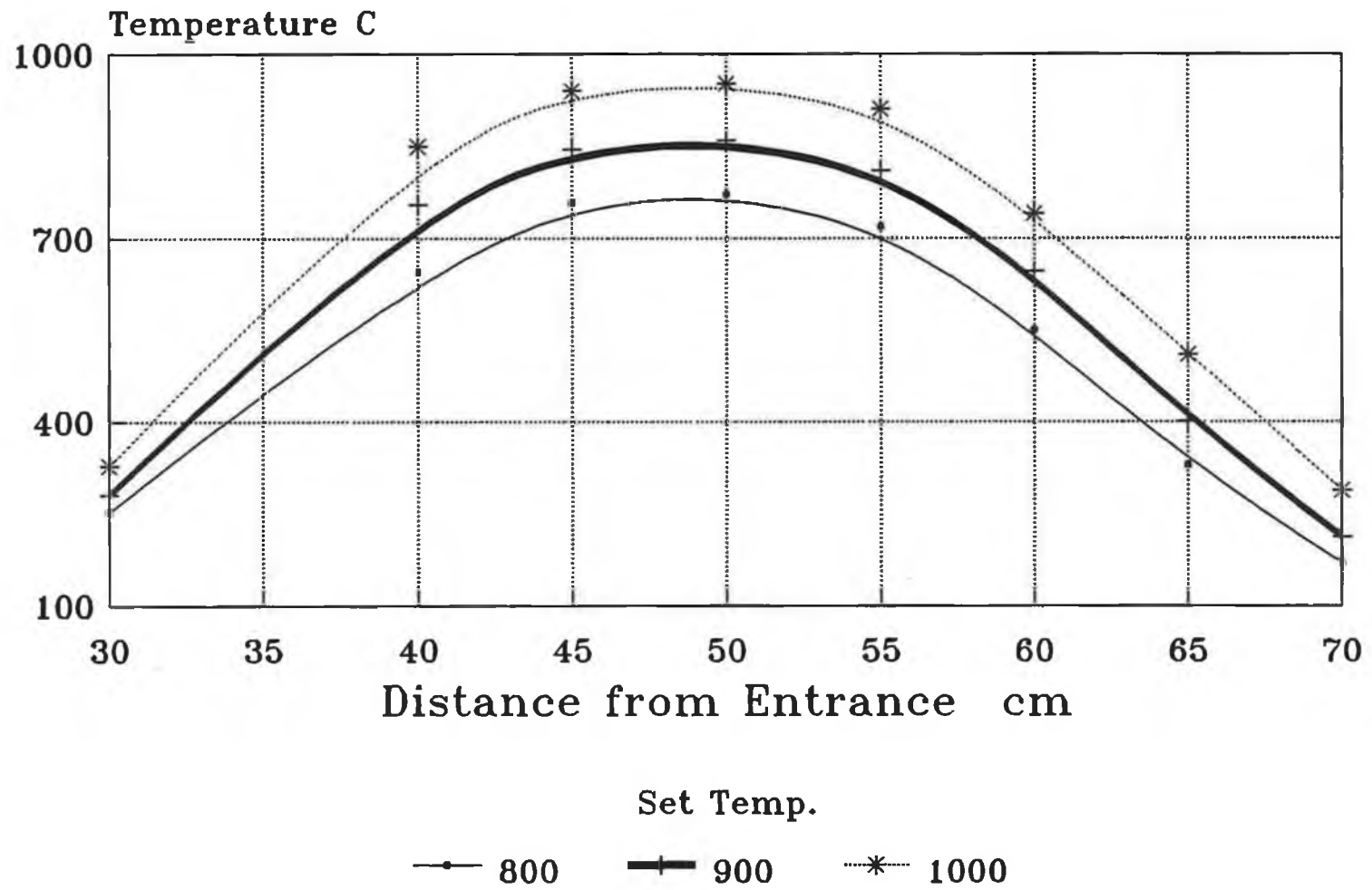


Figure 2.3 Assembly drawing of the 17mm diameter compaction die set.

Figure 2.4 Furnace calibration curves.



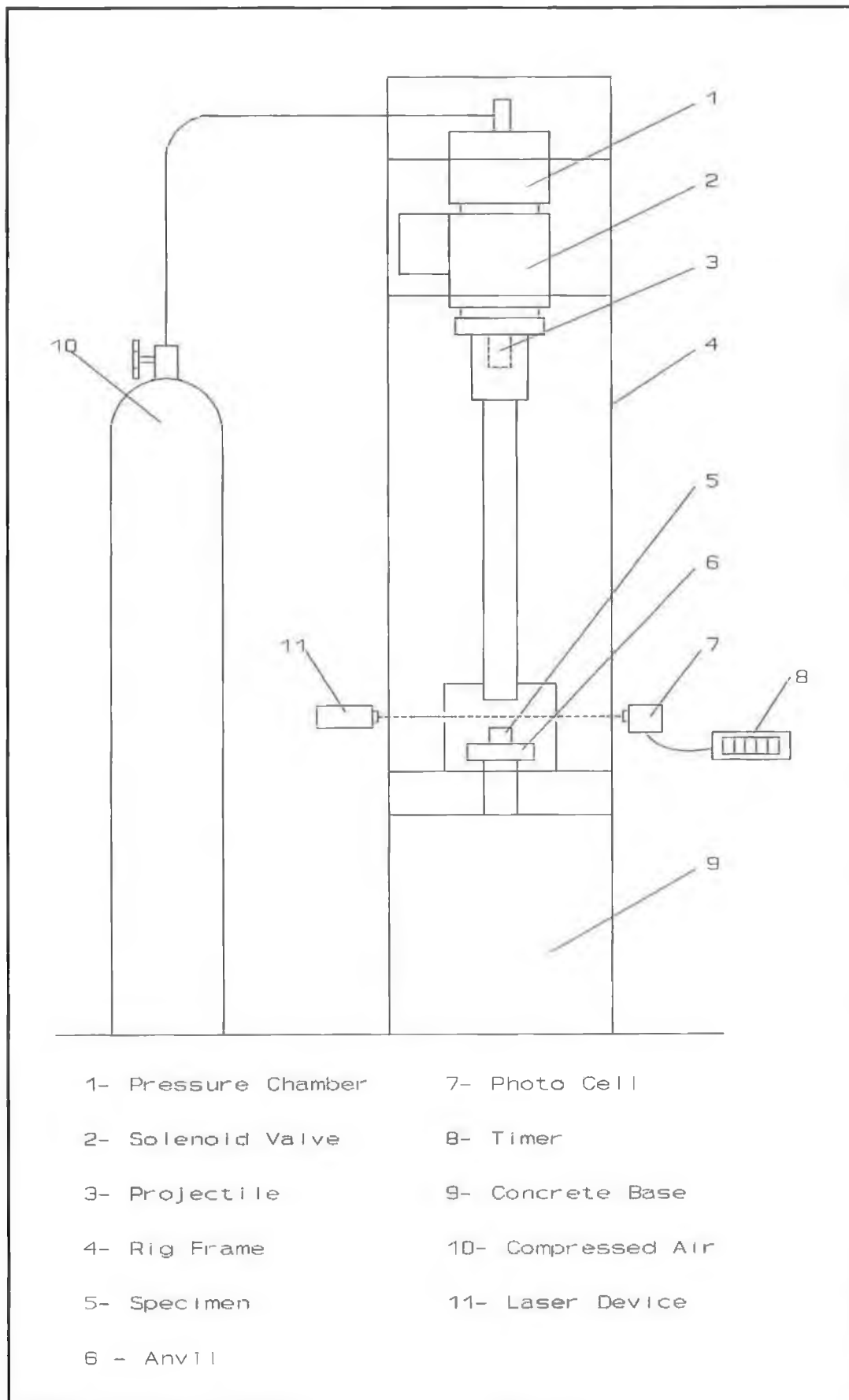


Figure 2.5 Schematic diagram of the ballistic testing machine.

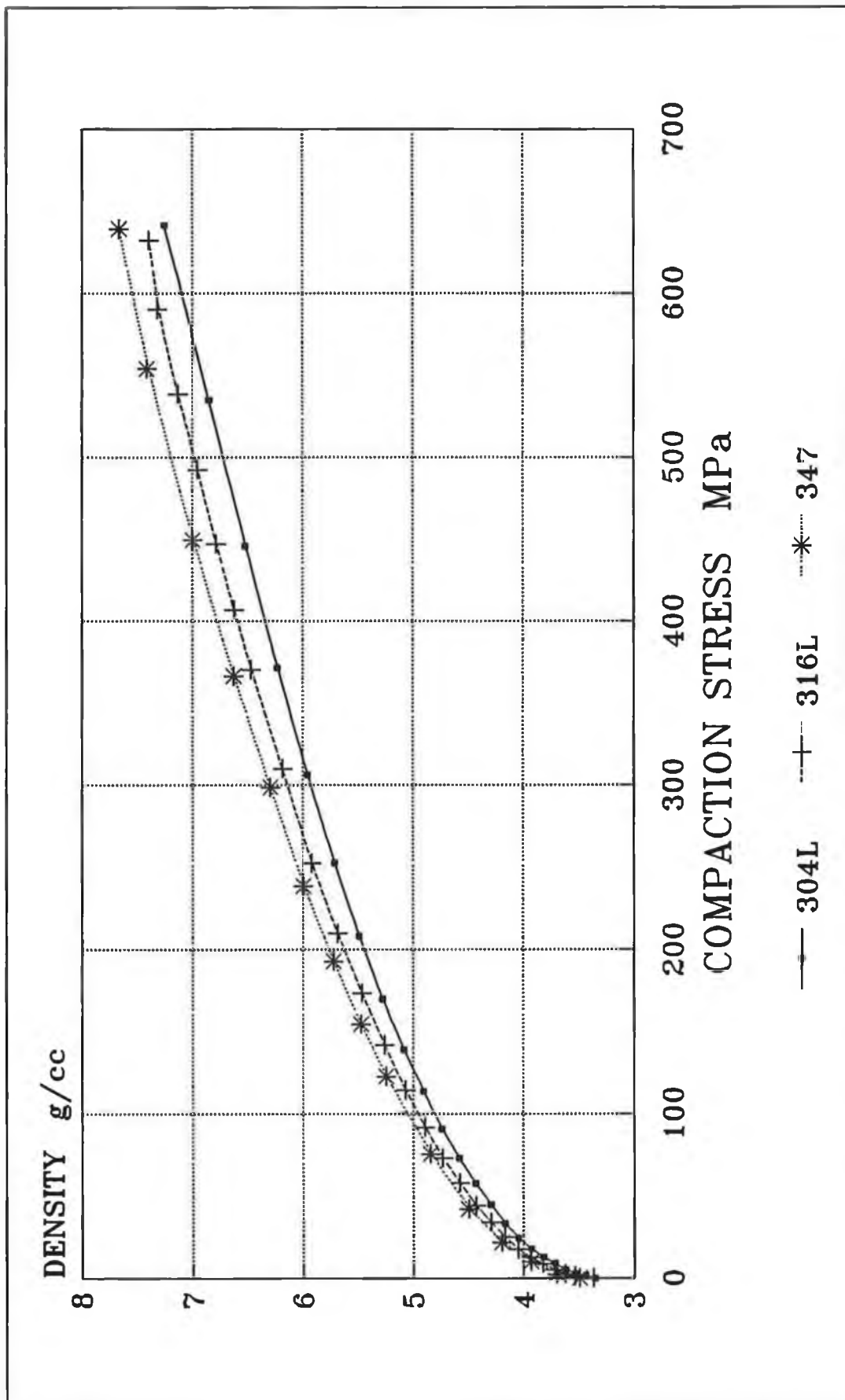


Figure 2.6 Compressibility curves for three stainless steel powders.

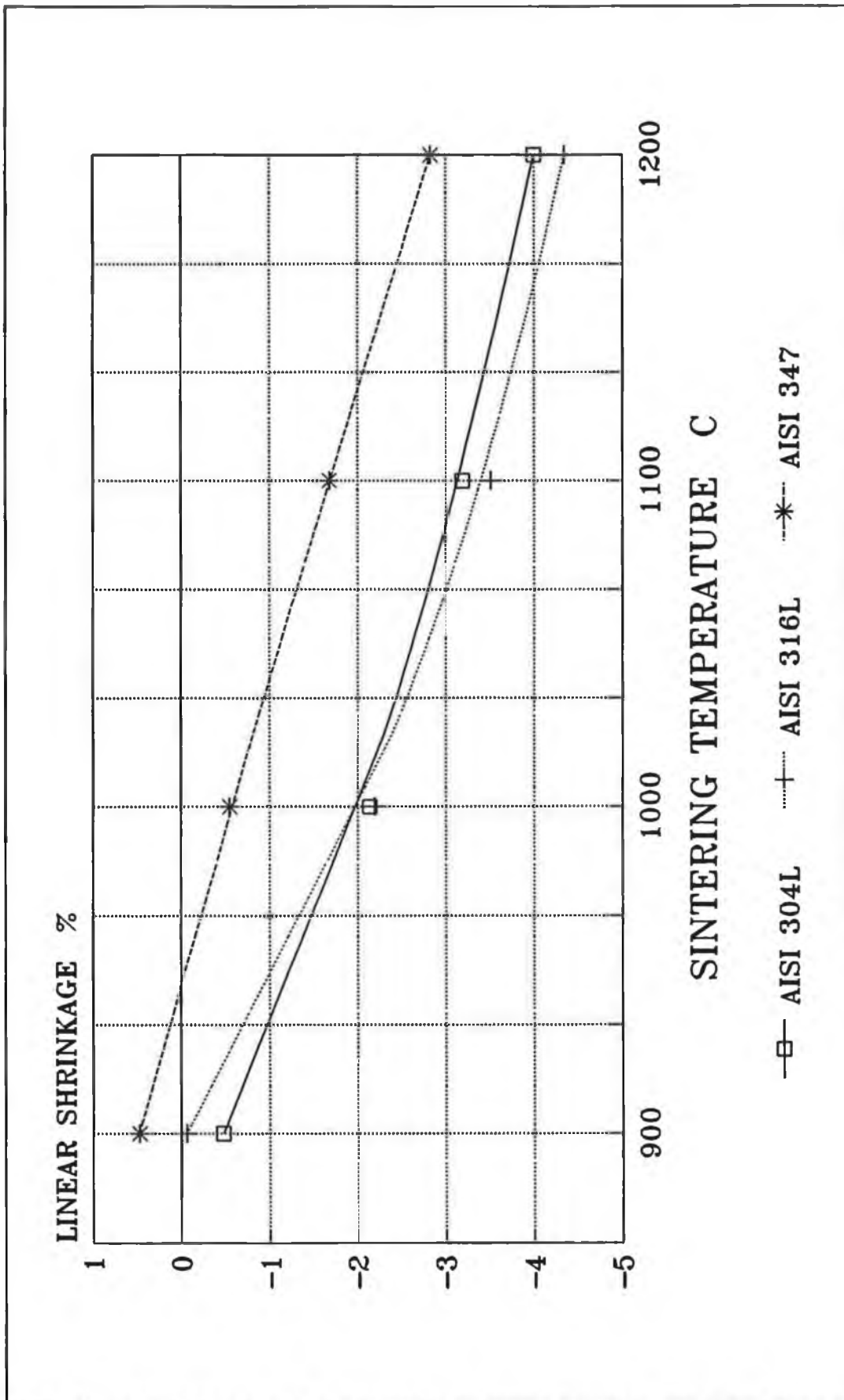


Figure 2.7 Effect of sintering temperature on the linear shrinkage of stainless steel compacts.

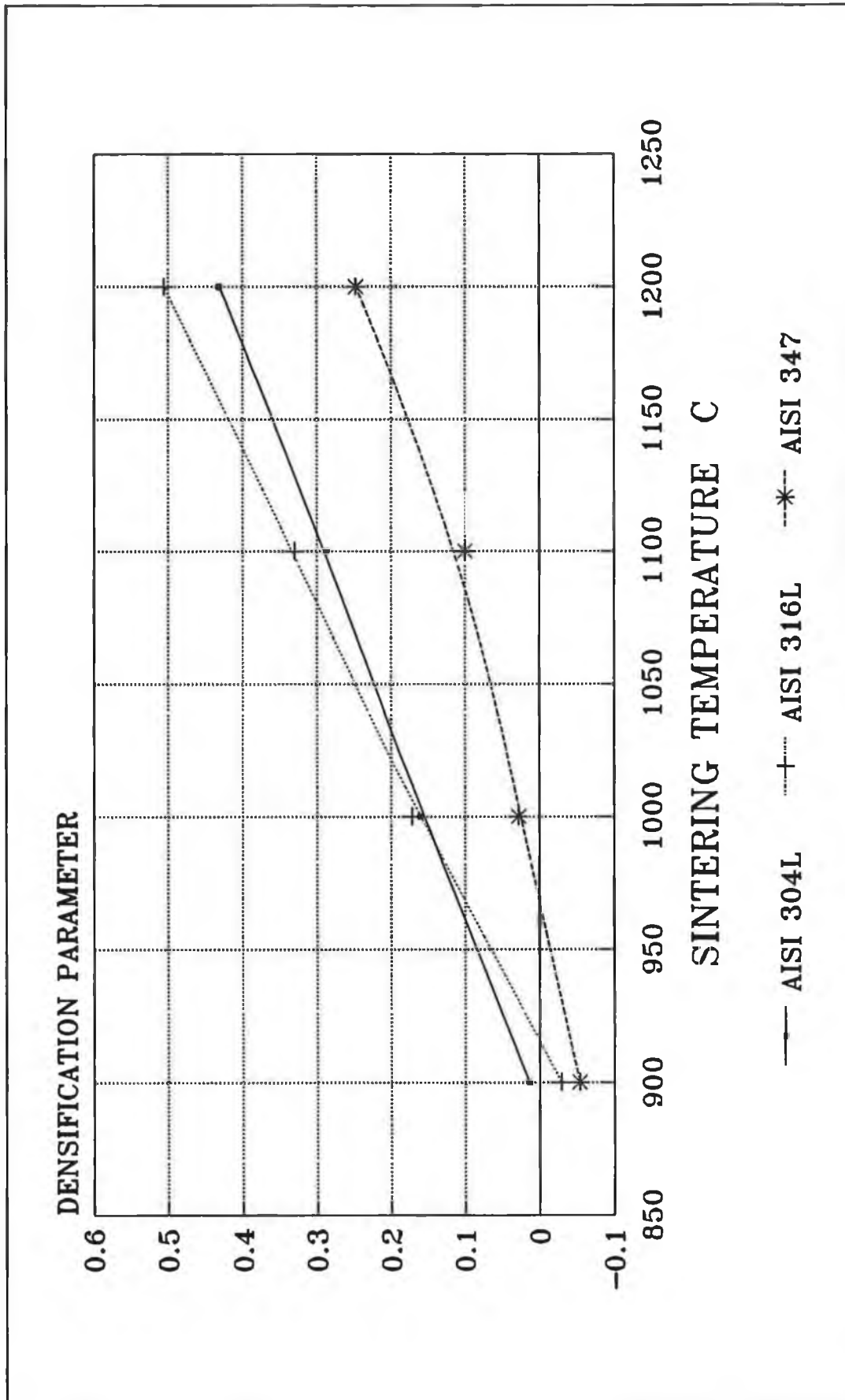


Figure 2.8 Effect of sintering temperature on densification of stainless steel compacts.

CHAPTER THREE

TEST PROCEDURE AND RESULTS

3.1 INTRODUCTION:

Sintering has a major influence on the mechanical properties of sintered compacts, since it influences the degree of diffusion between powder particle, the grain size and the status of alloys and phases of the material. In a controlled furnace atmosphere the main two sintering parameters are time and temperature. The effect of sintering temperature on the mechanical properties of stainless steel compacts at high strain rates and under static loading have been studied in this work. For this purpose four sintering temperatures (900, 1000, 1100 and 1200°C) were chosen for examining the mechanical properties of three types of stainless steel powder AISI 304L, AISI 316L and AISI 347. It was mentioned earlier that some difficulties have been observed in compacting and handling the compacts of AISI 347 and upon examining the sintered compacts of AISI 347 which were sintered at 900°C it was found that they did not sinter properly and the compacts' dimensions have been increased. This indicates that swell takes place which degraded the compact's mechanical properties. For these reasons the

compacts of AISI 347 which were sintered at 900°C were excluded from this work.

Two kinds of tests have been carried out on the sintered compacts. The first is a simple static compression test using lubricant to establish a constitutive equation to describe the relation between stress and strain. The second test was a dynamic compression test which was carried out by firing a projectile onto the sintered compact.

3.2 STATIC TEST PROCEDURE:

3.2.1 RESULTS:

The sintered compacts were quasi-statically compressed at room temperature between polished flat platens with the use of polyethylene sheets as a lubricant to reduce the friction between the compact and the platens. Different kinds of lubricants had been tried e.g. Petroleum jelly, Graphite and graphite mixed with petroleum jelly. However, none of these was as effective as the polyethylene sheets in reducing the friction significantly and minimizing the barrelling of the specimen. During compression the load was interrupted to introduce a new sheet at intervals of 0.05 strain and to measure the height and diameter of the compressed compact. During these tests the specimen kept its cylindrical shape and negligible barrelling had occurred due to the use of the polyethylene sheets.

Calculation of the current density was done by measuring the current height, current diameter and weight of specimen under test. As for the stress, it was calculated from the recorded load and the current diameter.

3.2.2 DISCUSSION:

Figures (3.1), (3.2) and (3.3) show the stress strain curves for AISI 304L, AISI 316L and AISI 347 respectively, which were sintered at 4 sintering temperatures. It should be noted that figure (3.3) shows the stress strain curve for AISI 347 compacts sintered at three temperatures. The sintering at 900°C was excluded due to the difficulty which was mentioned earlier. It can be seen from these figures that there is a strain hardening effect in all the curves. Moreover, by comparing figure(3.1) and (3.2) it can be noticed that the stress-strain curve for the materials sintered at 900°C follow a different pattern from the other sintering temperatures, where it can be seen that the material shows higher tendency to deformation at lower loads. This could be due to the lower sintering temperature. As for the other sintering temperatures it can be seen that the flow stress did not change after sintering at temperatures higher than 1000°C. Furthermore, It can be seen that the strain hardening slope increases with the increase in sintering temperature. This could be due to the increase in density which gives the material higher resistance to deformation.

The density of the compacts was measured during the

static test to find out the amount of densification taken place during compression. Figures (3.4), (3.5) and (3.6) show the densification curves during compression for AISI 304L, AISI 316L and AISI 347 respectively. It can be seen that the curves seem to fit a linear relationship. Moreover, it can be noticed that the slope of the curves decrease with the increase in the initial density of the compact. Furthermore, the amount of additional densification is decreased with the increase in sintering temperature or the initial density of the sintered compact, where it can be seen that for a given strain the compacts which are sintered at 900°C, as shown in figures (3.4) and (3.5), densify more than the compacts sintered at higher temperatures. It should also be mentioned that compacts made from AISI 347 which were sintered at 900°C, were not included in the experiments.

Two equations are developed from the above results. The first equation relates the stress, strain and density for stainless steel compacts. As known, the stress-strain property of sintered compacts is dependent on the density of the compact because, as seen before, the density of the compact increases during deformation. The equation has the form:

$$\sigma_s = A R_0 e^{B R_0^C} \quad (3.1)$$

where: σ_s is the stress.

R_0 is the initial relative density.

ϵ is the axial strain.

A , B and C are constants.

The constants A , B and C were determined using the least square method in regression and their values are listed in table (3.1) for each material and sintering temperature.

Table 3.1 Values of the constants in equation 3.1 for three types of stainless steel.

Material	Sintering Temperature °C	Constants		
		A	B	C
AISI 304L	900	1500	0.45	-1.3
	1000	1098	0.25	-2.6
	1100	1213	0.3	-2.5
	1200	1266	0.35	-2.4
AISI 316L	900	1261	0.3	-2.6
	1000	1048	0.25	-2.6
	1100	1135	0.24	-2.2
	1200	1290	0.26	-2.3
AISI 347	1000	1185	0.37	-2.
	1100	1030	0.24	-3.
	1200	1100	0.29	-2.1

The second equation which describes the density changes with respect to strain was formulated. This equation is useful for calculating the resultant density due to a given amount of straining. The equation has the form:

$$\rho_c = \rho_0 + m \epsilon \quad (3.2)$$

where: ρ_c is the current density.

ρ_0 is the initial density.

ϵ is the axial strain.

m is a constant which represent the slope of the curve.

The constant m was determined using the least square method in regression and the values of the constant are shown in table (3.2) for each material and sintering temperature.

3.3 BALLISTIC TEST PROCEDURE:

Ballistic tests were carried out for all three types of stainless steel used in this work except for one batch of AISI 347 which was sintered at 900°C. Tests were carried out using the ballistic testing apparatus. The machine was first calibrated to find the relation between the speed of the projectile and the air pressure and the calibration curve is shown in figure (3.7). The projectile speed was consistent at a given air pressure due to the replacement of the ball valve with a solenoid valve. From the calibration curve, it was possible to set the air pressure in the apparatus to fire the projectile at a specified speed. It should be noted that the curve was used as a guide line for setting the air pressure and the exact speed of the projectile was determined in each test by means of the laser beam device.

The test was carried out as follows: the specimen was placed on the anvil of the machine between two polyethylene sheet to reduce friction and give the same conditions of

Table 3.2 Values of the constant m in equation 3.2 for three types of stainless steel.

Material	Sintering Temperature °C	Constant m
AISI 304L	900	1.260
	1000	0.862
	1100	0.506
	1200	0.393
AISI 316L	900	1.308
	1000	0.961
	1100	0.616
	1200	0.351
AISI 347	1000	1.177
	1100	1.116
	1200	0.904

compression as in the static test. The projectile was placed in the firing chamber and the pressure chamber was filled with air to a specified pressure. After this setting the solenoid valve was opened and the air was released to propel the projectile with the required speed to hit the specimen. The speed of the projectile was recorded by means of a laser beam device and the dimensions of the specimen after impact were measured.

3.3.1 RESULTS:

Figure (3.8) shows results of the ballistic testing apparatus for compacts made from AISI 304L sintered at four sintering temperatures. This figure shows the resultant axial strain vs. the impact speed where it can be seen that there is only small difference in the amount of deformation for different sintering temperatures. However, it can be noticed that the specimens sintered at 1200°C show the greatest

amount of deformation. Figure (3.9) shows the results of axial strain vs. impact speed for AISI 316L for four sintering temperatures. It can be seen that the difference in the amount of the deformation for the four different sintering temperatures is greater than the one in the previous figure. Moreover, the slope of the curves increases significantly with the increase in sintering temperature. Figure (3.10) shows the results of axial strain vs. impact speed for AISI 347 for three sintering temperatures. It can also be seen that the curves are close to each other with the specimens sintered at 1200°C showing the greatest deformation at speeds in excess of 70 m/sec.

3.3.2 DISCUSSION:

The amount of straining resulting from impact gives an indication to the material sensitivity to high strain rate deformation. It can be seen from figure (3.8) that sintering temperature has some effect on the strain rate sensitivity of stainless steel AISI 304L even though this effect is unclear from the figure where it can be seen that the deformation curves are close to each other. However, in figure (3.9) the effect of sintering temperature on the strain rate sensitivity for AISI 316L is much clearer than in AISI 304L. It can be seen from the figure that the sensitivity to high strain rate deformation increases with the increase in sintering temperature. As for AISI 347 it can be noticed that the effect of sintering temperature on the high strain rate deformation is not as clear as for AISI 316L as shown in

figure (3.10), where it can be seen that the curves are close to each other. In general, by comparing figures (3.8), (3.9) and (3.10) together it can be seen that there is a degree of scattering in the results of the test. Moreover, the test shows that the specimens sintered at 1200°C show the biggest straining at a given impact speed.

An equation relating the impact speed to the amount of straining has been developed. The equation has the form:

$$\epsilon = C_1 + C_2 \cdot V \quad (3-3)$$

where: ϵ is the axial strain.

V is the impact speed.

C_1 , C_2 are constants relating to the material properties.

The constants C_1 and C_2 were determined from the experimental results using the least square method in regression. Their values are shown in table (3.3) for each material and each sintering temperature.

Table 3.3 Values of constants C_1 and C_2 in equation 3.3 for three types of stainless steel.

Material	Sintering Temperature °C	Constants	
		C_1	C_2
AISI 304L	900	-.116	.0054
	1000	-.099	.0050
	1100	-.133	.0053
	1200	-.233	.0067
AISI 316L	900	.098	.0029
	1000	-.055	.0043
	1100	-.187	.0054
	1200	-.416	.0085
AISI 347	1000	-.211	.0074
	1100	-.168	.0068
	1200	-.284	.0083

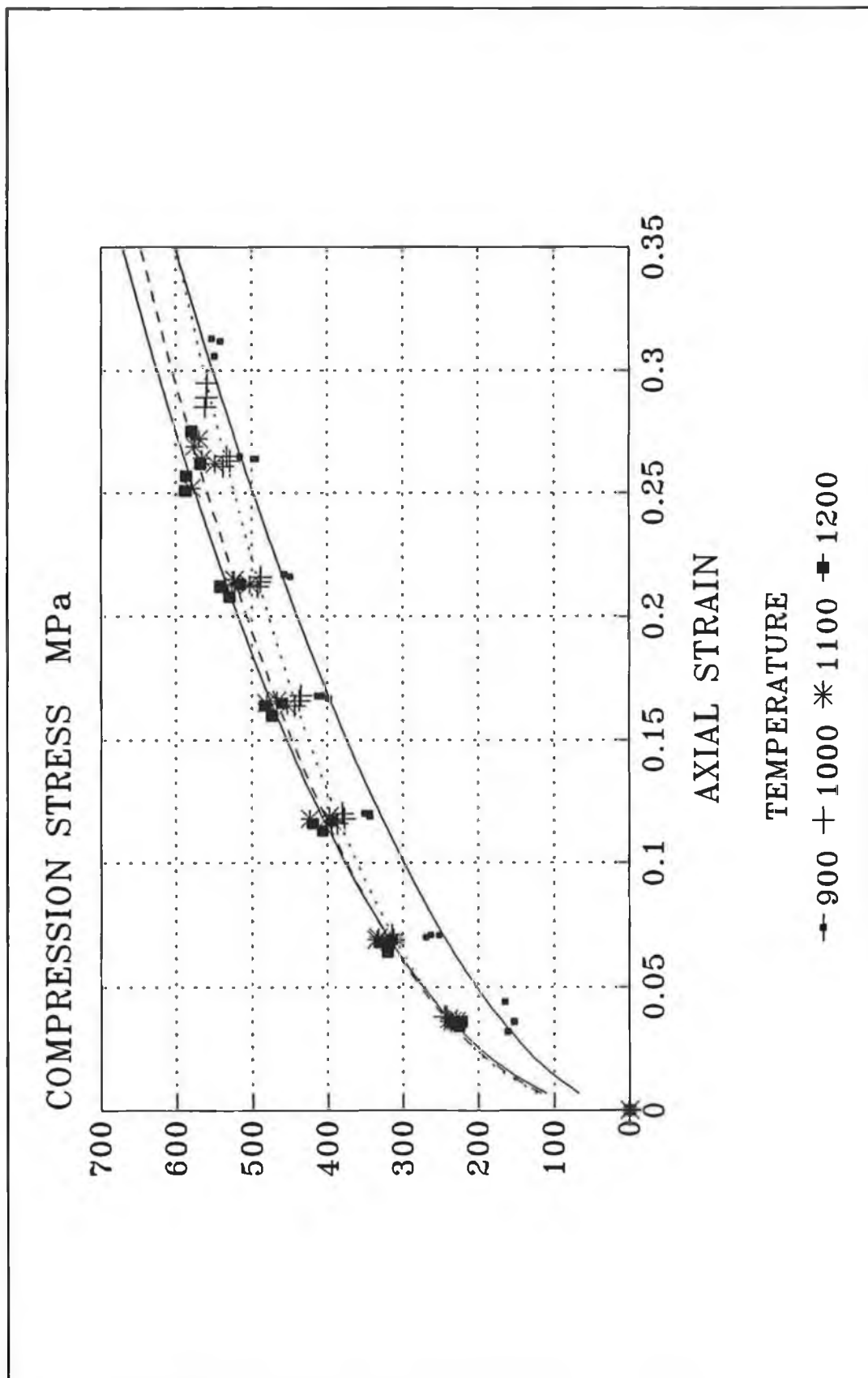


Figure 3.1 Stress strain curves for AISI 304L compacts sintered at 4 sintering temperatures.

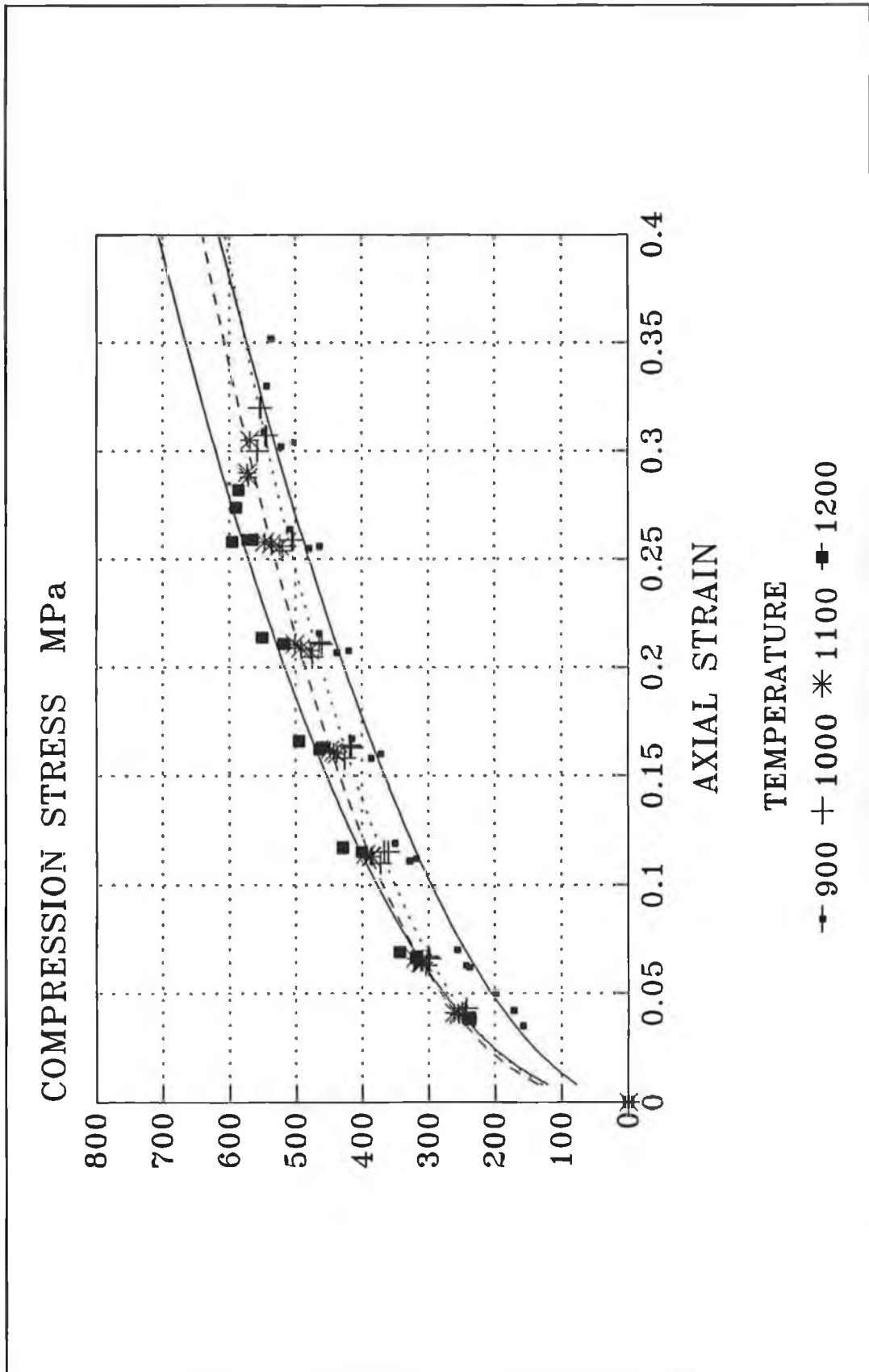


Figure 3.2 Stress strain curves for AISI 316L compacts sintered at 4 sintering temperatures.

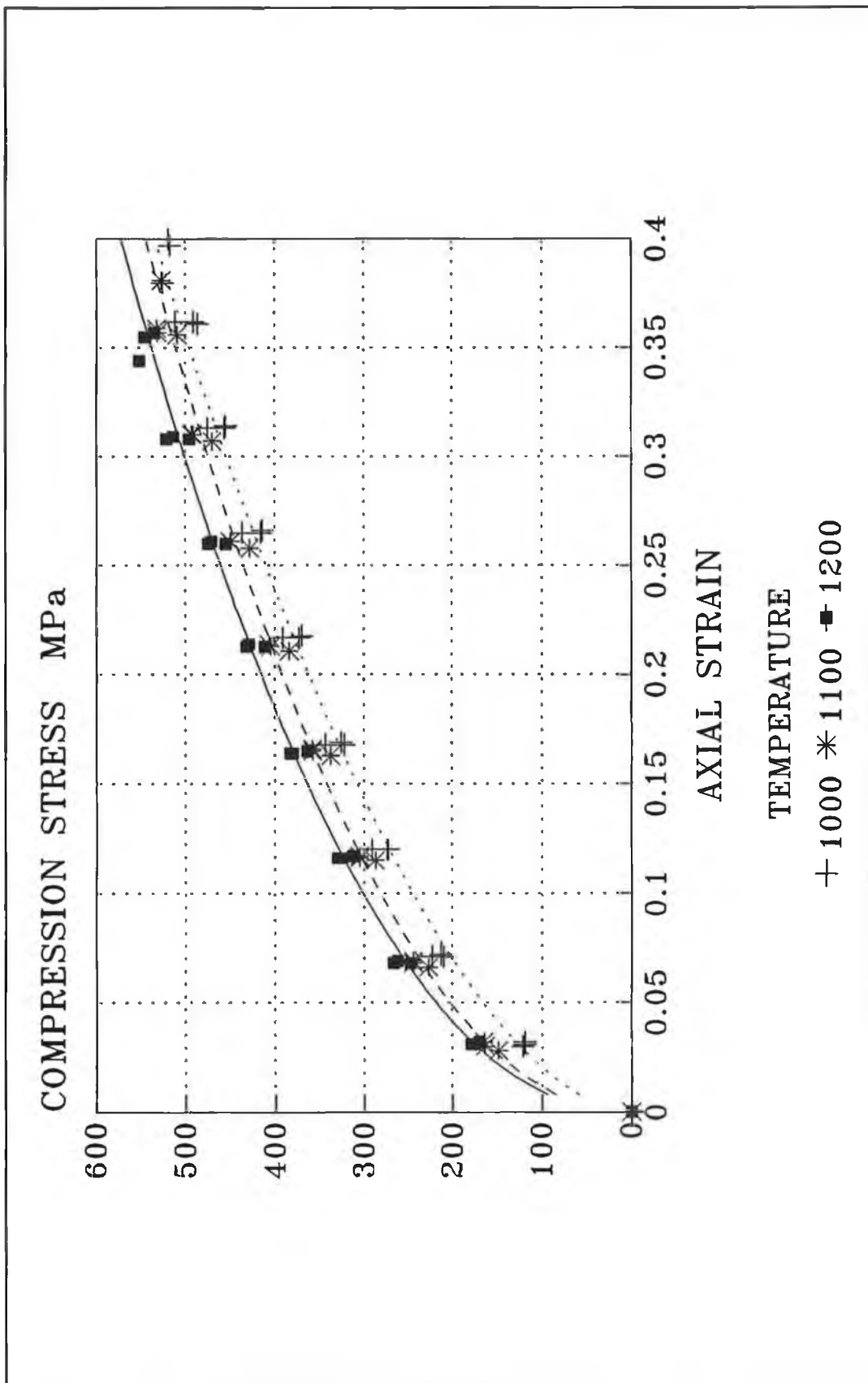


Figure 3.3 Stress strain curves for AISI 347 compacts dintered at 3 sintering temperatures.

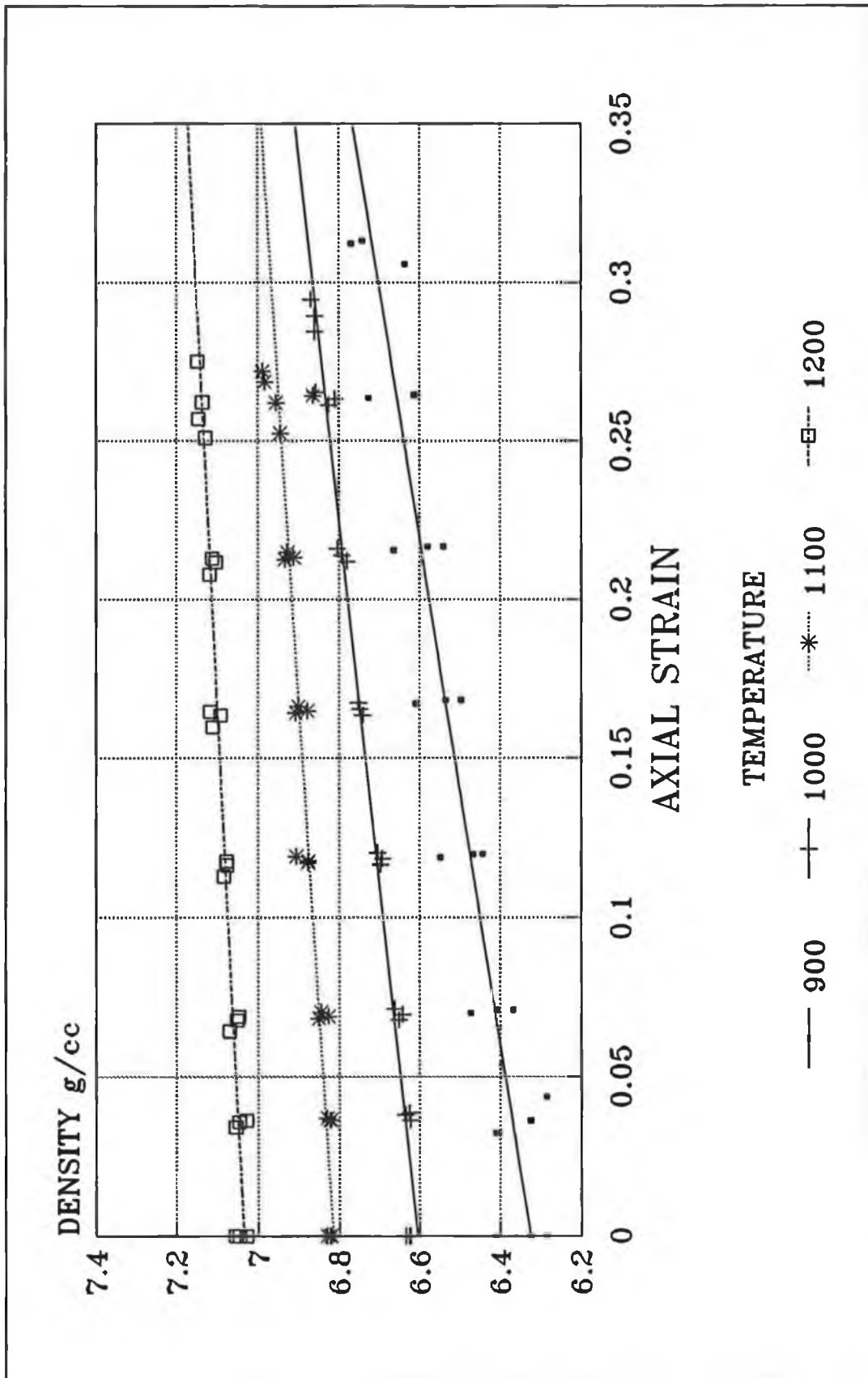


Figure 3.4 Densification of AISI 304L during compression tests for 4 sintering temperatures.

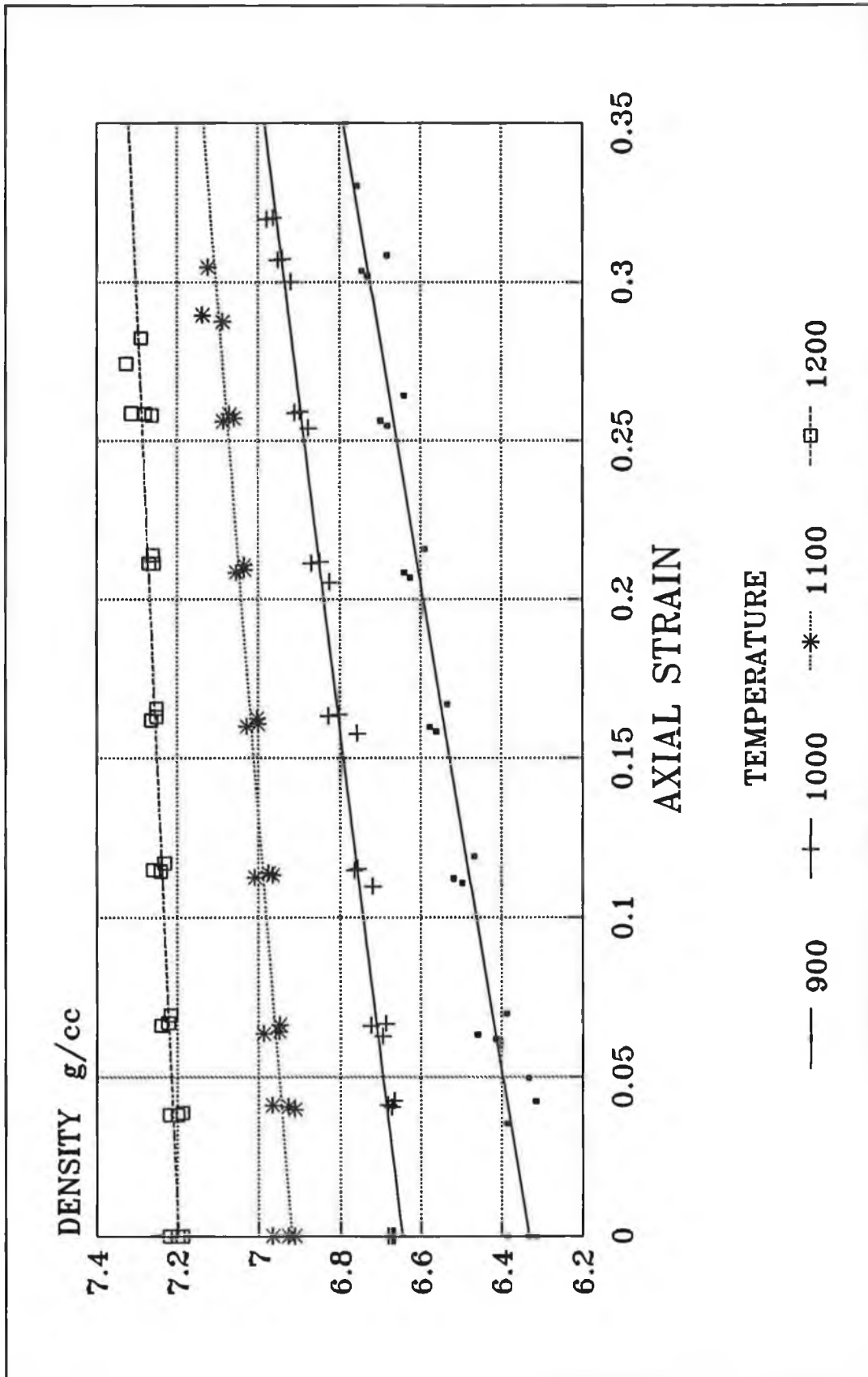


Figure 3.5 Densification of AISI 316L during compression for 4 sintering temperatures.

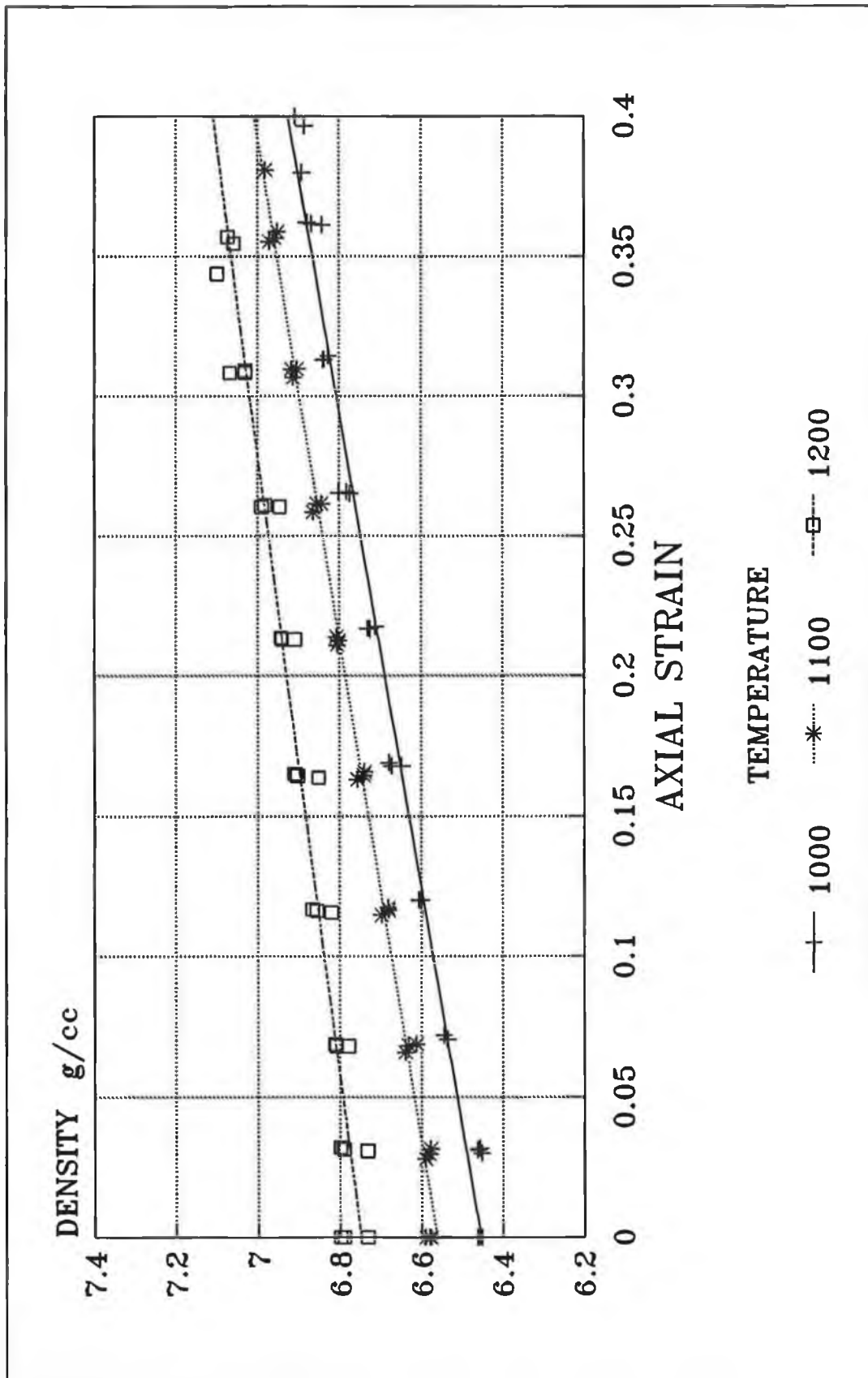


Figure 3.6 Densification of AISI 347 during compression for 3 sintering temperatures.

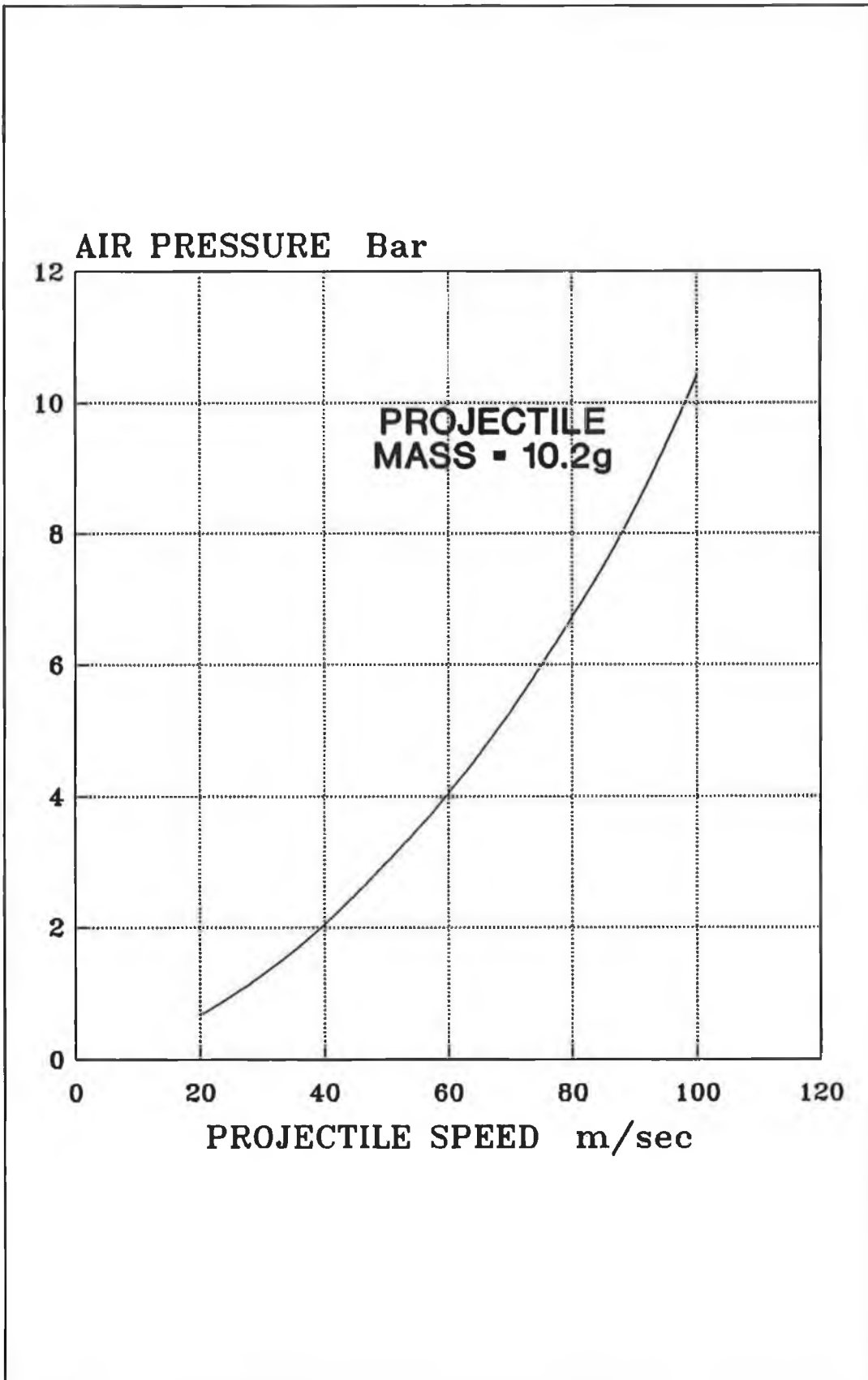
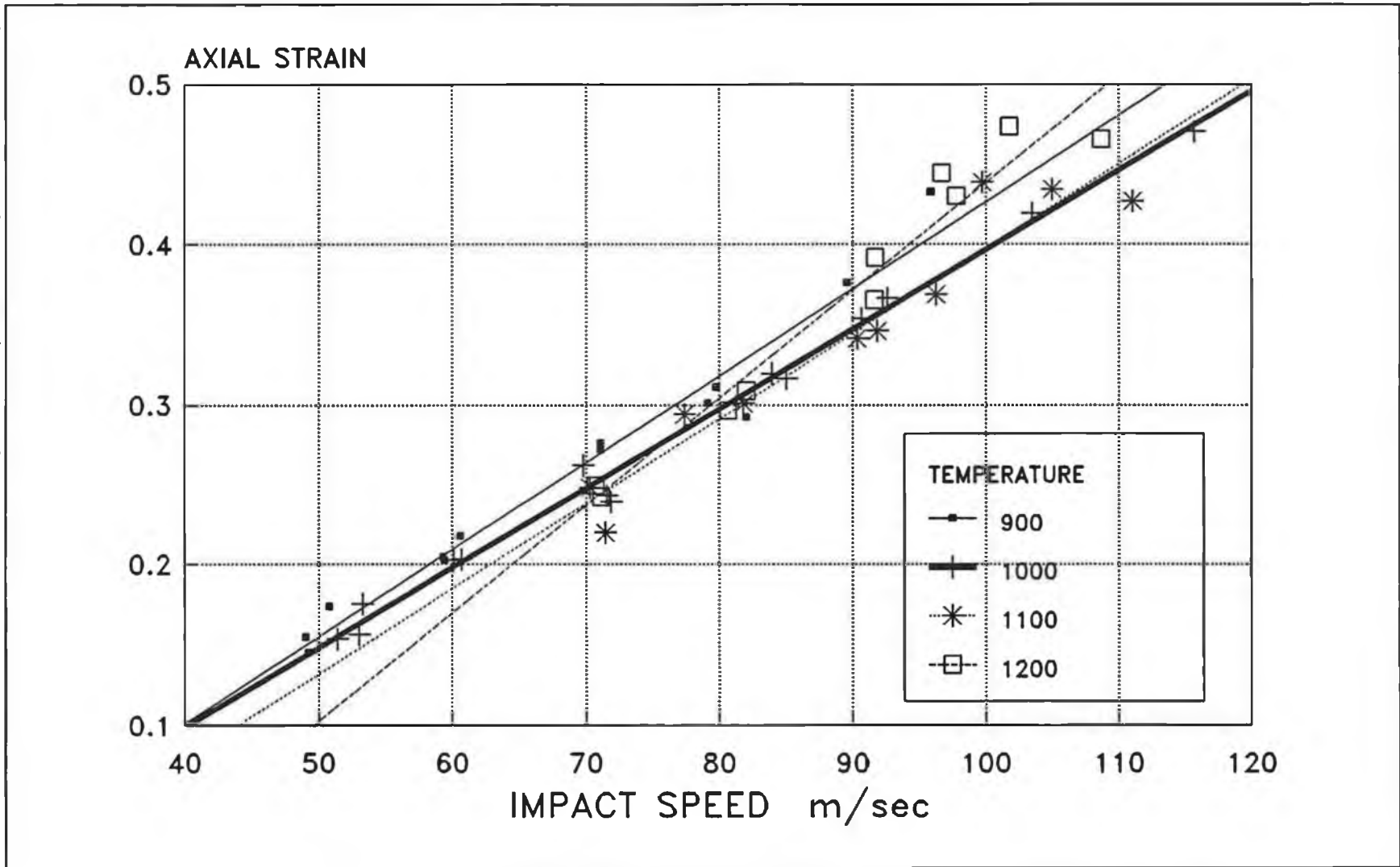


Figure 3.7 Calibration chart for the ballistic testing machine.

Figure 3.8 Axial strain vs. impact speed for AISI 304L.



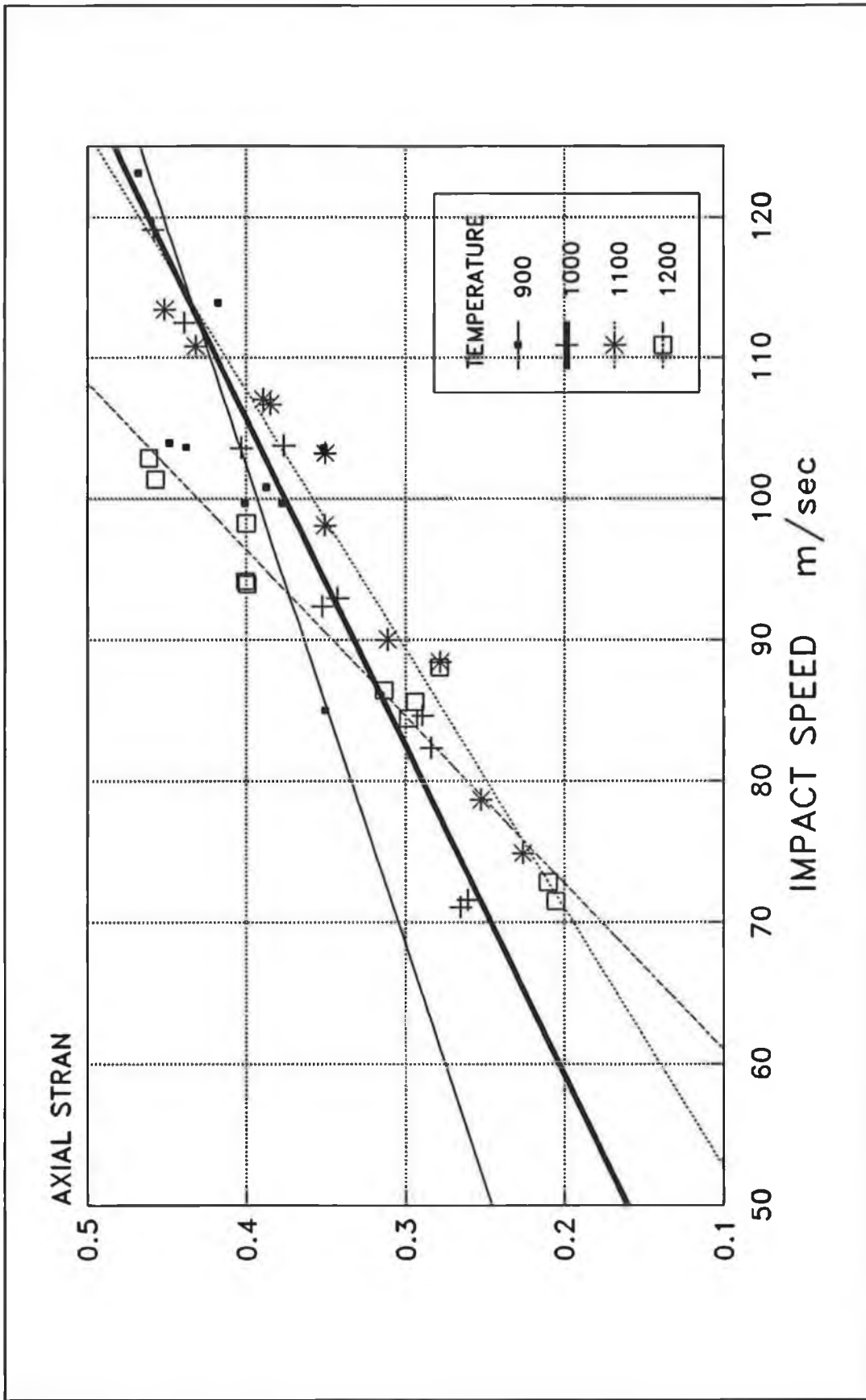
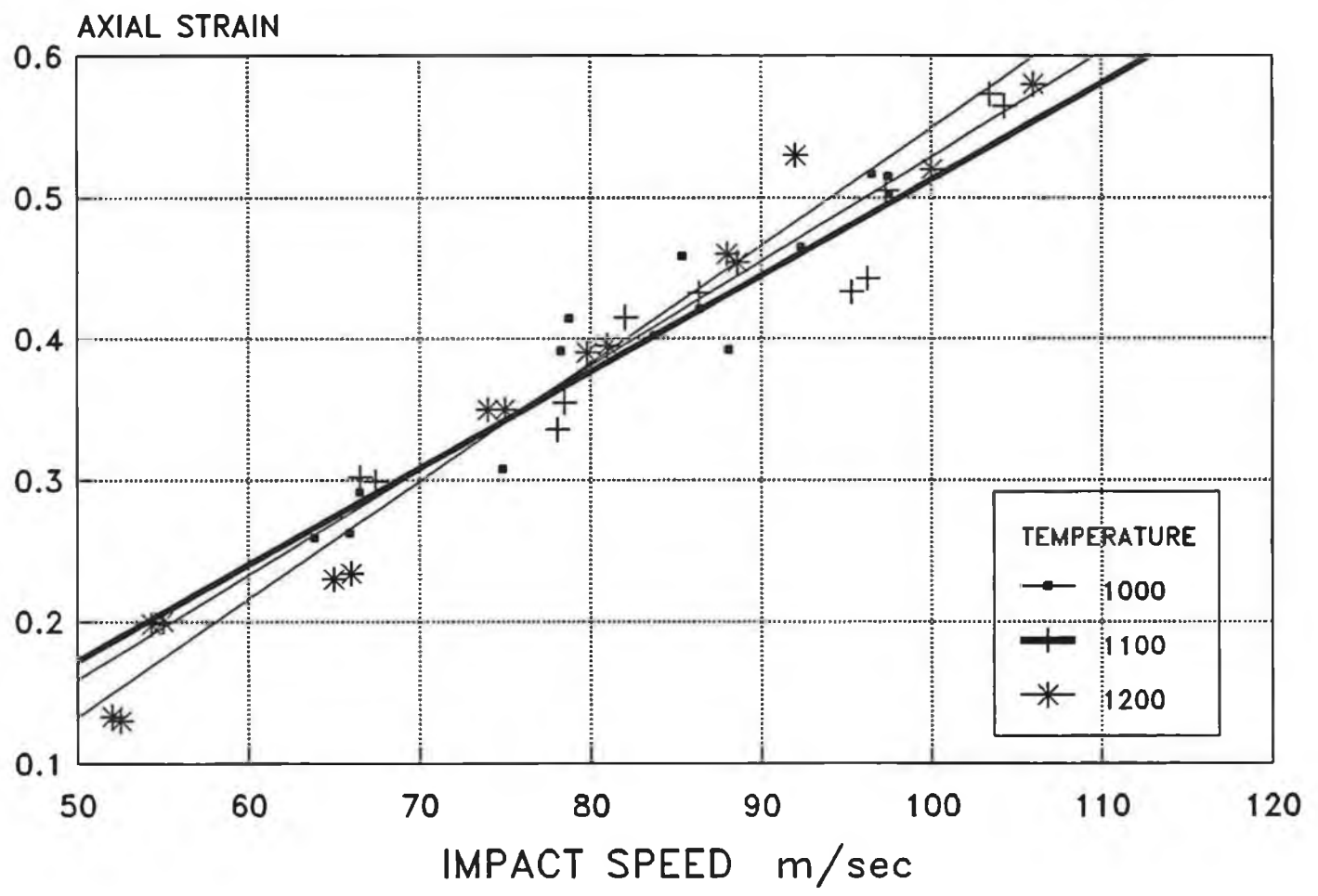


Figure 3.9 Axial strain vs. impact speed for AISI 316L.

Figure 3.10 Axial strain vs. impact speed for AISI 347.



CHAPTER FOUR

SIMULATION OF DYNAMIC BEHAVIOUR USING FINITE DIFFERENCE NUMERICAL TECHNIQUE

4.1 INTRODUCTION:

Material behaviour is significant over a very wide range of strain rates. Low strain rates of 10^{-12} to 10^{-5} per second are generally associated with creep whilst the range between 10^{-4} to 10^{-2} per second is known as the quasi-static range. Both of these ranges are of great interest to design engineers and material scientists especially at high temperatures.

The next range is very important as far as metal deformation and structural loading are concerned and is called the dynamic or high strain rate range. In this range inertia effects can become important and the temperature rises in the specimen during deformation needs to be considered. High strain rates of 10 to 10^5 are associated with mechanical loading from a moving mass or a chemical explosion. Any deformation analysis in this region must include strain rate as well as strain hardening and frictional effects.

Many experimental techniques have been proposed by researchers to determine stress-strain characteristics of materials at strain rates in excess of 10 per second during deformation. These purely experimental techniques become more sophisticated and expensive as strain rates increase.

This is one of the reasons for considering combined experimental and analytical techniques to determine stress-strain relationships at high strain rates. Taylor⁽⁷³⁾, conducted tests which involved impinging flat ended projectiles onto a rigid target to determine the dynamic yield stress. He used the momentum equation in his analytical work, assuming that radial inertia effects were negligible so that the stress can be considered constant over any cross section along the projectile. He reported that the dynamic yield stress estimated by his technique was underestimated.

In this study a numerical technique has been employed to study theoretically the deformation behaviour and to assess the influence of material inertia and strain rate sensitivity.

The technique is based on a proposed high strain rate constitutive equation, of sintered compacts during high strain rate upsetting operations and thus to determine the unknown constants of the proposed constitutive equation. This numerical technique was developed previously and reported⁽⁷⁴⁻⁷⁶⁾ in connection with analysing simple upsetting of cylindrical

specimens of elastic strain hardening and strain rate sensitive material. However, the stress-strain property of sintered compacts is, of course, dependent on the current density, a parameter which changes during the deformation process. This necessitates a variable for density dependent material property to be incorporated in any analytical method for predicting deformation characteristics of such materials. To this end the above mentioned numerical technique was modified and used to predict the simple upsetting of sintered metal compacts based on a proposed high strain rate constitutive equation with assumed values of the constants used in that equation.

4.2 THE MATHEMATICAL MODEL:

In this technique, a lumped mass model is used to represent the actual compact and the model is based on the following assumptions:

- The compact is made up of a number of concentrated connected masses linked to each other by massless links of circular cross section which possess the same strength properties as the material of the compact.

- The plane section remains plane throughout the deformation process.

- Uniform axial straining occurs within each individual

link.

- The friction stress in the compact-projectile interface is proportional to the normal stress in the face of the compact.

- The density of each element in the model is the same at the start of deformation.

- The radial expansion for each connecting link is governed by the condition of mass constancy.

- There is no resistance to radial expansion of any link from the neighbouring link except for the links in contact with the top and bottom platens in which case interface frictional force resists radial expansion.

The technique essentially uses a lumped mass model for the actual compact and the procedure amounts to expressing the dynamic force equilibrium equations for each lumped mass in finite difference form and relating the displacement of each lumped mass to the strain in the corresponding link. After each time interval the stress in each link and hence the axial force is determined from the material stress-strain characteristics. Figure (4.1) shows the model and the actual compact.

SYMBOLS:

A cross sectional area.
N Axial force.
m Mass per unit length.
 Δs Link length in the numerical model.
u Displacement.
t Time.
 ϵ Axial strain
 σ stress.

Subscripts:

i refers to the mass location and the related link.
j refers to the time interval
o refers to time is equal zero.
r refers to the layer.
l refers to the sub-layer.

4.3 FORMULATION OF EQUATIONS:

The general equation of motion for an element of the billet soon after deformation commences can be derived by considering the internal and inertia forces acting on the element as shown in figure (4.2) and is given by:

$$\frac{\partial N}{\partial s} = m \frac{\partial^2 u}{\partial t^2} \quad (4.1)$$

Figure (4.2) shows the lumped parameter model for a number of elemental lengths of the compact: This model replaces the actual compact by a mass-link system. Under the action of internal and inertia forces, the position of each concentrated mass in the model identifies the position of a corresponding elemental length of the actual compact. The finite difference equation for the elemental length at the i 'th location of the model is given by:

$$N_{i+1,j} - N_{i,j} = \Delta s_o m \ddot{u}_{i,j} \quad (4.2)$$

Equation (4.2) applies to all the elemental lengths along the compact and gives the instantaneous values of $u_{i,j+1}$ for and instant in time t_{j+1} when coupled with the following relationship between the acceleration and displacement in finite difference notation:

$$u_{i,j+1} = \ddot{u}_{i,j} (\delta t)^2 + 2u_{i,j} - u_{i,j-1} \quad (4.3)$$

where :

$$\delta t = t_{j+1} - t_j \quad (4.4)$$

The change in length $\delta(\Delta s)_{i,j+1}$ of the link i occurring during the time interval δt is:

$$\delta(\Delta s)_{i,j+1} = \Delta s_{i,j+1} - \Delta s_{i,j} \quad (4.5)$$

and hence the strain increment occurring in the link during that time interval is:

$$\delta e_{i,j+1} = \frac{\delta (\Delta s)_{i,j+1}}{\Delta s_{i,o}} \quad (4.6)$$

The total strain in the link can now be determined by:

$$e_{i,j+1} = e_{i,j} + \delta e_{i,j+1} \quad (4.7)$$

In order to facilitate the calculation of stress which may vary across the cross section of the compact, it is necessary to idealise the actual cross section to an equivalent section model which consists of a number of layers across each of which the stress is assumed to be uniform. The circular cross section of the compact is assumed to consist of n evenly spaced layers of material of tubular cross section area which can carry normal stress as shown in figure (4.3). These layers are considered to be separated by a material which can not carry any normal stress but has infinite shear rigidity.

With this simplification, the stress in the compact can be defined by the individual normal stresses at the n separate layer without having to contravene the assumption that plane sections remain plane throughout the deformation process. The cross sectional area of each tubular layer can be equating to that of the actual cross section of the compact.

In order to describe the elastic plastic stress state in the layers of the section model, further idealisation is made and each layer is assumed to consist of a number of sub-layers. This number is determined by the number of positive slopes in the approximated polygonal stress-strain diagram as shown in figure (4.4a).

The relation between the sublayer area and its parent layer area is established as follows: Referring to figure (4.4b) and assuming that the deformation has reached stage B, ie sublayer $A_{r,l-1}$ is loaded elastically to the condition $\sigma_1 \varepsilon_1$ and the remaining sublayer areas are loaded to the condition $\sigma_2 \varepsilon_2$. The stress σ_B is hypothetical stress that the sublayer area $A_{r,l}$ would have to be subjected to if it were stressed elastically to a strain value of ε_2 . σ_C is similarly related to ε_3 for the sublayer area $A_{r,l+1}$. So by equating forces and noting that:

$$A_r = A_{r,l-1} + A_{r,l} + A_{r,l+1} \quad (4.8)$$

$$\sigma_2 A_r = A_{r,l-1} \sigma_1 + A_{r,l} \sigma_B + A_{r,l+1} \sigma_B \quad (4.9)$$

Combining equations (4.8) and (4.9) and using the slopes in the stress-strain curve in figure (4.4b), it can be found that:

$$A_{r,l-1} = \frac{A_r}{E} [E - E_2] \quad (4.10)$$

Assuming the deformation has reached stage C, by using the same procedure the sublayer area $A_{r,l+1}$ will be:

$$A_{r,l+1} = \frac{E_3 A_r}{E} \quad (4.11)$$

and $A_{r,l}$ will be:

$$A_{r,l} = \frac{A_r}{E} [E_2 - E_3] \quad (4.12)$$

That is applicable when the stress-strain curve is approximated to three positive slopes. In general, the area of a sublayer is calculated as follows:

$$A_{r,l} = \frac{A_r}{E_1} [E_1 - E_{l+1}] \quad (4.13)$$

The layer area A_r which is used in the previous equations is calculated from the link area A_i . This link area in turn is determined using the concept of the conservation of mass after each time interval δt , thus:

$$A_{i,j+1} = \frac{\rho_{i,j} A_{i,j} \Delta S_{i,j}}{\rho_{i,j+1} \Delta S_{i,j+1}} \quad (4.14)$$

Knowing the sublayer stress $\sigma_{irl,j-1}$ at time t_{j-1} at the l 'th sublayer of the r 'th layer at the i 'th link and the strain increment $\delta \epsilon_{ir,j}$ at time t_j at the r 'th layer of the i 'th link, The sublayer stress $\sigma_{irl,j}$ at time t_j at the l 'th

sublayer is determined as follows:

First a trial value $\sigma_{irl,j}^t$ of the sublayer stress $\sigma_{irl,j}$ is calculated by assuming an elastic path:

$$\sigma_{irl,j}^t = \sigma_{irl,j-1} + E \delta \epsilon_{ir,j} \quad (4.15)$$

Once the trial value is calculated, the correct value can be ascertained by using the following conditions:

Let σ_{y1} be the sublayer yield stress and be given by $\sigma_{y1} = E \epsilon_1$ is the strain defining the 1'th corner of the approximated stress-strain diagram:

Donating $\sigma_{irl,j}$ as σ_1 for convenience:

$$\begin{aligned} \text{IF } -\sigma_{y1} < \sigma_1^t < \sigma_{y1} \quad \text{THEN } \sigma_1 &= \sigma_1^t \\ \text{IF } \sigma_1^t < -\sigma_{y1} \quad \text{THEN } \sigma_1 &= -\sigma_{y1} \\ \text{IF } \sigma_1^t > \sigma_{y1} \quad \text{THEN } \sigma_1 &= \sigma_{y1} \end{aligned} \quad (4.16)$$

This procedure is applied to all sublayers of each layer for all the links.

The values of the sublayer stresses for the links in immediate contact with the projectile and the anvil are then modified, to take into account the interface friction by using the general equation for compression with friction:

$$\sigma = \sigma_o [1 + \frac{2\mu}{h} (R - r)] \quad (4.17)$$

Following the terminology applied to the numerical model this equation could be written as:

$$\sigma_{irl,j}^f = \sigma_{irl,j} [1 + \frac{2\mu}{h} (R_{ir} - R_{irl} - \frac{T^2}{12 R_{irl}})] \quad (4.18)$$

where: μ is the interface friction coefficient.

$\sigma_{irl,j}^f$ stress in the sublayer including friction.

$\sigma_{irl,j}$ sublayer stress determined from equation(4.15).

T the thickness of the sublayer.

After this modification, the axial forces $N_{i,j}$ in each link are then determined from the equation:

$$N_{i,j} = \sum_{r=1}^n \sum_{l=1}^k \sigma_{irl,j} A_{l,j} \quad (4.19)$$

where: $A_{l,j}$ is the current sublayer area.

Taking the effect of inertia into account due to the high speed of deformation where the inertia forces have a remarkable effect on the deformation, the values of the sublayer stresses can be modified to take into account that effect using this equation:

$$\sigma_{irl,j}^r = \sigma_{irl,j} [\frac{3\rho_i V_i^2}{8h^2} (R_{ir}^2 - R_{irl}^2 - \frac{T^2}{4})] \quad (4.20)$$

where: $\sigma_{irl,j}^r$ the stress in the sublayer from the radial inertia effect.

ρ_i is the current density.

v_i is the speed of the link movement.

The density is calculated using equation (3.2) which was derived from the experimental compression test to relate the density of the compact to the amount of straining occurred in the compact. Applying this equation for the numerical model, it is assumed that the density for each element is constant, so by calculating the strain in each element at time t_j the current density at time t_j can be found using equation (3.2).

The speed v_i is calculated as follows:

$$v_i = \frac{\delta(\Delta S_i)}{\delta t} \quad (4.21)$$

The time increment δt used in this technique cannot be chosen arbitrarily. The value of the time increment should be much less than the time needed for the elastic stress wave to propagate through the length of the link.

4.4 SIMULATION:

In order to determine the high strain rate constants a density dependent material property was incorporated in the computer simulation of a simple upsetting process based on the lumped mass model. A computer program was developed to

simulate the deformation behaviour during impact for porous materials. The program is listed in appendix B. For the purpose of comparing experimental results with those predicted theoretically using the above mentioned numerical technique, data obtained at other stages of this project were used. In this program two equations established earlier were used. The first one is equation (3.1) which was used to calculate the stress during deformation in accordance with density changes. The second one is equation (3.2) which describes the density changes during deformation and was introduced to take such changes into account.

The proposed high strain rate constitutive equation is a function of:

$$\sigma_d = F(\sigma_s, \rho_o, \epsilon, \dot{\epsilon}) \quad (4.22)$$

where: ρ_o is initial relative density of the compact.

ϵ is the axial strain.

$\dot{\epsilon}$ is the strain rate

σ_s is the static stress.

σ_s is expressed previously as:

$$\sigma_s = F_1(\rho_o, \epsilon) \quad (4.23)$$

thus, equation (4.22) may be expressed in terms of σ_s and $\dot{\epsilon}$ giving:

$$\sigma_d = F_2(\sigma_s, \dot{\epsilon}) \quad (4.24)$$

So the proposed equation which describes the dynamic stress in terms of static stress and strain rate has the form:

$$\sigma_d = \sigma_s \left[1 + \left(\frac{\dot{\epsilon}}{D} \right)^P \right] \quad (4.25)$$

where D and P are constants which will be determined through the use of the computer program. The choice of this form of equation (4.25) is due to its simplicity and the availability of relevant data⁽³⁶⁾.

To determine the constants D and P , equation (4.25) was used in the program with arbitrary values for D and P and the program was executed for each impact speed and each sintering temperature. After the program execution, the impact speed was changed and the program was executed again and so on. The results of the final axial strain of the specimen from the program was used to fit a curve between axial strain and impact speed and this theoretical curve was plotted against the experimental curve to see how close the two curves are. Then the procedure was repeated again with changing D and P to find the curve which fits very closely with the experimental curve.

4.5 RESULTS AND DISCUSSION:

The dynamic response of sintered stainless steel

compacts is described in equation (4.25), which takes the static properties of such material and strain rate into account.

Figure (4.5) shows the iterative approach, which was described earlier, for finding the constants D and P for AISI 304L compacts sintered at 900°C. It can be seen from the figure that by changing the value of the constant D in the program the slope of the theoretical curve is changed until the best fit is obtained with the experimental one. This approach was employed for the other sintering temperatures and the other types of stainless steel compacts and the constants D and P are listed in table (4.1) for each material and each sintering temperature.

Table 4.1 The constants D and P for the dynamic constitutive equation.

Material	Sintering Temperature	Constants	
		D	P
AISI 304L	900	5.5×10^4	0.4
	1000	5.7×10^4	0.42
	1100	5.65×10^4	0.41
	1200	5.3×10^4	0.39
AISI 316L	900	5.95×10^4	0.45
	1000	5.7×10^4	0.43
	1100	5.65×10^4	0.41
	1200	5.1×10^4	0.37
AISI 347	1000	5.35×10^4	0.4
	1100	5.3×10^4	0.42
	1200	5.3×10^4	0.39

Figure (4.5) also shows that the constant D gives an indication of the strain rate sensitivity of the material.

When the magnitude of this constant is increased the strain rate sensitivity of the material is decreased.

The constants D and P are used in equation (4.25) along with equation (3.1) to calculate the dynamic stress for different strains at three strain rates (10^2 , 10^3 and 10^4). Figure (4.6) shows the stress-strain curves at three strain rates for AISI 304L compacts sintered at four temperature along with the static curve for each sintering temperature. It can be seen that at a certain amount of straining the stress increases with the increase in strain rate. This increase in stress seems to be small at relatively small strain rates and as the strain rate increases the increase in stress becomes bigger. Figures (4.7) and (4.8) show the same stress-strain curves for the other two types of stainless steel AISI 316L and AISI 347.

Figures (4.9), (4.10) and (4.11) show the predicted stress-strain curves for the program for the three types of stainless steels sintered at four temperatures. These curves were calculated at a strain rate of 10^3 per second. It can be seen that these curves are similar to the curves in figures (3.1), (3.2) and (3.3) respectively which were obtained from the static compression test. However, the magnitude of the stress is higher due to the effect of strain rate. The figures also show that the stress-strain curves for the compacts sintered at 900°C have different property than the other sintering temperatures. This was also noticed in the results of the static compression test.

Calculation of the dynamic to static stress ratio gives an indication of the strain rate sensitivity of the materials concerned. Figures (4.12), (4.13) and (4.14) show the dynamic to static stress ratio curves for AISI 304L, AISI 316L and AISI 347 respectively. The curves are plotted for each sintering temperature. The curves in figure (4.12) show that there is some effect of sintering temperature on the material strain rate sensitivity, where it can be seen that there is a small increase in the stress ratio with the increase in sintering temperature. This increase in the strain rate sensitivity could be related to the increase in the density of the compact during sintering as seen earlier. This can also be said for figure (4.13) and (4.14). However, the curves in figure (4.13) for AISI 316L show bigger increase in the stress ratio with the increase in sintering temperature. In other words, the effect of sintering temperature on the strain rate sensitivity is more prominent in figure (4.13) than the others.

Figures (4.15), (4.16), (4.17) and (4.18) show the dynamic to static stress ratio curves for each sintering temperature 900, 1000, 1100 and 1200°C respectively. The curves in these figures correspond to the three types of stainless steel along with the results which were obtained previously by the author⁽³⁶⁾ regarding iron powder compacts. It can be seen that all stainless steel compacts have lower strain rate sensitivity than iron compacts have. Moreover, the figures show that some of the stainless steel curves are very close to each other which may indicate that their

behaviour under high strain rate may be similar.

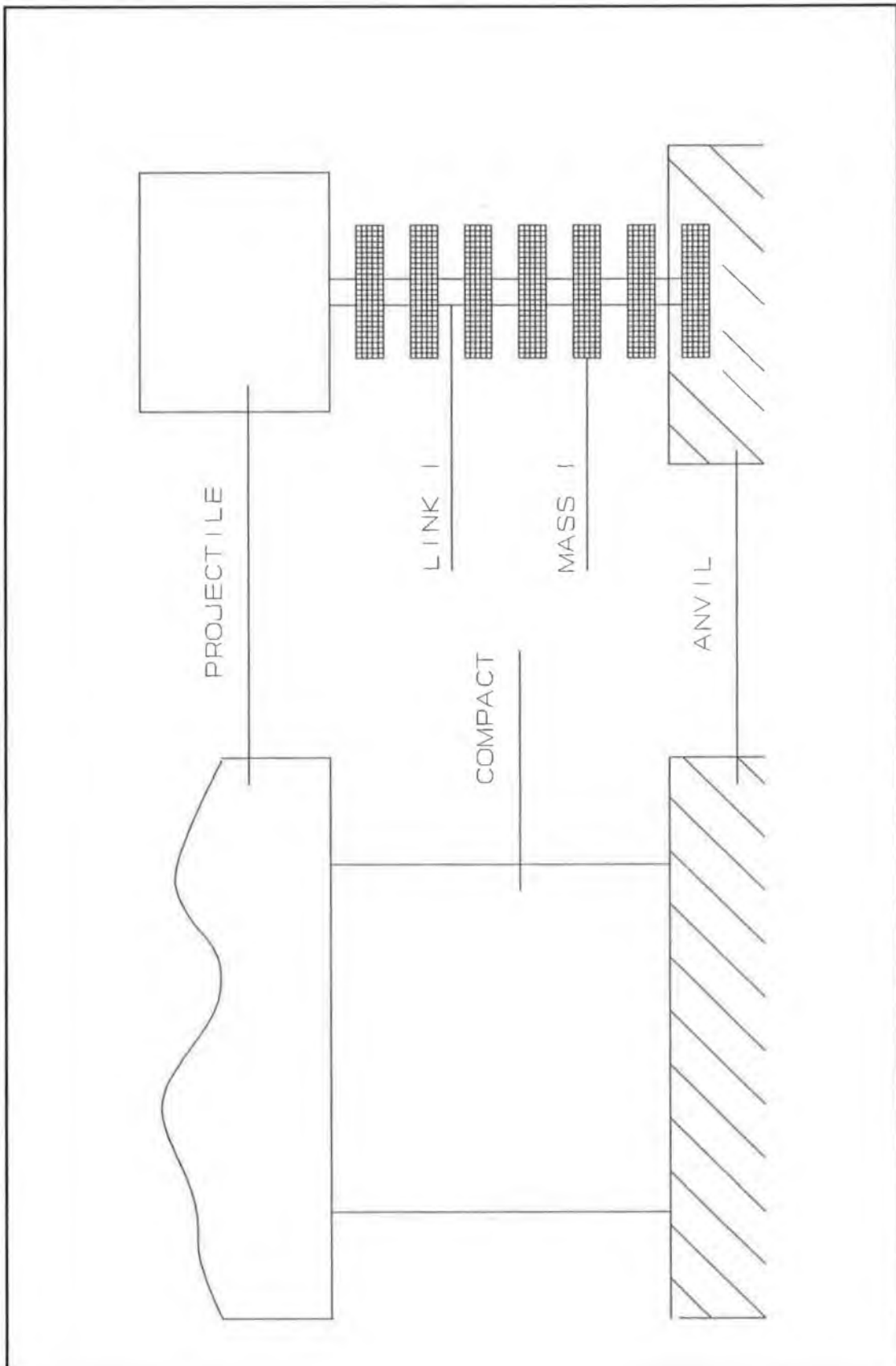
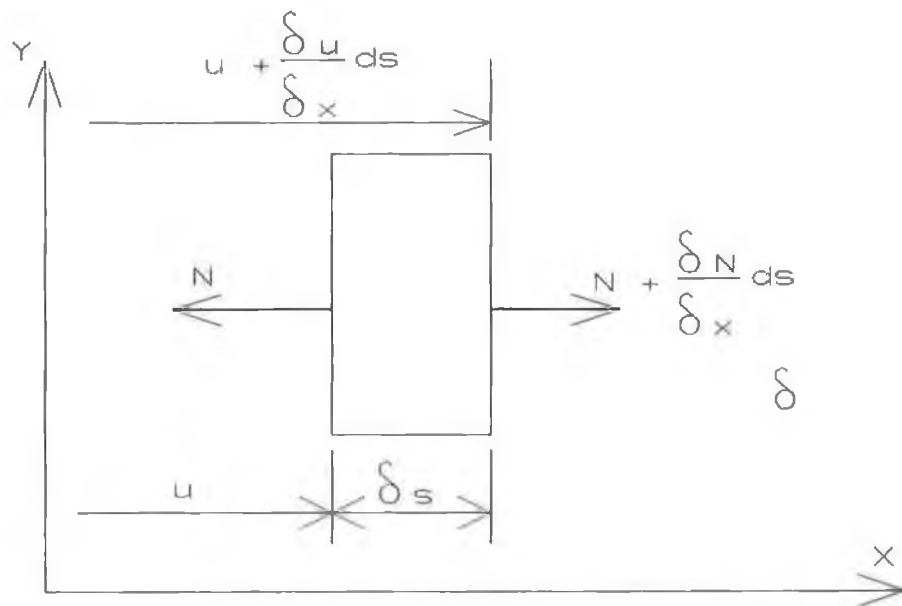
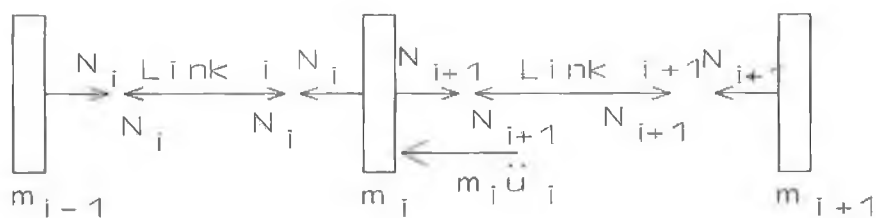


Figure 4.1 Actual loading configuration of the billet and its equivalent numerical model.



a- An element of the compact.



b- Equivalent finite difference model.

Figure 4.2 (a) An element of the compact and forces acting on it. (b) Numerical model of the element in (a).

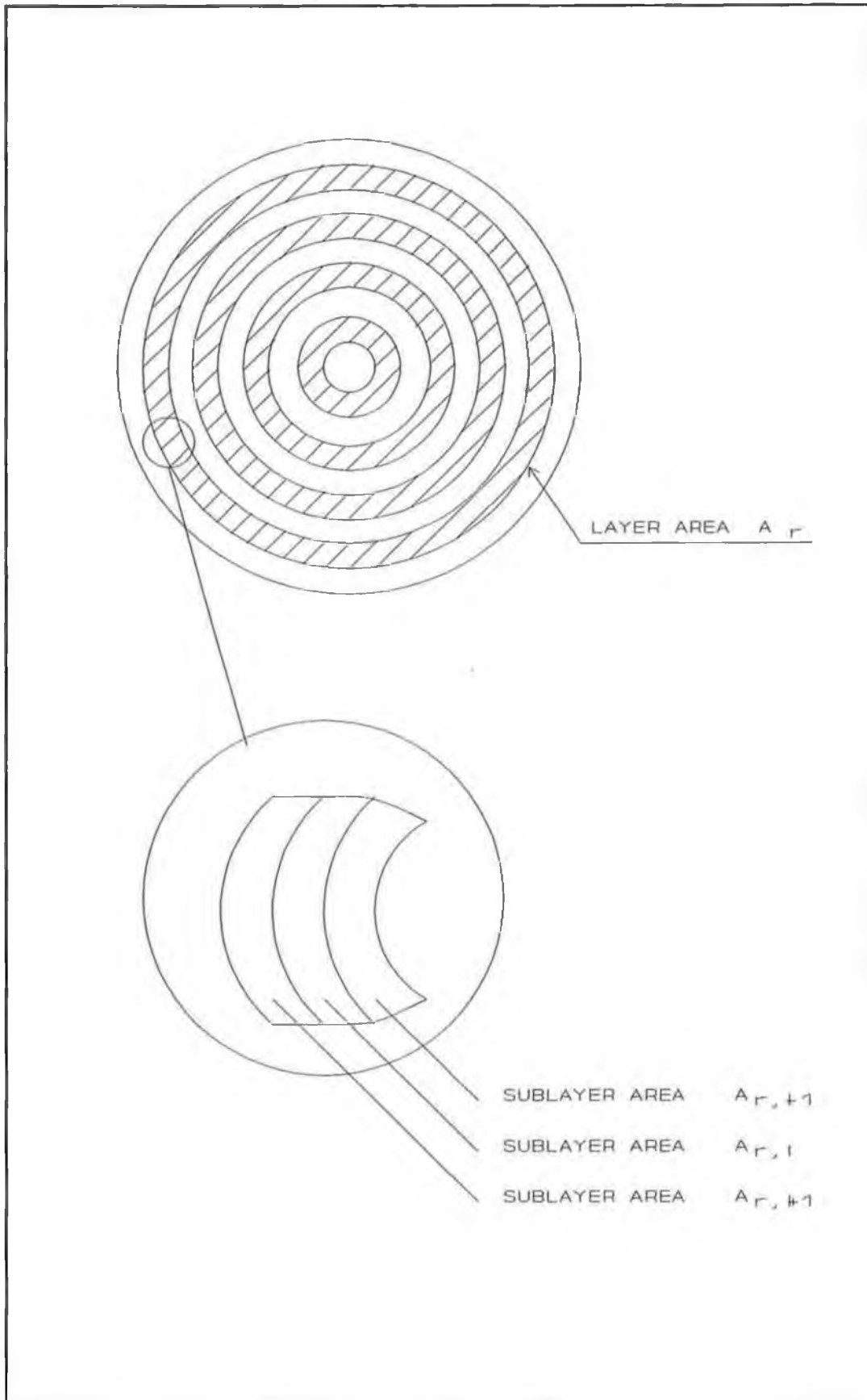


Figure 4.3 Cross section model of the compact.

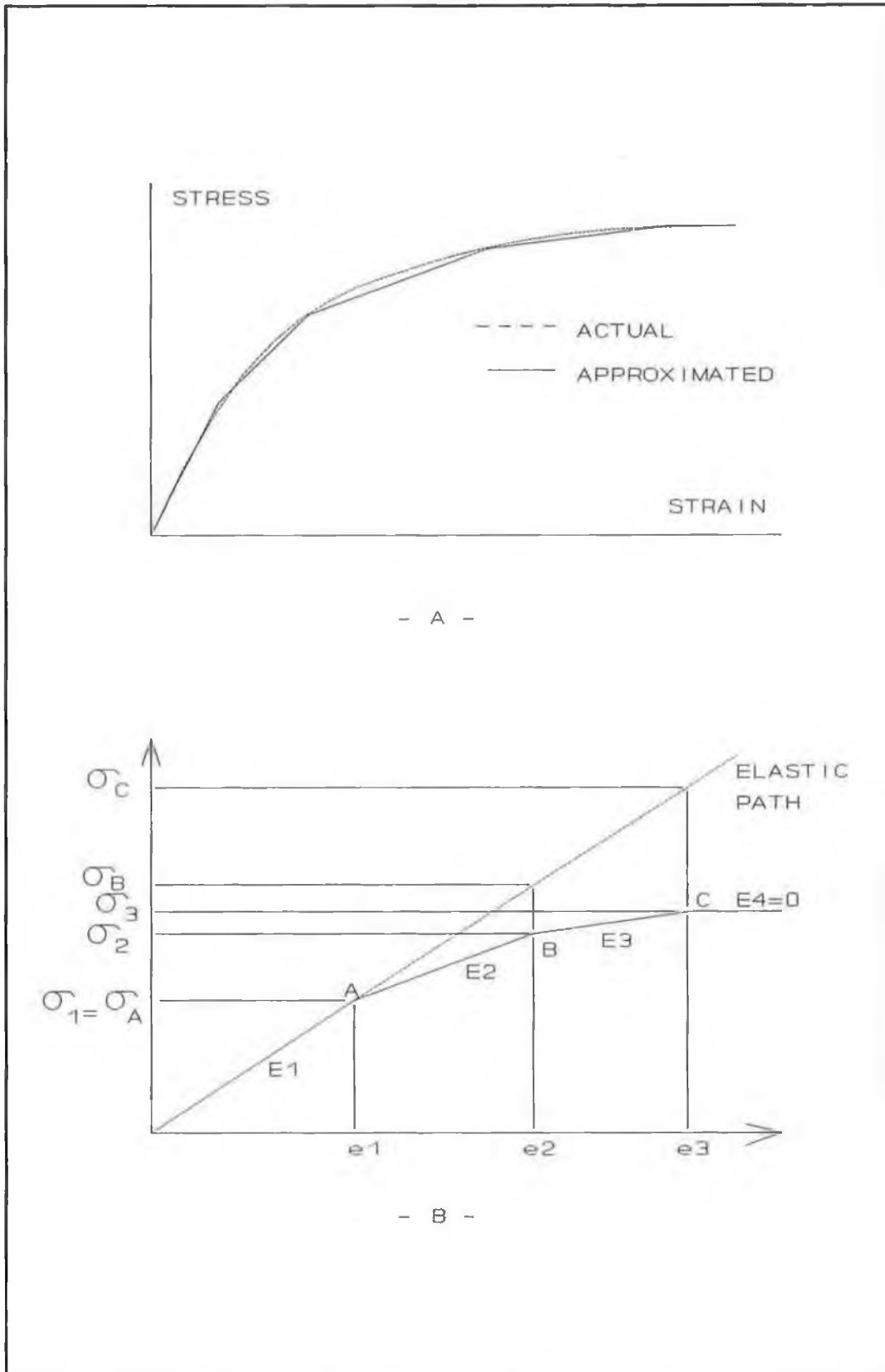


Figure 4.4 (a) Approximated polygonal stress-strain diagram. (b) Stress-strain diagram used in the theoretical analysis.

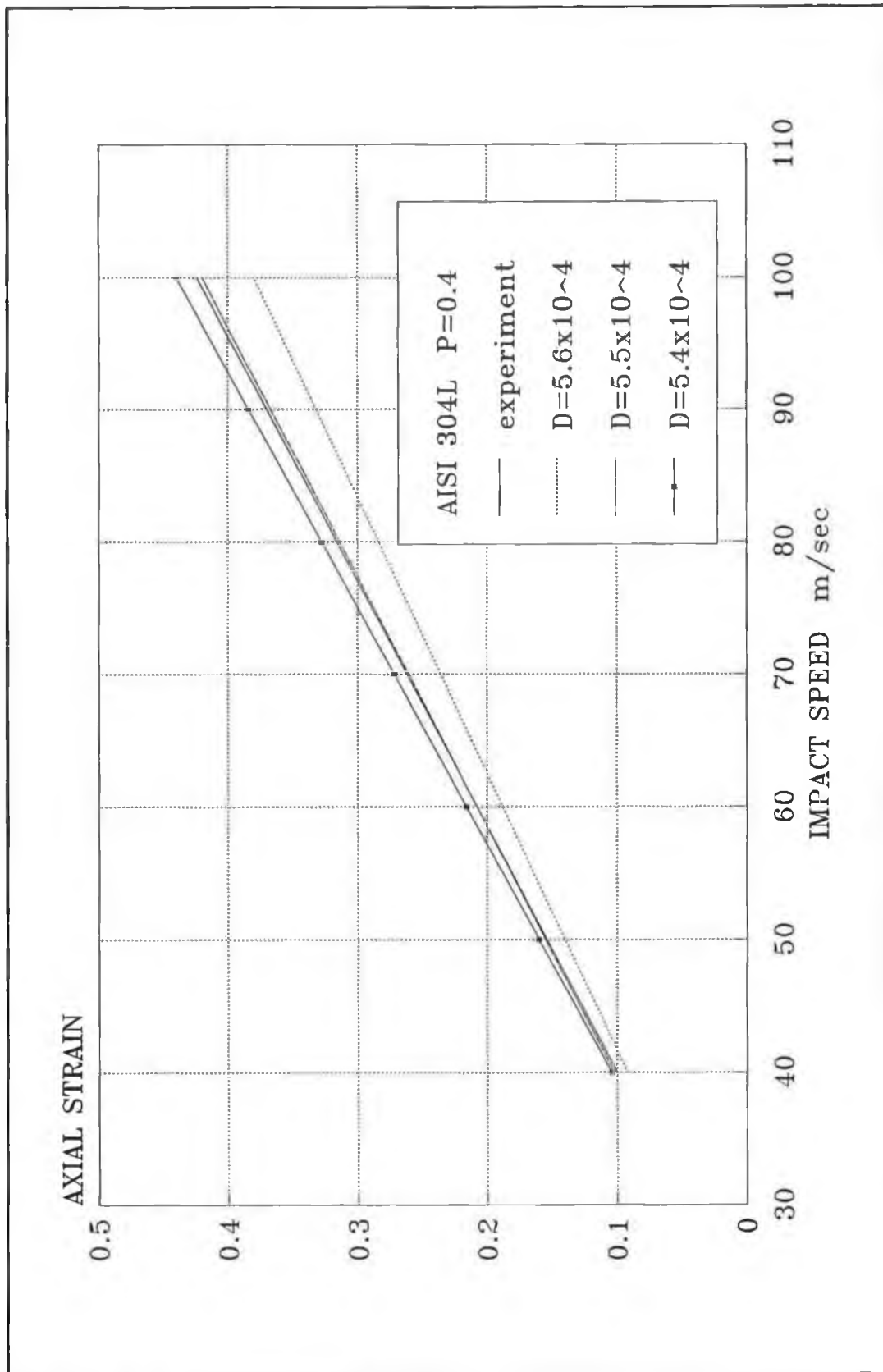
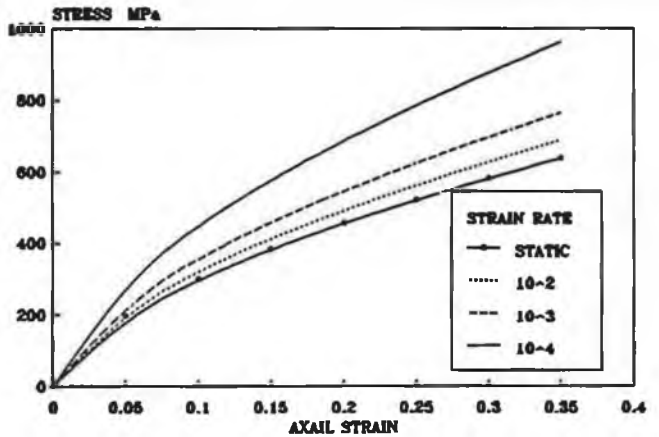
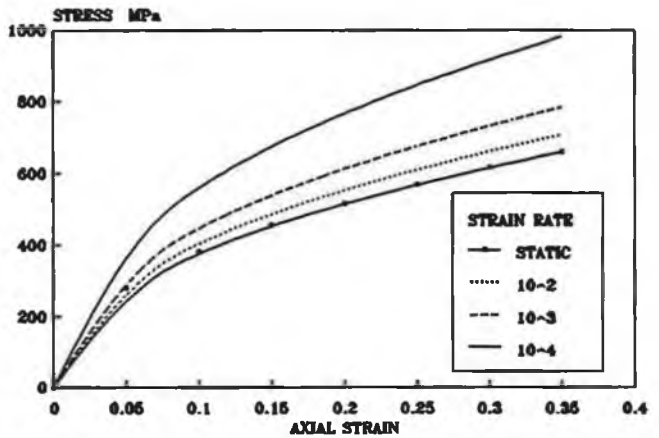


Figure 4.5 Theoretical results for finding the constant D for the dynamic constitutive equation for AISI 304L compacts sintered at 900°C.

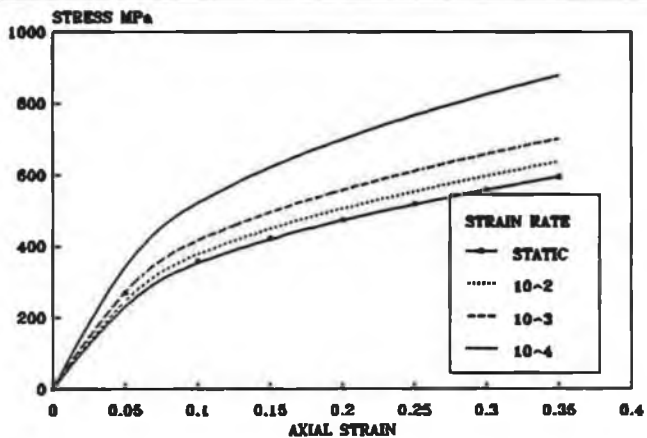
Figure 4.6 Stress-strain curves at 3 strain rates for AISI 304L compacts sintered at 4 temperatures.



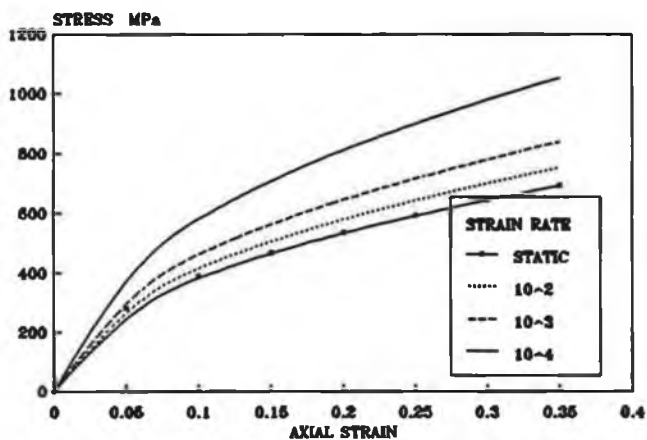
AISI 304L SINTERED AT 900 C



AISI 304L SINTERED AT 1100 C



AISI 304L SINTERED AT 1000 C



AISI 304L SINTERED AT 1200 C

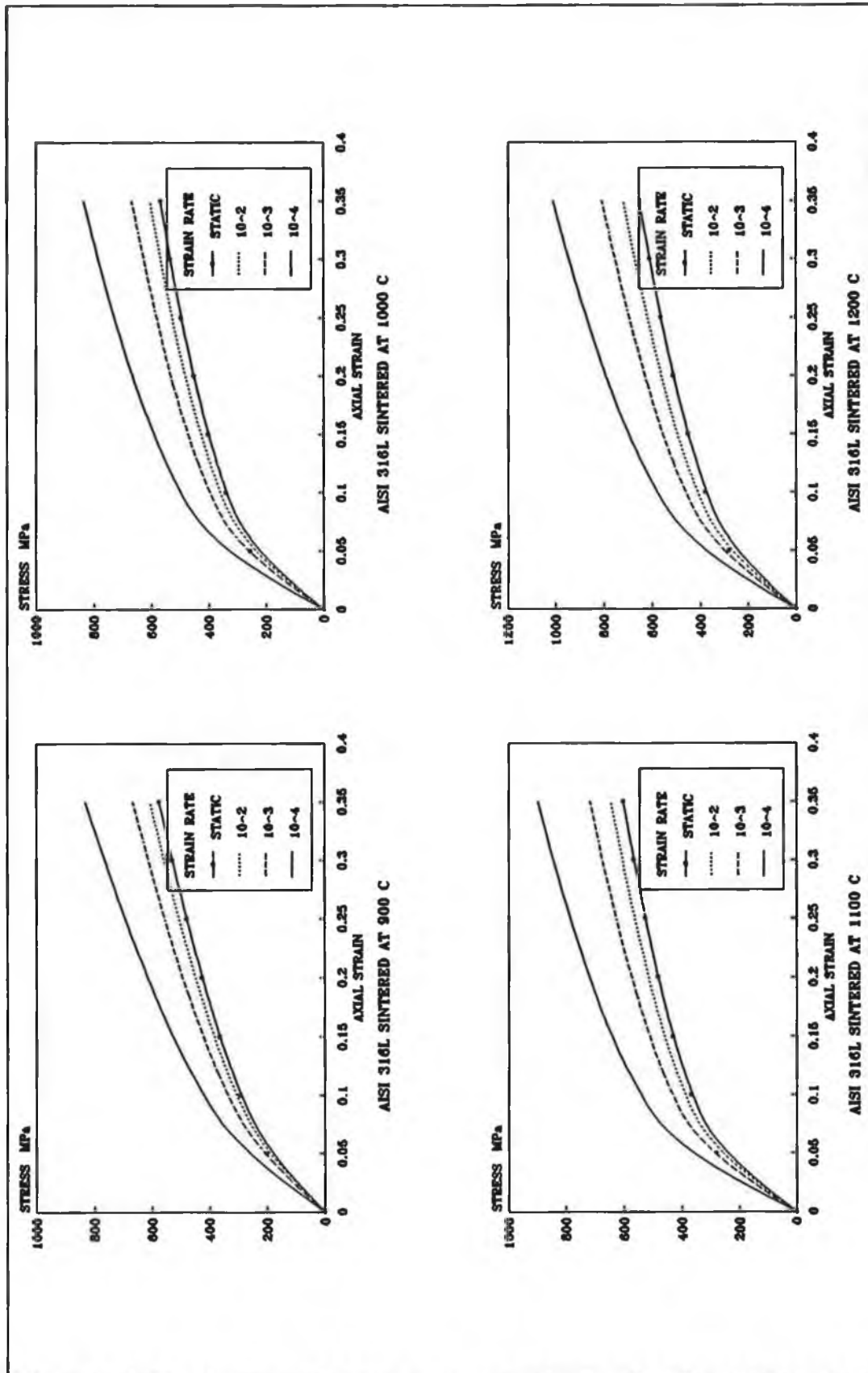


Figure 4.7 Stress-strain curves at 3 strain rates for AISI 316L compacts sintered at 4 temperatures.

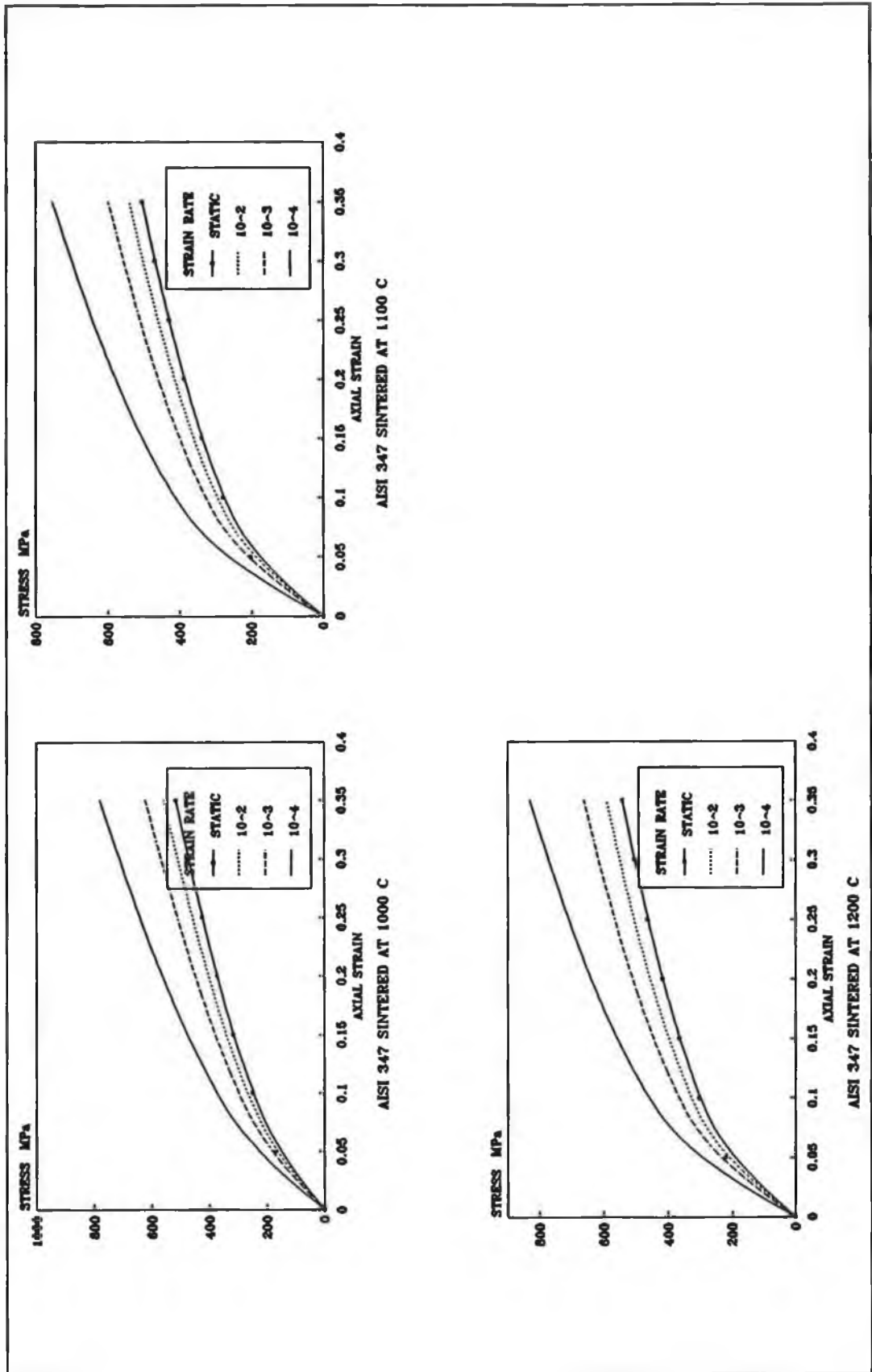


Figure 4.8 Stress-strain curves at 3 strain rates for AISI 347 compacts sintered at 4 temperatures.

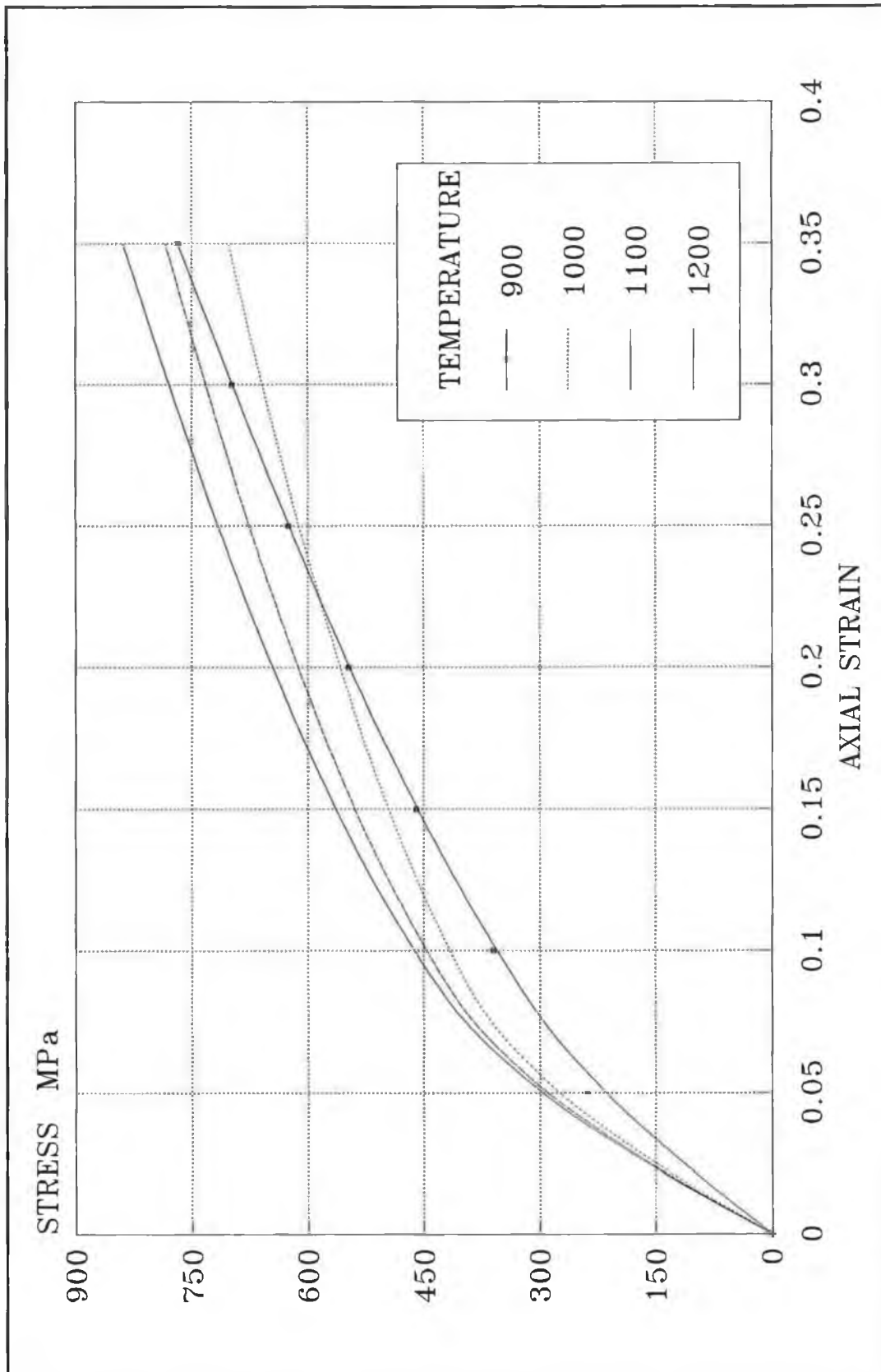


Figure 4.9 Effect of sintering temperature on the stress-strain curves for AISI 304L at strain rate of 10^3 per second.

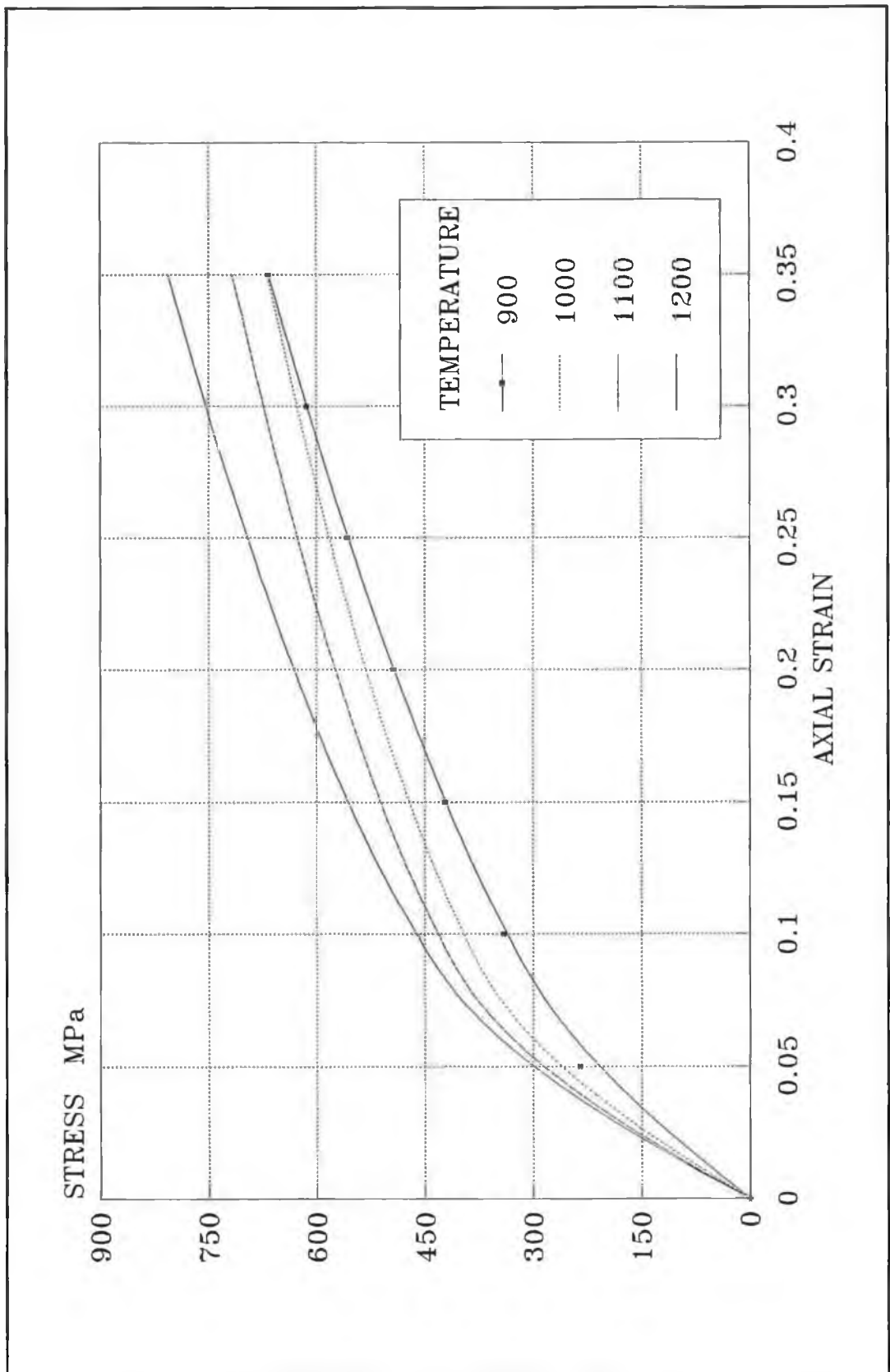


Figure 4.10 Effect of sintering temperature on the stress-strain curves for AISI 316L at strain rate of 10^3 per second.

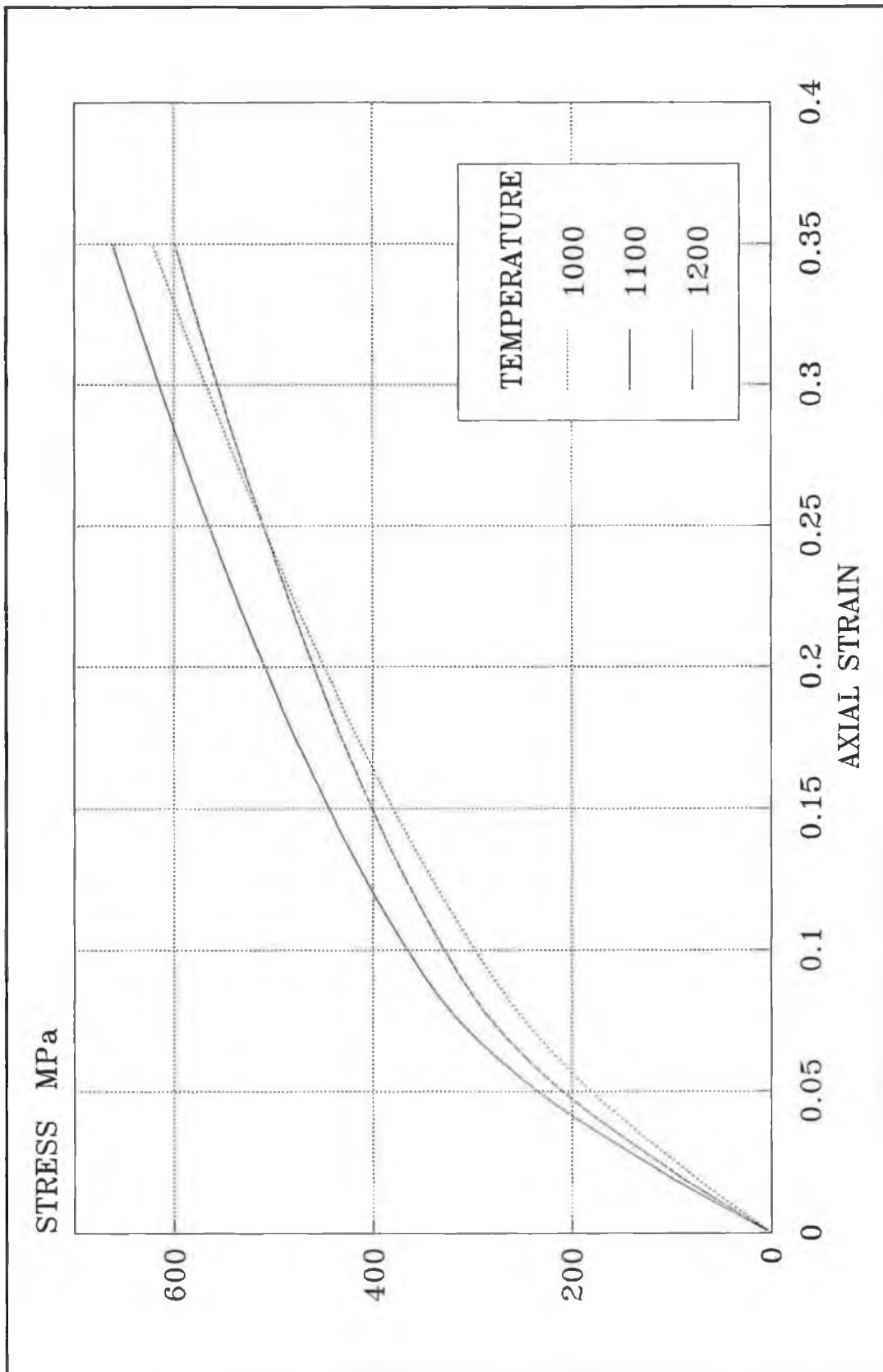


Figure 4.11 Effect of sintering temperature on the stress-strain curves for AISI 347 at a strain rate of 10^3 per second.

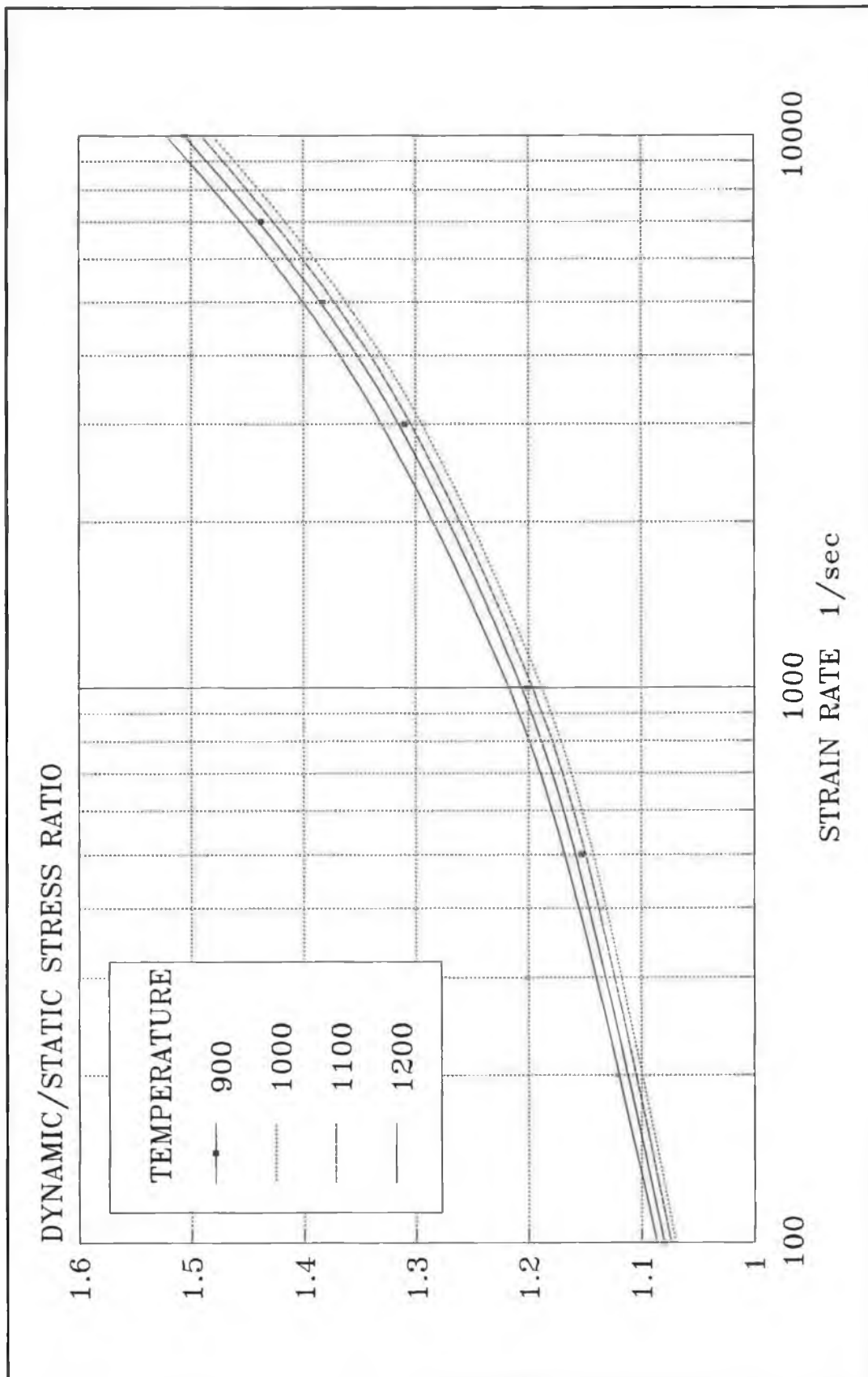


Figure 4.12 Dynamic/static stress ratio vs. strain rate for AISI 304L compacts at 4 sintering temperatures.

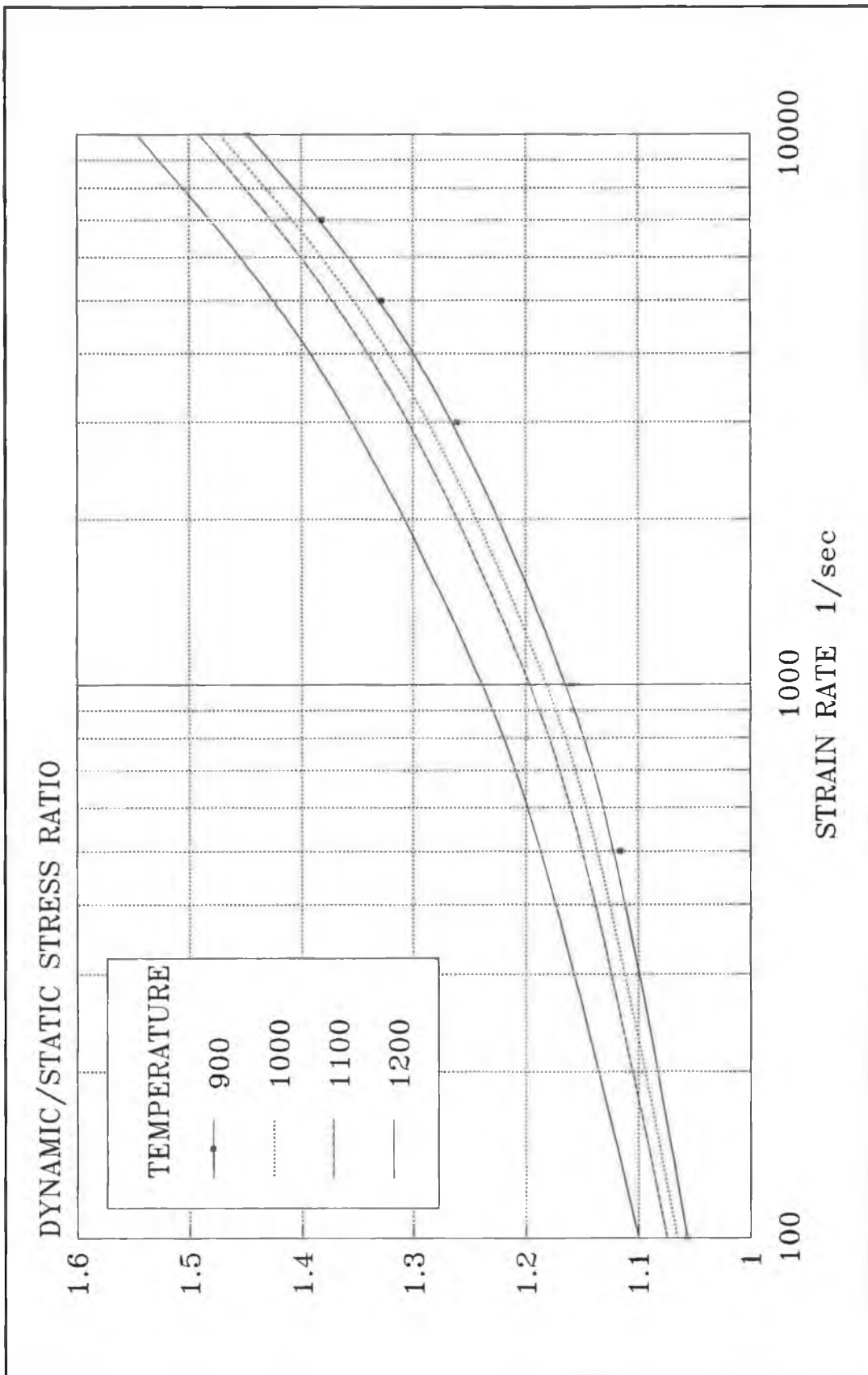


Figure 4.13 Dynamic/static stress ratio vs. strain rate for AISI 316L at 4 sintering temperatures.

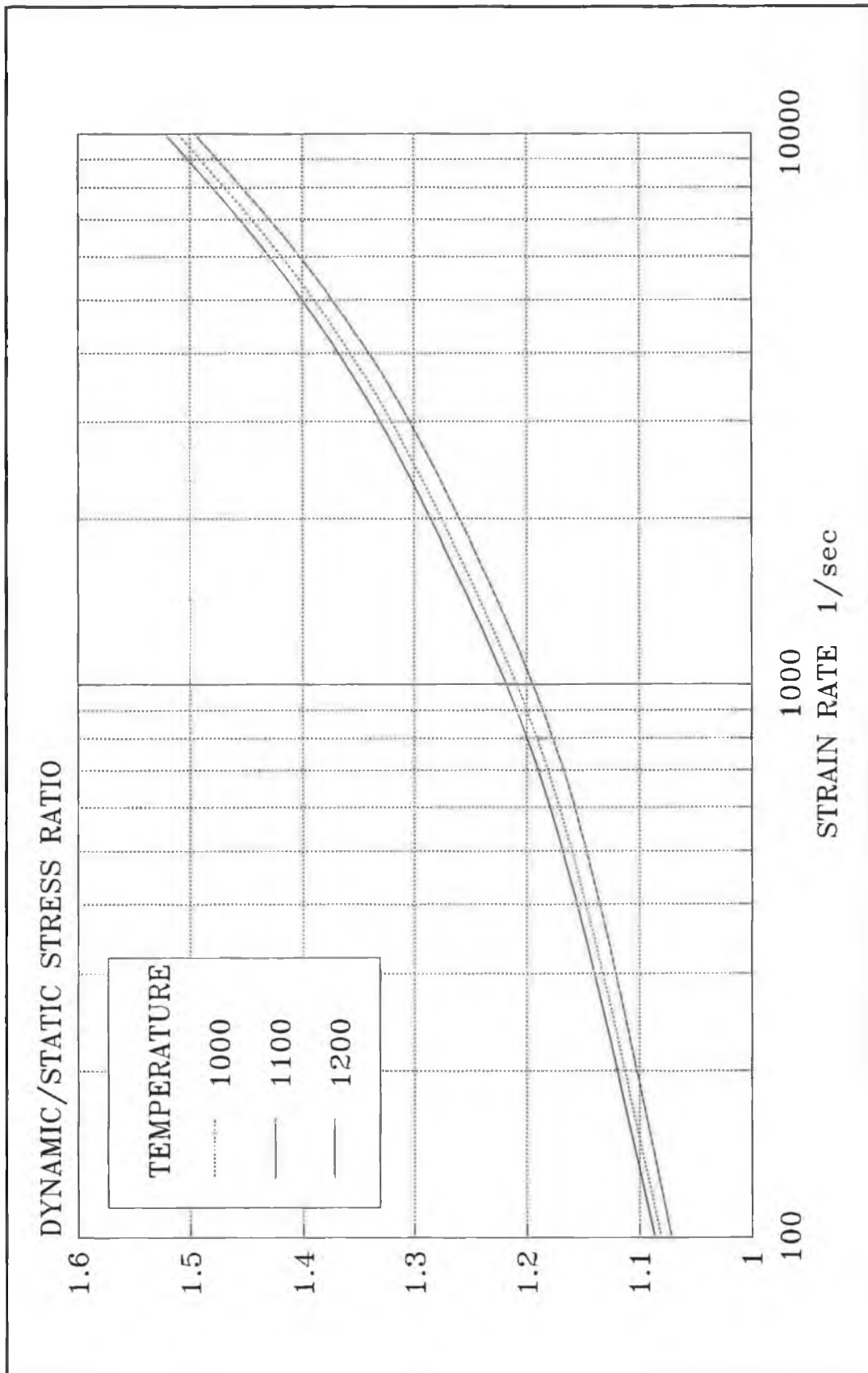


Figure 4.14 Dynamic/static stress ratio vs. strain rate for AISI 347 at 3 sintering temperatures.

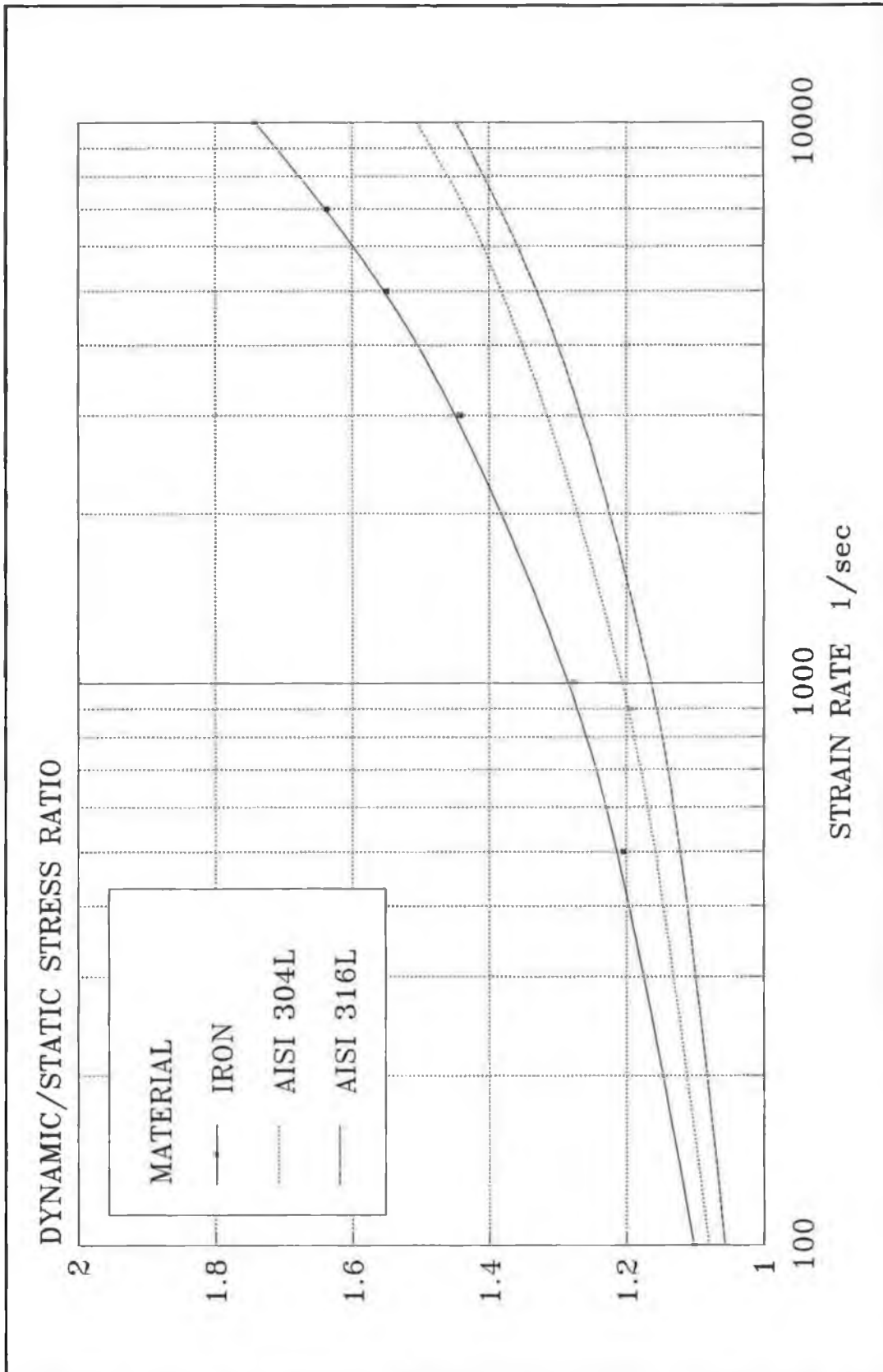


Figure 4.15 Comparison in the stress ratio between the stainless steel compacts and iron compact sintered at 900°C.

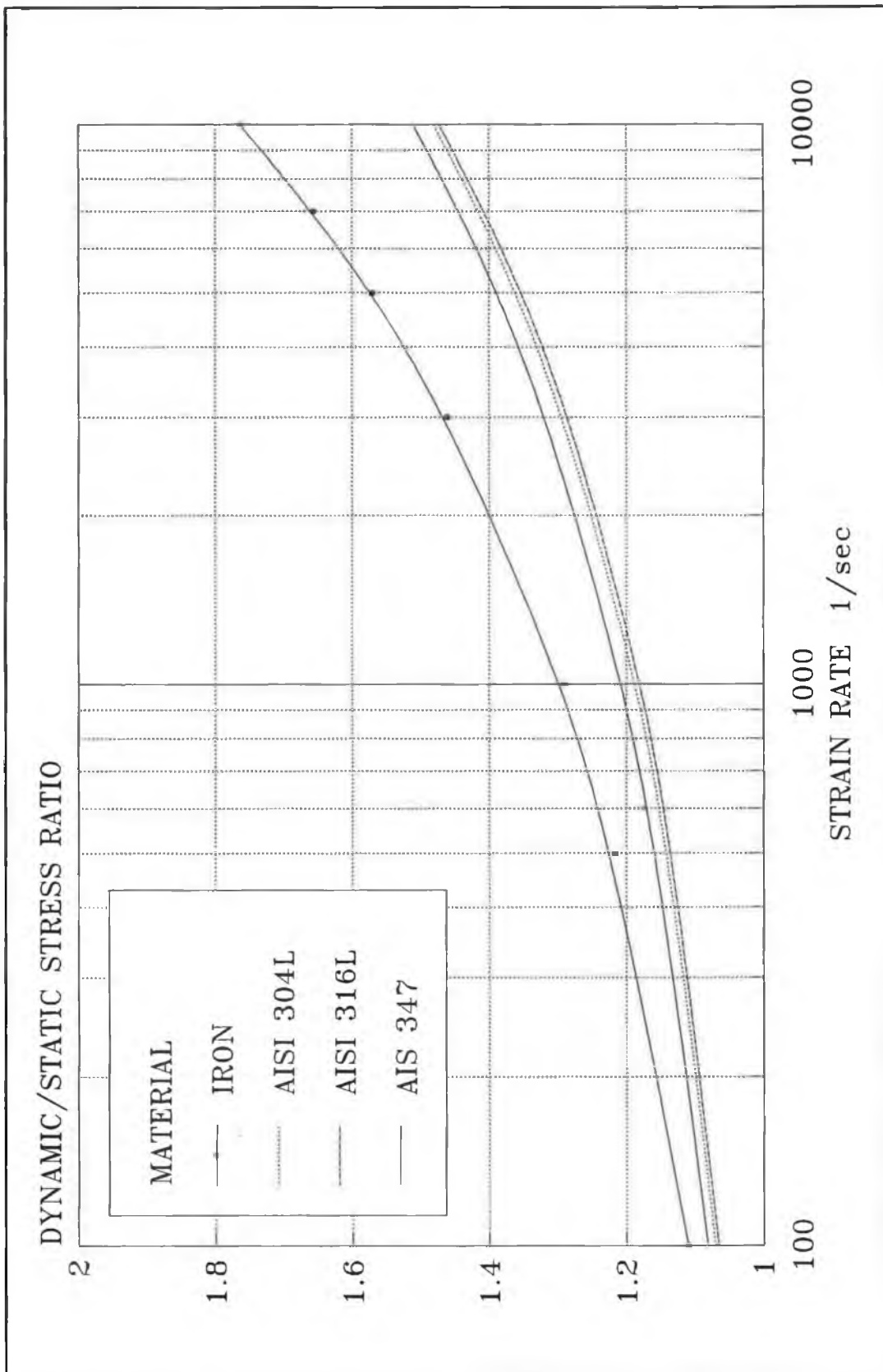


Figure 4.16 Comparison in the stress ratio between stainless steel compacts and iron compact sintered at 1000°C.

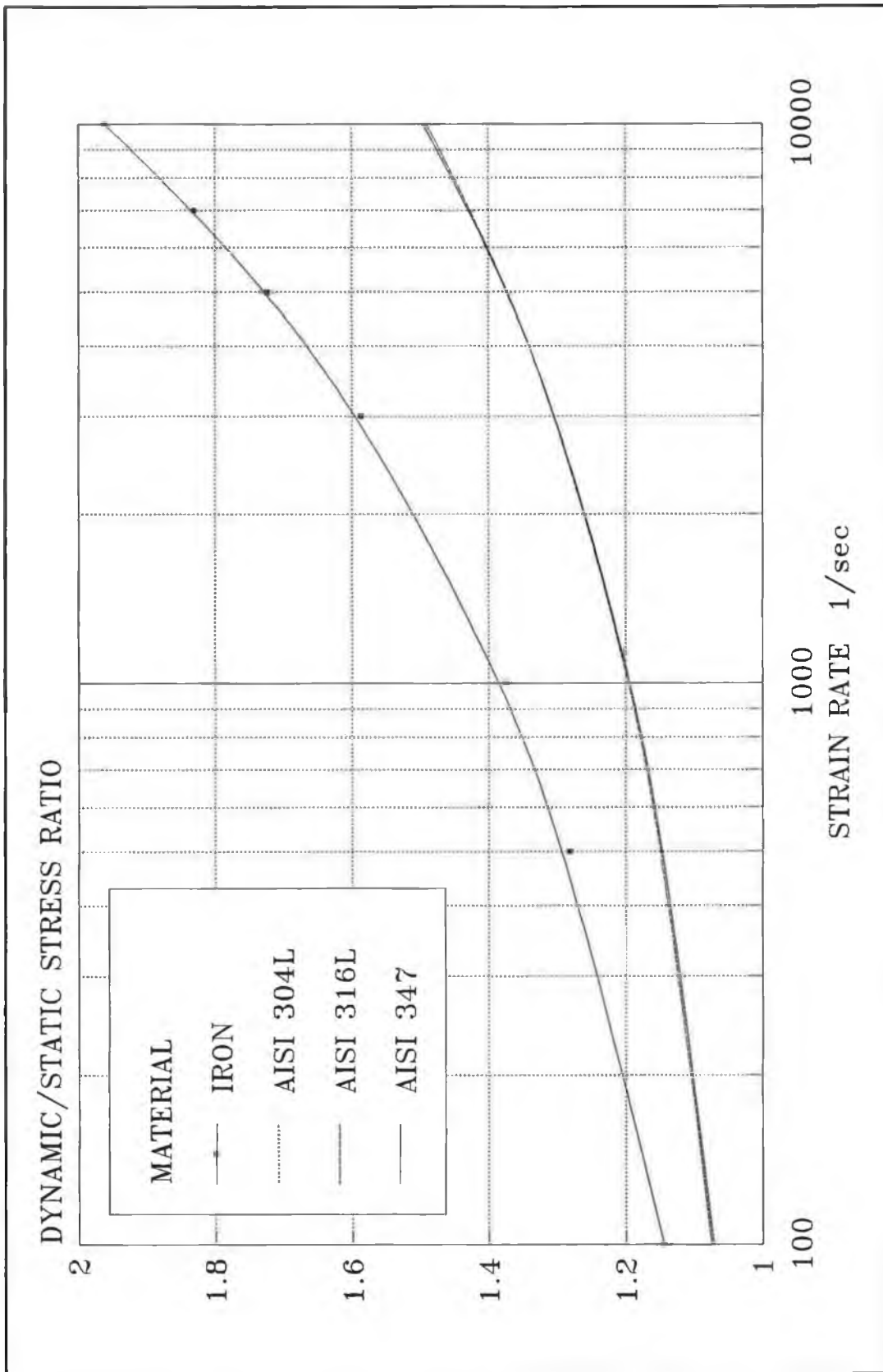


Figure 4.17 Comparison in the stress ratio between stainless steel compacts and iron compact sintered at 1100°C.

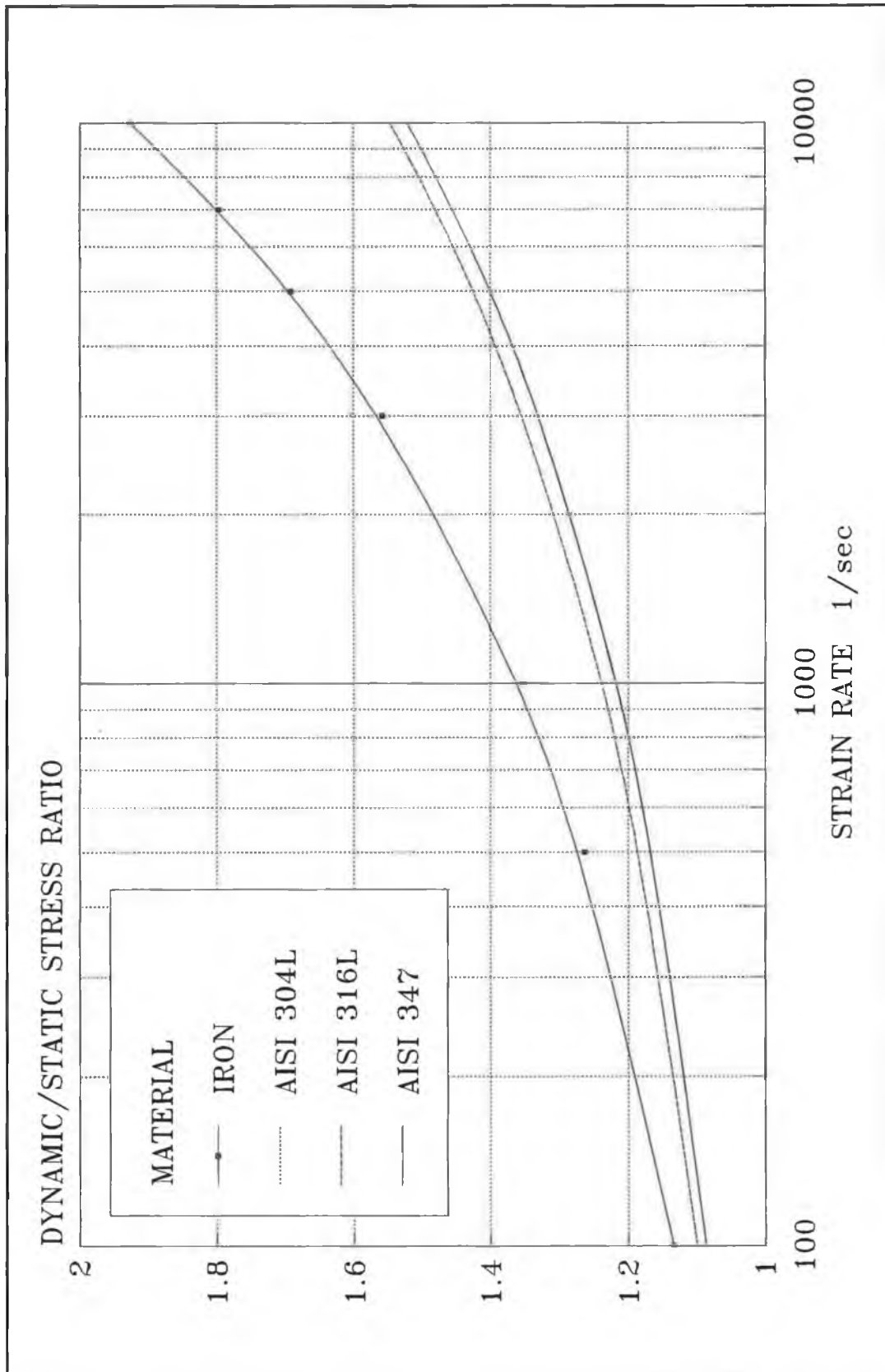


Figure 4.18 Comparison in the stress ratio between stainless steel compacts and iron compact sintered at 1200°C.

CHAPTER FIVE

CERAMIC COMPACTION AND STRENGTH

5.1 COMPACTION:

The general idea behind the compaction process is to shape the powder into a die and make the resultant compact strong enough for handling later on. However, there are several parameters which affect the compressibility of powders. These parameters could improve or degrade the properties of the compact such as green density, density distribution and green strength. Some of the parameters are related to the powder characteristics such as particle size, particle size distribution, particle shape and binder and lubricant additions, while others are related to the compaction process itself such as friction between powder particle and die walls and pressing action (single or double action).

In this work the compressibility of powder has been assessed in relation to particle size, binder type and binder content and lubricant content.

5.1.1 EXPERIMENTAL PROCEDURE:

As mentioned earlier, four different powders have been

used in this investigation. These powders were agglomerated spray-dried powders. Their characteristics are shown in table (2.1).

Compacts were produced by a uniaxial compaction process in a rigid die which was designed for this work. The compaction was carried out using a universal testing machine.

The compaction was carried out as follows: The die was assembled and placed on the anvil of the machine and powder samples were weighed and poured into the die cavity. The upper punch was placed into the cavity and the pressure was applied via the cross-head of the machine. The plotter was set to plot the resulting load vs. the displacement of the cross-head. This plot was converted later to a compressibility curve by calculating the applied stress from the plotted force and the punch diameter and calculating the density from the cross head movement, the compact's diameter and the mass.

It should be noted that single action pressing was carried out to assess the compressibility of powder while double action pressing was used to study the strength of green and fired compacts.

Zinc stearate was mixed with the powder D503 to evaluate the effect of lubricant additions on the compressibility. The mixing was carried out using a Turbula shaker-mixer and

different ratios of lubricant have been used . These ratios are 0.1, 0.25 and 0.5% . Mixing time was 15 minutes to avoid the breaking of the agglomerates due to excessive mixing.

5.1.2 RESULTS AND DISCUSSION:

Figure (5.1) shows the compressibility curve for the first powder D503. This figure shows that there is a sharp increase in the green density at the beginning of the compaction process then it starts to slow down at higher pressures. This sharp increase in the curve is due to the particles rearrangement where particles try to occupy the smallest place. As the pressure increases the particles start to deform and fracture and this leads to further densification by the fact that the newly formed small pieces can move into the remaining pore spaces between the larger particles. Moreover, after releasing the load it can be noticed from the load-displacement curve that there is a reduction in the density. This is due to the spring back effect where the compact recovers elastically.

Figures (5.2), (5.3) and (5.4) show the compressibility curves for D504, D505 and D506 respectively and it can also be seen that the curves have the same trend as D503, where the density increases sharply at the beginning then the increase starts to slow down.

Figure (5.5) shows the compressibility curves for the

first two powders D503 and D504. These two powders were spray dried with two different nozzles, where the powder D504 was sprayed with the smaller nozzle. Upon sieve analysis the two powders did not show any variation in the average particle size. However, the figure shows that the compressibility of the second powder D504 is better than the compressibility of the first D503. It can be seen that at a certain compaction stress the powder D504 reaches higher density than the powder D503 apart from at lower compaction stress, because as described earlier at lower compaction stress the main dominant factor in powder densification is the rearrangement of powder particles.

Binders are added to ceramic powders to improve the green strength of the compact. Figure (5.6) shows the compressibility curves for two powders D503 and D505. These powders have almost the same binder content but they have different binding systems. Powder D503 has binder system type A whereas powder D505 has binder system type B. The figure illustrates that powder D505 shows better compressibility properties than powder D503.

Regarding the binder content, figure (5.7) shows the effect of binder content on the compressibility of two powders D505 and D506. Powder D505 has a binder content of 16.5 g/kg whereas powder type D506 has a binder content of 24.1 g/kg. The figure shows that powder type D505 has better compressibility property than powder type D506 where it can

be seen that for a given compaction stress compacts made from powder type D505 have higher density than compacts made from powder type D506. This is due to the increase of the binder content in the powder.

To sum up, figure (5.8) shows the compressibility curves for the four powders. This figure illustrates that the powder type D505 shows the best compressibility among all the powders.

In respect to the effect of lubricant additions, powder D503 was mixed with three percentages of zinc stearate (0.1, 0.25 and 0.5%) to evaluate its effect on the powder compressibility. Figure (5.9) shows the compressibility curves for the powders. It can be seen that lubricant additions have good effect on the compressibility, where it can be seen that for a given compaction stress the powders with lubricant additions give higher densities compared to the powder with no lubricant additions. Moreover, a closer look at the figure shows that the density of the compact increases with the increase in lubricant percentage up to 0.25% and then it starts to decrease where the 0.25% concentration of lubricant gives the highest compactibility.

5.2 CERAMIC STRENGTH:

Forming a green body is a key element in the manufacture of a ceramic object. Regardless of the process for compacting

the powder, the strength of the green body is an important factor. Firstly, because unreliable green compacts lead to unreliable final product. The distribution of large flaws in the green body remains unchanged through sintering unless further flaws are introduced by grain growth⁽⁷⁷⁾. This assumption is tested by measuring the Weibull modulus of the green and the fired ceramic. Secondly, it is important that the compact has a sufficient strength for handling purposes. It has been suggested that a tensile strength of 5MPa is sufficient for metal powder bodies⁽⁷⁸⁾. However, most ceramic green bodies are weaker than that, the strength being usually 1 to 2MPa⁽⁷⁷⁾.

5.2.1 FRACTURE THEORY:

There are two classes of theories to predict the strength of brittle materials. The first is derived from Griffith's flaw theory⁽⁷⁹⁾, which assumes the presence of flaws of a specific shape, and there is always one with the least favourable orientation and that the crack growth from this flaw causes failure. These theories ignore the statistical nature of the problem. The second class is statistical but it fails to specify the nature of the flaw.

Griffith⁽⁷⁹⁾ developed an equation to calculate the tensile strength for brittle materials:

$$\sigma_t = \frac{1}{Y} \left(\frac{2E\gamma_i}{C} \right)^{1/2} \quad (5.1)$$

where: Y is a geometrical constant.

E is Young's modulus.

γ_i is the effective surface energy.

C is the flaw size.

Because a given ceramic will have a range of flaw sizes there will be a corresponding variation in strength and that is not taken into account by equation (5.1).

The Weibull approach⁽⁸⁰⁾ for predicting the probability of failure of a structure is by dividing the total volume into many volume elements, each element has a small probability of failure. The probability of survival of the part as a whole is then found by multiplying together the probabilities of survival of all the elements. The elements are considered to be similar to the links of a chain, with the weakest link determining the strength of the chain. Thus the properties of a volume element as inferred from the statistics of fracture in simple tension or bending played a central role in Weibull's theory.

The theory states⁽⁸¹⁾ that the probability that rupture will occur within a given volume subjected to any uniform stress is assumed to be completely determined by a quantity σ , which may be calculated from the three principal stresses.

In the case of a solid subjected to any load, the probability that the ultimate strength will not be reached is equal to the probability that rupture does not occur in any part of the solid. If a solid is imagined to be divided into n volume elements for which the individual probability of rupture are $S_1, S_2 \dots S_n$ respectively, the probability of rupture S for the solid as a whole is therefore given by the equation:

$$1-S=(1-S_1)(1-S_2)\dots(1-S_n) \quad (5.2)$$

This equation may be taken to be the fundamental formula for all regular materials. If all individual element probabilities are equal to S_0 , we have:

$$(1-S)=(1-S_0)^n \quad (5.3)$$

For infinitely small elements S_0 becomes infinitely small. In this case we may omit the infinitely small quantities of higher order and thus obtain:

$$S=n \cdot S_0 \quad (5.4)$$

This equation means that the probability of rupture is proportional to the volume. Consequently the distribution function for an infinitely small volume dV may be written as follows:

$$S_0=f(\sigma) \cdot dV \quad (5.5)$$

From equation (5.2) we obtain :

$$\log(1-S)=\sum_{i=1}^n \log(1-S_i) \quad (5.6)$$

If n increases indefinitely, S_i converges towards zero. Then we have :

$$\log(1-S_i) = -S_i \quad (5.7)$$

and by using equation (5.5) we have:

$$\log(1-S) = -\int f(\sigma) \cdot dV \quad (5.8)$$

The function f is determined by the distribution constants of the material. If these constants and the distribution of stresses is known, the quantity B known as the "Risk of Rupture" may be computed from the following equation:

$$B = \int f(\sigma) \cdot dV \quad (5.9)$$

According to equation (5.8) the distribution function takes the form:

$$S = 1 - \exp^{-\int f(\sigma) \cdot dV} \quad (5.10)$$

For an isotropic solid subjected to a uniform stress, the formula takes a simpler form:

$$S = 1 - \exp^{-V \cdot f(\sigma)} \quad (5.11)$$

Thus the computation of the strength properties of a solid begins with a calculation of the risk of rupture B from equation (5.9). The calculation of the risk of rupture starts by assuming that the stress distribution function $f(\sigma)$ has this form:

$$f(\sigma) = \left(\frac{\sigma}{\sigma_0}\right)^m \quad (5.12)$$

where m and σ_0 are constants.

Thus, by substituting equation (5.12) into equation (5.11) we have:

$$S = 1 - \exp\left[-V\left(\frac{\sigma}{\sigma_0}\right)^m\right] \quad (5.13)$$

The constants m and σ_0 are determined using the least square method. Equation (5.13) can be rewritten as:

$$\log\log\left(\frac{1}{1-S}\right) = \log V - m \cdot \log \sigma_0 + m \cdot \log \sigma \quad (5.14)$$

where S , which is the probability of rupture, is calculated from the number of specimens under test, by giving each specimen a rank after sorting the stress values from the tests in an ascending order:

$$S = \frac{2i-1}{N+1} \quad (5.15)$$

where i is the test rank

N is the number of the tested specimens

5.2.2 RESULTS AND DISCUSSION:

To study the strength of the ceramic powders under study, a number of discs were prepared. Powder samples of 11 g mass were weighed and poured into the die cavity and the compacts were produced using the universal testing machine with the die as a floating one to produce double action

pressing. The compacts were cylindrical with diameter of 17 mm. and a height of 15.2 mm. and these were pressed to a density of 3.15 ± 0.05 g/cc.

The green strength of the compacts was measured using the diametral compression test. This test is performed by placing the compact between two flat surfaces as shown in figure(5.10). The force is applied along a diametral plane of the compact. This loading produces a biaxial stress distribution within the specimen. This stress distribution consists of a tensile stress at the plane where the force is applied and a compressive stress which acts along the loaded diameter^(82,83). By measuring the force, the tensile stress is calculated from this equation^(83,84):

$$\sigma = \frac{2 \cdot P}{\pi \cdot h \cdot D} \quad (5.16)$$

where:

σ is the tensile stress

P is the applied force

h is the height of the compact

D is the diameter of the compact

The diametral test was carried out on 10 specimens of each powder compact. The results of the tests were used to calculate the probability of failure for brittle materials using Weibull theory of the strength of brittle materials⁽⁵³⁾.

Figure (5.11) shows the probability of failure curves for the green powder compacts. It can be seen from the figure that the powder type D503 shows the highest strength among the others and the powder D504 comes next. This is due to the effect of particle size as can be seen in figure (5.5) that the powder D504 shows higher compressibility and hence, less load is needed to press the discs than for powder D503. As for powder D505 it is observed that it has the lowest strength among all the powders. This is also due to the higher compressibility of this powder as can be seen in figure (5.8). Another factor which affects the strength could be due to the effect of the binding system where the binder type B was chosen has little plasticizing material in its system. However, powder type D506 shows a remarkable increase in strength in comparison with D505. This could be due to the addition of binder C to binder B in the binding system of powder D506. We can conclude that the binder C has an improved plasticizing agent in it which gives the discs that increased strength.

The slope of the curves in figure (5.11) which is called the Weibull Modulus, gives an indication of the reliability of the strength and the repeatability of the results. The higher the modulus the better the repeatability is. This figure shows that the first three powders D503, D504 and D505 have a moderate Weibull modulus. However, this is acceptable in ceramics. As for the powder D506, it has the highest modulus of 70 which is remarkably good. This is also an

indication of the addition of binder C to the powder that improved its plasticity.

Another set of green discs were compacted to the same density of 3.15 ± 0.05 g/cc having a diameter of 17 mm and 15.2 mm height. These discs were fired using a standard temperature profile. The dimensions of the fired discs were 14 mm diameter and 12.6 mm height with an average density of 5.44 ± 0.05 g/cc. These discs were used for the diametral compression test to measure the fired strength. The test was carried out on 10 samples of each powder compact and the results of the test were used to calculate the probability of failure for them as was done above for the green discs.

Plate(5.1) shows a photograph of some of the fractured samples where it can be seen that two modes of failure have taken place. The first mode is called Normal Tension Failure where the specimen is split symmetrically about the loaded diameter into two pieces. The second mode is the Triple-Cleft Failure. In this mode of failure the specimen is split symmetrically about the loaded diameter into four pieces. The "Tongue-and-Groove" shapes of the outer surfaces and the clean central fracture are characteristics of this fracture mode. This kind of fracture is a variation of normal tensile fracture⁽⁸³⁾.

Figure (5.12) shows the probability of failure for the fired discs. It can be seen that the curves of the fired

discs did not show the big variation in strength among them as was seen for the green discs in figure (5.11). The curves become closer to each other which is logical because they all have the same composition and the binder in them has been eliminated. Moreover, it can be noticed that the curves' modulus has become smaller.

Putting the two figures (figure (5.11) and figure (5.12)) together for comparison, it can clearly be noticed from figure (5.13) the big difference in strength between the green and the fired discs can be clearly noticed. Moreover, the curves of the fired discs become closer because they represent the same material under test.

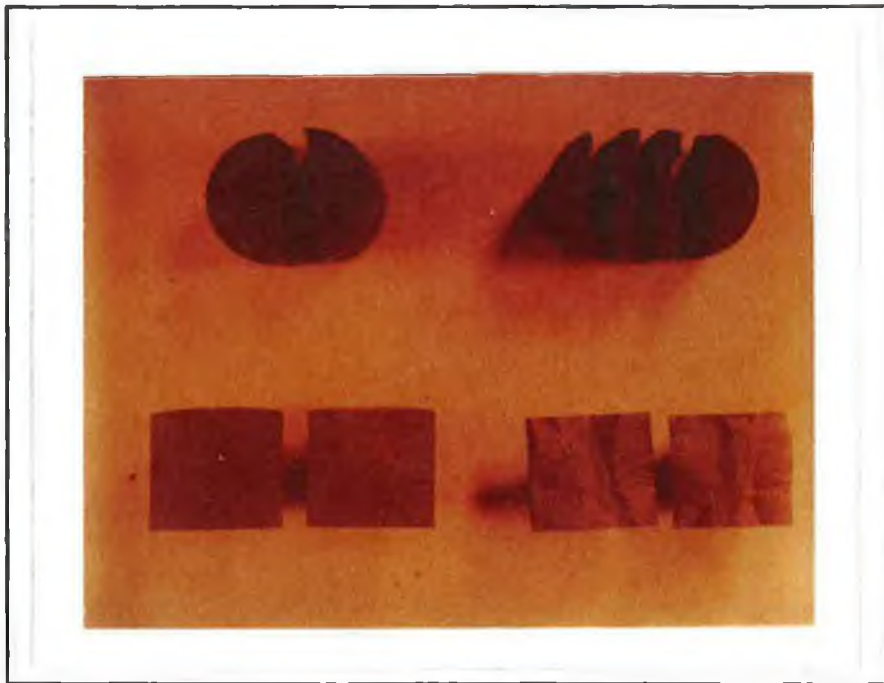


Plate 5.1 Photograph of the fractured specimens using the diametral compression test.

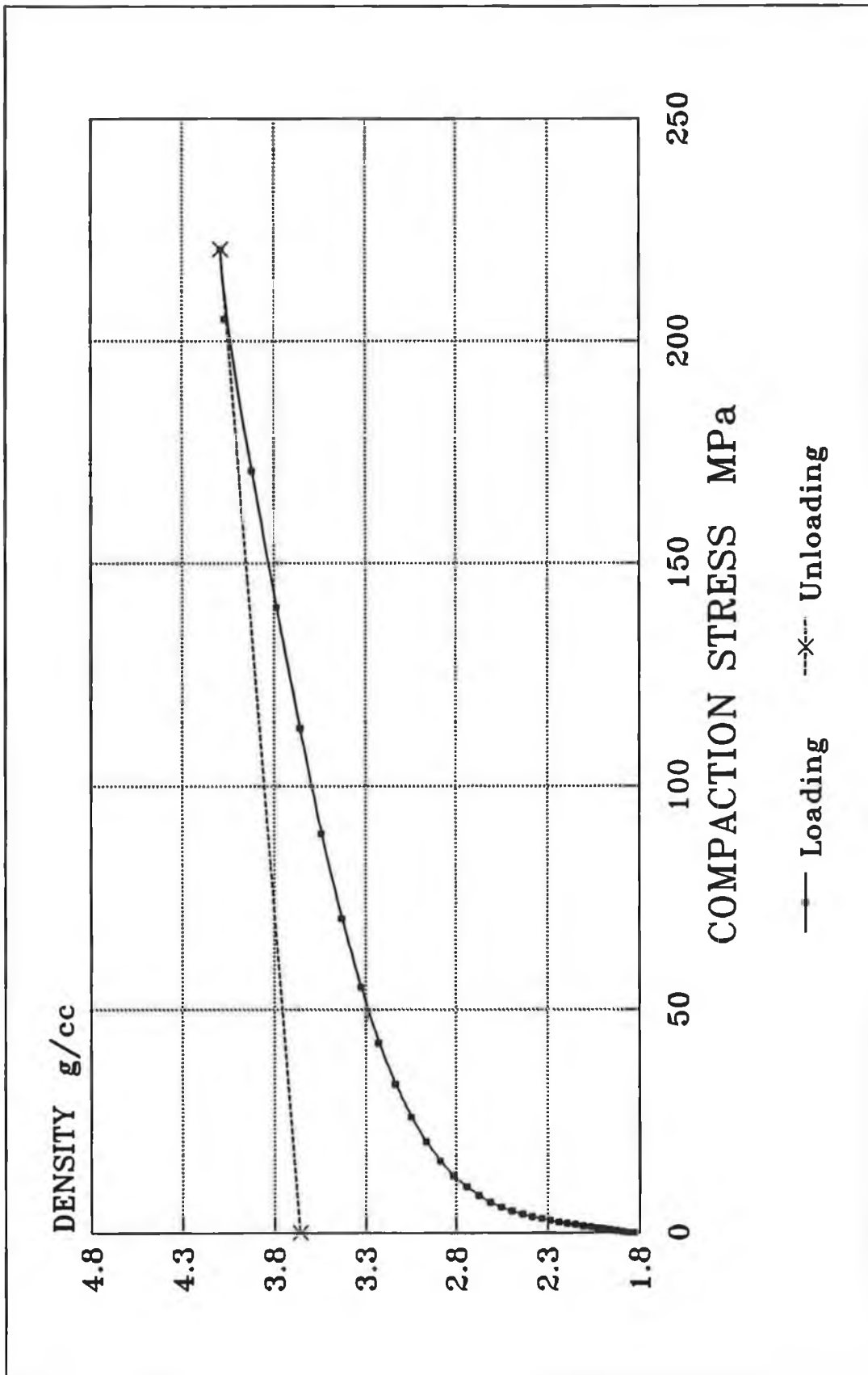


Figure 5.1 Compressibility curve for D503 without using lubricant.

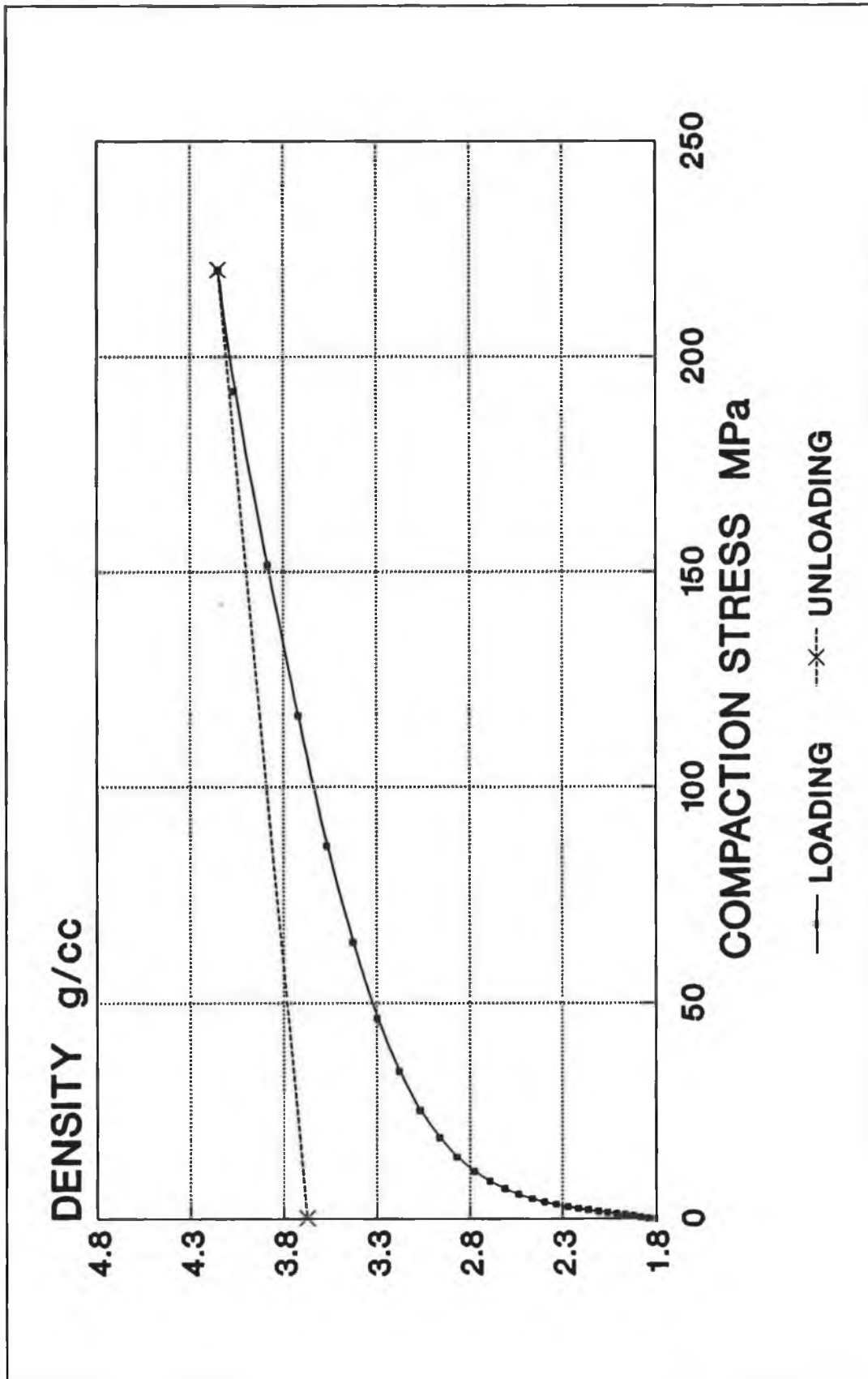


Figure 5.2 Compressibility curve for D504 without using lubricant.

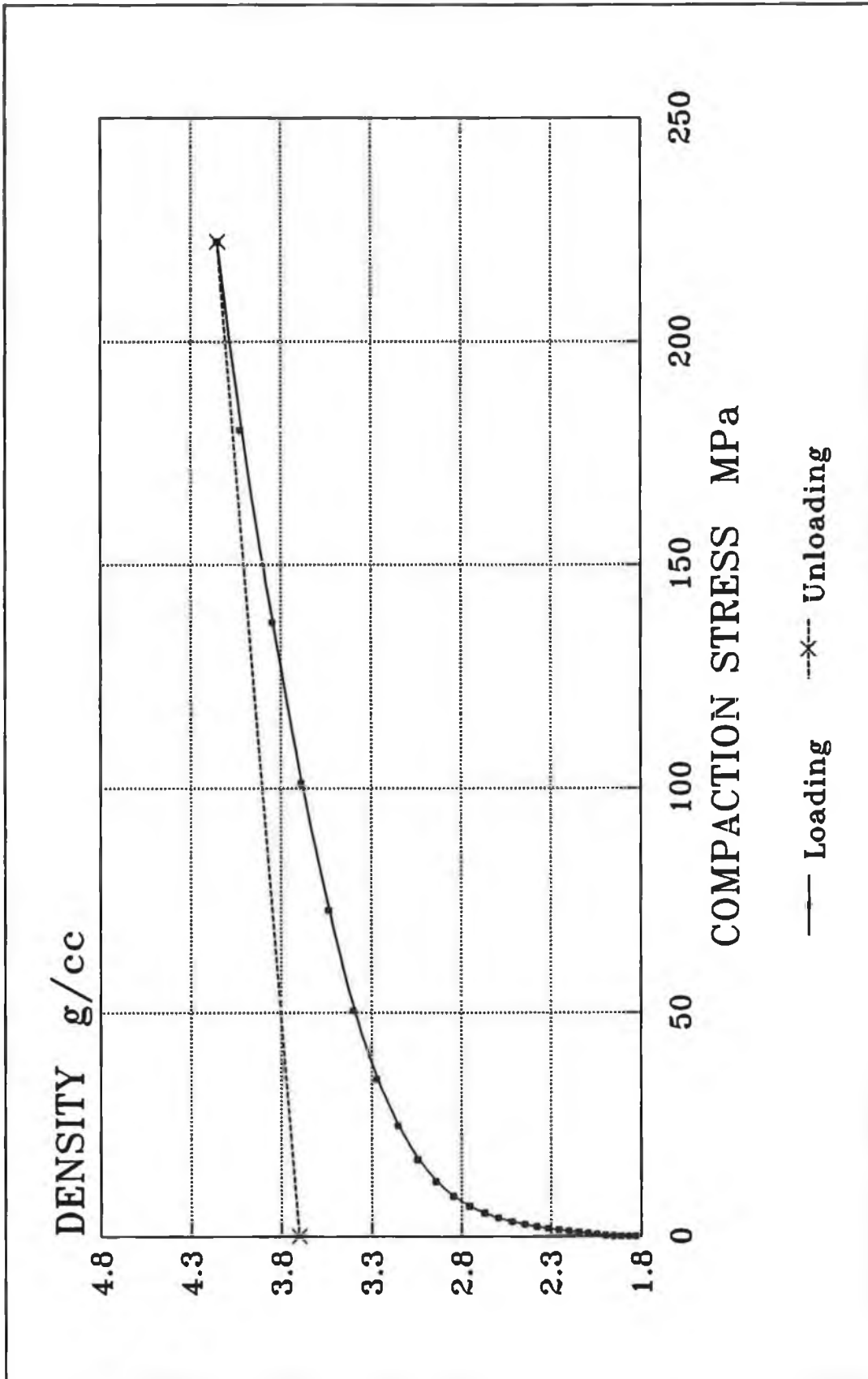


Figure 5.3 Compressibility curve for D505 without using lubricant.

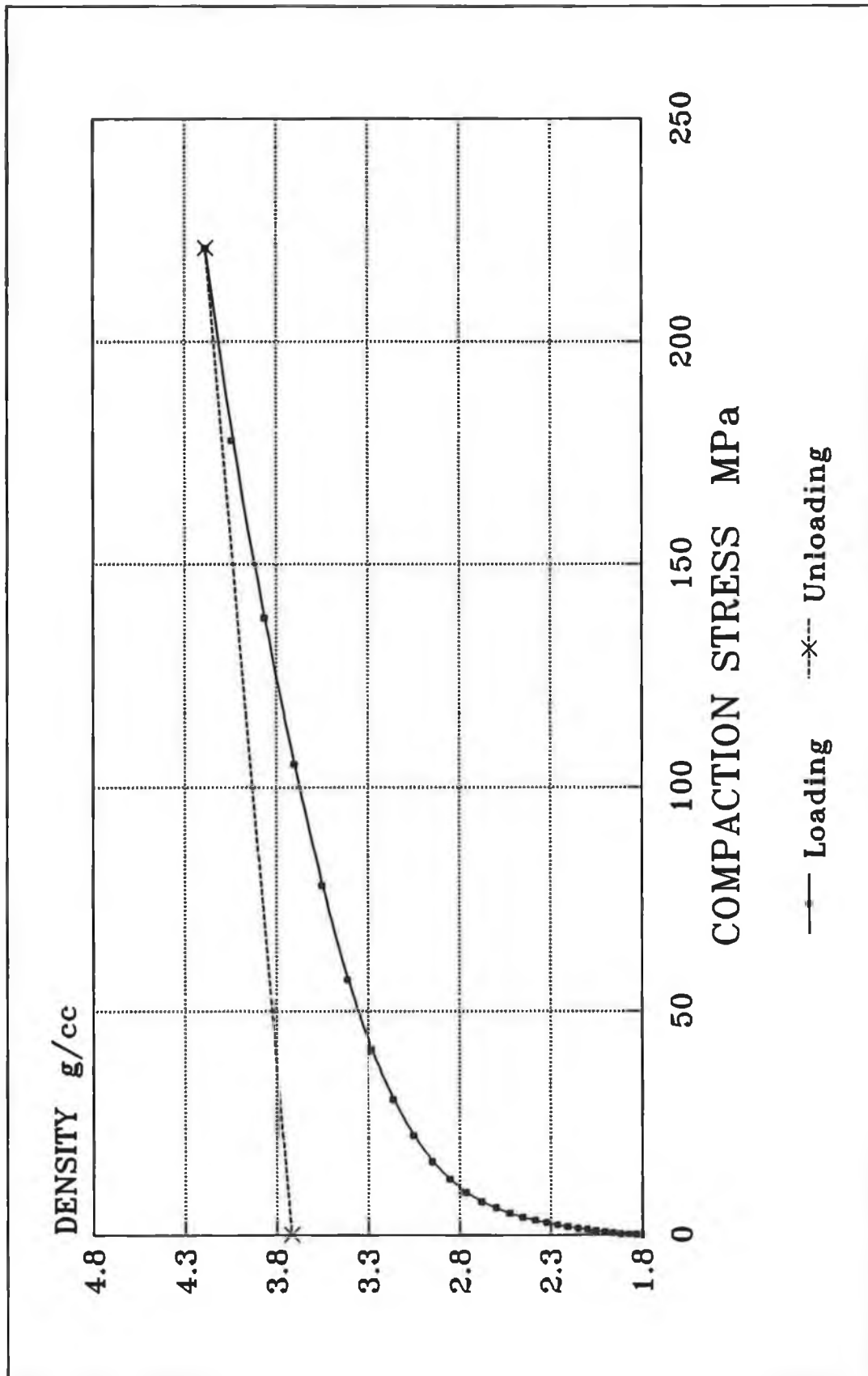
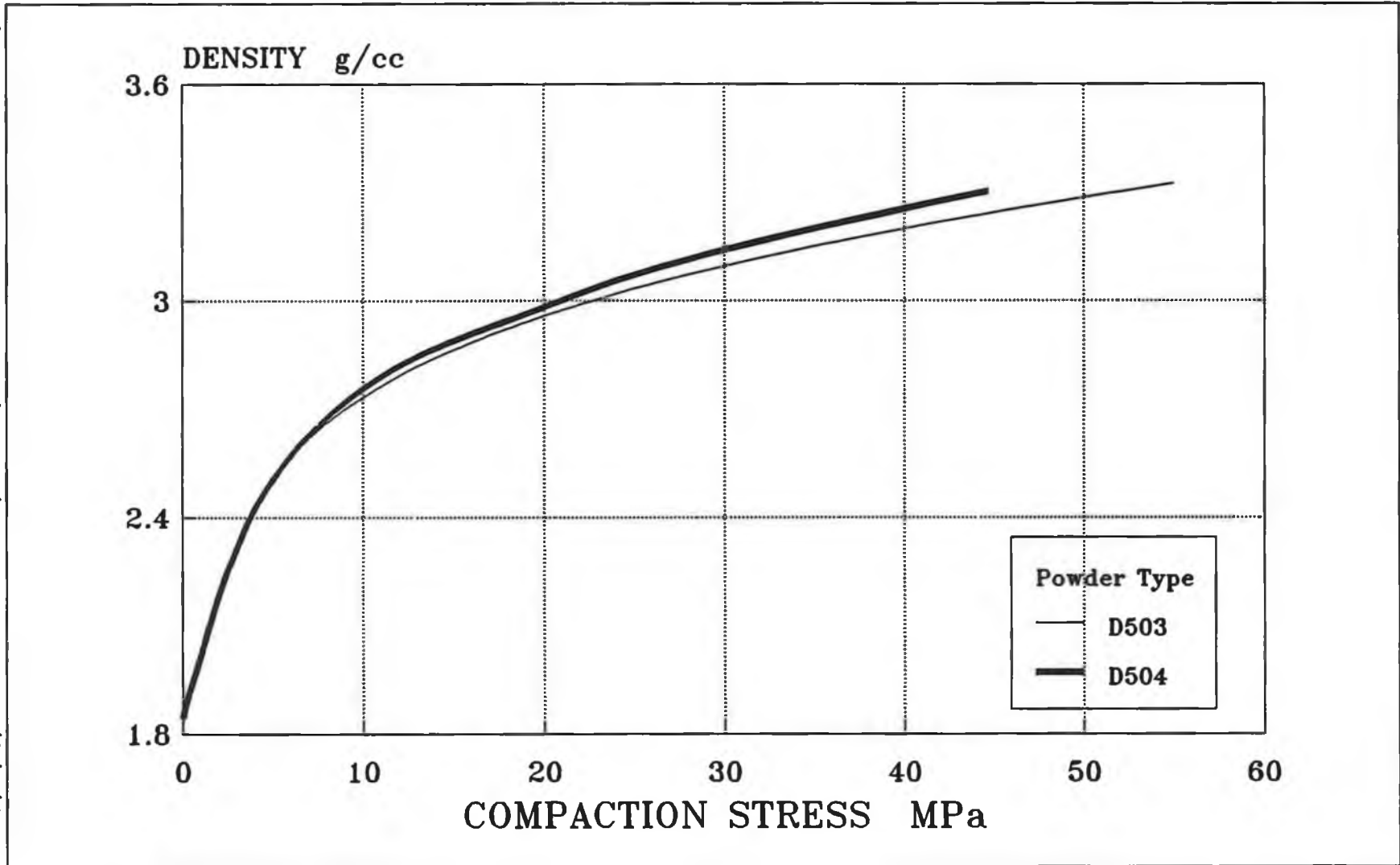


Figure 5.4 Compressibility curve for D506 without using lubricant.

Figure 5.5 Effect of particle size on compressibility.



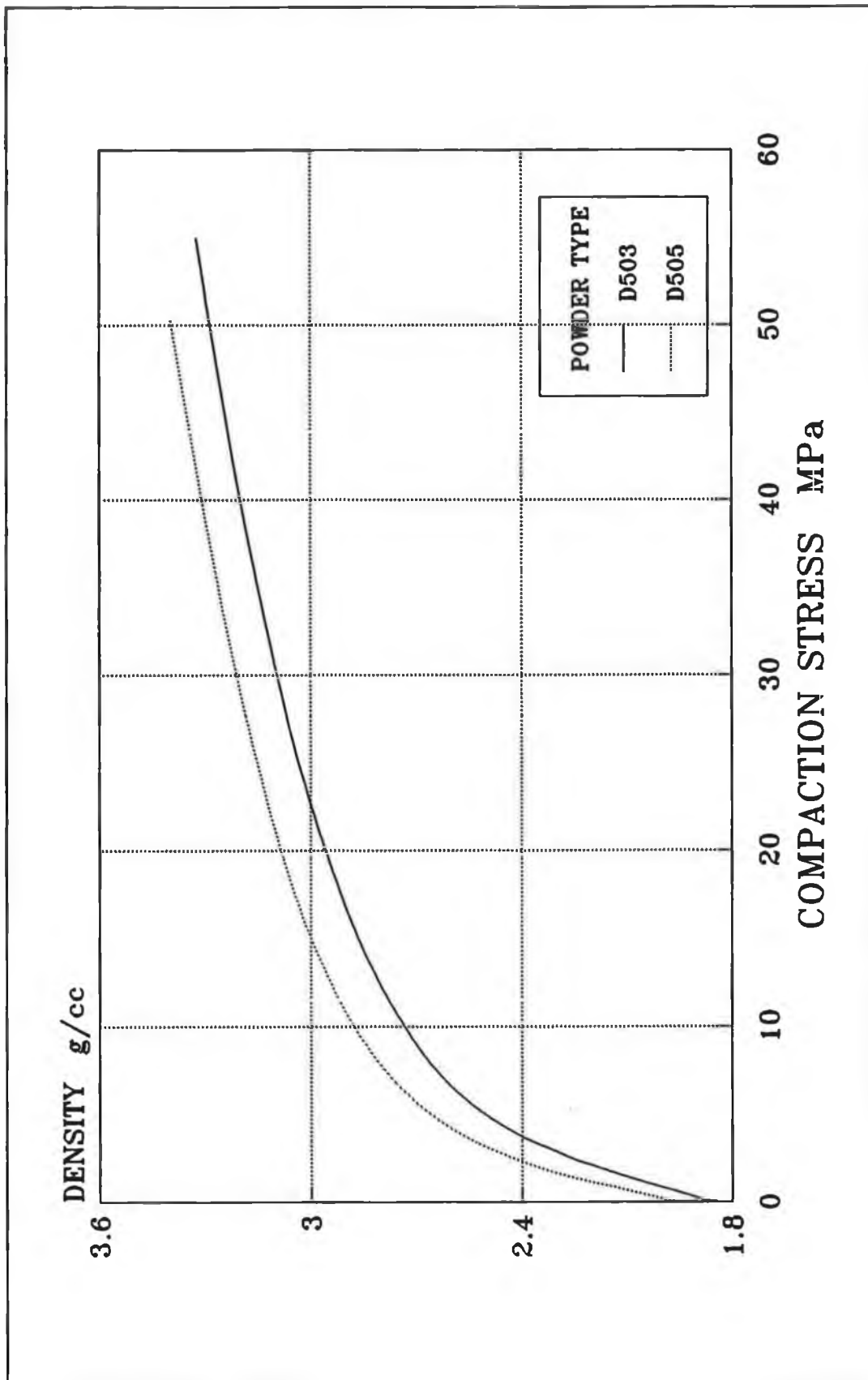


Figure 5.6 Effect of binder type on the compressibility of ceramic powder.

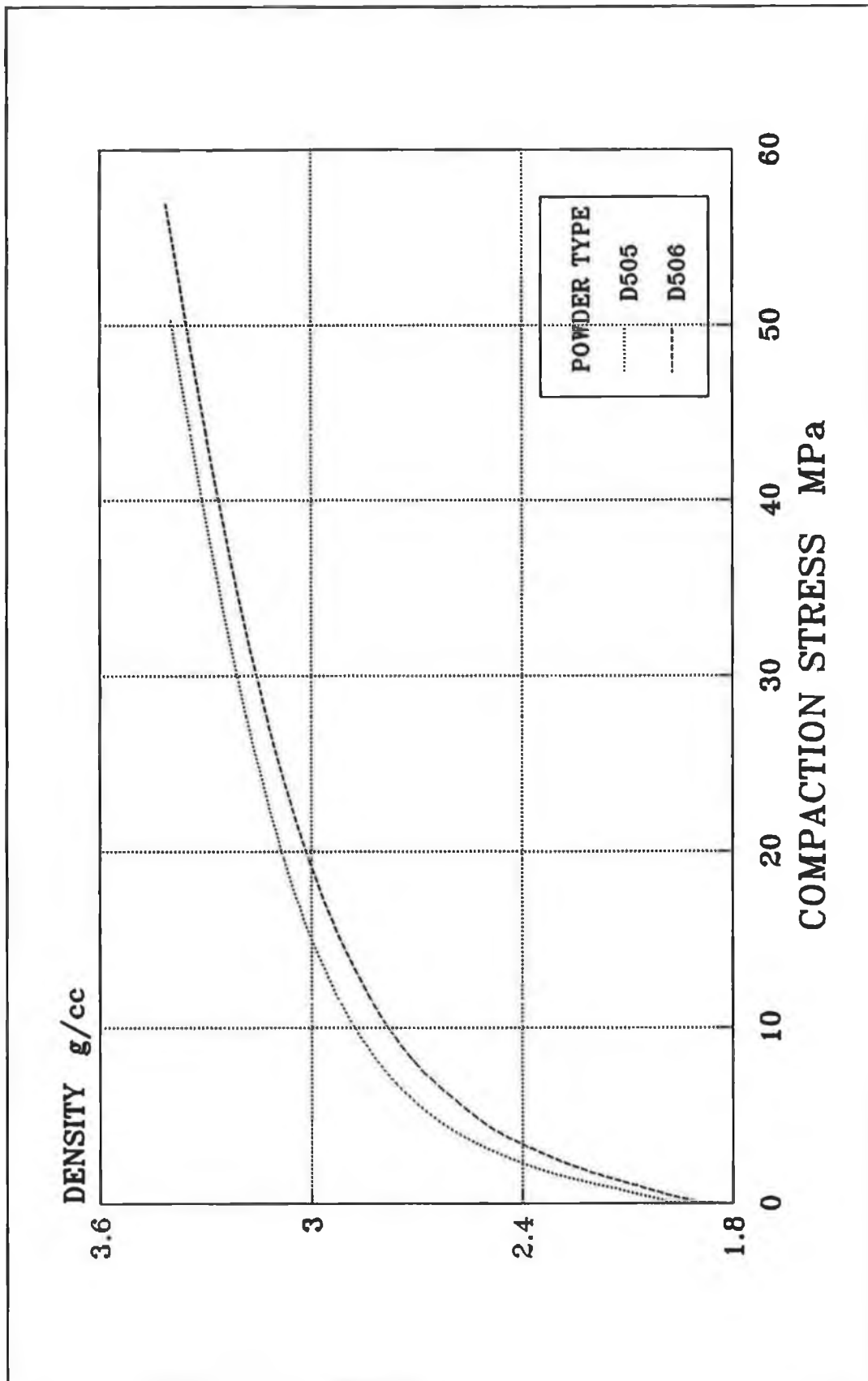


Figure 5.7 Effect of binder content on the compressibility of ceramic powder.

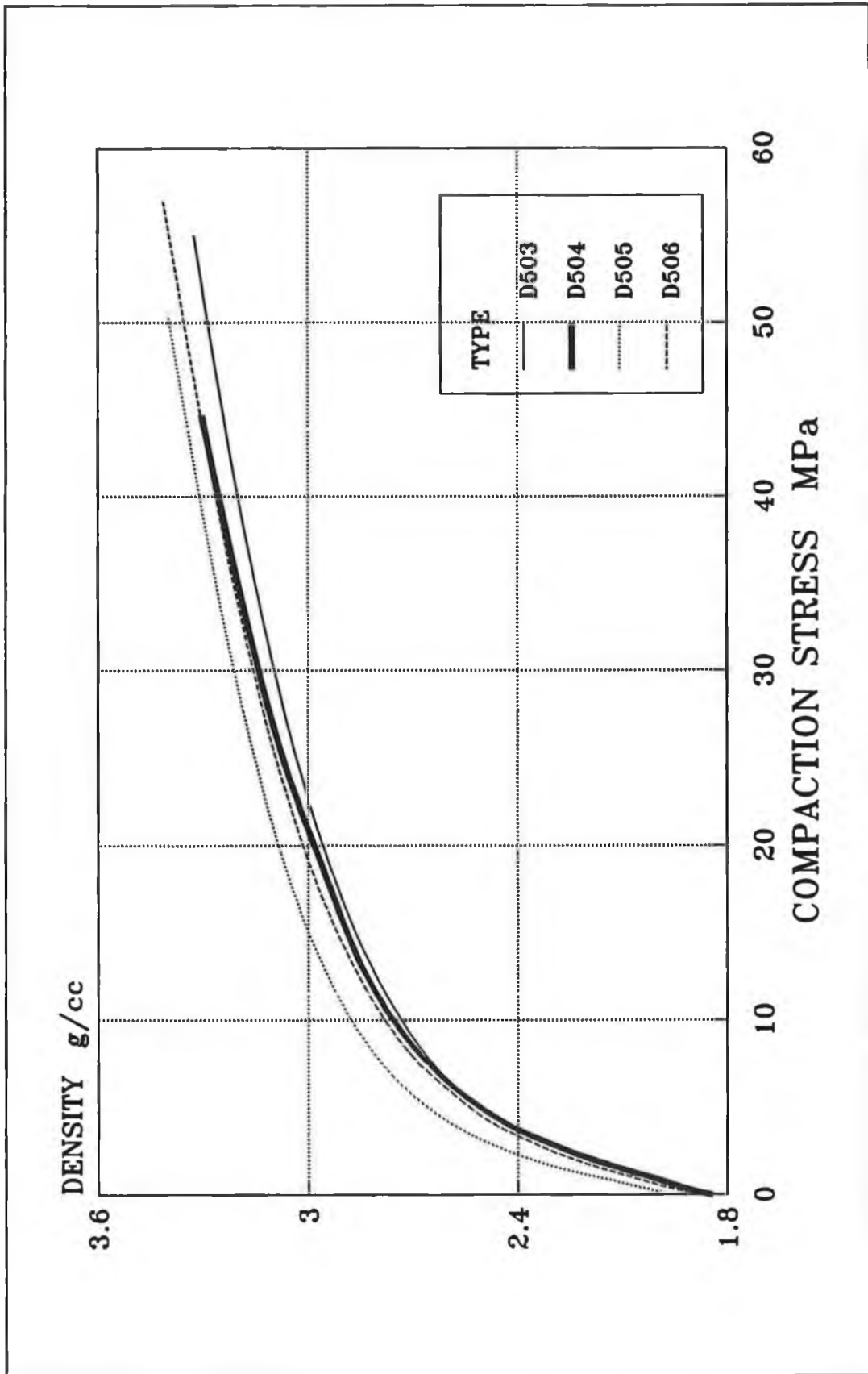


Figure 5.8 Compressibility curves for the 4 powders used in the study.

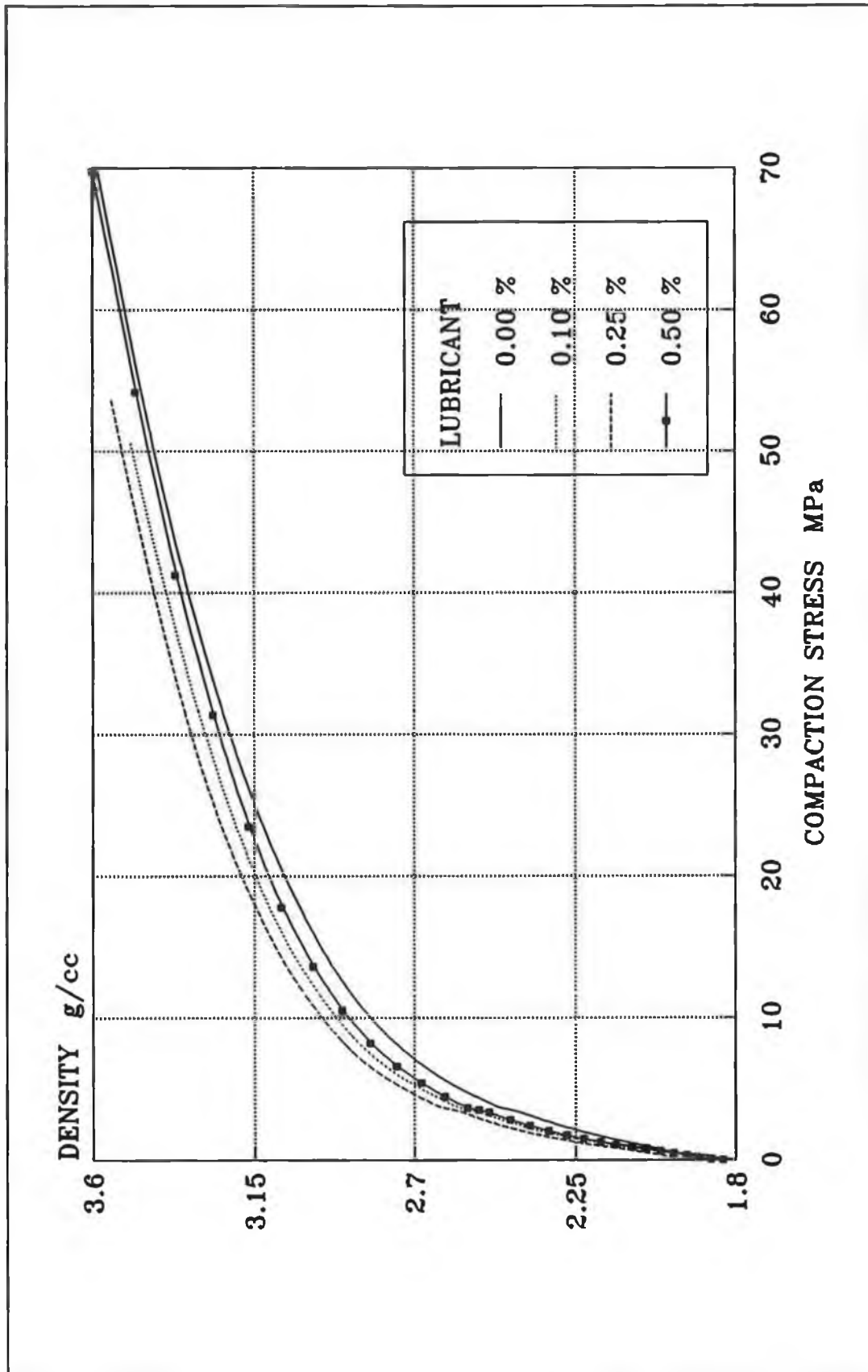


Figure 5.9 Effect of lubricant addition on the compressibility of ceramic powder.

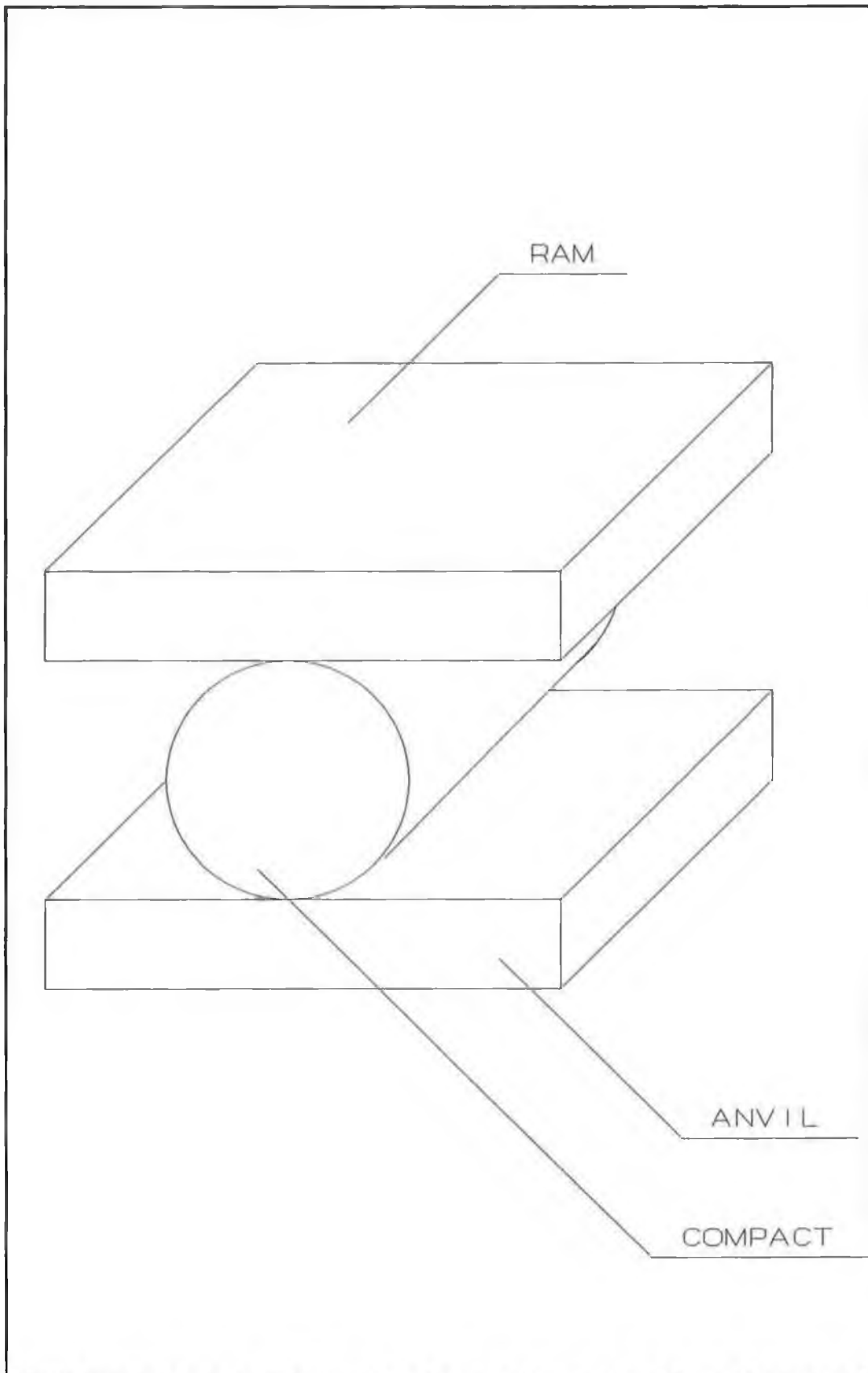


Figure 5.10 Drawing of the setup of the diametral compression test.

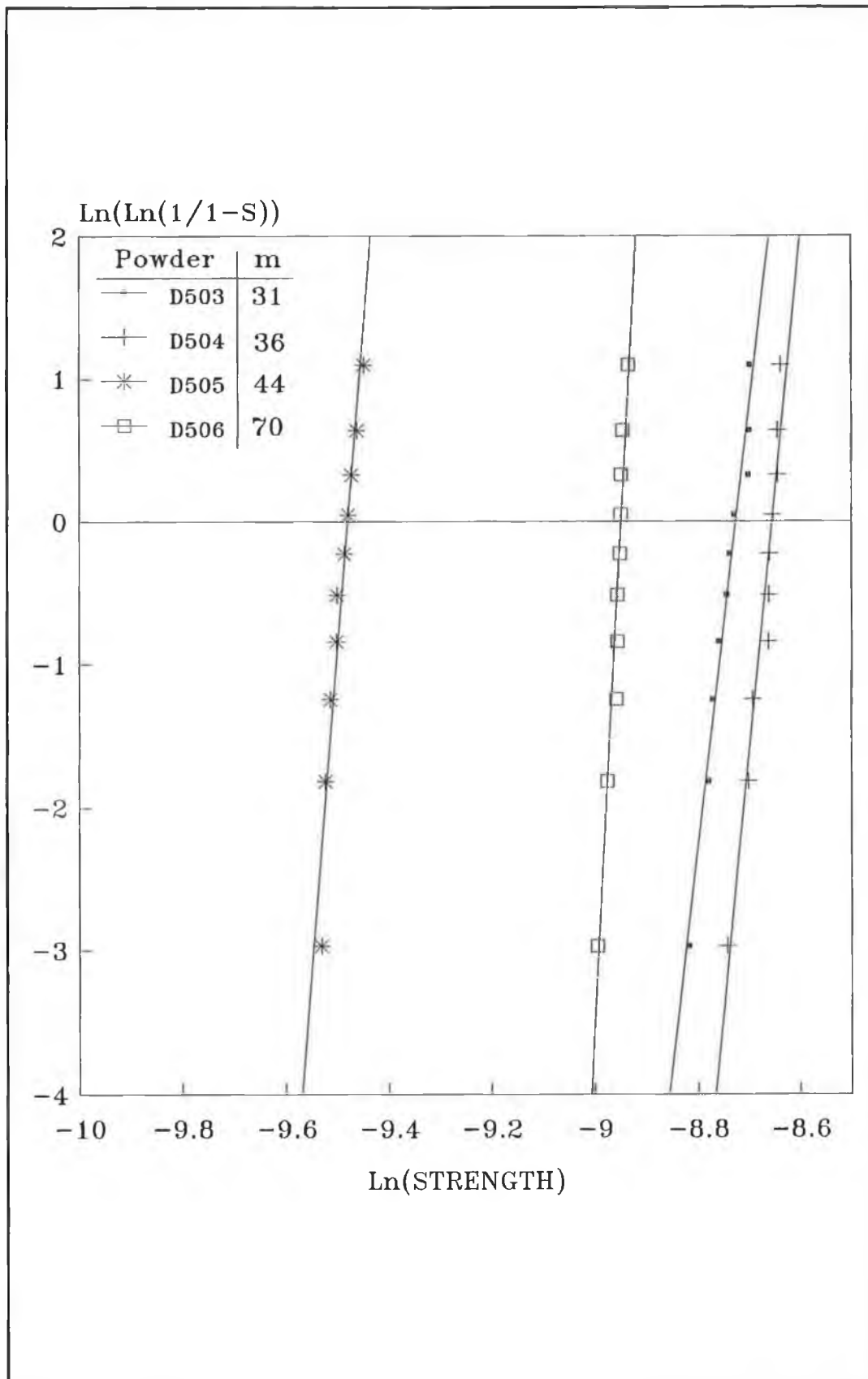


Figure 5.11 Probability of failure for 4 different green powder compacts.

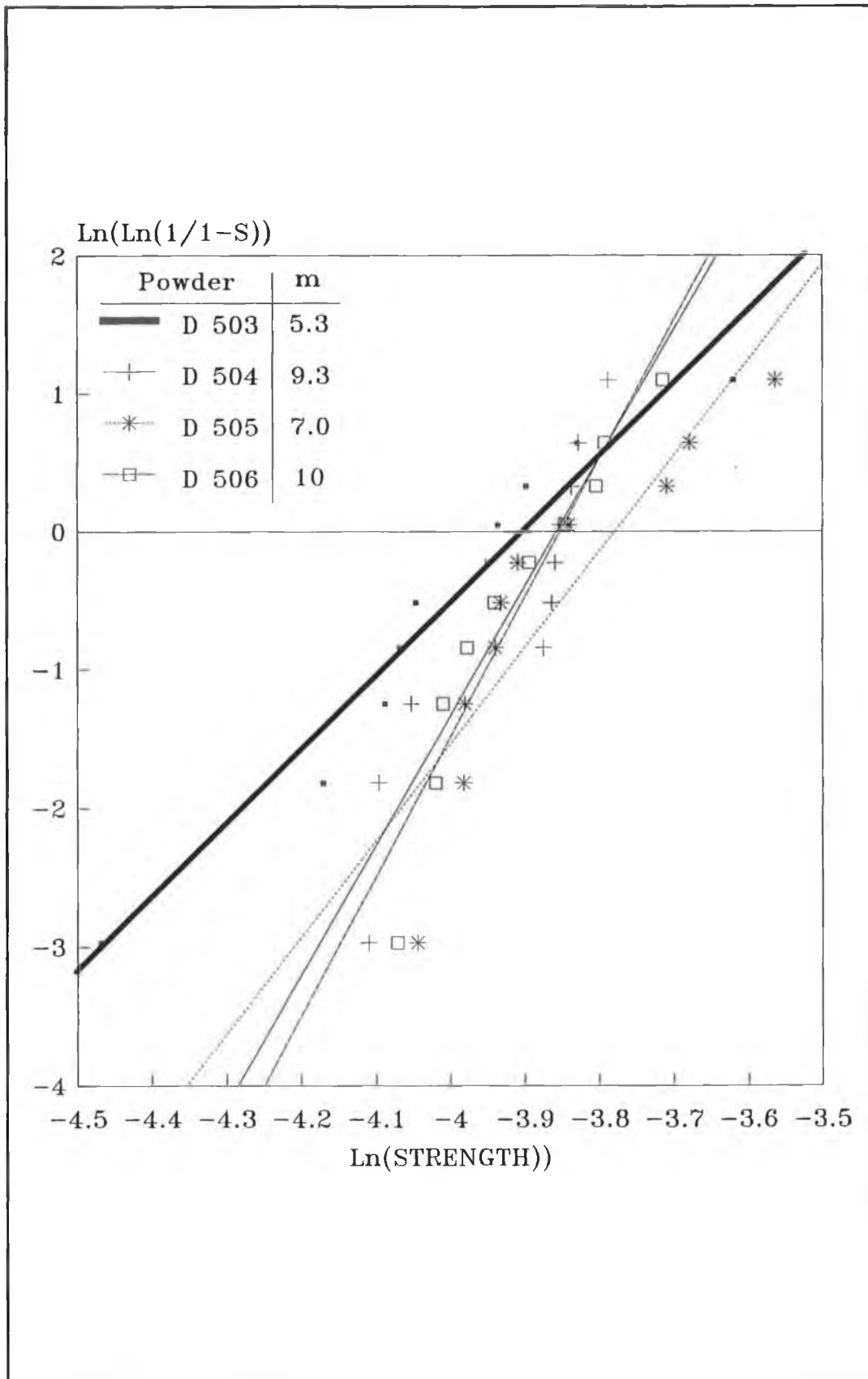


Figure 5.12 Probability of failure for 4 difference fired powders compacts.

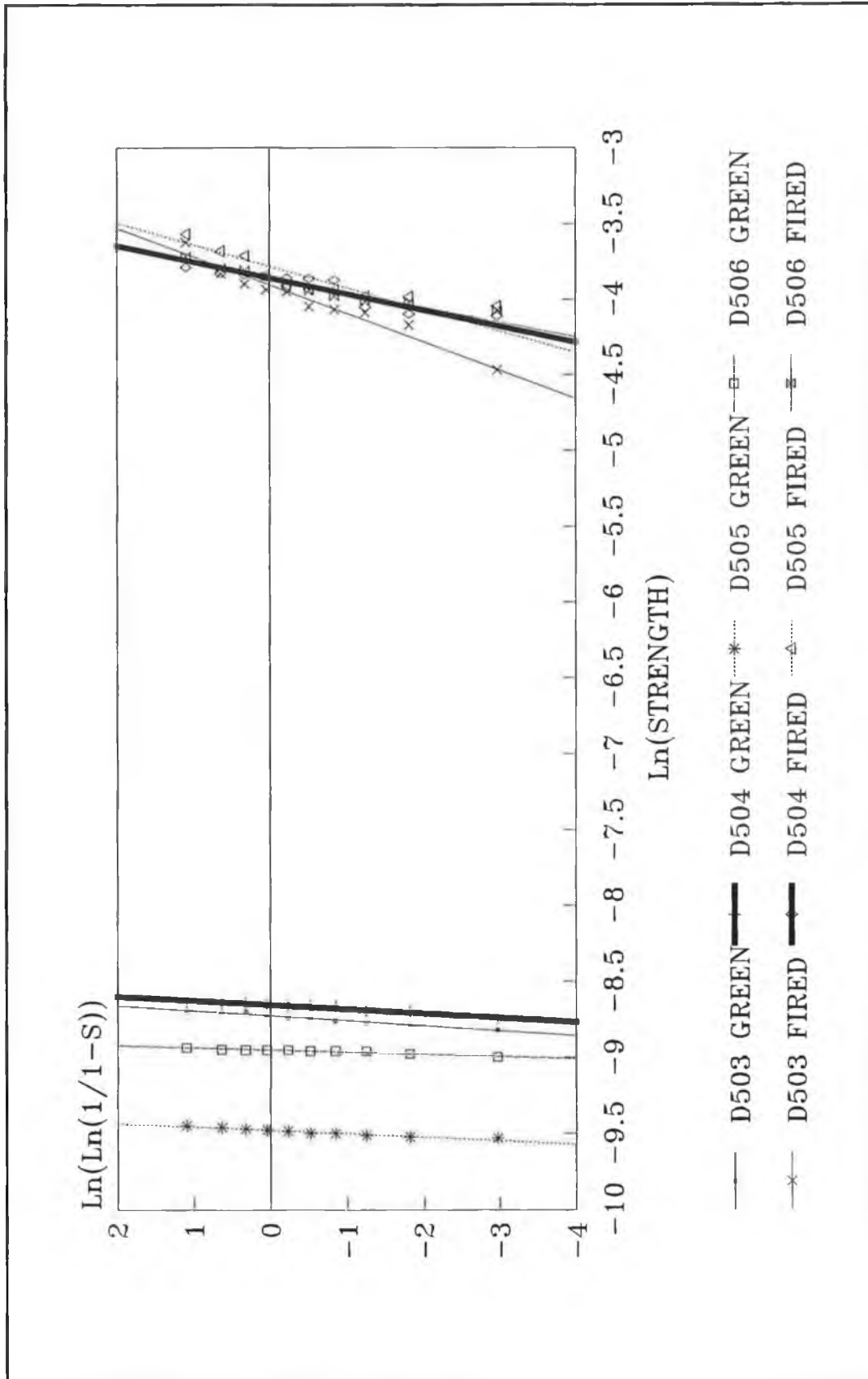


Figure 5.13 Comparison between the green and fired strength of 4 different powders.

CHAPTER SIX

SINTERING

6.1 WEIGHT LOSS:

Binders are added to the powder to give it the necessary plasticity required for compaction and the necessary strength required for subsequent handling. These binders will no longer be of use in the finished product and they might do some harm to the finished product if they still exist in it. To remove the binder system from the compact, a stage in the firing process called binder burn out is used to burn and remove all the organic binders. This stage is essential in the firing process which can affect the quality of the finished product.

6.1.1 MANUALLY CONTROLLED WEIGHT LOSS:

In this work, an attempt has been made to control the binder burn out by manipulating the temperature profile used in the firing process. Usually, the temperature profile used in a firing process consists of a number of ramps and holds usually developed on a historical trial and error basis. In this work, the same procedure is used but by monitoring the weight of the compacts during firing and at the end of the

firing, changing the profile in an attempt to control the binder burnout at a constant rate.

6.1.1.1 EXPERIMENTAL SET UP:

The experimental set up for weight loss control is shown in figure (6.1). The balance was placed underneath the pot furnace and a stand was put on the balance with a vertical rod passing through a hole in the furnace. It was made sure that the rod did not touch the furnace body at any point which will affect the balance read out. The green discs were loaded into the furnace and placed on the stand. The balance was connected to a personal computer through a communication link to transfer the weight of the samples to the computer. Plate (6.1) shows a photograph of the equipment lay out, while plate (6.2) shows the actual layout of the samples inside the furnace.

A preset temperature profile was given to the furnace through the programmable controller and a computer software was developed to read the weight from the balance at a predetermined time interval and store it in a file. Figure (6.2) shows a simplified flow chart of the software.

After the completion of the firing cycle the software calculates the weight loss and the weight loss rate.

6.1.1.2 RESULTS AND DISCUSSION:

To start with, four different temperature profiles with different constant heating rates (10, 7.5, 5 and 2.5°C/min) were used in the firing cycle. These heating rates were chosen arbitrarily to see how the weight loss and the weight loss rate vary in relation to heating rate. The discs used for these tests were 125 mm in diameter and 45 mm in height. One disc was loaded into the furnace and was fired using the above mentioned heating rates and the results for the weight loss and weight loss rate are shown in figures (6.3) to (6.6) respectively.

Calculation of weight loss was done using the following formula:

$$WL = \frac{W_i - W_o}{W_o} \quad \frac{g}{kg} \quad (6.1)$$

where: WL weight loss.

w_i compact weight at time t_i .

w_o initial compact weight before the firing starts.

The weight loss rate was calculated as follows:

$$WLR = \frac{\frac{W_{i+1} - W_i}{W_o}}{t_{i+1} - t_i} \quad \frac{g/kg}{h} \quad (6.2)$$

where: WLR weight loss rate.

w_{i+1} compact weight at time t_{i+1} .

$t_{i+1}-t_i$ the time interval which is set in the software.

Figure (6.3) shows the weight loss and the weight loss rate curves vs. firing time at a heating rate of 10°C/min. It can be seen that the weight loss curve shows a sharp drop which indicates that the binder is burning at very high rate as can be seen from the weight loss rate curve, where the weight loss rate reaches a maximum of about 24 g/kg/h. Moreover, the weight loss curve shows another drop after the binder has been eliminated. This indicates that some oxide material undergoes a reduction reaction and it can be noticed in the weight loss rate curves another peak of about 15 g/kg/h. However, reoxidation appears to take place afterwards which can be seen in the weight loss curve as an increase in weight.

Looking at figure (6.4) it can be seen that the curves of weight loss and weight loss rate for a heating rate of 7.5°C/min show some similarity with figure (6.3), where there are two drops in the weight loss curve and these correspond with the two peaks in the weight loss rate curve. The first one corresponds with binder burn out while the second corresponds to the oxide reduction. However, these drops in the curves are less steep than in figure (6.3) where the weight loss rate curve shows the first peak of about 20 g/kg/h and the second peak of about 13 g/kg/h. Furthermore, reoxidation takes place afterwards as in figure (6.3).

As for figure (6.5) where the heating rate is 5°/min, it can be noticed that the weight loss and the weight loss rate curves have the same trend of two drops in the weight loss then increase in weight as in the previous two figures. However, the weight loss rate curve shows a reduction in the rate at which the binder is burnt out where the maximum weight loss rate is about 17 g/kg/h. Moreover, the amount of oxide reduction reaction is reduced, which can be seen in the figure that the maximum weight loss rate is about 5 g/kg/h.

Regarding figure (6.6) in which the heating rate is 2.5°C/min, it can be seen from the weight loss curve that oxide reduction reaction and reoxidation have disappeared and the rate at which the binder is burnt out is decreased as seen from the weight loss rate curve, where the weight loss rate reaches a maximum of 13 g/kg/h.

The fired discs from the first three heating rates (10, 7.5 and 5°C/min) were very distorted. These shrunk unevenly and became conical in shape with concave and convex surfaces at the top and the bottom of the discs respectively. Moreover, some cracks on the surface can be seen with the naked eye. These discs were mechanically degraded due to the high heating rate. As for the discs which were fired at 2.5°C/min, they showed minimal distortion but no sign of cracks as seen above. Plate (6.3) shows a photograph of the distorted discs.

Going back to figure (6.6), where the heating rate is

2.5°C/min, it can be noticed that the weight loss curve shows some linearity at the beginning of firing. So, by doing some modification to the temperature profile and introducing some ramps at different heating rates, the temperature profile No. 01 as shown in figure (6.7) was achieved. In this figure, the weight loss and the weight loss rate are plotted as a function of firing time. It can be seen that the weight loss has been spread over the firing time longer than the previous firing profiles and the maximum weight loss rate has been reduced to about 5 g/kg/h. Moreover, three major zones can be noticed in the weight loss rate curve. The first zone (zone I) corresponds to moisture evaporation which starts during the first ramp as can be seen from the temperature profile. The other two zones (zone II and zone III) correspond to the binder and plasticizer burn out. Furthermore, it can be noticed that there is a dead time between moisture evaporation and the binder burn out during which, practically no weight loss takes place. This dead time lasts for almost 2 hours.

The temperature profile was modified to minimize that time where there is no weight loss. Figure (6.8) shows the weight loss and weight loss rate curves for temperature profile No. 04. This temperature profile was the result of some modifications in temperature profile No. 01. This figure shows the three major zones of moisture evaporation and binder burn out. Moreover, the dead time between moisture evaporation and binder burn out has been reduced.

Furthermore, the maximum weight loss rate has been reduced to about 3 g/kg/h. The figure also shows that there is another dead time between zone II and zone III.

To minimize this new gap, the dwell time after the first ramp at 210°C which lasts for 3 hours in temperature profile No.04 (refer to figure (6.8)), has been changed to a ramp at a heating rate of 0.08°C/min for 2 hours. This is called temperature profile No. 06, as shown in figure (6.9). This figure shows the weight loss curve seems to be straight enough apart from the beginning where the gap between moisture evaporation and binder burn out still exists as can be seen in the weight loss rate curve. This is due to the big difference in temperature where the moisture evaporates and the binder burns out. Moreover, even though the gap is found at around 200°C where theoretically the binder should start to burn, this does not happen because of the temperature gradient inside the disc, where the measured temperature is the temperature of the surroundings and not the temperature of the disc. Finally the weight loss in figure (6.9) seems to be held at a constant rate of 2 g/kg/h as can be seen from the weight loss rate curve.

Another test has been carried out using the latest temperature profile No. 06 but with different set of discs. These discs were the second set of discs of 50 mm diameter and 41 mm height. The furnace was loaded with 8 discs and their weight was almost equal to the 125 mm disc and firing

was done using temperature profile No. 06. Figure (6.10) shows the weight loss and weight loss rate vs. firing time for these discs. The weight loss curve shows a difference in comparison with figure (6.9) as well as the weight loss rate curve, even though the mass of the discs and the temperature profile used were both the same. This is due to the higher ratio of surface area to volume, where the smaller discs have a surface to volume ratio of 1.28 cm^{-1} whereas the bigger discs have a surface to volume ratio of 0.76 cm^{-1} . This higher ratio favours the elimination of binder at higher rates, where it can be seen from the figure that the weight loss rate is not constant as in figure (6.9) and it reaches a maximum of 4 g/kg/h.

6.1.2 COMPUTER CONTROLLED WEIGHT LOSS:

After the successful attempt in controlling the binder burn out at a certain rate, another attempt has been made to control the binder burn out in a different way. This method is based upon a feed back loop to update the furnace programmer according to the current weight loss.

The need for this kind of control arises from a number of disadvantages of the previous method. These disadvantages are:

- Tedious work is involved to find the optimum temperature profile for binder burn out.

- The method has to be repeated to control the weight loss at other constant rates.
- It also has to be repeated for other sets of discs having different dimensions as seen previously.
- It also has to be repeated for different kind or different concentration of binding system in the discs.

The advantages of the feed back loop control can be summarized by that the tediousness of the previous method has been eliminated. That means the required temperature profile for binder burn out can be found by running the furnace along with the software once.

6.1.2.1 EXPERIMENTAL SET UP:

The experimental set up for the feed back loop control is shown in figure (6.11). This set up is almost the same as the one shown in figure (6.1) except that, in figure (6.11), the furnace controller is connected to the personal computer through a communication link to sustain the feed back loop.

A computer software was developed to control the weight loss. The software works as follows: The weight is read by the software at a predetermined time interval, then the weight loss and the weight loss rate are calculated using equations (6.1) and (6.2) and the current weight loss rate is

compared with a weight loss rate limit which was previously incorporated in the software. Upon this comparison the software gives commands to the furnace controller to increase or decrease the heating rate of the furnace. Figure (6.12) shows a simplified flow chart of the software and the source code of the software is shown in appendix C.

The maximum heating rate was set in the software to 2.5°C/min as seen previously where this heating rate did not have adverse effects on the finished product.

6.1.2.2 RESULTS AND DISCUSSION:

A relation between the heating rate and weight loss rate has been established. This relation was used in the software to calculate the heating rate according to the weight loss rate and then the calculated heating rate was used to update the furnace controller.

The relation has this form:

$$HR = F(WLR) \quad (6.3)$$

where: *HR* is the heating rate.

WLR is the current weight loss rate.

Three different functions were used in this equation to find which function gives the best results in controlling the

weight loss. These functions are shown in figure (6.13).

The first curve in figure (6.13), curve (1), was part of an ellipse. This function was used in the software to control the weight loss rate at 2 g/kg/h and the results are shown in figure (6.14). This figure shows the weight loss and weight loss rate vs. firing time where it can be seen in the weight loss rate curve that there is a big over shoot at the beginning of binder burn out. This is due to the proposed function used in controlling the weight loss. A closer look at figure (6.12) shows that at weight loss rates which are close to the limit set in the software, the heating rate is high enough to give that over shoot in the weight loss rate curve in figure (6.14). After the first over shoot, in the weight loss rate curve, the curve shows some oscillation due to the same effect.

Using function (2) in figure (6.13) which is an exponential decay function, the results of weight loss curves are shown in figure (6.15). It can be seen that controlling of the weight loss rate was good at the beginning then it started to lose control after a while. This is due to the low heating rate that the equation provides even at low weight loss rates, as can be seen from figure (6.13) where at high weight loss rates (that is close to the limit) the heating rate is small which is preferable. However, at low weight loss rates the heating rate is not high enough to produce the desired weight loss rate. This can be overcome by changing

the constants which describe function(2). However, if we take function (3) in figure (6.13) which is a straight line, it is easier to manipulate this line by changing its slope to give the required results.

Figure (6.16) shows the results of weight loss rate using linear equation for heating rate and the weight loss rate was also set at 2 g/kg/h. The weight loss curve shows a good linearity apart from at the beginning of the curve, where the moisture evaporates. The weight loss rate curve shows a small over shoot at the beginning of binder burn out. However after that the weight loss rate does not exceed the set limit. The figure also shows the resultant temperature profile for weight loss rate of 2 g/kg/h. Taking a closer look at that profile and comparing it with the temperature profile set for the weight loss rate experiments without feed back loop in figure (6.9), it can be seen that these two profiles have the same pattern. These both consist of three major ramps. The first one at high heating rate while the other two at low heating rate. However, the temperature at which the second ramp starts is higher in figure (6.9). This is due to the difference of the loaded compacts in the furnace where the ones in figure (6.9) are the 125 mm diameter whereas the ones in figure (6.16) are the 50 mm diameter. This difference was discussed earlier and was related to the ratio of the surface area to the volume and can be seen from figure (6.10) that the big over shoot in the weight loss rate curve at the beginning of the second ramp.

The linear equation which relates the heating rate with the weight loss rate was used to control the weight loss rate at other rates than 2 g/kg/h. It was used to control the weight loss rate at 1.5 g/kg/h, then it was used to control the weight loss rate at 1 g/kg/h. Figures (6.17) and (6.18) shows the results of weight loss, weight loss rate and temperature profile for 1.5 and 1 g/kg/h respectively. It can be seen from the figures that the linearity of the weight loss curve seems to improve as the weight loss rate limit is decreased.

The resultant temperature profiles which were generated from the software at the above three weight loss rate limits were put together in figure (6.19). It can be seen that all the profiles seem to have three major ramps. The first ramp in these profiles seems to have the same heating rate. As for the second ramp, it can be noticed that it starts at different temperature for each weight loss rate limit. The starting temperature seems to increase with the increase in the weight loss rate limit. This is due to the more heat needed to burn the binder at the higher weight loss rate. Moreover, the slope of the second ramp increases with the increase in weight loss rate limit. This is also due to the binder burn out at higher rate which requires more heat. The same thing could be said about the third ramp. These resultant three ramps could be related to the binding system in the discs. It could be said that the first ramp corresponds with moisture evaporation, while the second and

the third ramps correspond to the organic binder and plasticizer burn out which constitute the binding system.

The resultant temperature profile for weight loss rate of 1 g/kg/h was approximated to a few ramps as shown in table (6.1) and it was fed to the furnace controller and the weight was monitored via the computer This was done to see how accurate the feed back loop control process is.

Table 6.1 Temperature profile for weight loss rate of 1 g/kg/h.

Ramp Temperature	Ramp Time	Dwell Time	Heating Rate
150	1:30	0:00	1.44
165	0:50	1:00	0.3
200	5:00	0:00	0.12
275	5:40	0:00	0.22
340	1:00	0:00	1.08

The results of this test was shown in figure (6.20). The weight loss curve shows a remarkable linearity and it can also be seen from the weight loss rate curve. This indicates that the feed back loop control process is accurate enough to produce reliable results of temperature profile for binder burn out at certain rate.

6.1.3 TEMPERATURE GRADIENT:

Monitoring the temperature gradient within the disc gives a good idea about the behaviour of binder burn out, the temperature distribution in the disc and the behaviour of

binder burn out. To monitor the temperature within the disc, a hole was drilled in the middle of the 50 mm cylindrical disc. Its depth was half the disc height as shown in figure (6.21). A thermocouple was inserted in the hole to measure the temperature inside the disc and the whole assembly was put inside the furnace. Another thermocouple was used to measure the surrounding temperature in the furnace. Plate (6.4) shows a photograph of the disc with the thermocouple. These two thermocouples were connected to the thermocouple card in the computer. A program was developed to read the temperature of the thermocouples at a predetermined time interval during which the furnace was ramped to 400°C at constant heating rate. Different heating rates were used for this test and these were 2, 1.5, 1, 0.5, 0.25 and 0.125°C/min. These heating rates almost cover the entire range of heating rates at which the binder is burnt out.

Figure (6.22) shows the temperature curves inside and outside the disc for a constant heating rate of 2°C/min. It can be seen that there is a difference between the temperature outside the disc and the programmed temperature. This is due to the position of each thermocouple. The thermocouple which controls the furnace temperature is situated at the side of the furnace whereas, the other thermocouple is situated in the middle of the furnace. This thermocouple gives more accurate results than the one for the controller since it is exposed to the heating elements from all sides. The figure also shows that the outside temperature

is higher than the inside temperature. This is true because of the heat conductivity of the disc which gives that difference in temperature. Afterwards, it can be noticed that the temperature inside the disc becomes higher than the outside temperature. This indicates that an exothermic reaction is taking place which means that the binder is burning and thus giving this rise in temperature. This temperature increase keeps on until the completion of binder burn out where the inside temperature starts to drop below the outside temperature as can be seen from the figure.

A good description of what is happening during heating is obtained by plotting the difference in temperature between the outside and the inside against the programmed temperature as can be seen in figure (6.23). This figure contains 6 curves one for each of the heating rates used. These curves show a sharp increase in temperature difference at the beginning of heating. This is due to the bad thermal conductivity of the disc which gives some time lag for the temperature difference to stabilize as can be seen later on, where the difference become nearly constant for a while. Afterwards, the temperature difference starts to decrease. This indicates that the inside temperature starts to increase at higher rates than the outside temperature. This means that the binder is started to burn out. The decrease in temperature difference keeps on going until the completion of the binder removal, where it can be seen that the difference in temperature starts to increase again to return to the same

situation where the difference in temperature become stabilized. However, this stabilization in temperature difference after the binder has been burnt out is not clear enough at the first three heating rates and it could become clearer for temperatures higher than 400°C. The figure also shows that the difference in temperature is getting smaller as the heating rate is decreased. Moreover, the slope of the curve during the binder burn out is getting smaller as the heating rate is decreased. This gives a good indication about the rate at which the binder is burning out. In other words, the binder is not burning at a constant rate.

For verification of this, the temperature gradient within the disc was measured using the temperature profile in table (6.1) for weight loss rate limit of 1 g/kg/h and the results of the difference between the outside and the inside temperature is shown in figure (6.24). This figure shows that the time from heating up to the start of binder burn out has been reduced. Afterwards, a sharp drop in temperature difference takes place and then it can be noticed that virtually no temperature difference remains. This means that there is no temperature gradient within the disc during the binder burn out using temperature profile listed in table (6.1) and the temperature is the same throughout the whole disc.

6.2 SHRINKAGE:

Packed powders will bond together when heated to temperatures in excess of approximately half the absolute melting temperature. This phenomenon is termed sintering. There are different form of sintering (solid state sintering, liquid phase sintering). However, a common characteristics of all forms of sintering is a reduction in surface area with accompanied compact strengthening. This occurs through the formation of interparticle bonds brought about by atomic motion at the sintering temperature.

In a general categorization of sintering techniques, pressure is the first consideration. Most sintering is performed without an external pressure. For many high-performance applications, high densities are attained using external pressure sources. Such techniques as hot pressing, hot isostatic pressing, hot forging and hot extrusion use a combination of temperature, stress, and strain rate to densify powder compacts. However, liquid phase sintering exhibits sufficient internal force through liquid capillary action on the particulate solid that external forces are not required. The magnitude of the capillary force is equivalent to very large external pressures.

During liquid phase sintering a liquid phase coexists with a particulate solid at the sintering temperature. The liquid phase usually enhances the rate of interparticle

bonding during sintering. Accompanying interparticle bonding causes significant changes in the pore structure and compact properties⁽⁸⁵⁾.

In liquid phase sintering, densification takes place in three overlapping stages. The first stage is called rearrangement, where the liquid starts to form and causes rapid initial densification due to the capillary force exerted by the wetting liquid on the solid particles. The amount of densification attained by rearrangement is dependent on the amount of liquid, particle size and solubility of the solid in the liquid.

The second stage is termed solution-precipitation, where the solubility and diffusivity become dominant. In this stage, material is transported from the small grains to the large grains by diffusion and this results in a progressive growth of the larger grains giving fewer grains with a wider spacing.

The last stage is referred to as solid state controlled sintering. Densification is slow in this stage because of the existence of a solid skeleton. The rigidity of that skeleton inhibits further rearrangement although microstructural coarsening continues by diffusion.

6.2.1 EXPERIMENTAL SETUP:

To study the shrinkage behaviour of ceramic compacts a dilatometer was used. The samples were prepared from a pressed disc and it was cut to a rectangular block of square cross section of 3x3 mm and a length of 12 mm. The dilatometer used was not capable of controlling the shrinkage at a certain rate. It was used to measure the shrinkage during firing. This necessitates building a new instrument to measure and control the shrinkage at a certain rate. Besides, the new set up was able to accommodate large sample such as those compacts produced in the manufacturing line. This will give a more realistic evaluation of the shrinkage evolution during sintering.

The new instrument consists of a furnace with a programmable controller, a linear variable differential transducer to measure the shrinkage and a personal computer. The set up is shown in figure (6.25).

The transducer was mounted on a stand with X-Y-Z movement capability and a ceramic rod was attached to the armature of the transducer. The disc was placed inside the furnace and the transducer was lowered until the ceramic rod touched the disc. The transducer was energized from a signal conditioner unit which converts the electrical signal from the transducer to a digital one. The signal conditioner is connected to the personal computer through a communication

link to transfer the shrinkage data to the computer. The furnace controller was also connected to the computer through a communication link as was done for controlling the binder burn out.

Some metal sheets were placed around the ceramic rod which pass through the furnace vent to radiate and dissipate the heat coming from the vent for the protection of the transducer. Plate (6.5) shows a photograph of the set up, while plate (6.6) shows the actual set up inside the furnace.

Before starting the experiments on shrinkage, the instrument has to be calibrated. A fired disc was placed into the furnace and the furnace was heated at a constant heating rate up to 1250°C. During heating the thermal expansion of the whole unit was measured by the transducer. A plot of the total expansion of the unit and temperature is shown in figure (6.26). This curve is used later during the shrinkage measurements to calculate the disc shrinkage during firing.

6.2.2 RESULTS AND DISCUSSION:

Using the high temperature dilatometer a sample prepared from a pressed disc was loaded into the dilatometer and it was fired up to 1100°C and the shrinkage results are shown in figure (6.27). It can be noticed that there is some expansion during heating up, then shrinkage starts at about 800°C. This expansion at the beginning of firing which lasts up to 800°C

is due to the sample thermal expansion which was not accounted for during the calibration of the dilatometer. Because of this expansion, the results from the dilatometer were not as accurate as required to calculate the shrinkage and shrinkage rate during firing. Besides, it was not possible to control the shrinkage of the sample at a certain rate. This necessitated building the new instrument which is capable of measuring the shrinkage and controlling the shrinkage at a certain rate if required.

To do this, a computer software was developed to measure the disc contraction during firing. This was done to find out how the shrinkage takes place and at what temperature it starts and ends. The software works as follows: The furnace controller was set to ramp at a constant heating rate to the firing temperature. During the firing cycle, the current height from the transducer and the current temperature from the furnace controller were read at a predetermined time interval. This height was subtracted from a correction table which takes into account the unit expansion to find the pure contraction of the disc. The shrinkage and the shrinkage rate were then calculated from the following equations:

$$\delta = \frac{l - l_o}{l_o} \quad (6.4)$$

$$\delta = \frac{\frac{l_{i+1} - l_i}{l_o}}{t_{i+1} - t_i} \quad (6.5)$$

where: δ is the shrinkage.

δ' is the shrinkage rate.

l_0 is the initial height of the disc.

l_i is the current height at time t_i .

l_{i+1} is the current height at time t_{i+1} .

A set of experiments were carried out using this software without a feed back loop for controlling the shrinkage at a certain rate. These experiments were carried out to find the shrinkage during firing at a constant heating rate. Five heating rates were used for firing. These heating rates were: 2.5, 2, 1.5, 1 and 0.5°C. A 50 mm diameter green disc was loaded into the furnace and the furnace was heated up to 1200°C at one of the above mentioned heating rates. The current displacement measurements from the transducer were recorded in the computer during heating at a predetermined time interval. The shrinkage results of the test carried out at a heating rate of 2.5°C are shown in figure (6.28). Figure (6.28a) shows three curves, the first curve which is called "unit" curve is the expansion curve for the whole unit which is the same as the curve in figure (6.26). The second curve is the curve of the actual results of the current displacement taken from the transducer. The third curve is the pure contraction curve of the disc which is the result of subtraction of the previous two curves. That curve shows that there is some noticeable shrinkage between 200 and 400°C over which the binder is burning out. This could be due to the binder migration characteristics of the binder, where

it turns into a liquid at these temperatures and the capillary forces try to pull the disc together. After that, the total contraction remains constant until about 700°C where some contraction starts to take place. Then the major shrinkage takes place at around 850°C where it can be seen that the curve's slope is increasing. At the end the slope of the curve starts to decrease. Figure (6.28b) shows the shrinkage and shrinkage rate curves. It can be seen that the shrinkage rate increases rapidly and reaches a very high magnitude (about 130 $\mu\text{m}/\text{mm}/\text{h}$) and remains nearly constant for a while then it starts to decrease.

Figure (6.29) shows the shrinkage and shrinkage rate curves during firing at a heating rate of 2°C/min. It can be seen that the maximum shrinkage rate has reached a value of 100 $\mu\text{m}/\text{mm}/\text{h}$ which is less than the result at 2.5°C/min heating rate. As the heating rate decreases it was found that the maximum shrinkage rate decreases where it can be seen from figure (6.30), which corresponds to firing at a heating rate of 0.5°C/min, that the maximum rate at which the shrinkage takes place is about 30 $\mu\text{m}/\text{mm}/\text{h}$.

A similar approach, as the one adopted for the weight loss control, was adopted here to control the shrinkage during firing was carried out by developing a software which gives commands to the furnace controller according to the current shrinkage rate. This software works as the one which was described earlier, but after the shrinkage rate is

calculated, it is compared with a shrinkage rate limit set in the software. Upon this comparison the software gives commands to the furnace controller to increase or decrease the heating rate. A simplified flow chart of the software is shown in figure (6.31).

A relation between the heating rate and the shrinkage rate has been established. It was found that a linear relationship between the heating rate and the shrinkage rate is the best suitable to control the shrinkage at a certain rate. This is due to its simplicity as it was found earlier for controlling the binder burn out. The relationship has this form:

$$HR = A + m \cdot SR \quad (6.6)$$

where: 'A' represents the maximum allowable heating rate which corresponds to a shrinkage rate of zero. 'A' was set in the software to 2.5°C/min.
m is the slope of the line.
SR is the current shrinkage rate.

The slope *m* should be chosen in such a way that it will give the required heating rate to keep the shrinkage at the needed rate.

Starting with a small value for the slope $m = 1$, figure (6.32) shows the corresponding shrinkage and shrinkage rate

curves. The software was set to control the shrinkage at 25 $\mu\text{m}/\text{mm}/\text{h}$. The figure shows that shrinkage commences at about 800°C in a linear manner, then it starts to divert which can be noticed more clearly in the shrinkage rate curve. This is due to the low value of m which was set in the software. The value of m is not large enough to give the required heat to compensate for the drop in the shrinkage rate.

By increasing the value of m in the software to $m = 2$ and running another test, figure (6.33) shows the results of this test which was set to control the shrinkage at 25 $\mu\text{m}/\text{mm}/\text{h}$. It can be seen that there is an overshoot at the start of shrinkage. This is due to the higher value of m . However, this value is not high enough because near the end of shrinkage there is a drop in the shrinkage rate as can be noticed.

If the value of m is increased again, the shrinkage rate near the end of shrinkage could be maintained at the limit set in the software. However, a bigger overshoot in the shrinkage rate curve will occur at the beginning of shrinkage as seen earlier in figure (6.33). So, a small value of m is needed at the beginning of shrinkage and a large value of m is required near the end of shrinkage. To do this, the equation which controls the heating rate, equation(6.6), was used with two values for m . The first value ($m = 1$) was used at the beginning of shrinkage up to a certain amount of shrinkage, while the second value ($m = 2.25$) was used for the

rest of the shrinkage.

Figure (6.34) shows shrinkage and shrinkage rate curve using the new approach. It can be seen that the overshoot has been eliminated from the beginning of shrinkage in the shrinkage rate curve. It can also be noticed that there is some increase in the time needed to reach the temperature where the shrinkage commences.

Another test has been carried out using the new approach of using two values for m . The shrinkage rate limit was set to $20 \mu\text{m}/\text{mm}/\text{h}$. Figure (6.35) shows the resultant shrinkage and shrinkage rate curves from this test. It can be seen that there is no sign of overshoot in the shrinkage rate curve at the beginning of shrinkage. Also, figure (6.36) shows the shrinkage curve during firing at shrinkage rate limit of $30 \mu\text{m}/\text{mm}/\text{h}$.

The temperature profiles which were generated from the software at the above mentioned shrinkage rate limits were plotted together for comparison in figure (6.37). This figure shows that the three curves show a similar shape. These can be divided into three ramps. The first ramp is at high heating rate where no shrinkage has been detected yet. When the shrinkage is detected the heating rate starts to adjust to control the shrinkage as can be seen in the beginning of the second ramp. The heating rate in the second ramp seems to increase with the increase in the shrinkage rate limit. The

third ramp corresponds to the final stage of shrinkage where the heating rate is increased again to keep the shrinkage rate at the preset level. This third ramp seems to start at around 975°C for all the shrinkage rate limits.

6.3 GRAIN SIZE:

The effect of heating rate during the shrinkage stage and soaking time at the sintering temperature have been studied briefly. For that purpose, three heating rates were used 2.5, 1.5 and 0.5°C/min and three soaking times (0, 2 and 5 hours). These soaking times were used for the first heating rate. Green compacts were loaded into the furnace and fired using the temperature profile listed in table(6.2) and table (6.3).

Table 6.2 Temperature profile used for the study of the grain growth.

Stage	Ramp Temperature	Ramp Time	Dwell Time	Heating Rate
1	150	1:30	0:00	1.44
2	165	0:50	1:00	0.3
3	200	5:00	0:00	0.12
4	275	5:40	0:00	0.22
5	340	1:00	0:00	1.08
6	600	1:44	0:00	2.5
7	1170	Refer to table (6.3)		
8	20	7:40	0:00	2.5

The first part of this temperature profile was the resultant temperature profile from the instrument which controls the weight loss at 1 g/kg/h. After the binder has

Table 6.3 The Parameters in stage 7 in table (6.2) for the temperature profile used to study the grain growth.

Heating Rate	Ramp Temperature	Ramp Time	Dwell Time
2.5	1170	3:48	0:00
	1170	3:48	2:00
	1170	3:48	5:00
1.5	1170	6:20	0:00
0.5	1170	19:00	0:00

been eliminated, the furnace was heated to 600°C at a heating rate of 2.5°C/min, since there is no shrinkage before this temperature as seen earlier. After reaching 600°C, using one of the heating rates in table (6.3) the furnace was ramped to the sintering temperature of 1170°C.

After the sintering cycle has ended the sintered compacts were cut, mounted, polished and etched for the grain size evaluation under the scanning electron microscope. Plates (6.7), (6.8) and (6.9) show copies of the photographs taken from the electron microscope.

Grain size evaluation was carried out using the line count method⁽⁸⁶⁾. The results of the heating rate effect on the grain growth are shown in figure (6.38). This figure shows that the average grain size increases with the decrease in heating rate. This is due to the longer time needed to reach the sintering temperature. Moreover, the figure shows that there is no difference in the grain size between the centre and the edges of the compact. Figure (6.39) shows the grain growth as a function of soaking time for a heating rate

of 2.5°C/min. It can be seen that the average grain size increases with the increase in soaking time at the sintering temperature. By comparing this figure with figure (6.38) it can be noticed that at the highest heating rate with 5 hours soaking time the average grain size is about 11µm, while at the lowest heating rate and no soaking time the average grain size is around 9.5µm. This shows that the soaking time at the sintering temperature has more effect on the grain growth than the time needed to reach the sintering temperature.

6.4 VARISTOR TESTING:

Constructing a temperature profile for the firing cycle of the varistors discs was done by combining the two temperature profiles which were resulted for the two instruments. The first part was up to 400°C where the binder is burnt out. The part was chosen for weight loss rate of 1 g/kg/h. The second part was concerned with the shrinkage and it starts from 600°C to the sintering temperature. The temperature profile used for that part was for shrinkage rate of 20 µm/mm/h. As for the profile between 400°C and 600°C the profile was at a constant heating rate of 2.5°C/min. The rest of the temperature cycle was kept as it was in the standard sintering cycle. The sintered discs were passed through the electrical tests of classification and electrical strength testing and they all passed these tests. They also passed the simulated lightning strike test where a electrical current of 100 kA was passed through them and they survived.

From these results it is clear that by using the temperature profiles generated from the two instruments, good quality components can be produced and big savings in terms of the time and energy employed for the sintering process can be accomplished. However, these savings in time can be reduced further by knowing the critical rates at which the binder should burn out and the shrinkage should take place.

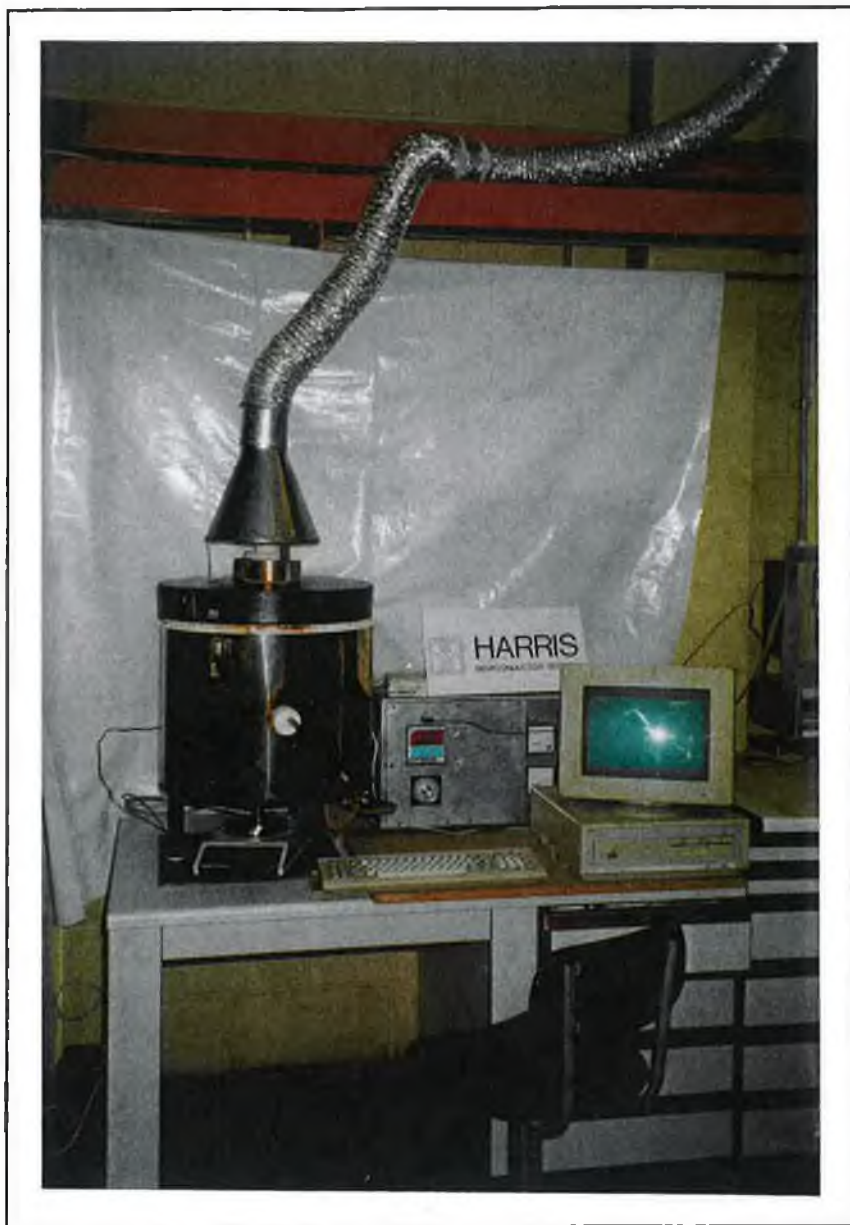


Plate 6.1 Photograph of the experimental setup for the weight loss experiment.

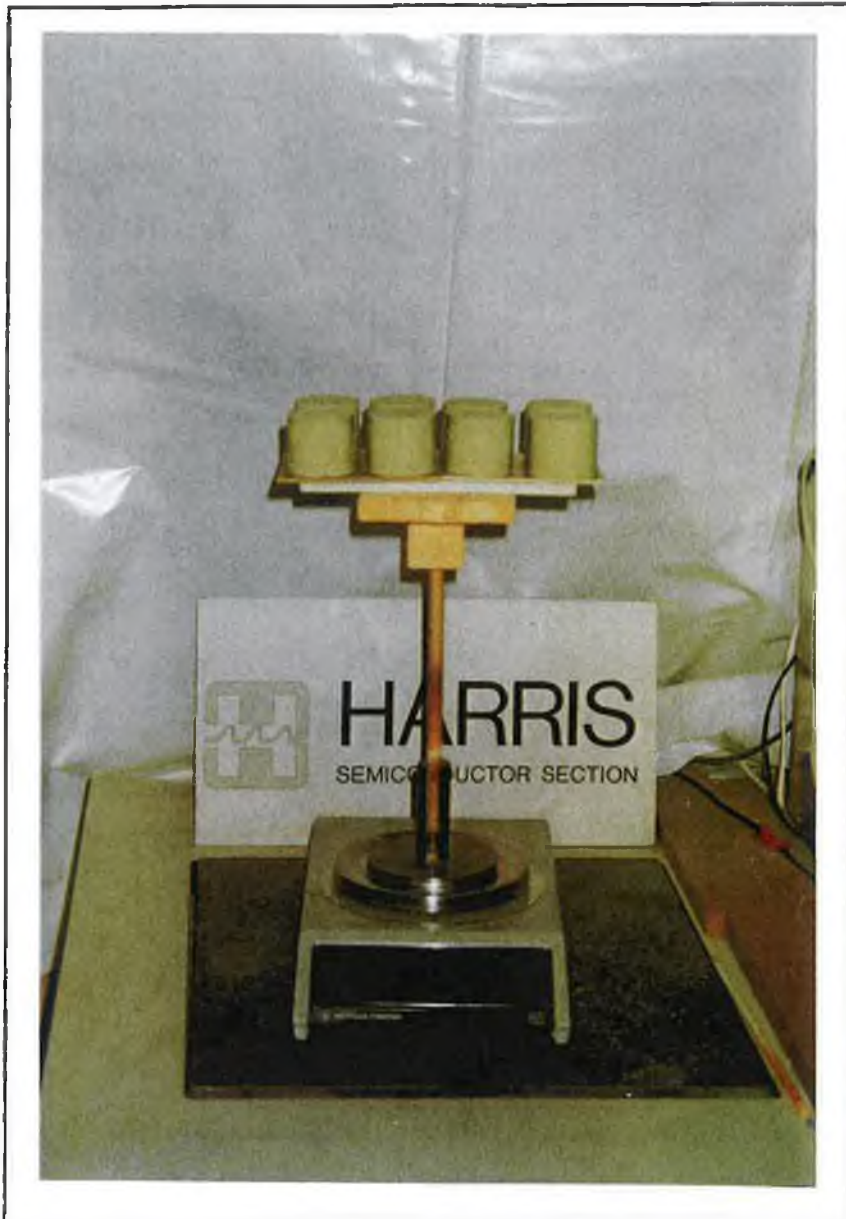


Plate 6.2 The layout of the samples inside the furnace for the weight loss experiment.



Plate 6.3 Photograph of the distorted discs due to the sintering at a high heating rate.

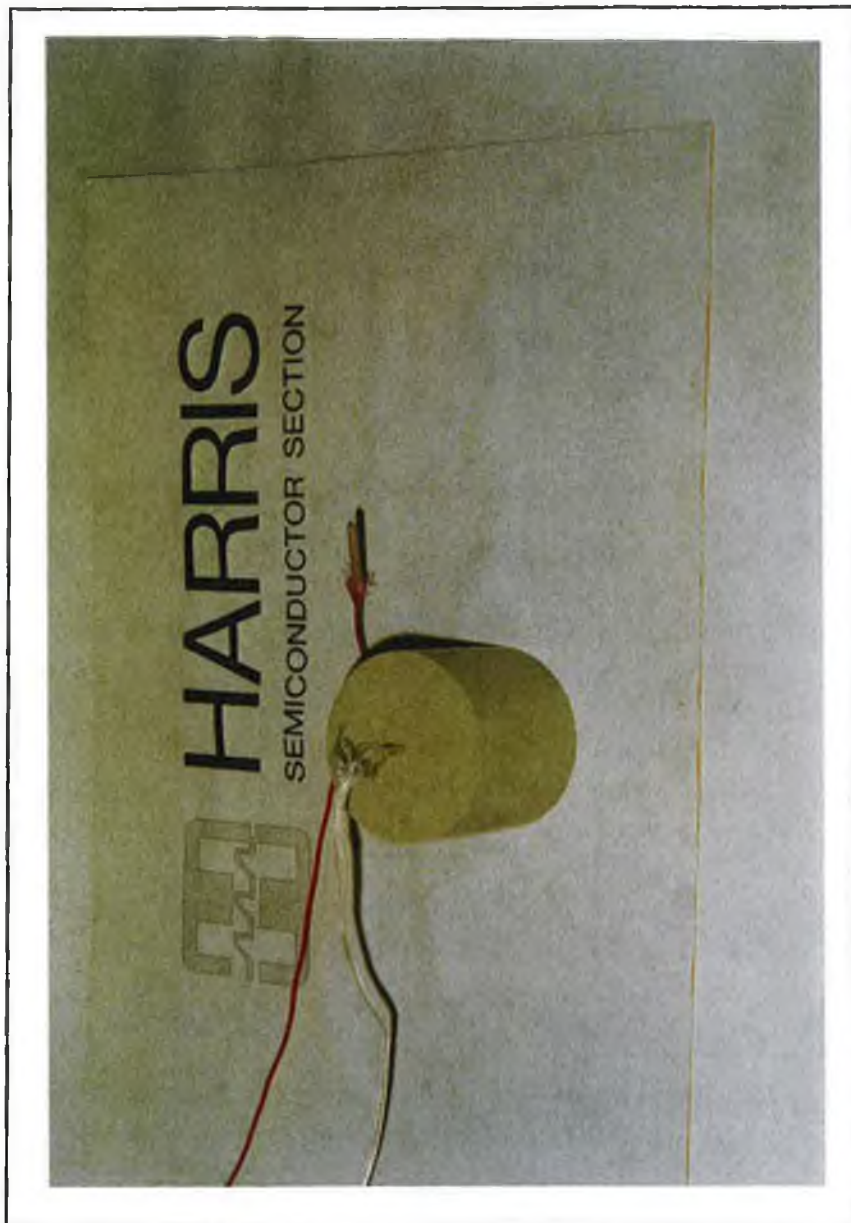


Plate 6.4 Photograph of the thermocouples and the disc for the temperature gradient.

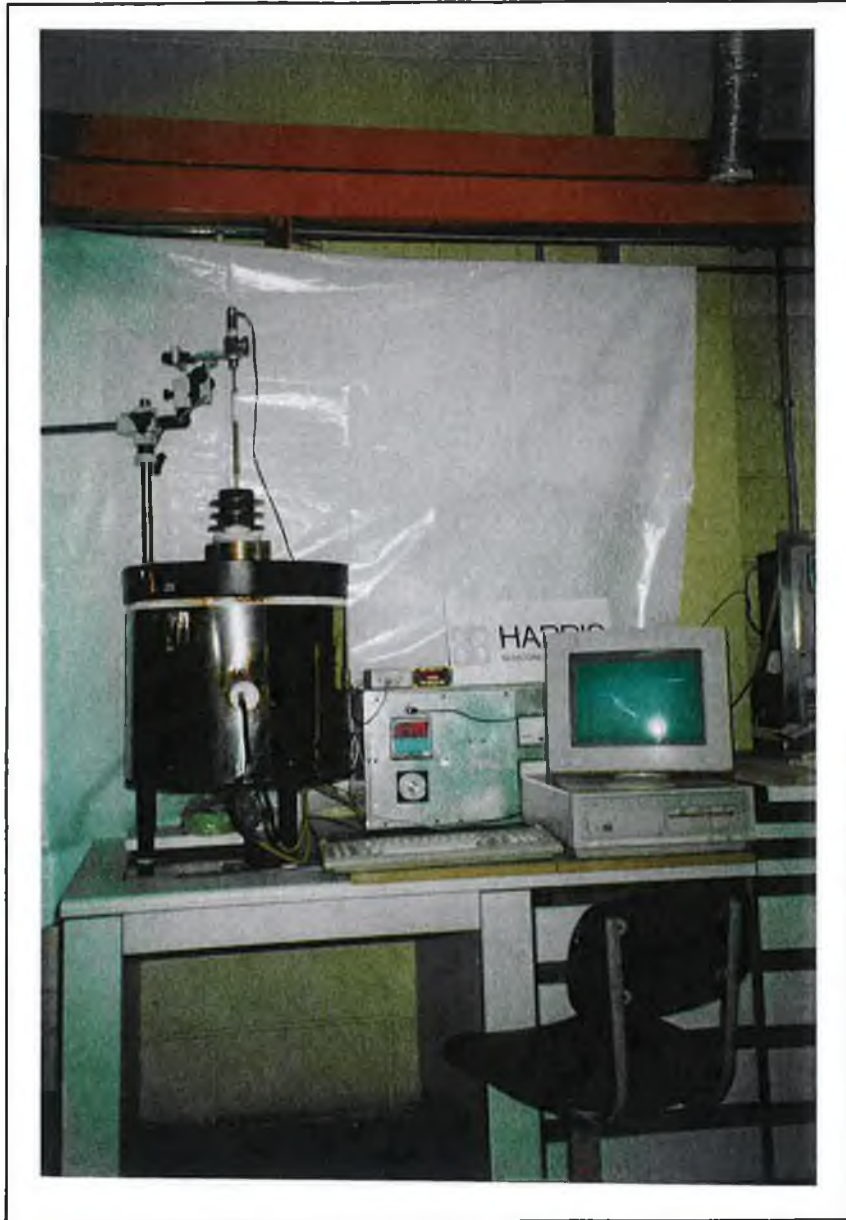


Plate 6.5 Experimental setup for controlling the shrinkage during firing.

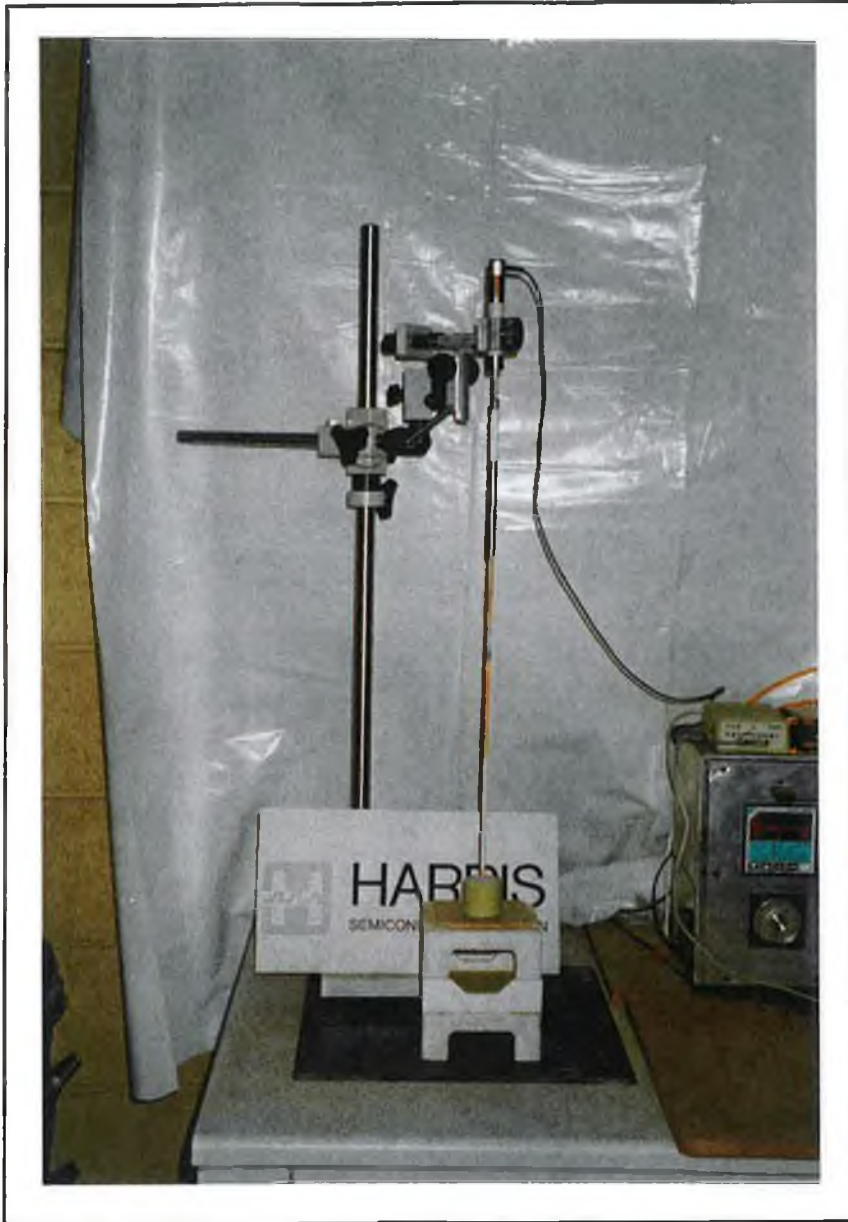


Plate 6.6 The layout of the transducer and the sample inside the furnace for shrinkage measurements.

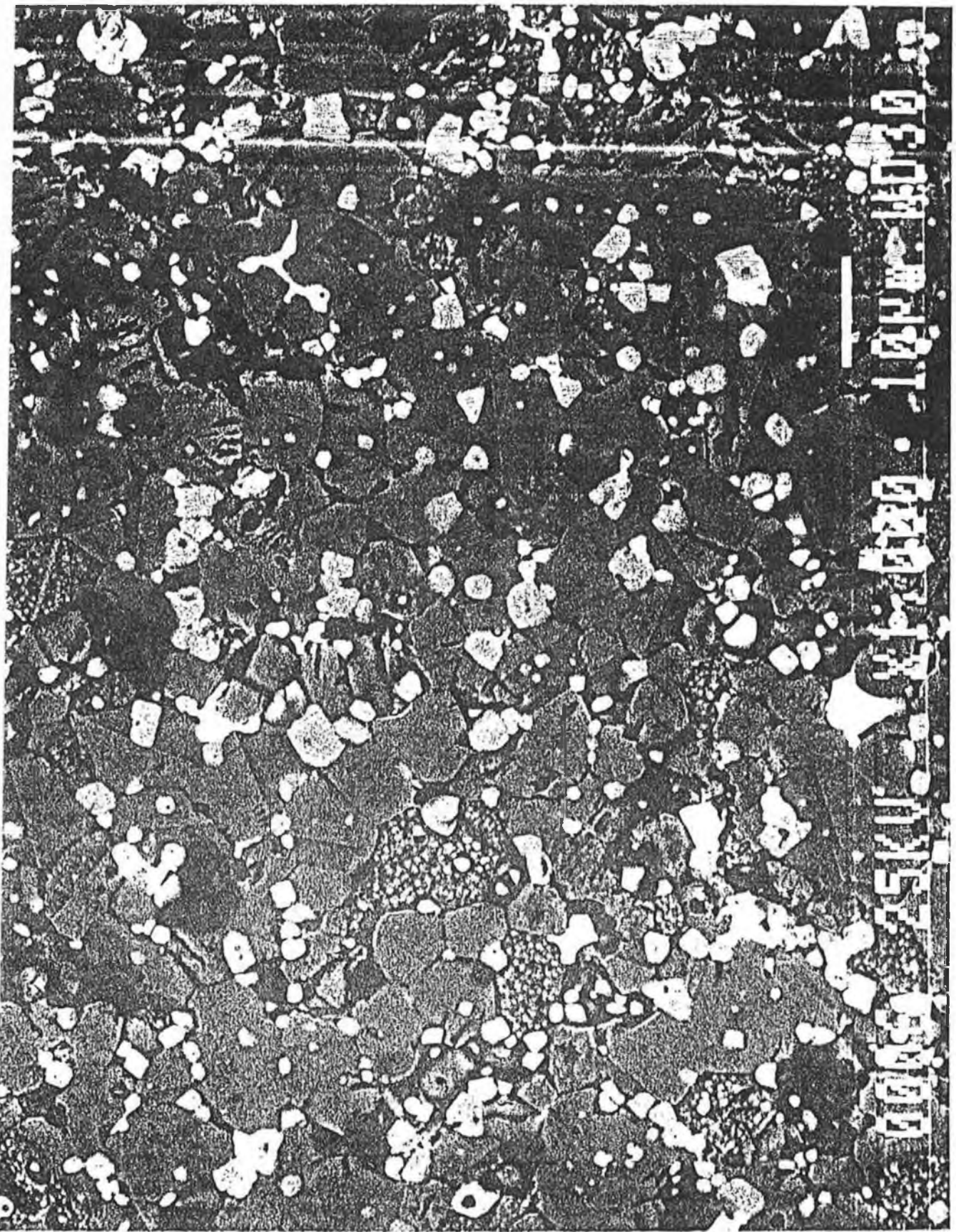


Plate 6.7 SEM photograph of a disc fired at 2.5°C/min.

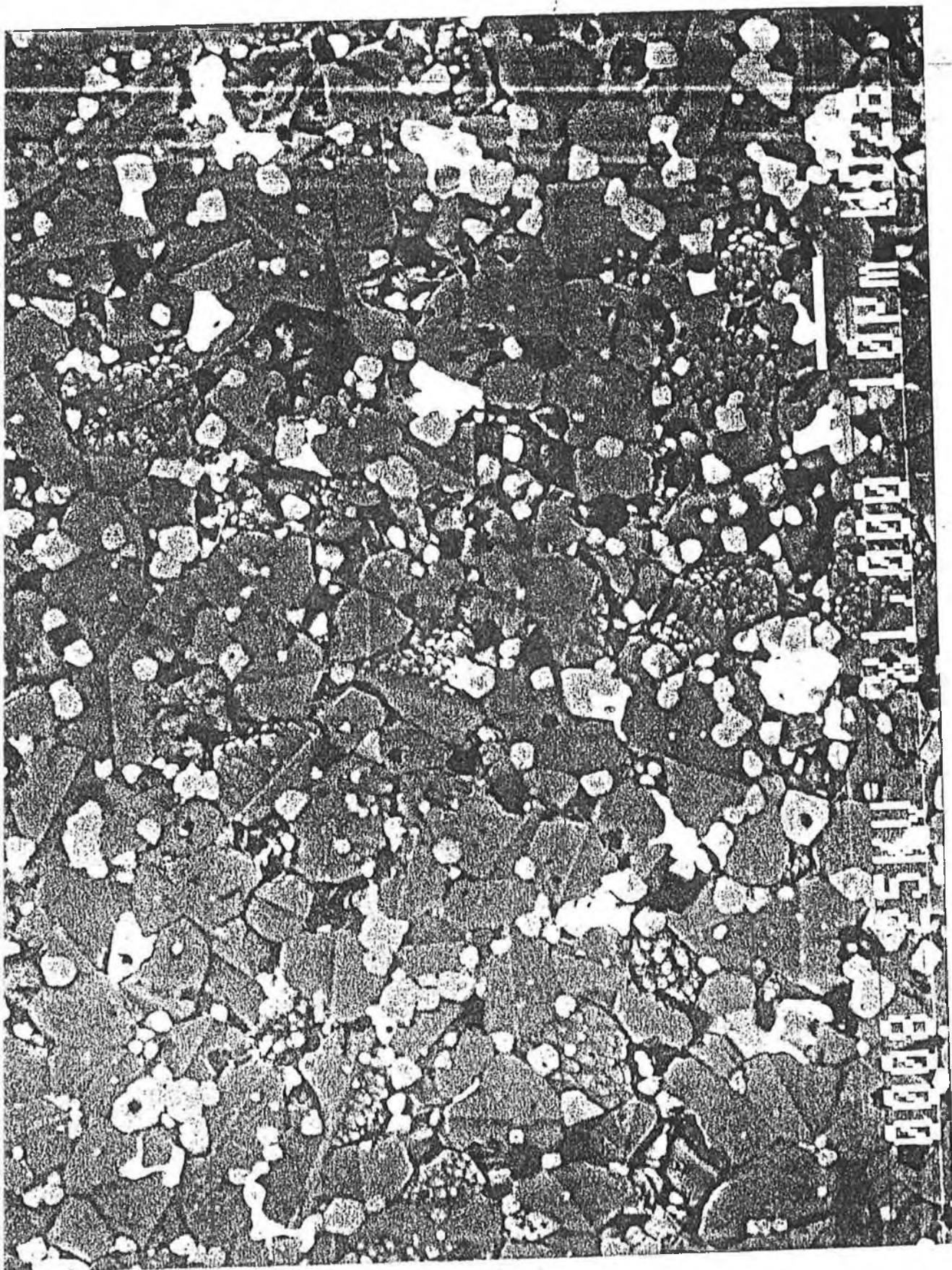


Plate 6.8 SEM photograph of a disc fired at 1.5°C/min.

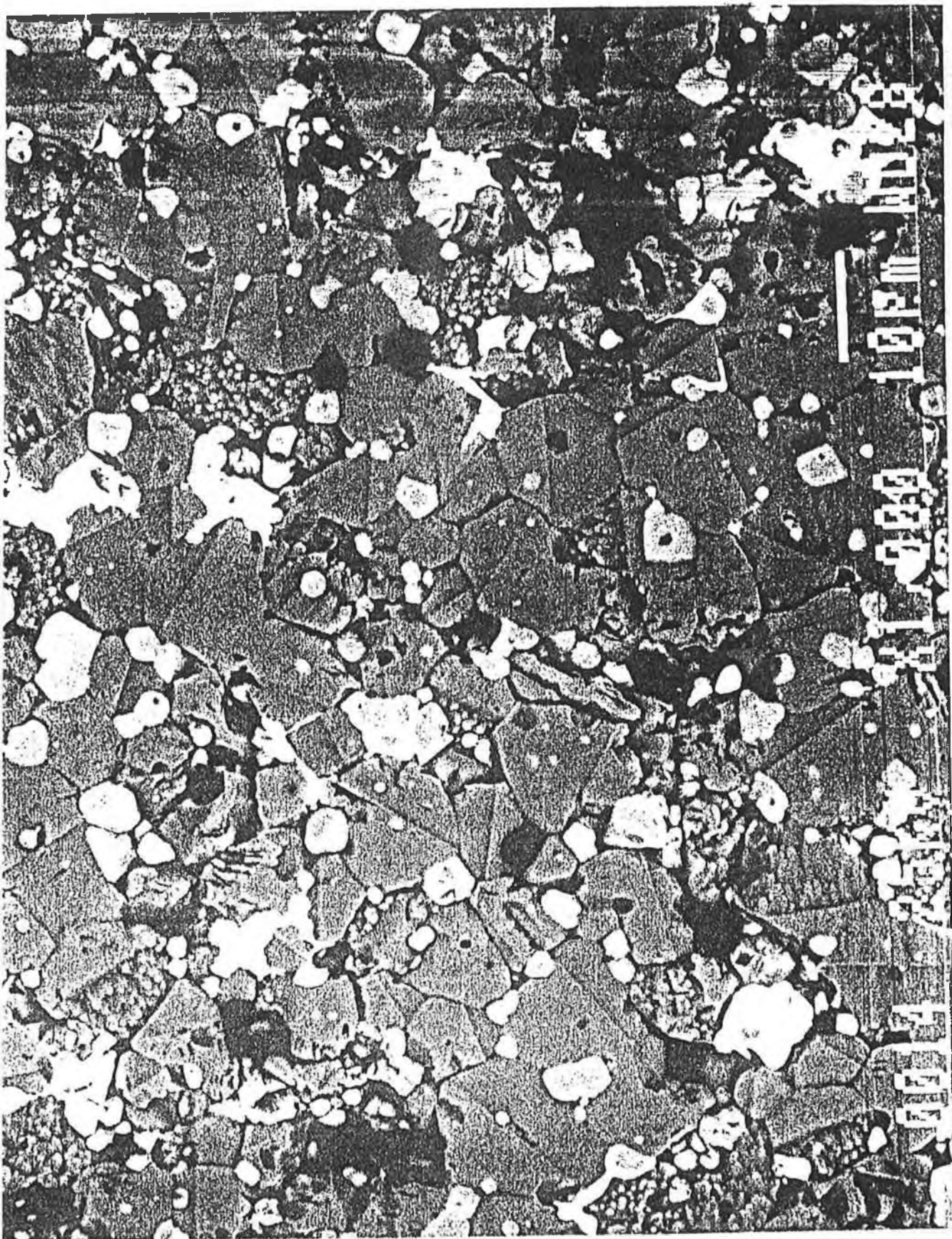


Plate 6.9 SEM photograph of a disc fired at 0.5°C/min.

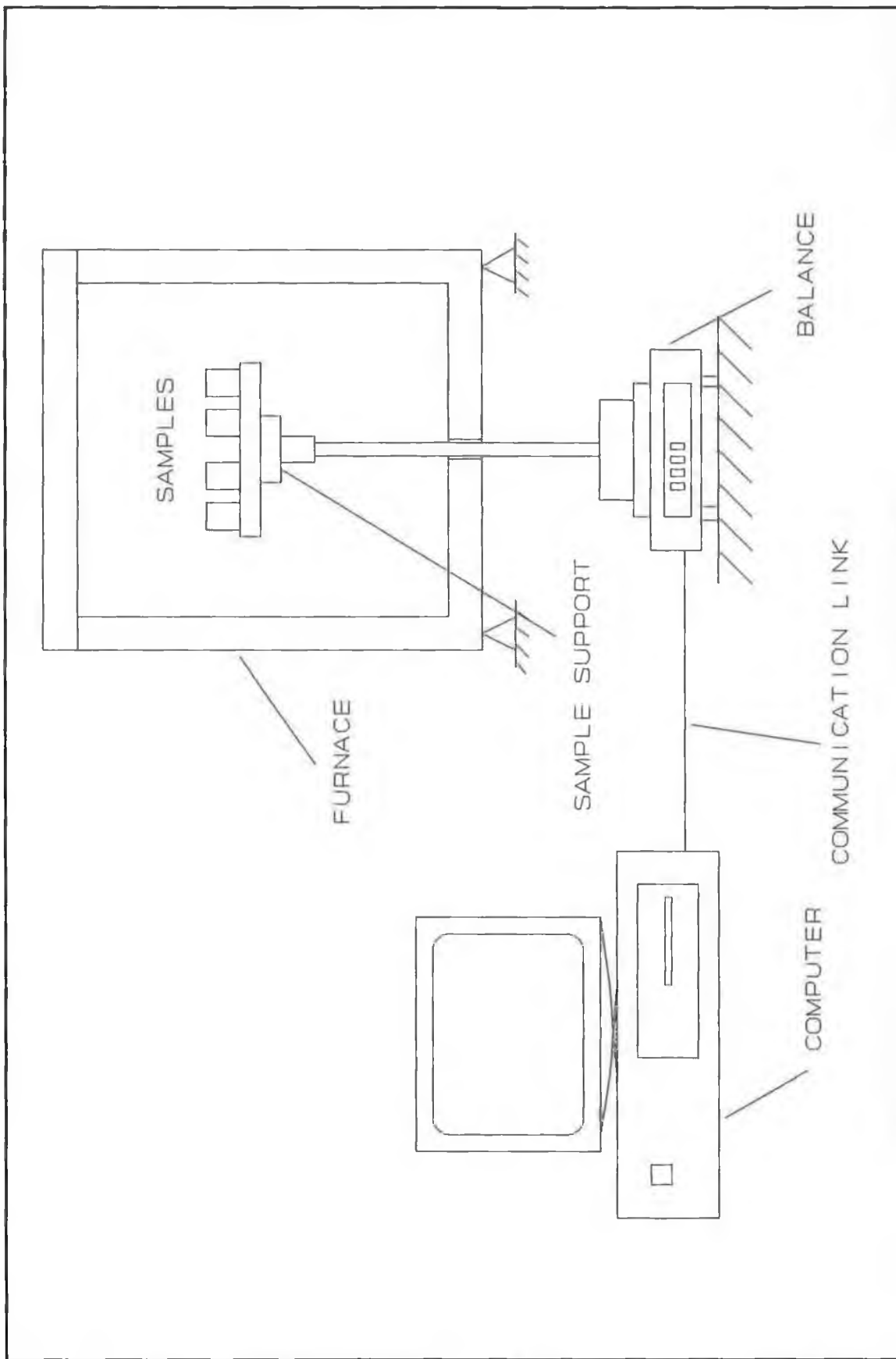


Figure 6.1 Equipment setup for weight loss experiment.

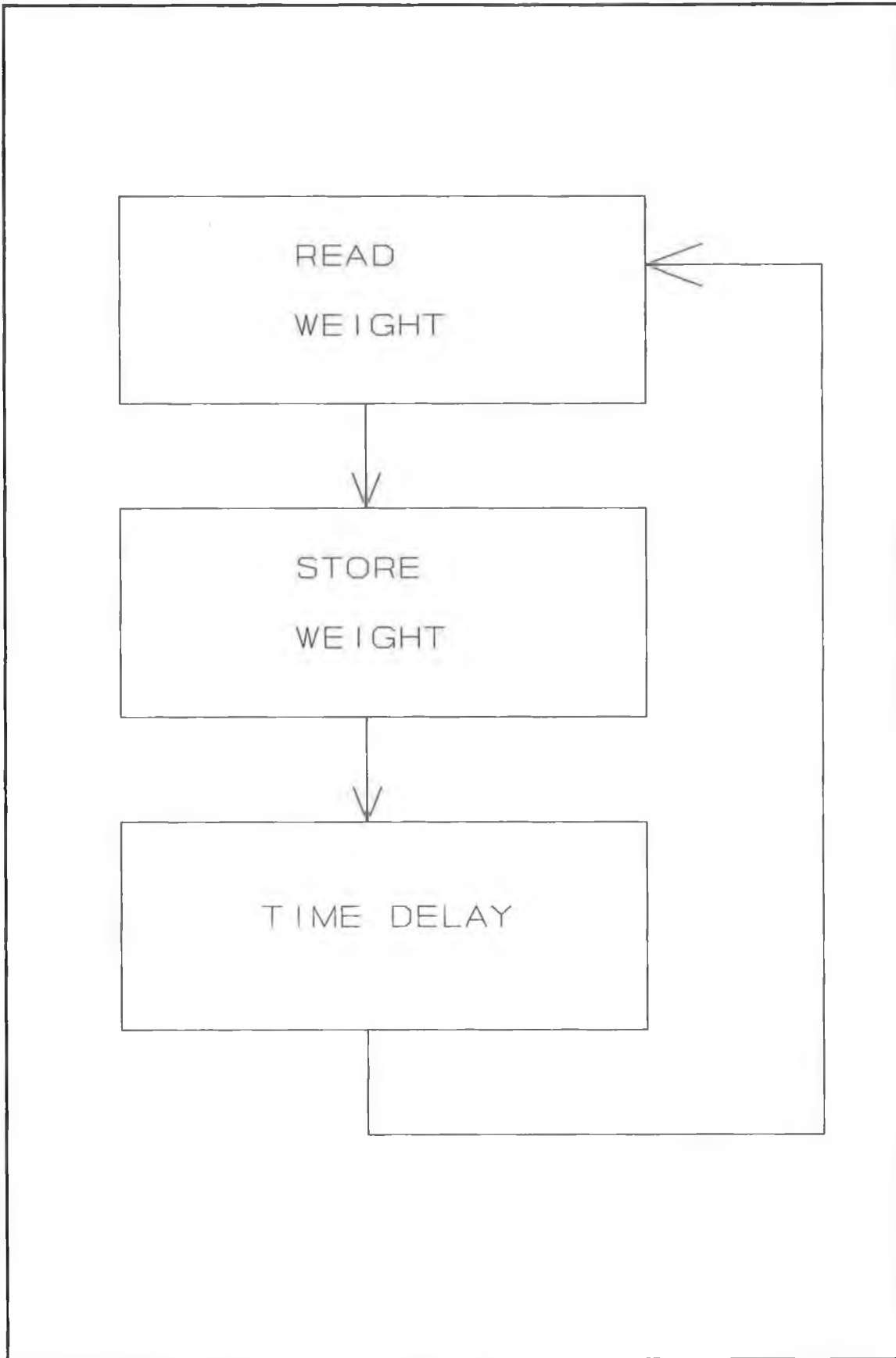


Figure 6.2 Flow chart for the weight loss software.

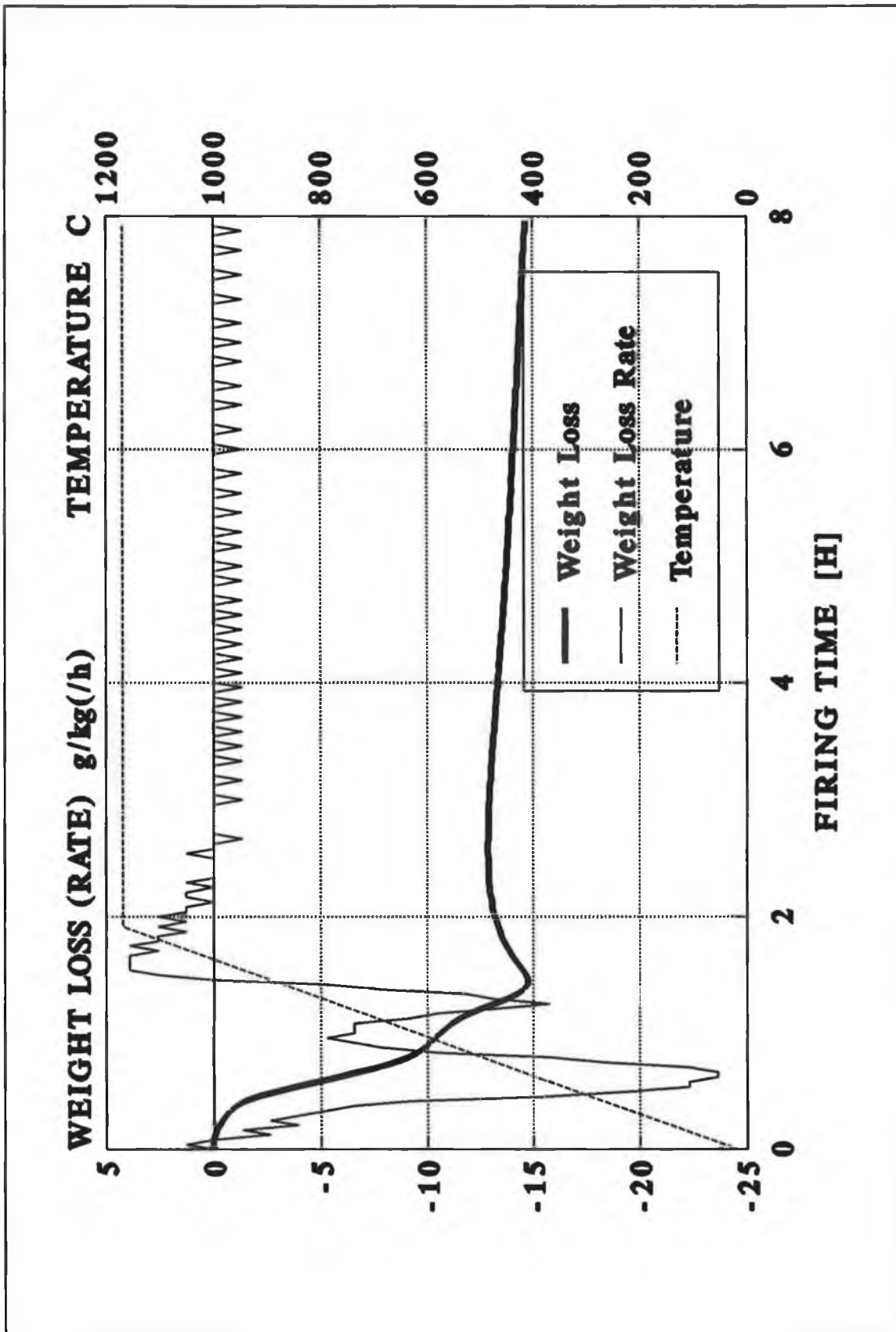


Figure 6.3 Weight loss, weight loss rate and temperature vs. firing time for 10°C/min heating rate.

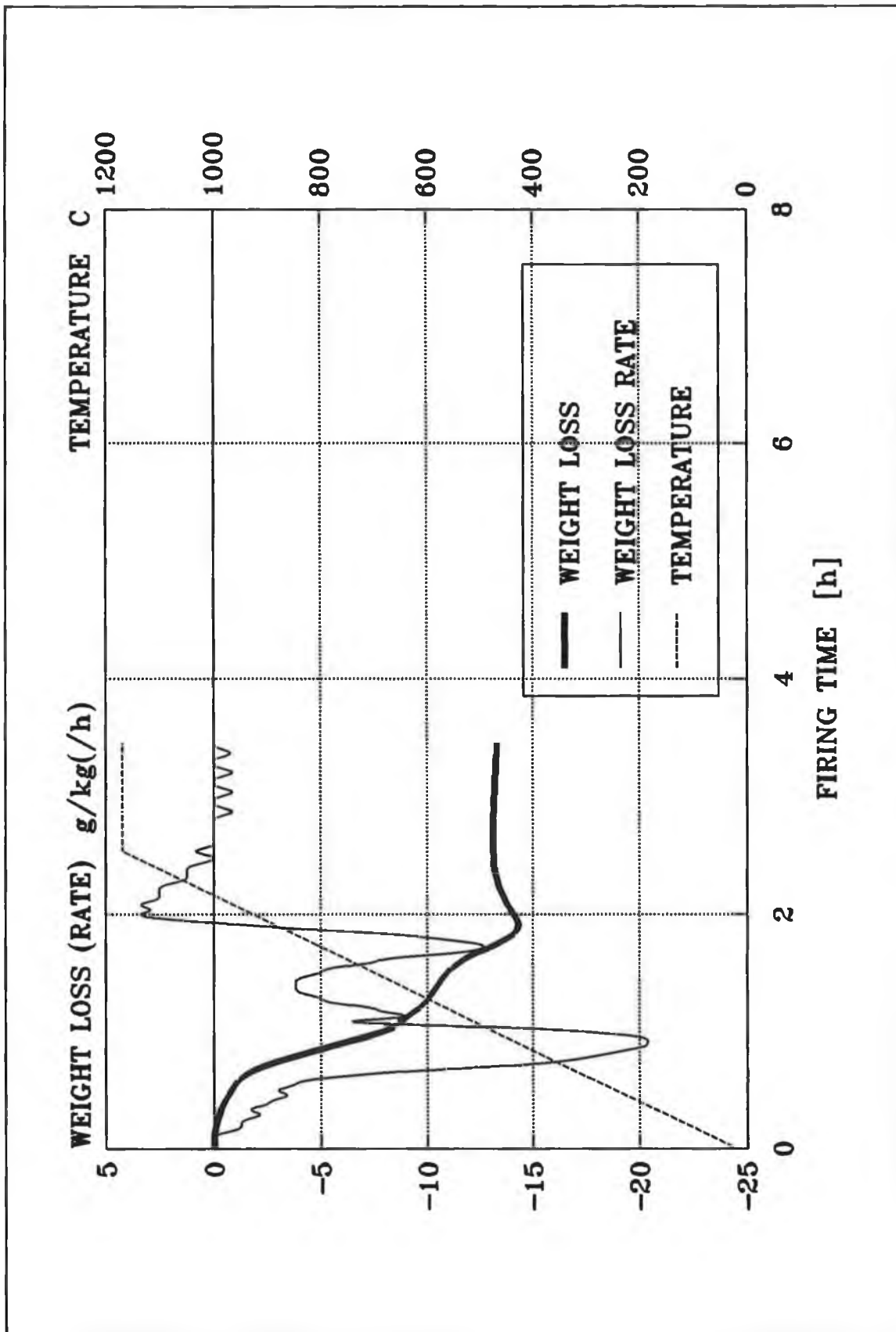


Figure 6.4 Weight loss, weight loss rate and temperature vs. firing time for 7.5°C/min heating rate.

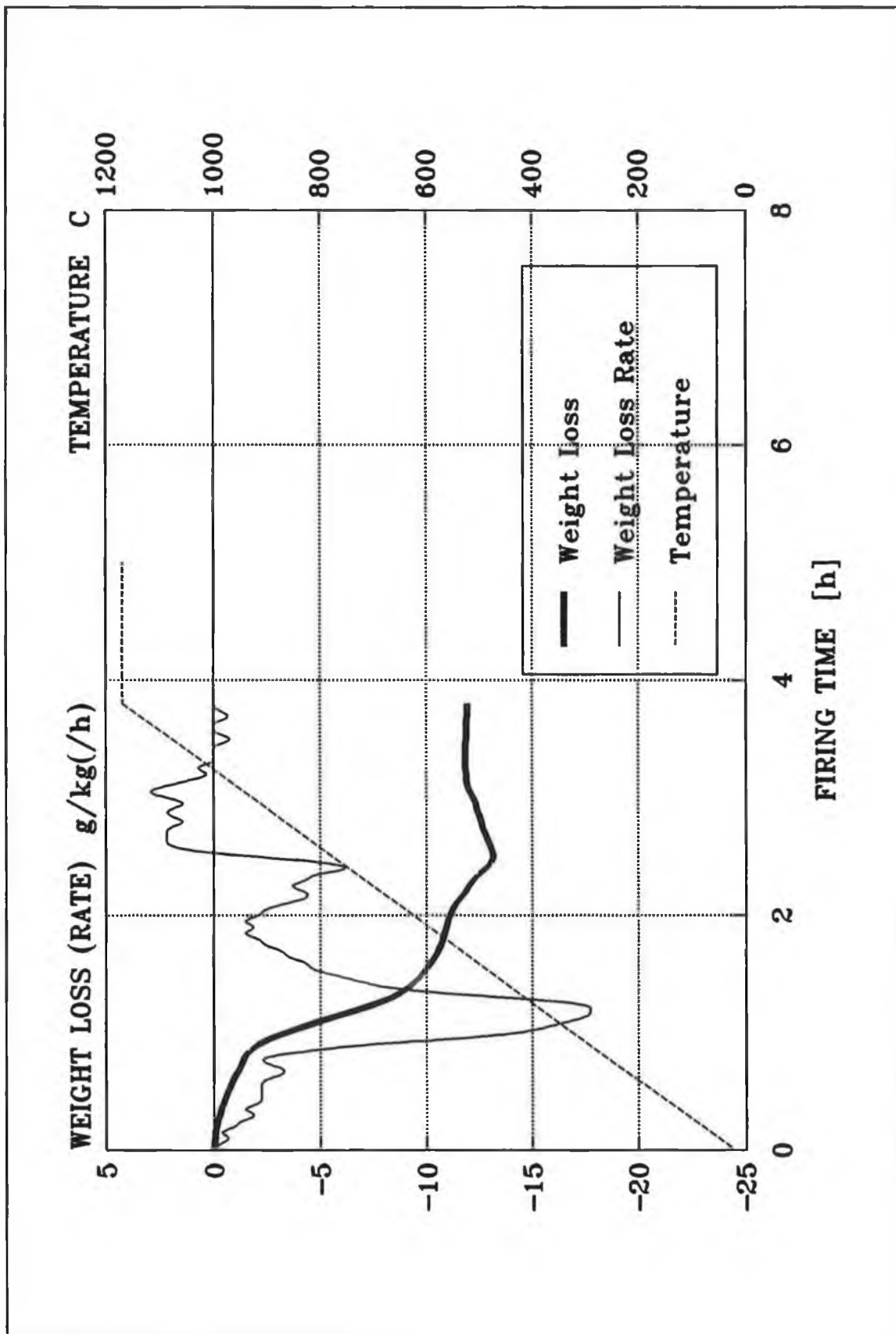


Figure 6.5 Weight loss, weight loss rate and temperature vs. firing time for 5°C/min heating rate.

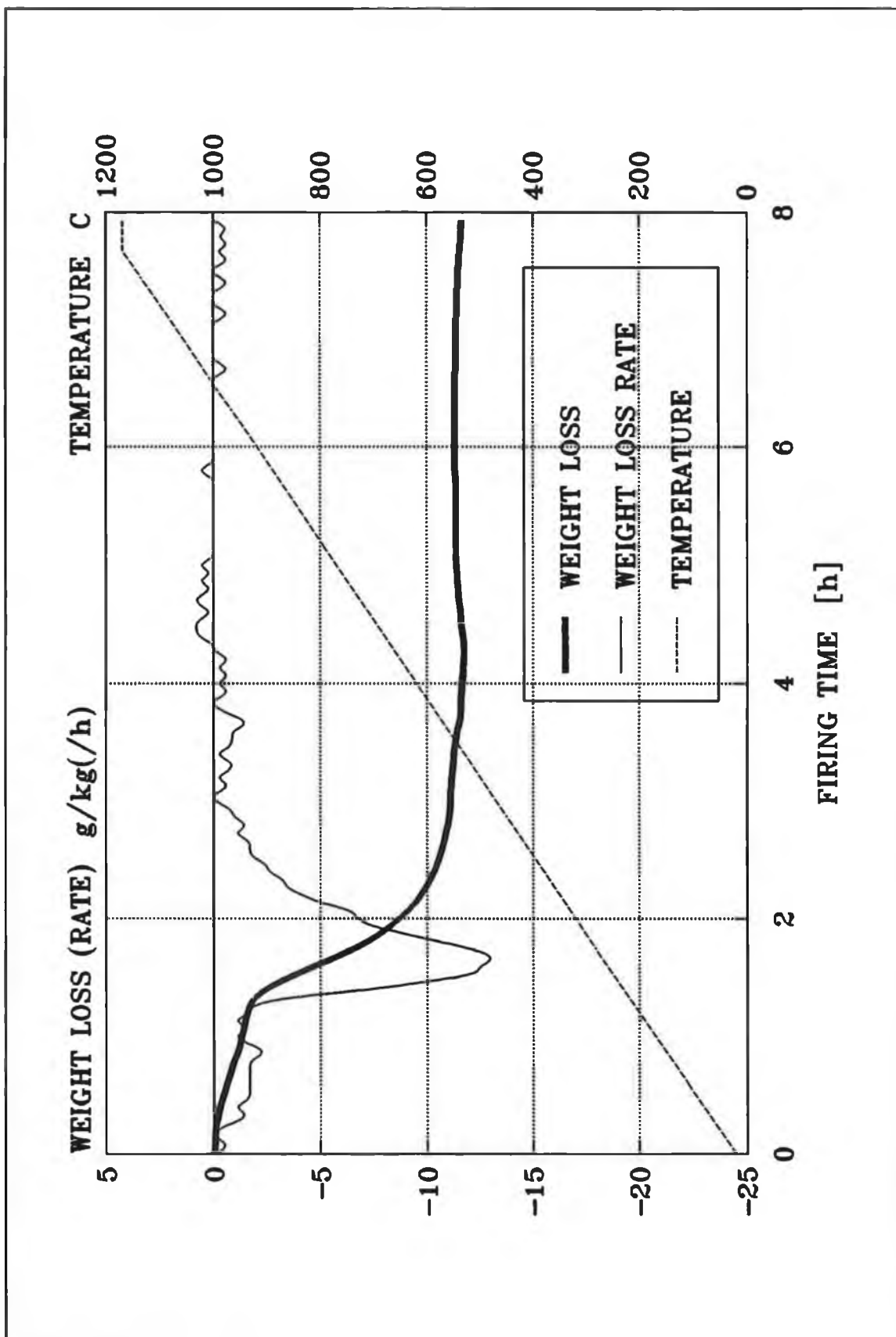


Figure 6.6 Weight loss, weight loss rate and temperature vs. firing time for 2.5°C/min heating rate.

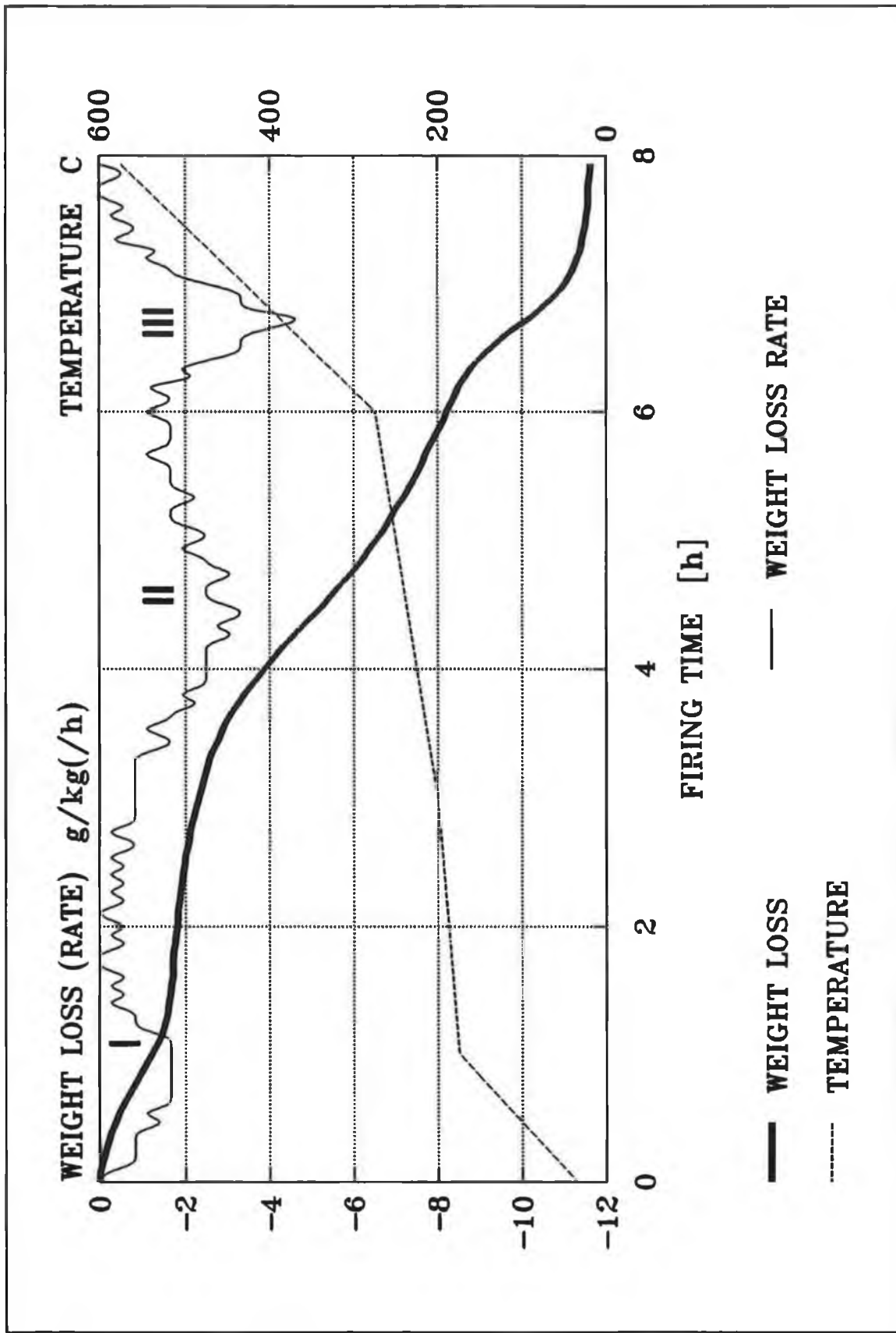


Figure 6.7 Weight loss, weight loss rate and temperature vs. firing time for temperature profile No. 01.

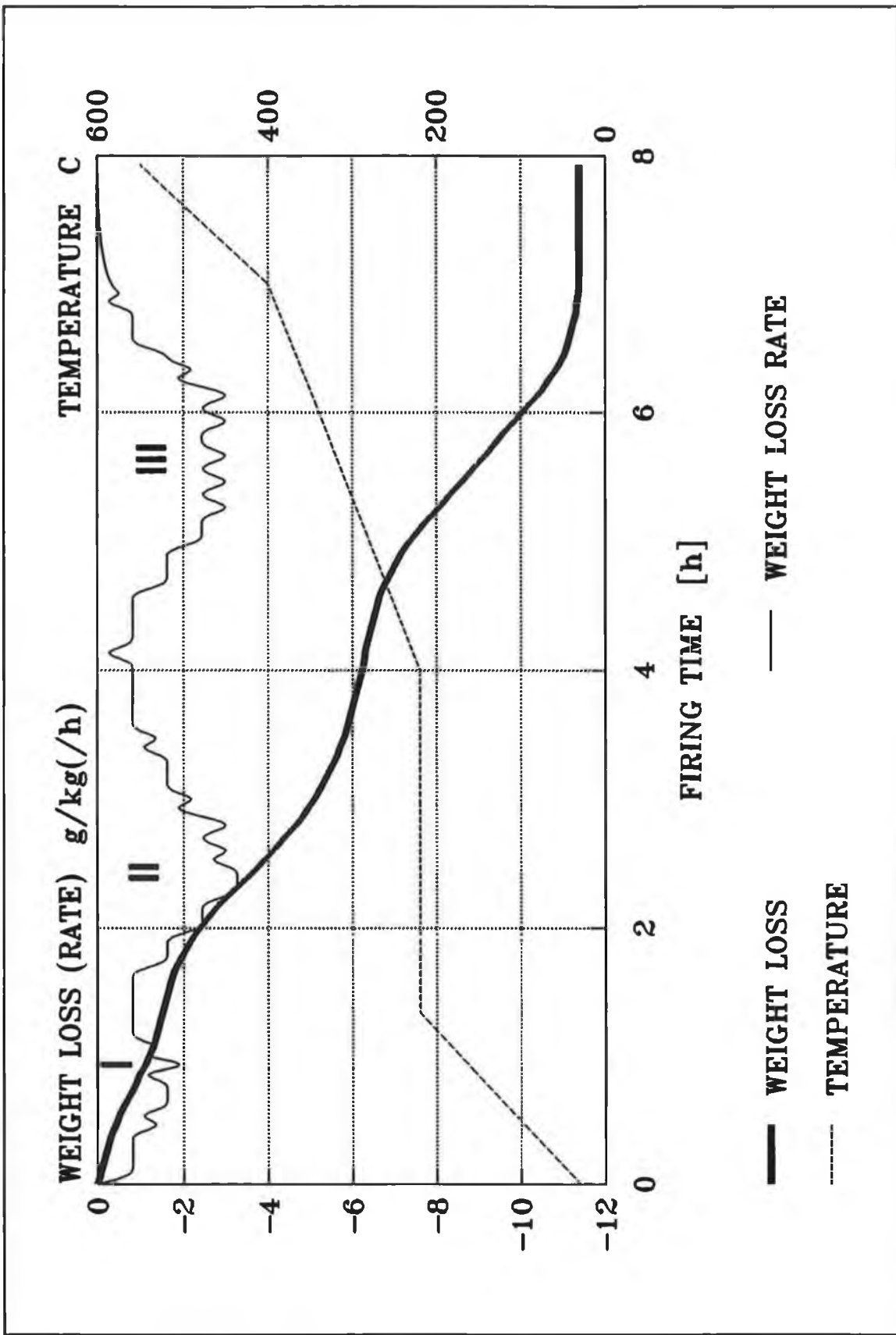


Figure 6.8 Weight loss, weight loss rate and temperature vs firing time for temperature profile No.04.

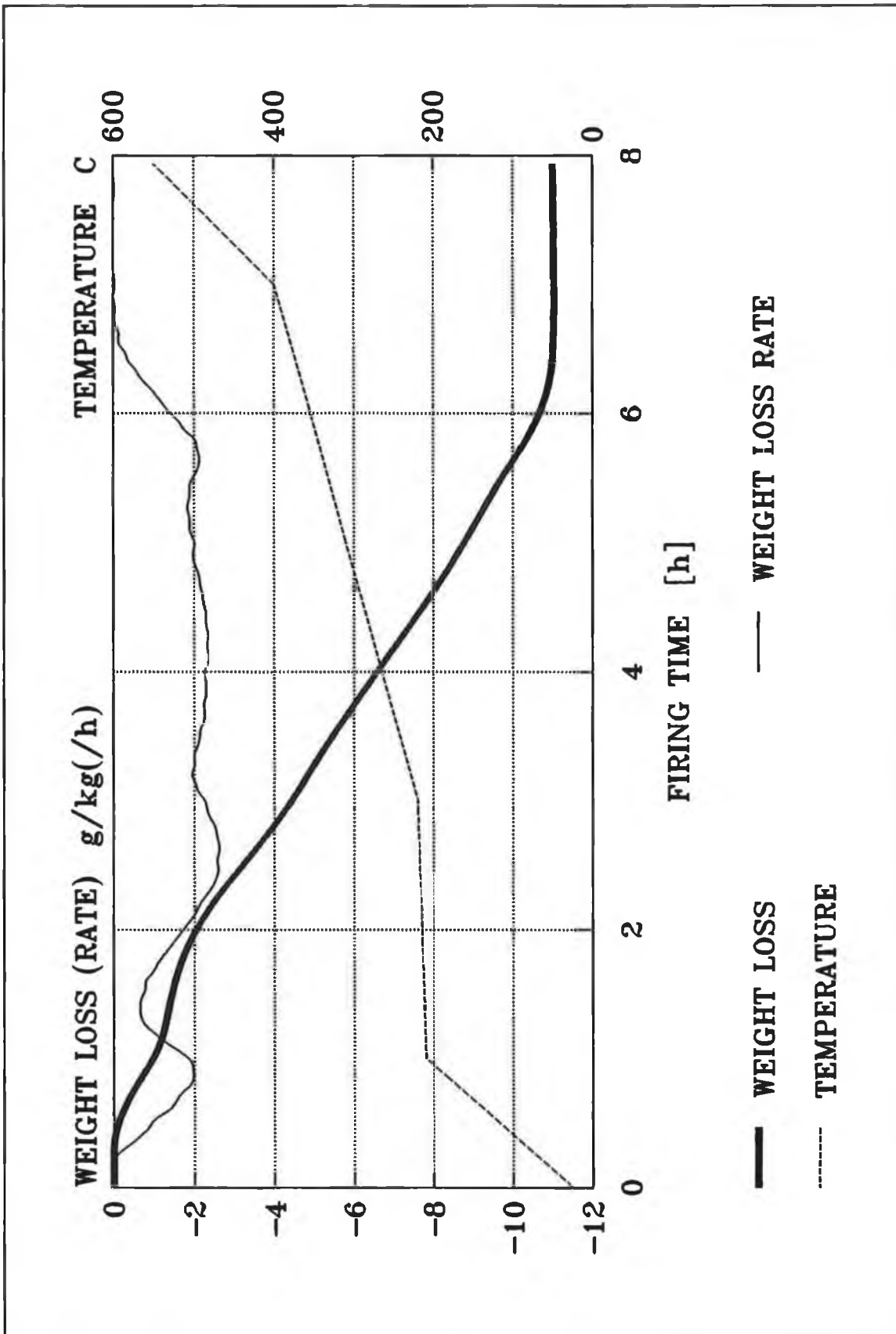


Figure 6.9 Weight loss, weight loss rate and temperature vs. firing time for temperature profile No.06.

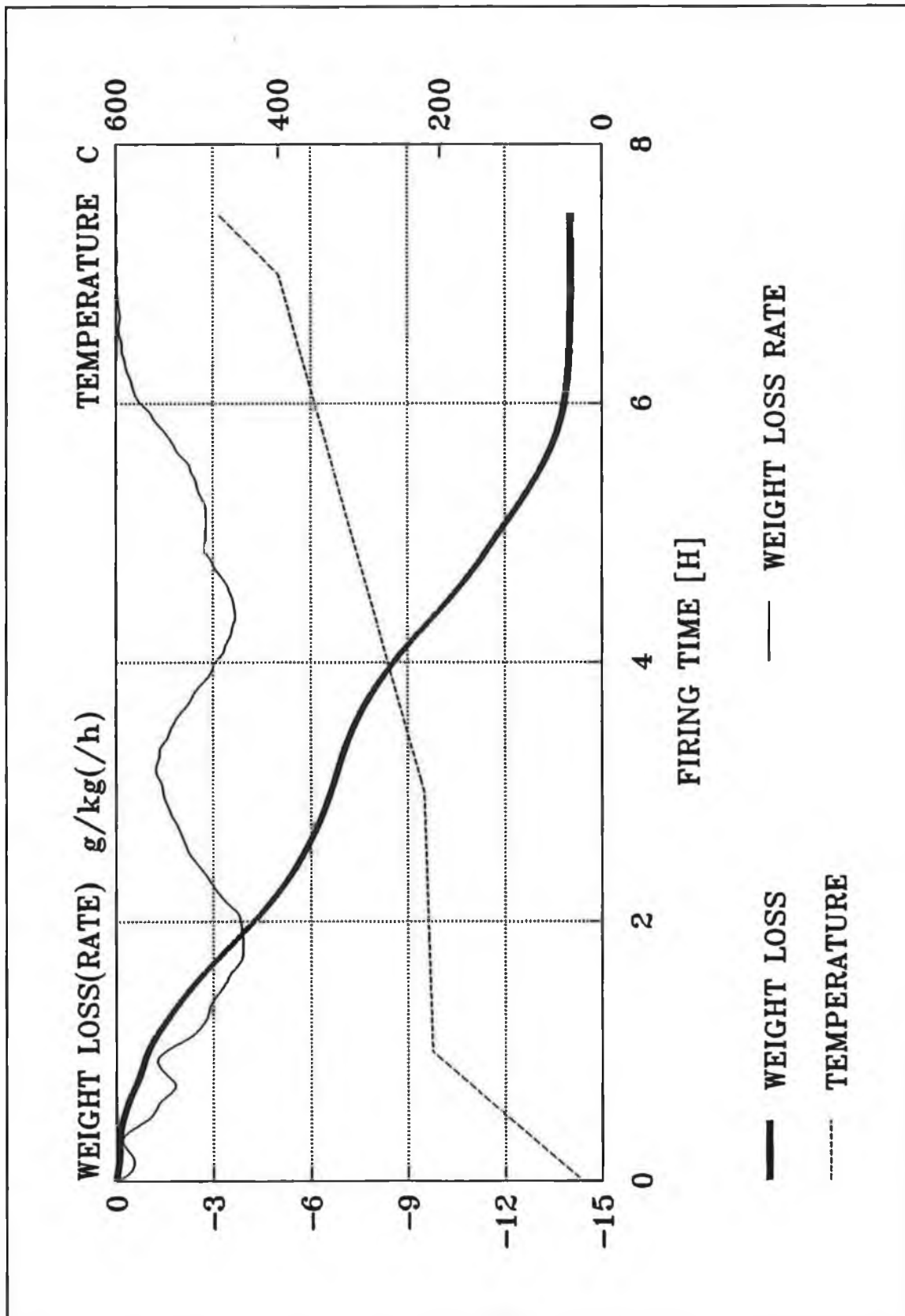


Figure 6.10 Weight loss, weight loss rate and temperature vs. firing time for discs with higher ratio of surface area to volume using temperature profile No. 06.

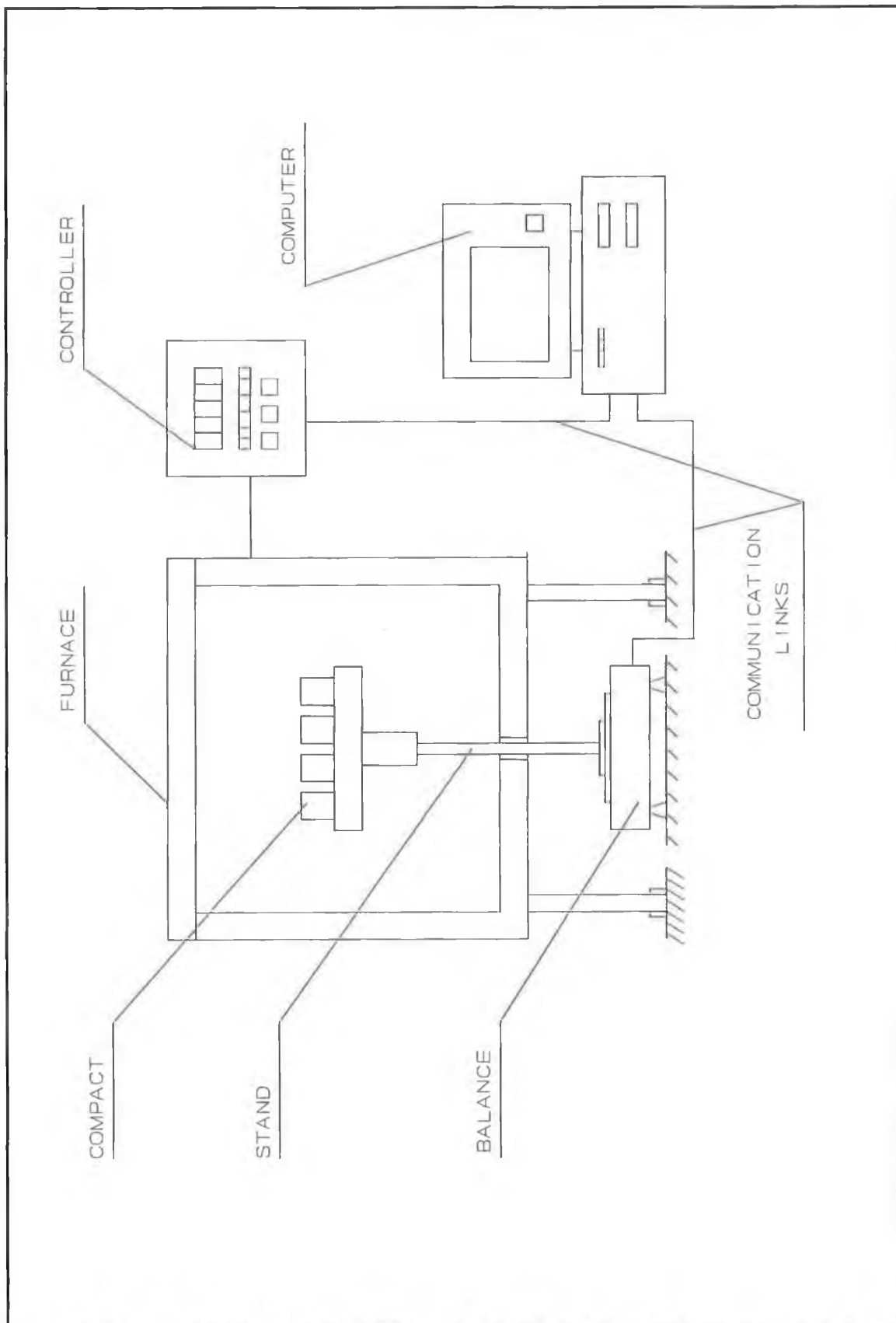


Figure 6.11 Experimental setup for feed back loop control of weight loss rate.

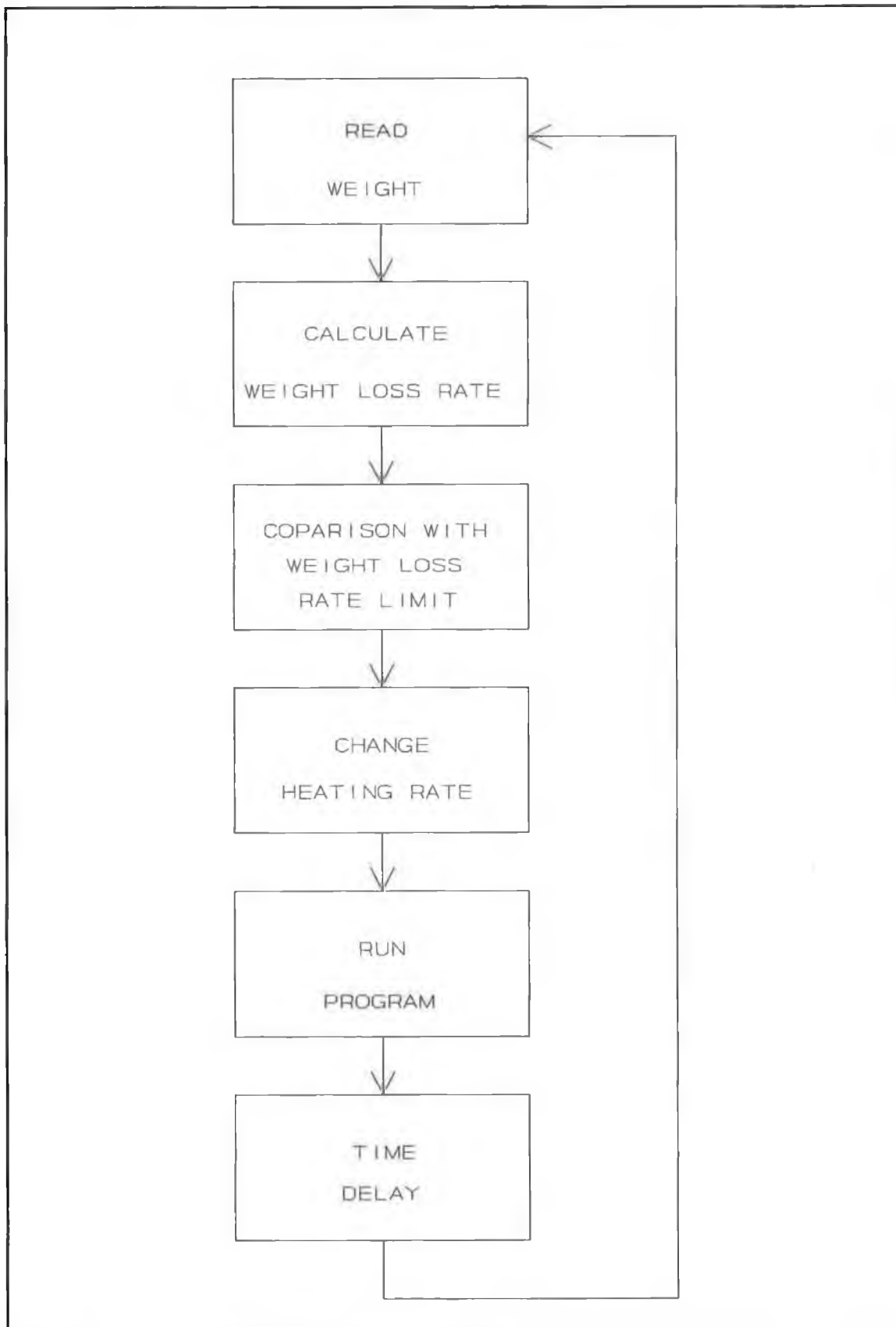


Figure 6.12 Flow chart for the feed back loop control of the weight loss rate.

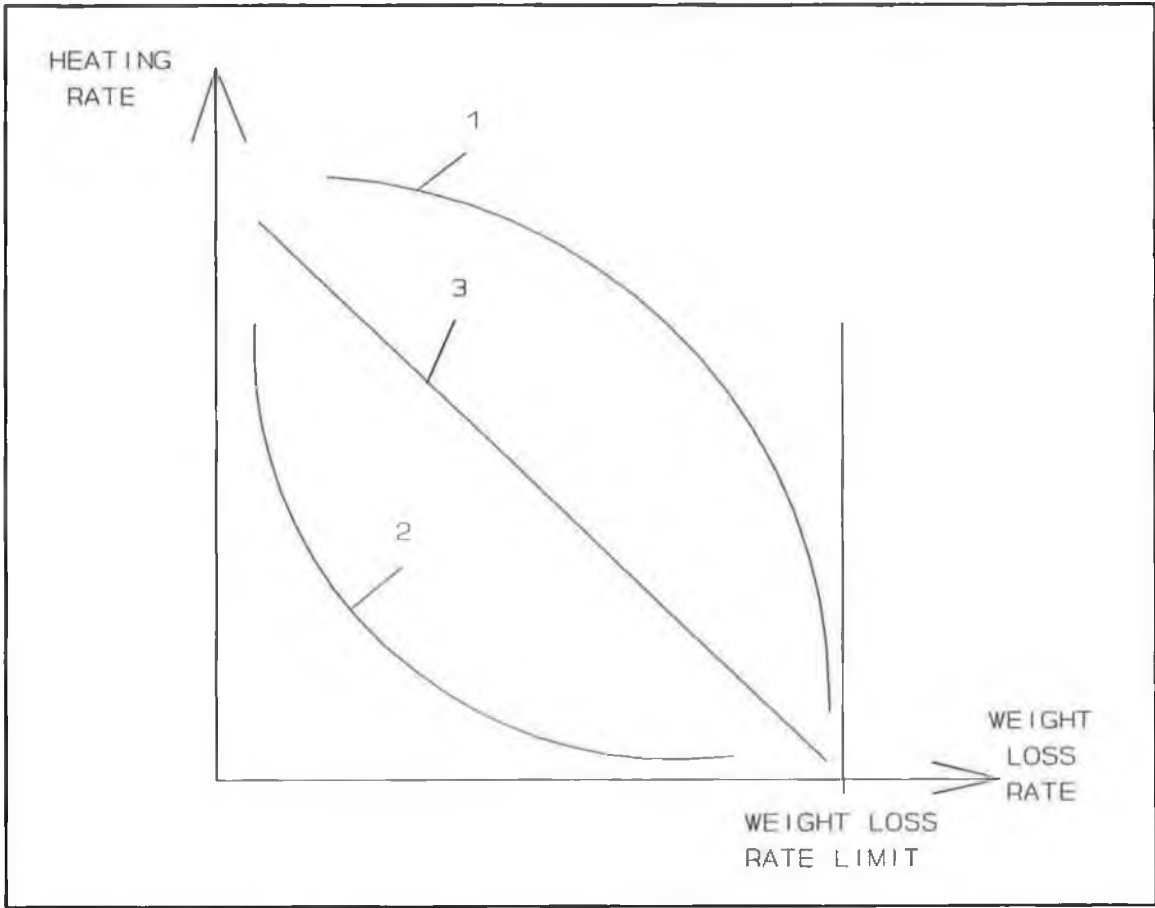


Figure 6.13 Proposed functions for the relation between the heating rate and the current weight loss rate.

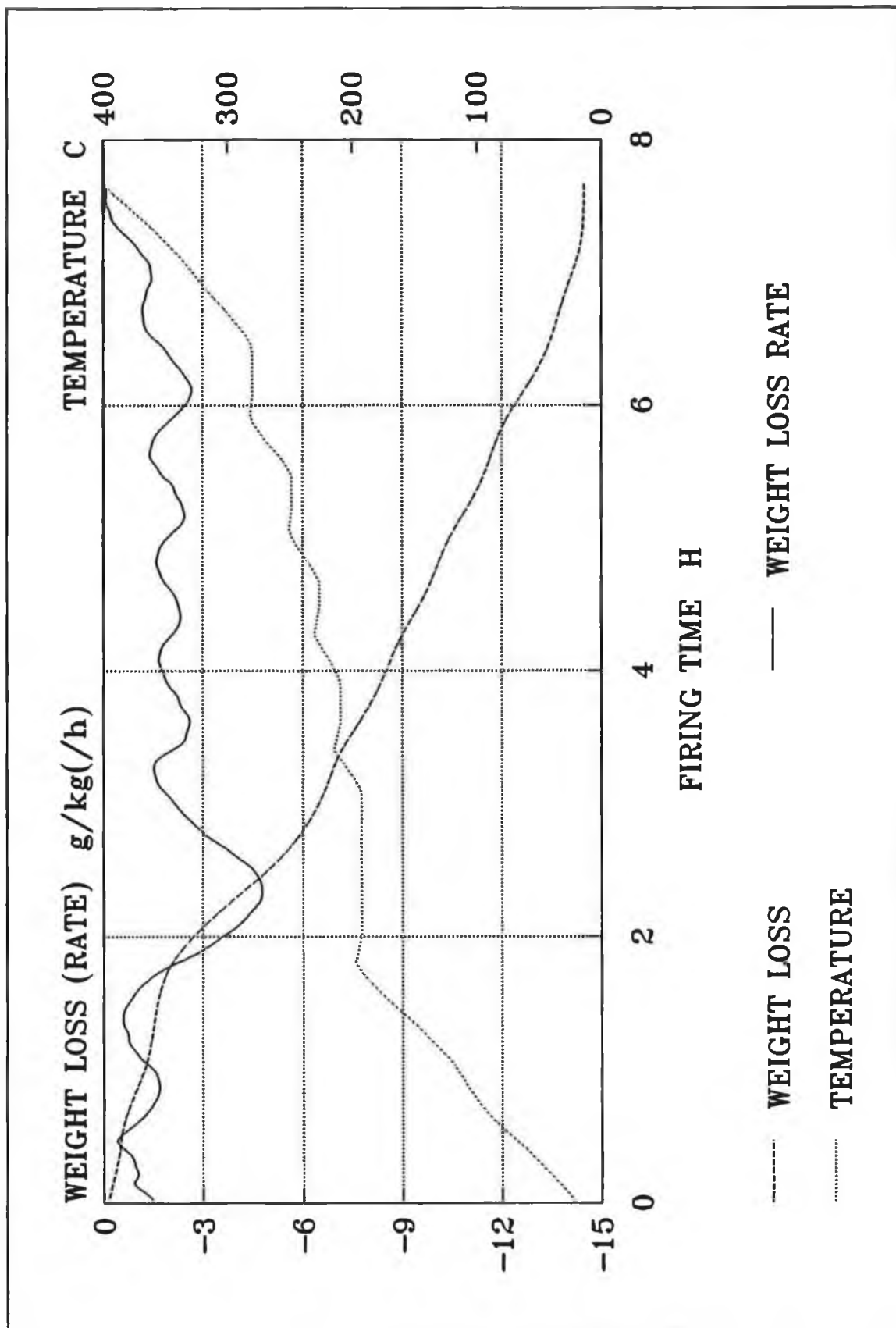


Figure 6.14 Weight loss and weight loss rate curves using an ellipse equation for control.

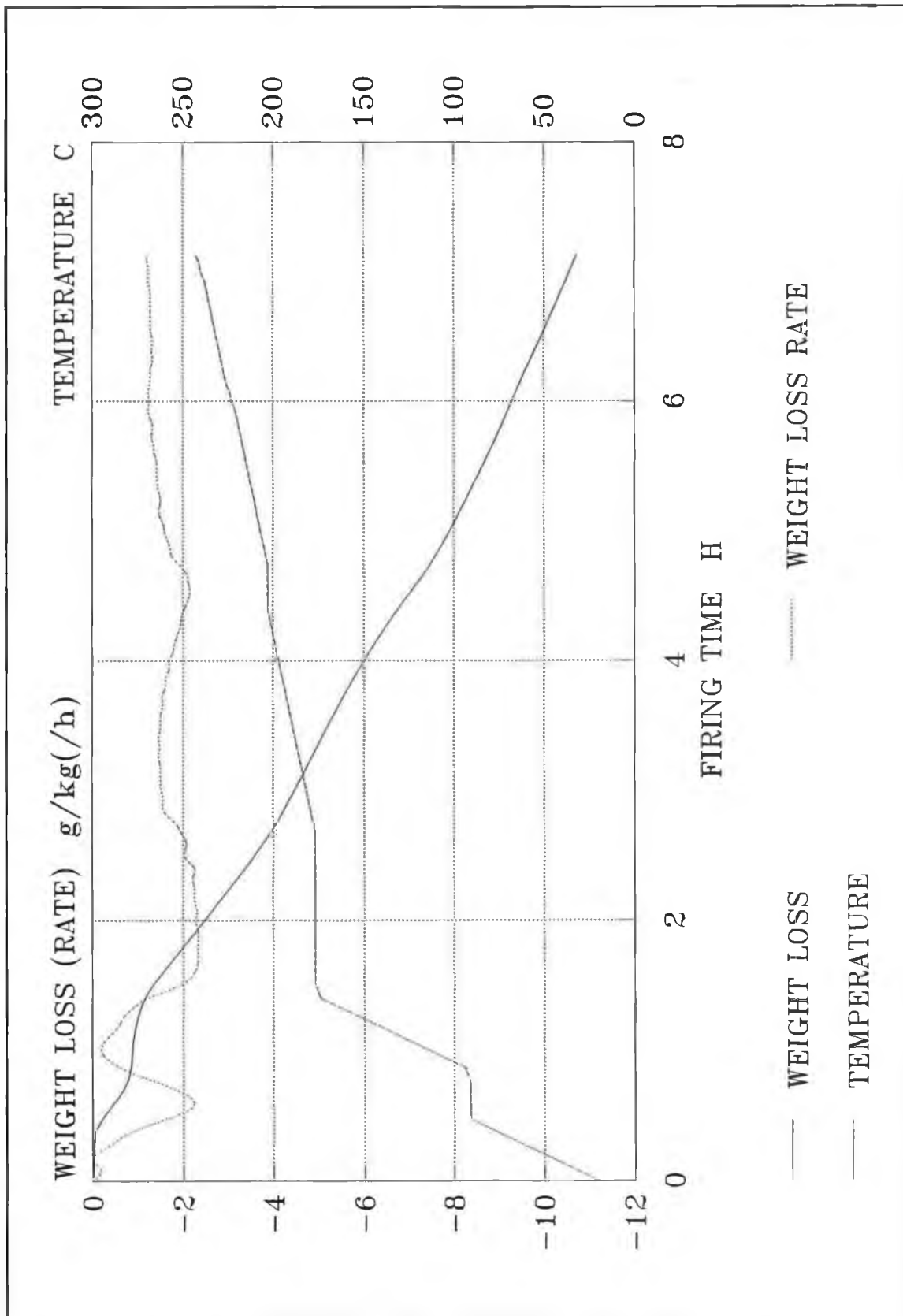


Figure 6.15 Weight loss and weight loss curves for an exponential decay equation to relate the heating rate with the weight loss rate.

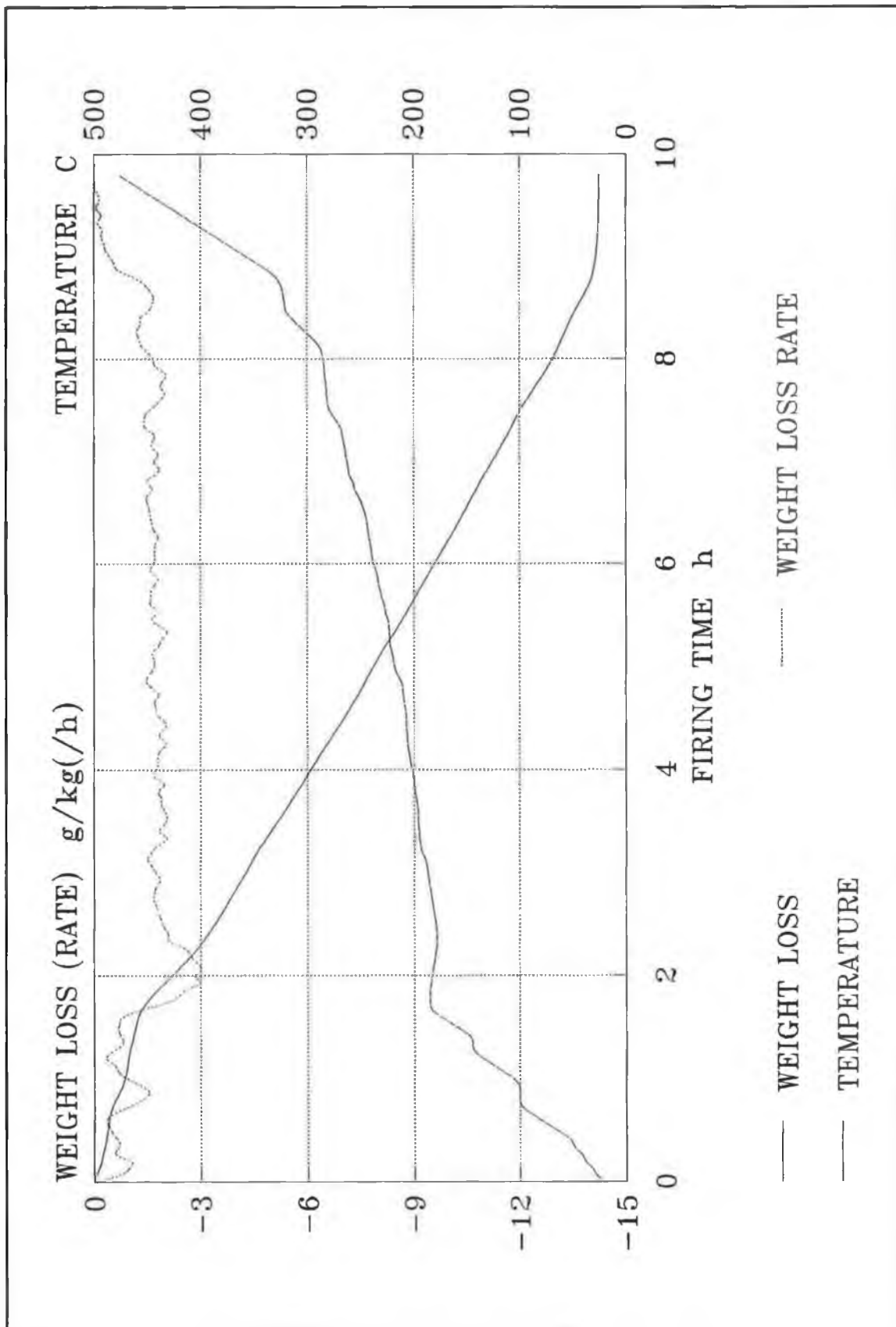


Figure 6.16 Weight loss and weight loss rate curves vs. firing temperature using linear heating rate equation.

Figure 6.17 Weight loss rate controlled at 1.5 g/kg/h.

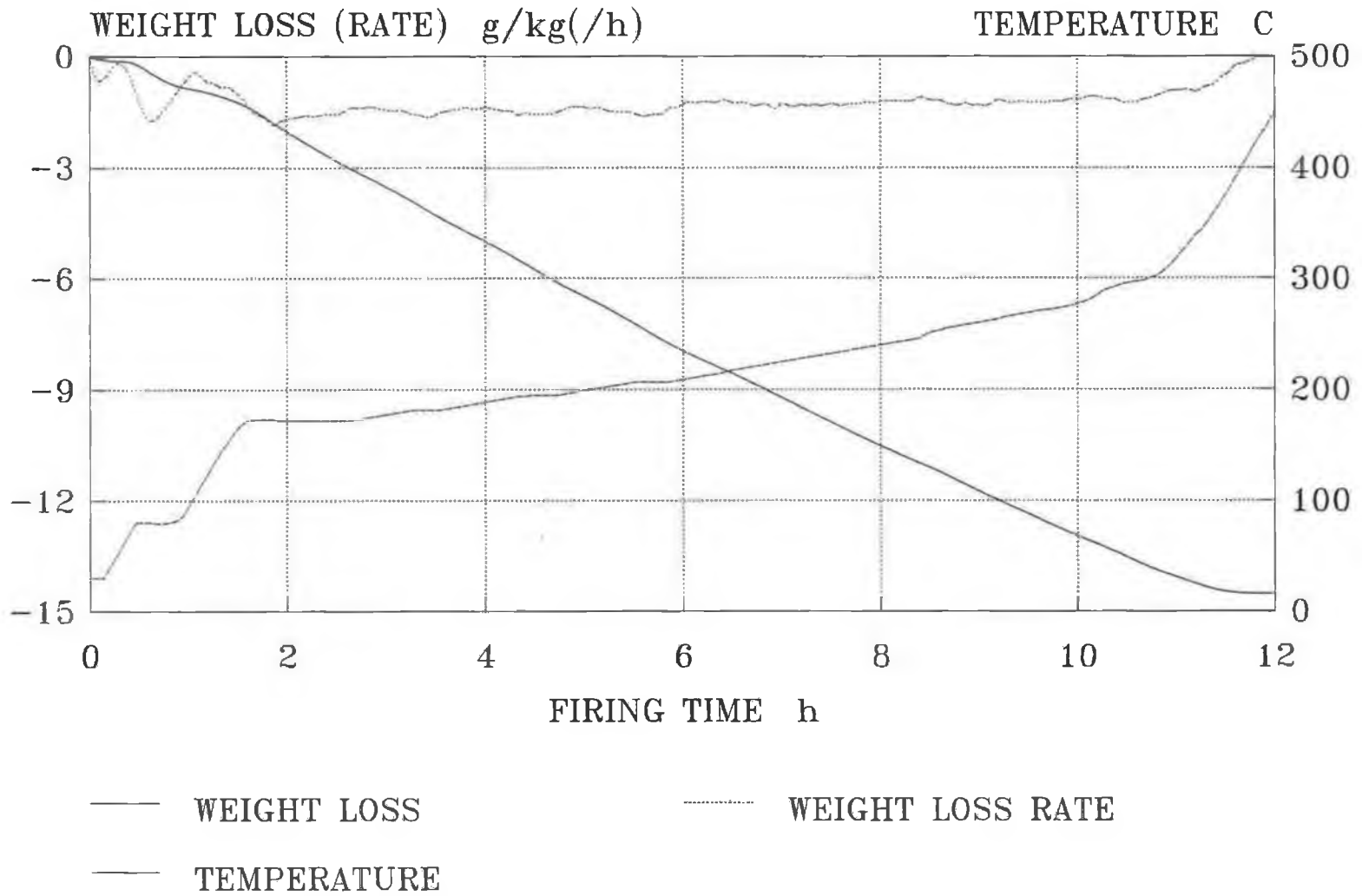
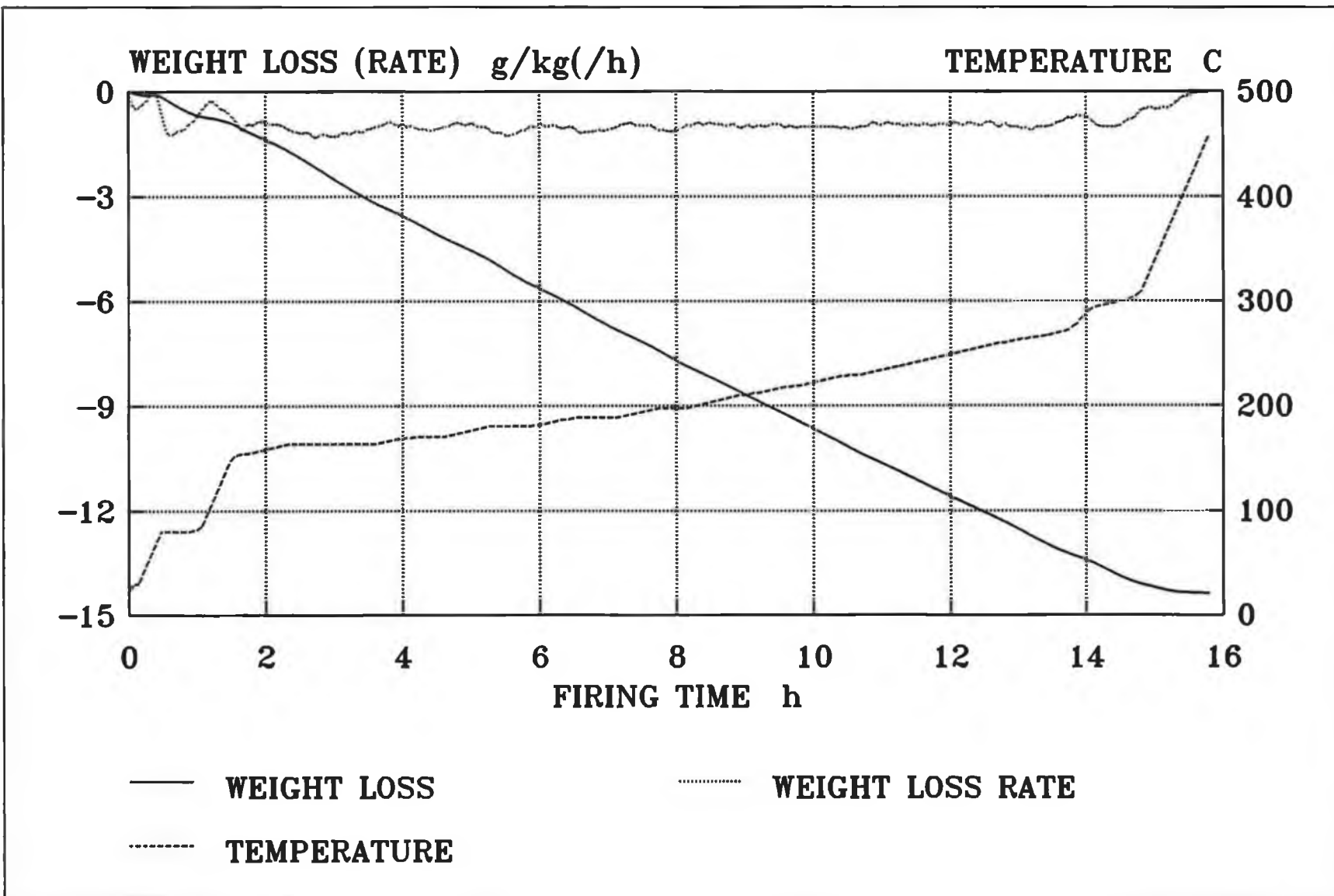


Figure 6.18 Weight loss rate controlled at 1 g/kg/h.



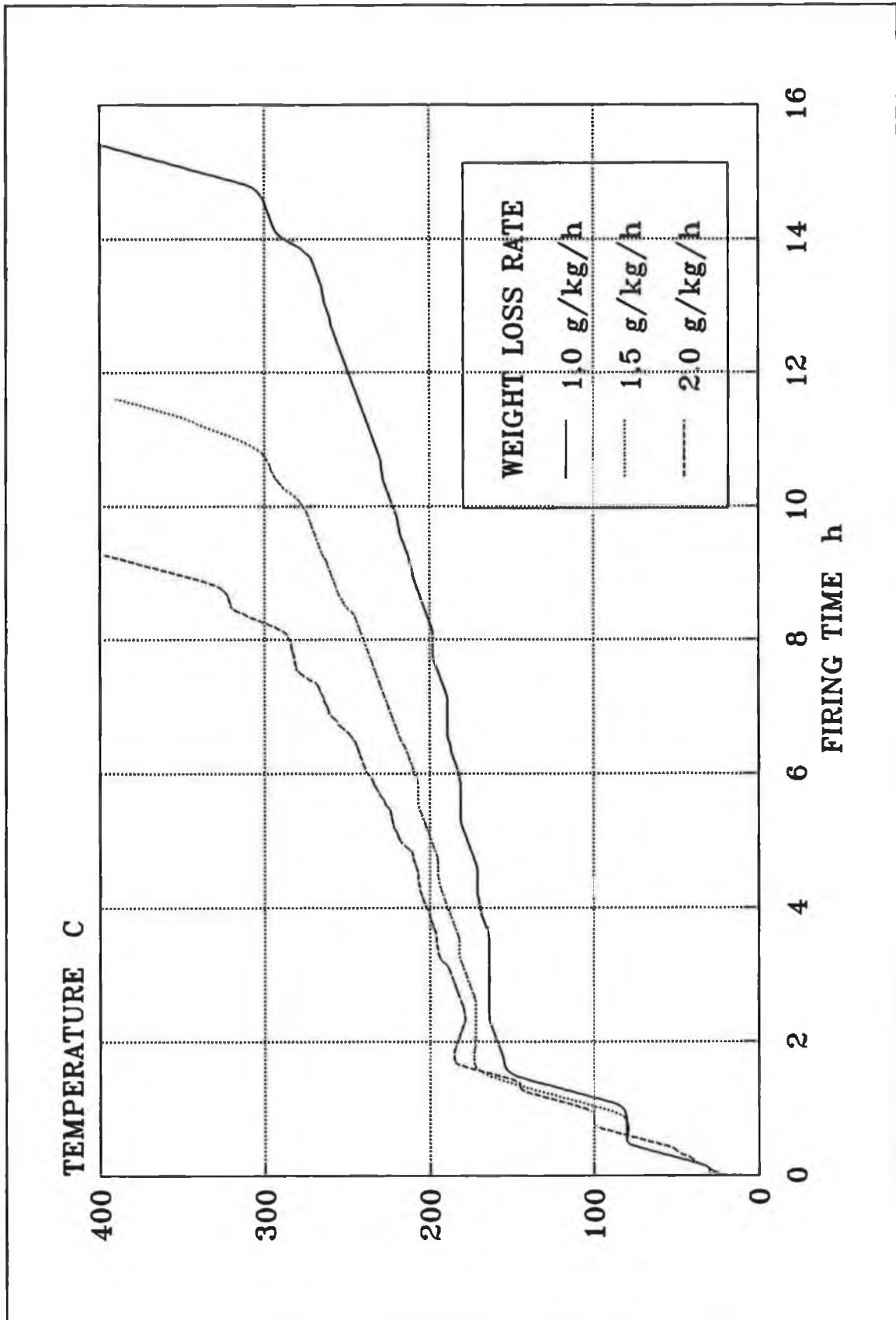


Figure 6.19 Temperature profiles generated at preprogrammed weight loss rates.

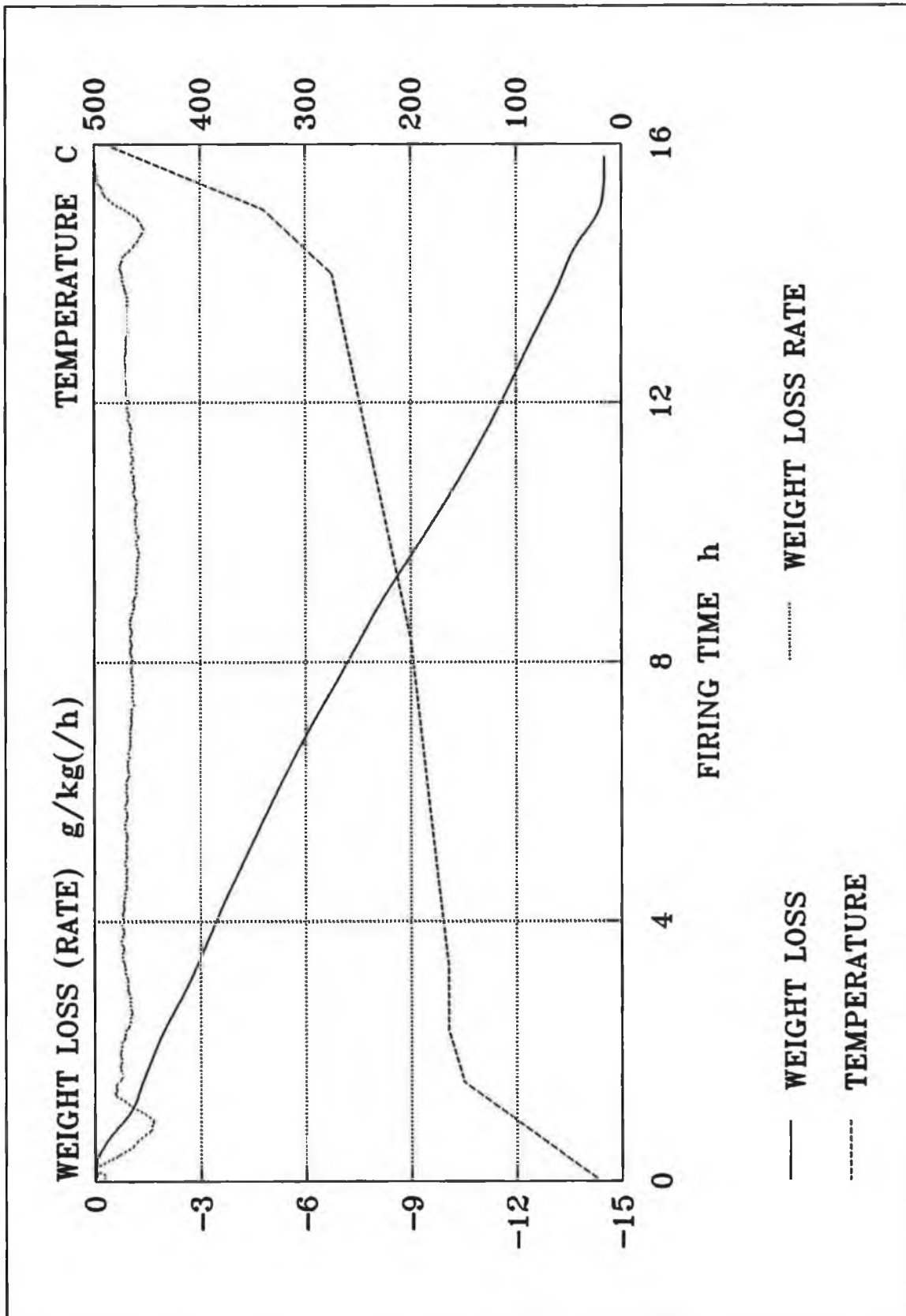


Figure 6.20 Weight loss and weight loss rate curves for temperature profile which was approximated from the results of weight loss rate of 1 g/kg/h.

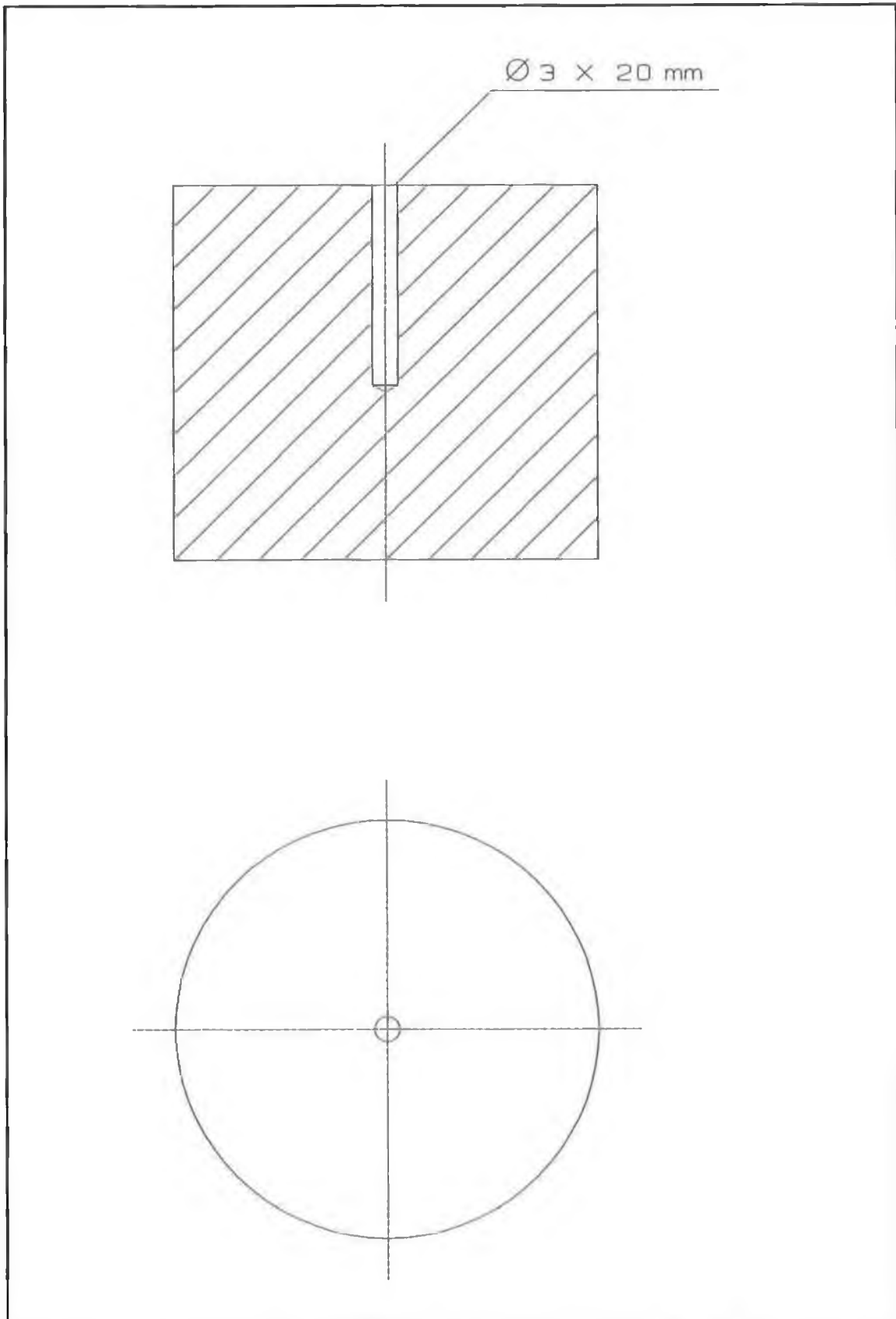
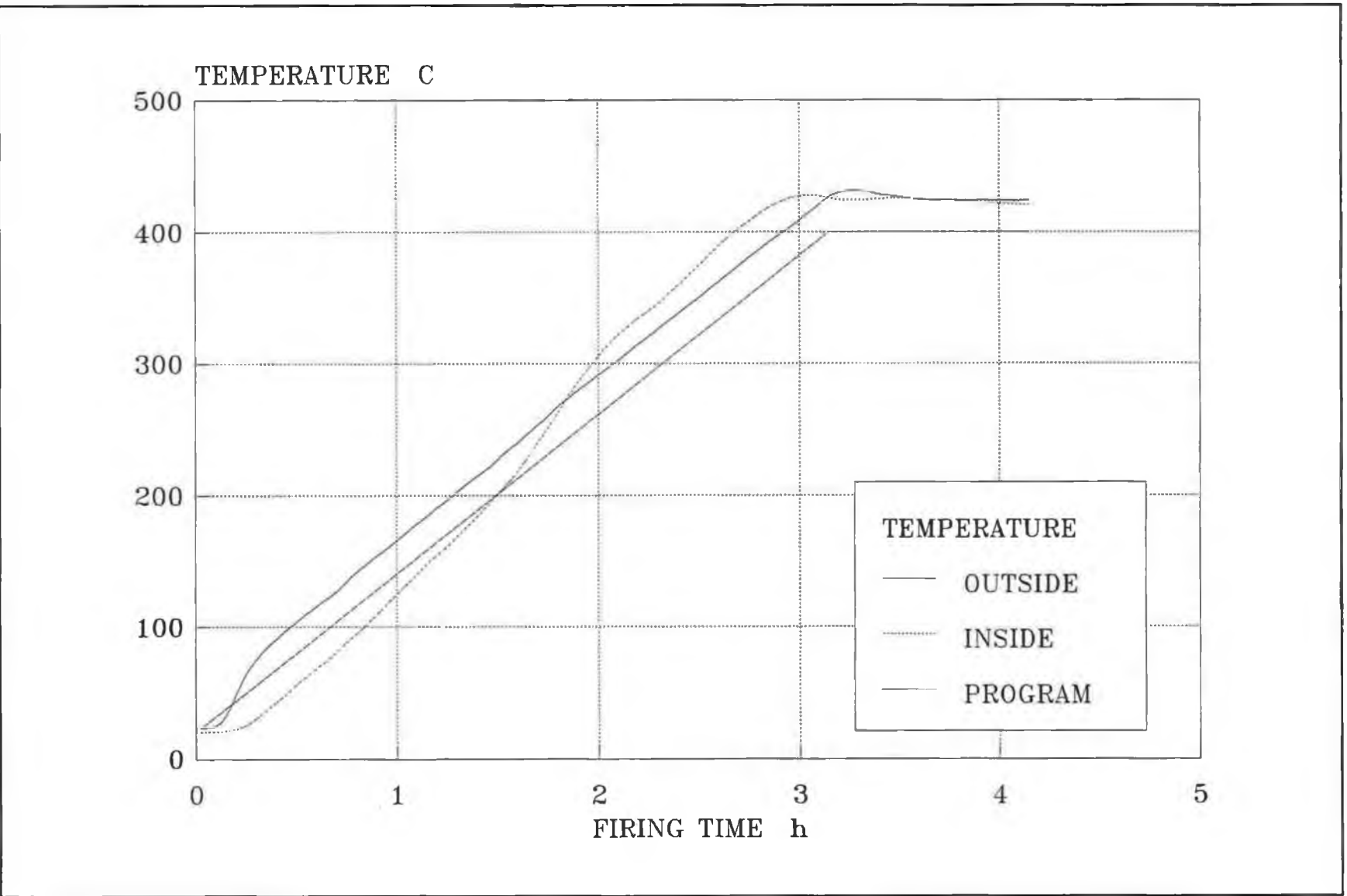


Figure 6.21 Drawing of the green disc with the hole for the temperature gradient experiment.

Figure 6.22 Temperature gradient within the disc.



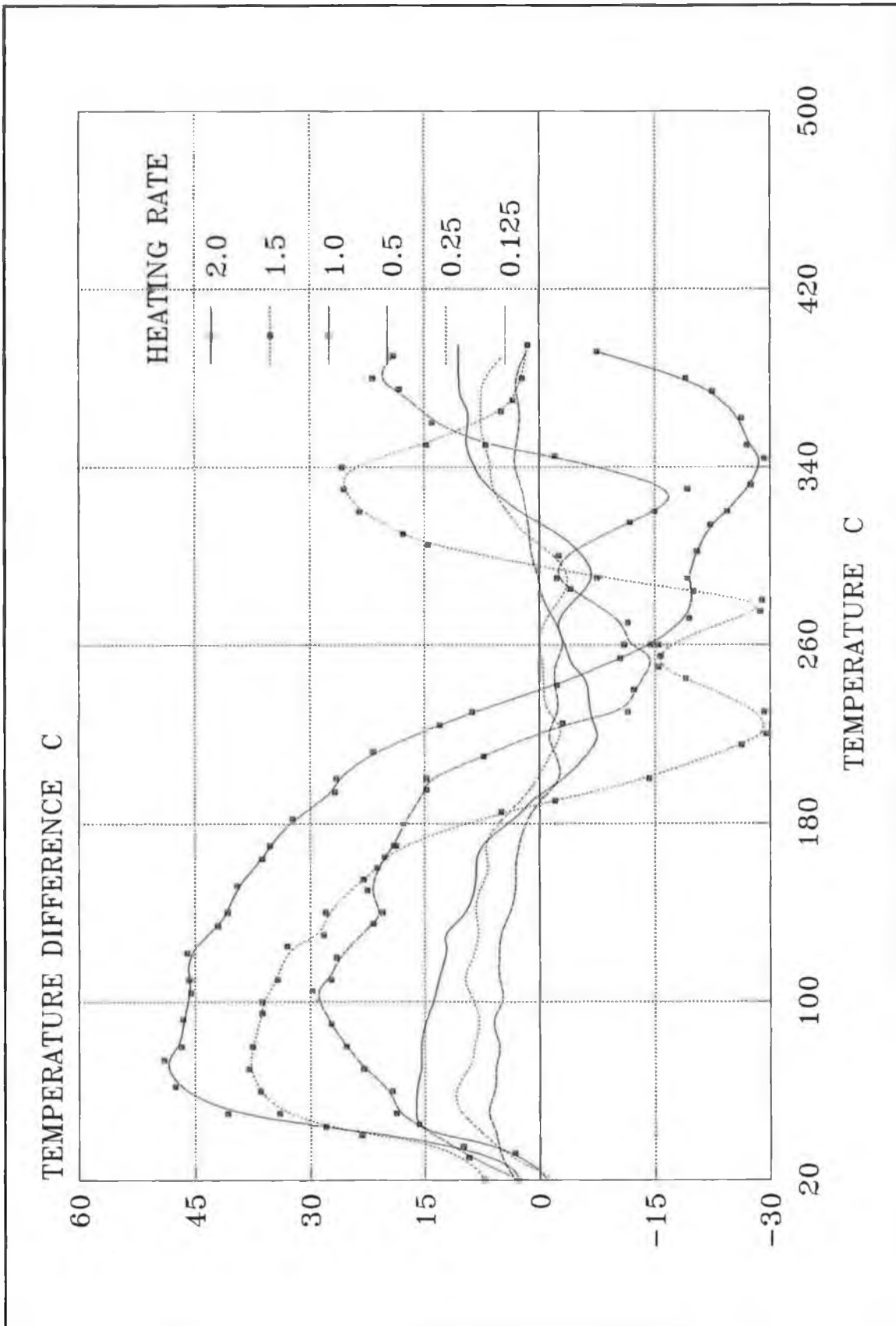


Figure 6.23 Temperature difference within the disc between the inside and the outside for 6 heating rates.

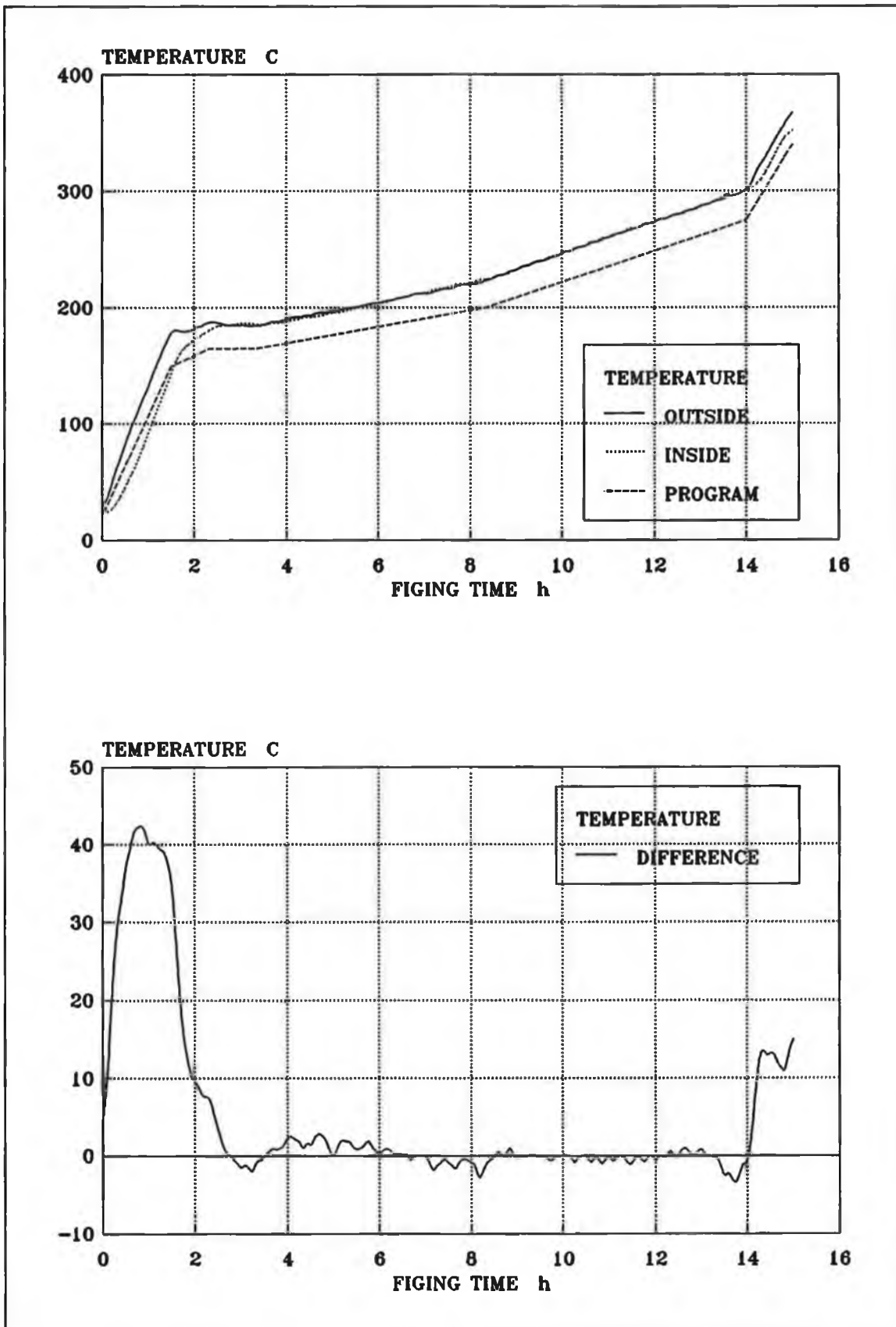
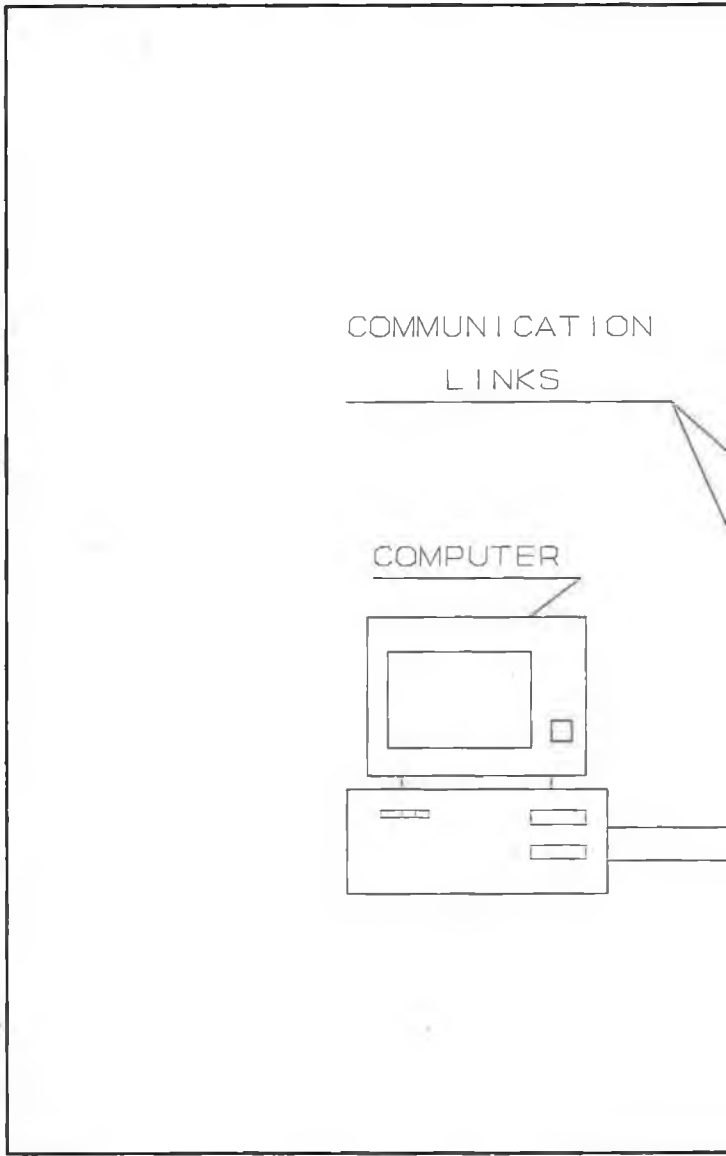
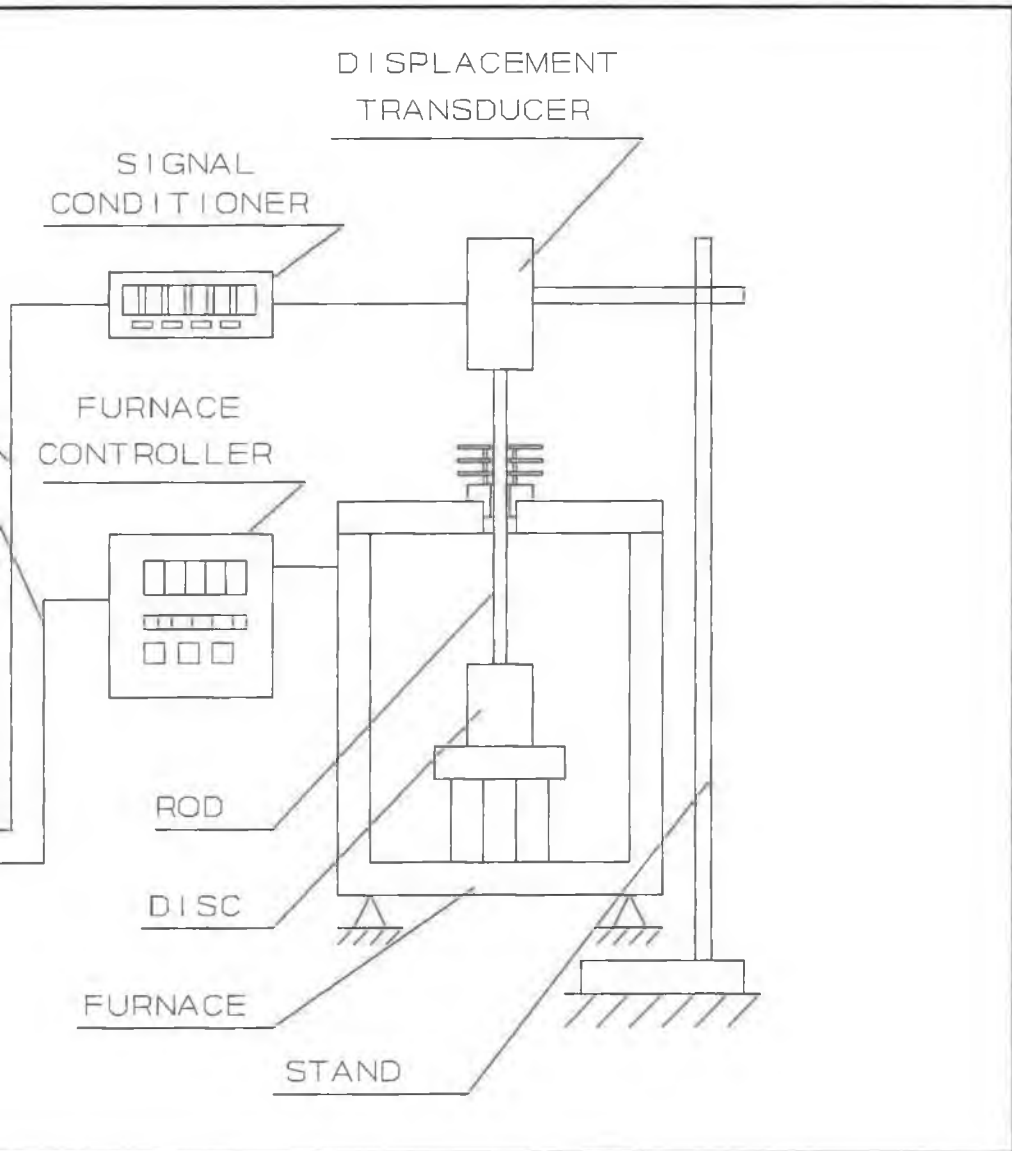


Figure 6.24 Temperature gradient within the disc using temperature profile for weight loss rate limit of 1g/kg/h.

Figure 6.25 Experimental set up for shrinkage control.





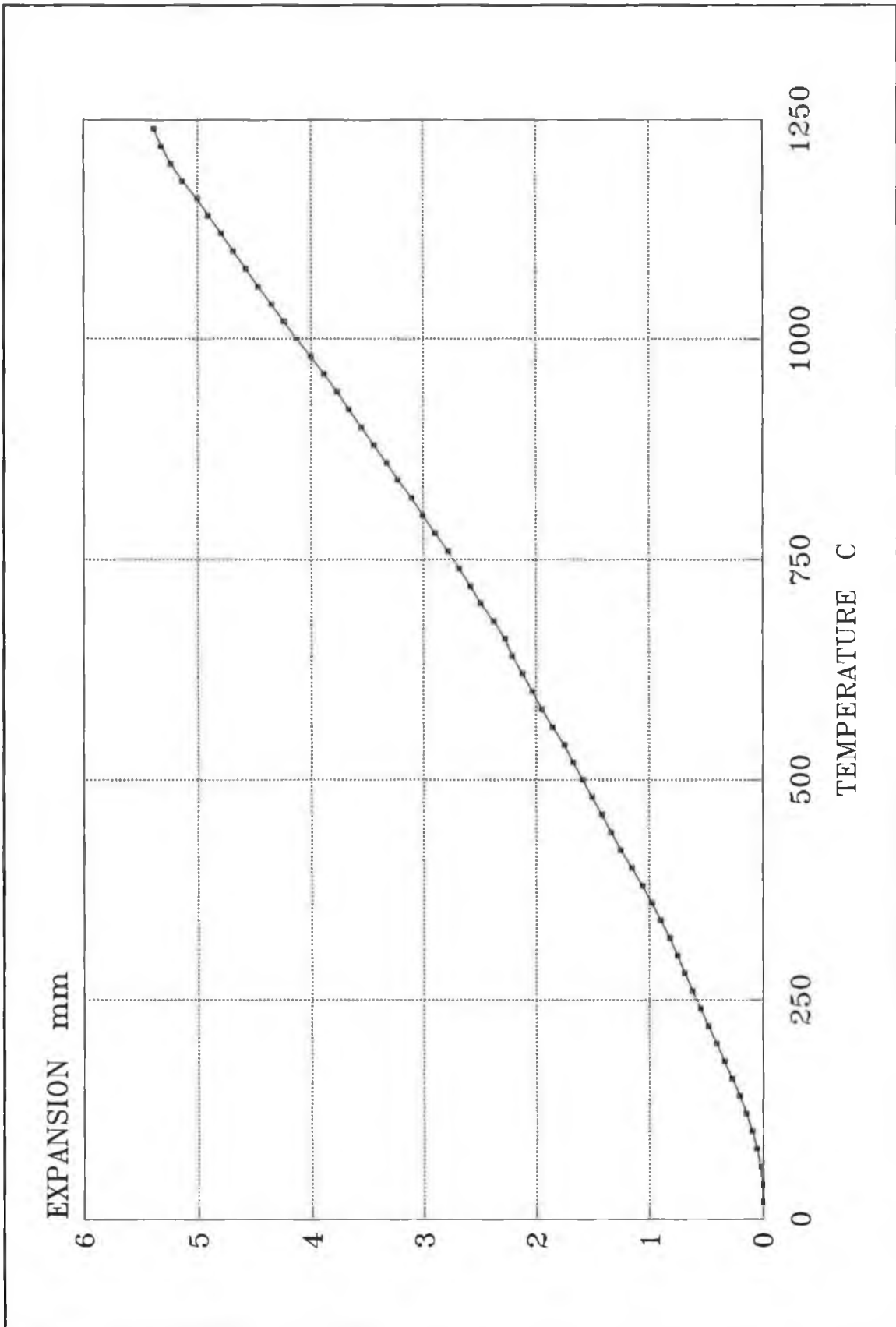


Figure 6.26 Calibration curve for the controlled shrinkage instrument.

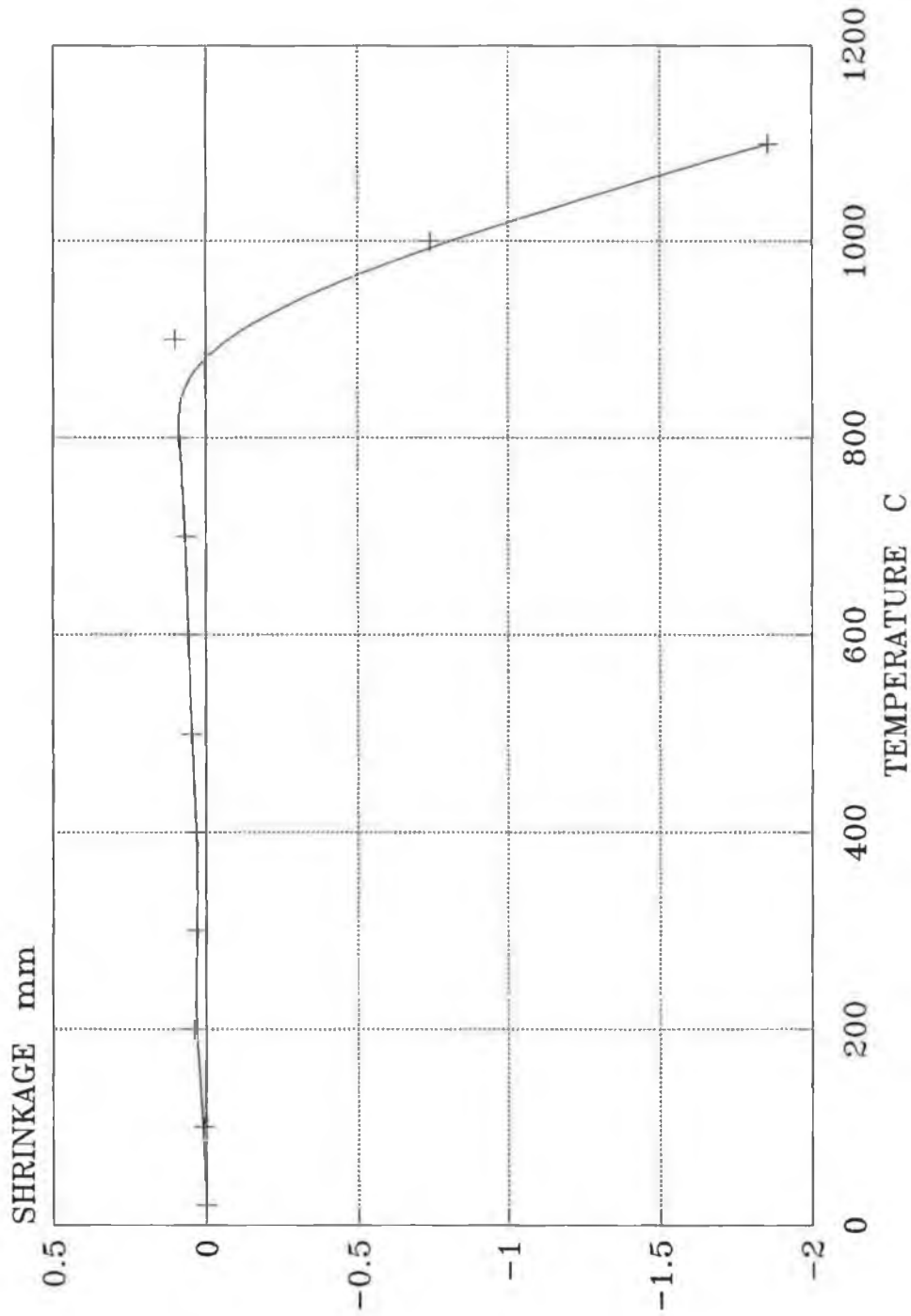


Figure 6.27 Shrinkage results using the high temperature dilatometer.

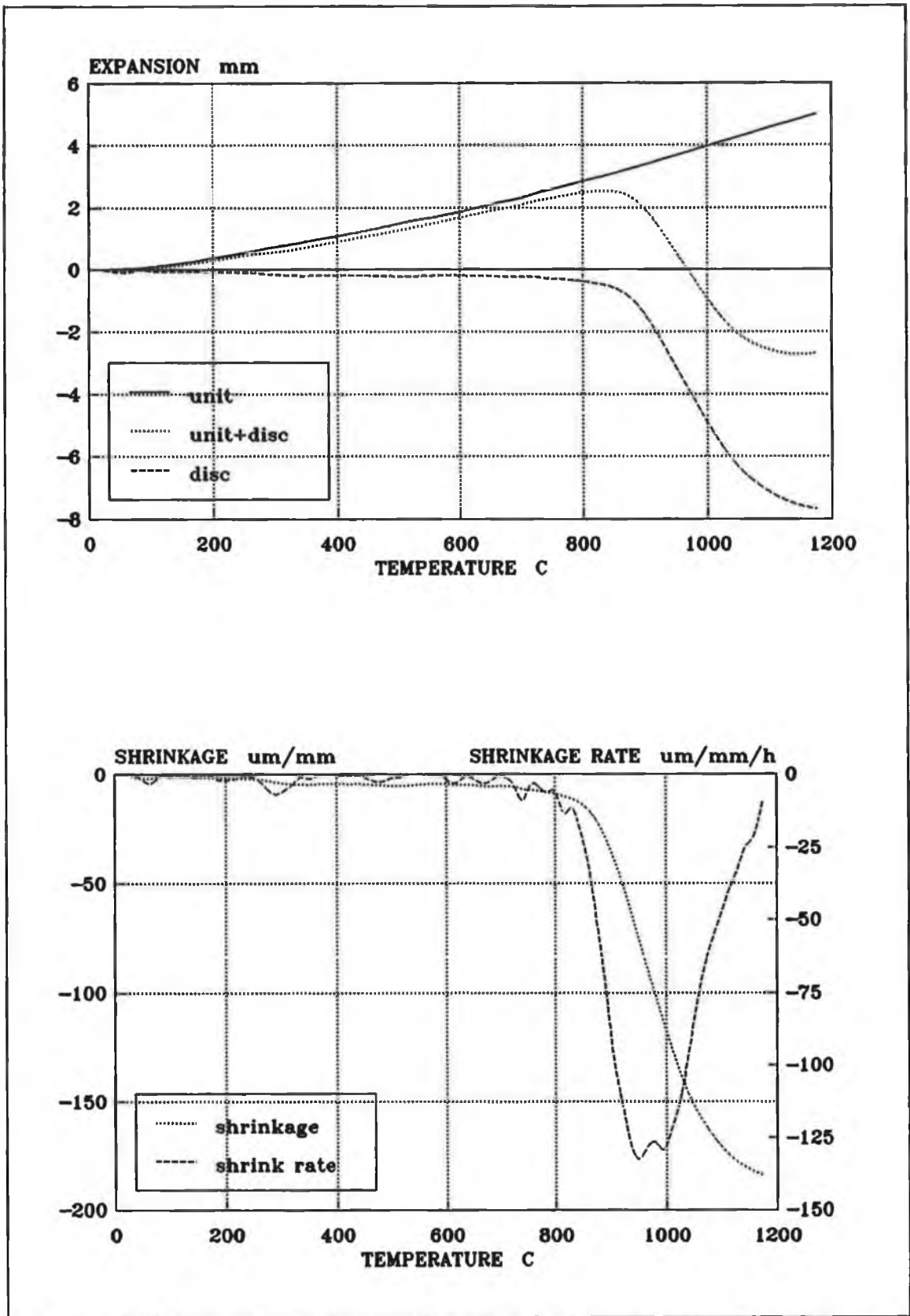


Figure 6.28 a- Expansion and contraction curves for the unit and the disc. b- Shrinkage and shrinkage rate for the same disc at heating rate of 2.5°C/min.

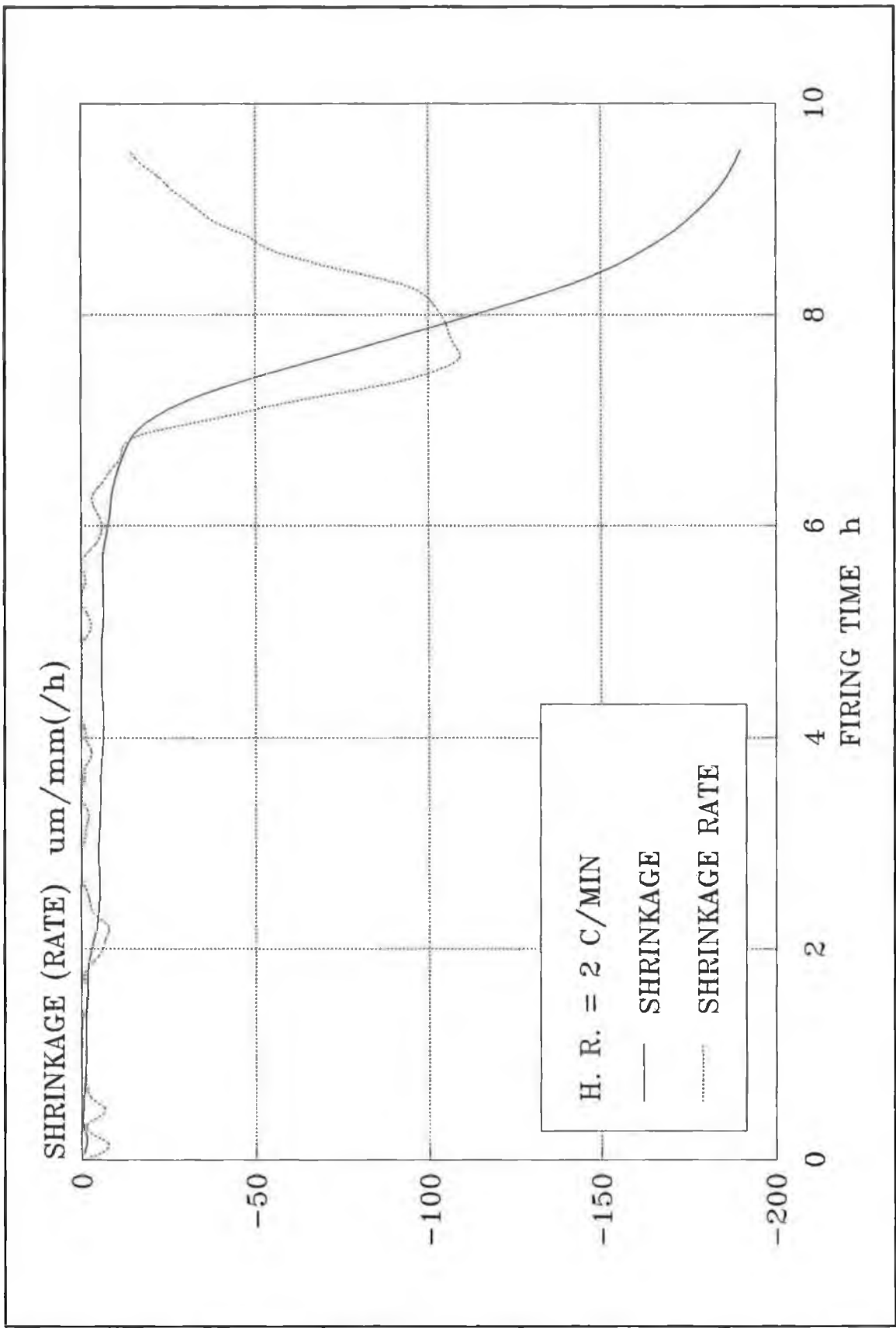


Figure 6.29 Shrinkage and shrinkage rate curves during firing at a heating rate of 2°C/min.

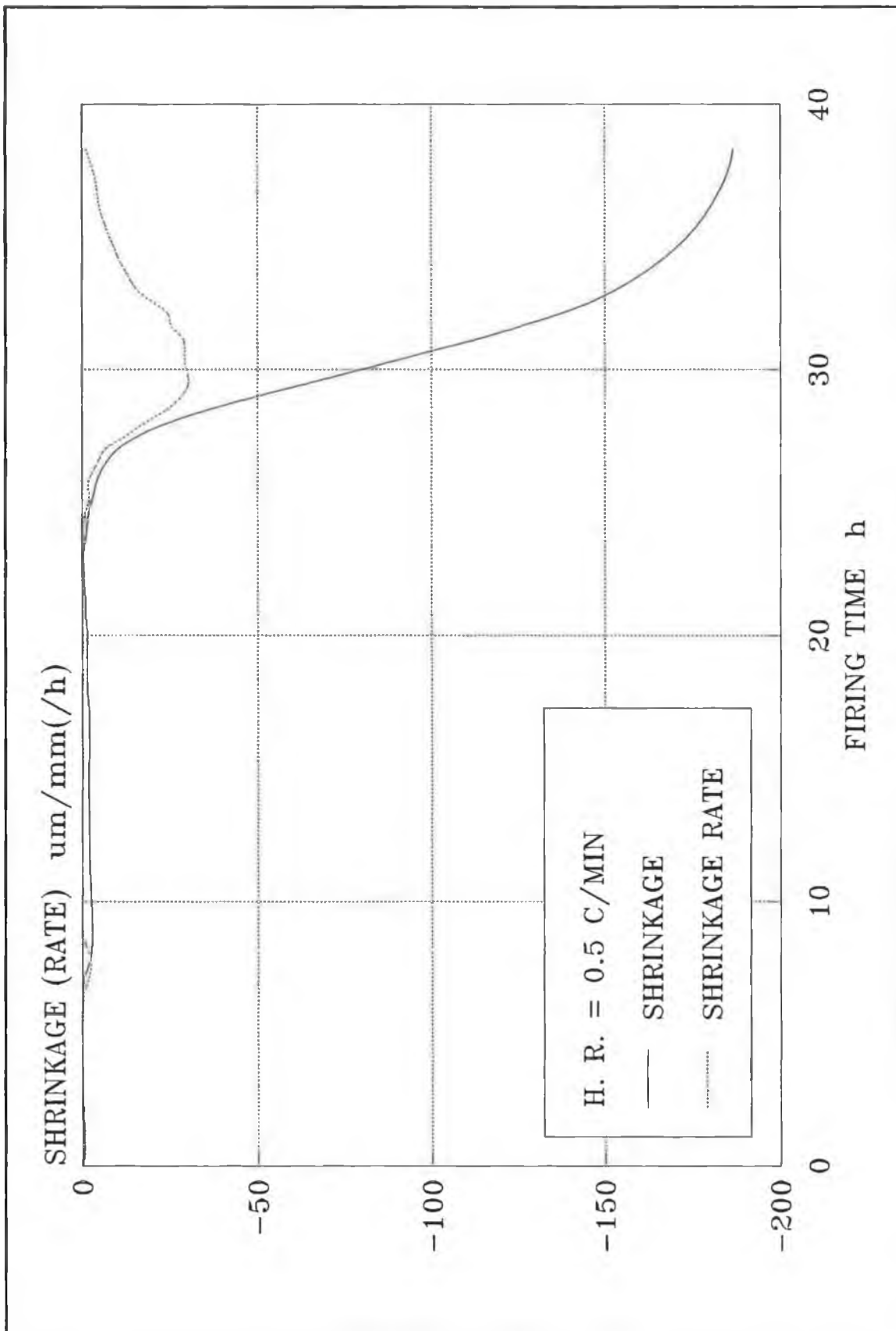


Figure 6.30 Shrinkage and shrinkage rate curves during firing at a heating rate of $0.5^{\circ}\text{C}/\text{min}$.

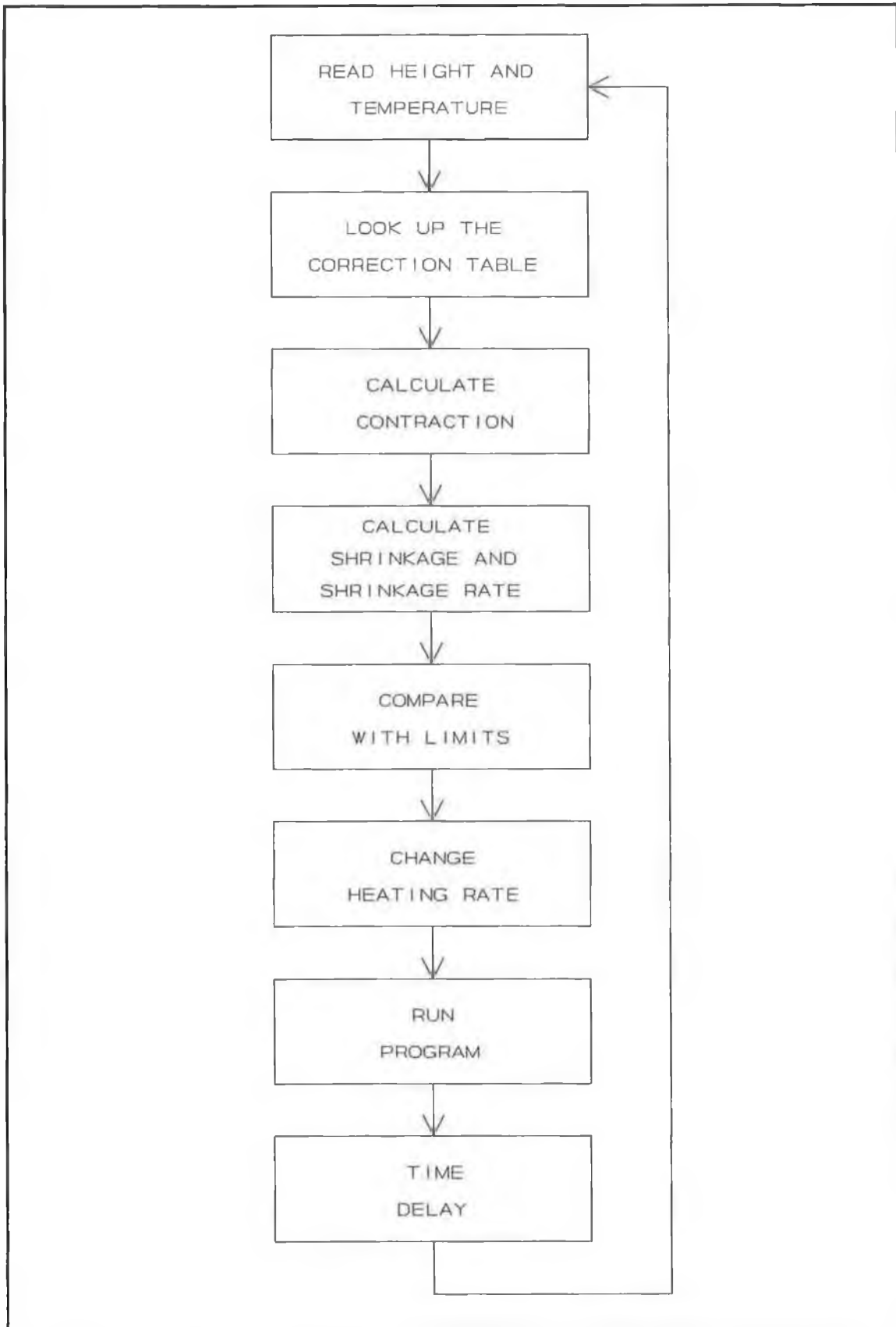


Figure 6.31 flow chart for the software for controlling the disc's shrinkage.

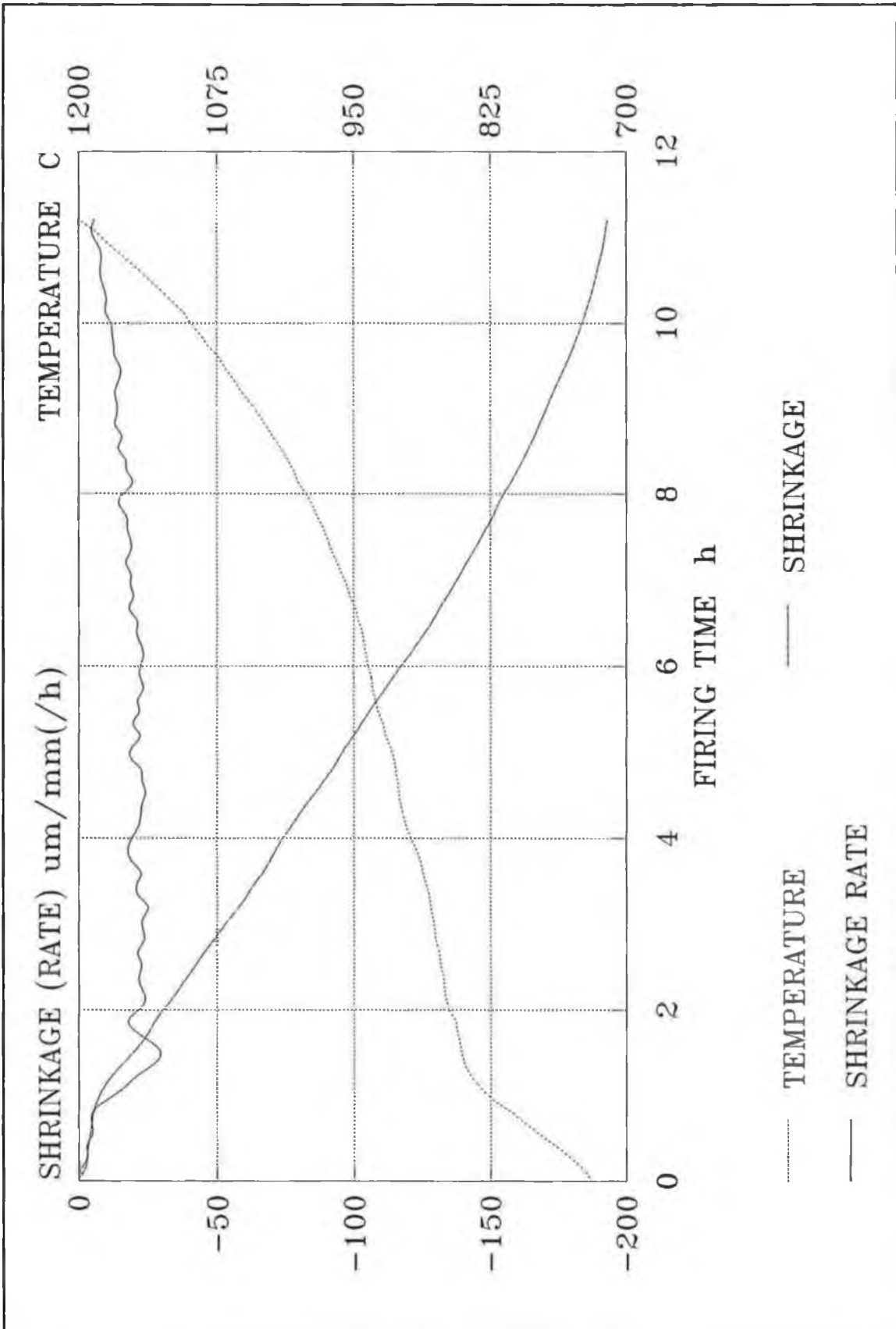


Figure 6.32 Shrinkage and shrinkage rate curves for a shrinkage rate limit of $25 \mu\text{m}/\text{mm}/\text{h}$ and a slope m of 1.

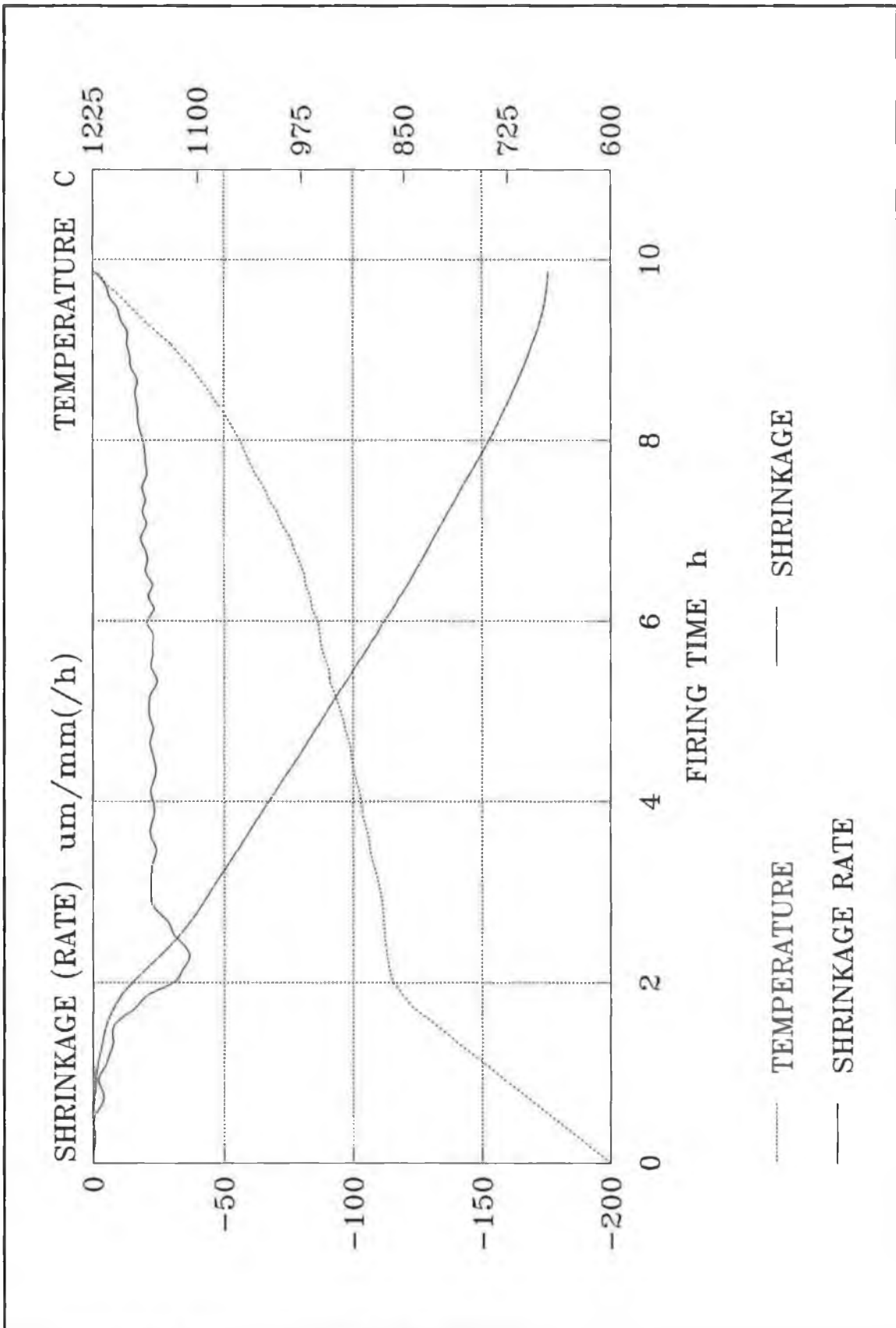


Figure 6.33 Shrinkage and shrinkage rate curves for shrinkage rate limit of $25 \mu\text{m}/\text{mm}/\text{h}$ and slope m of 2.

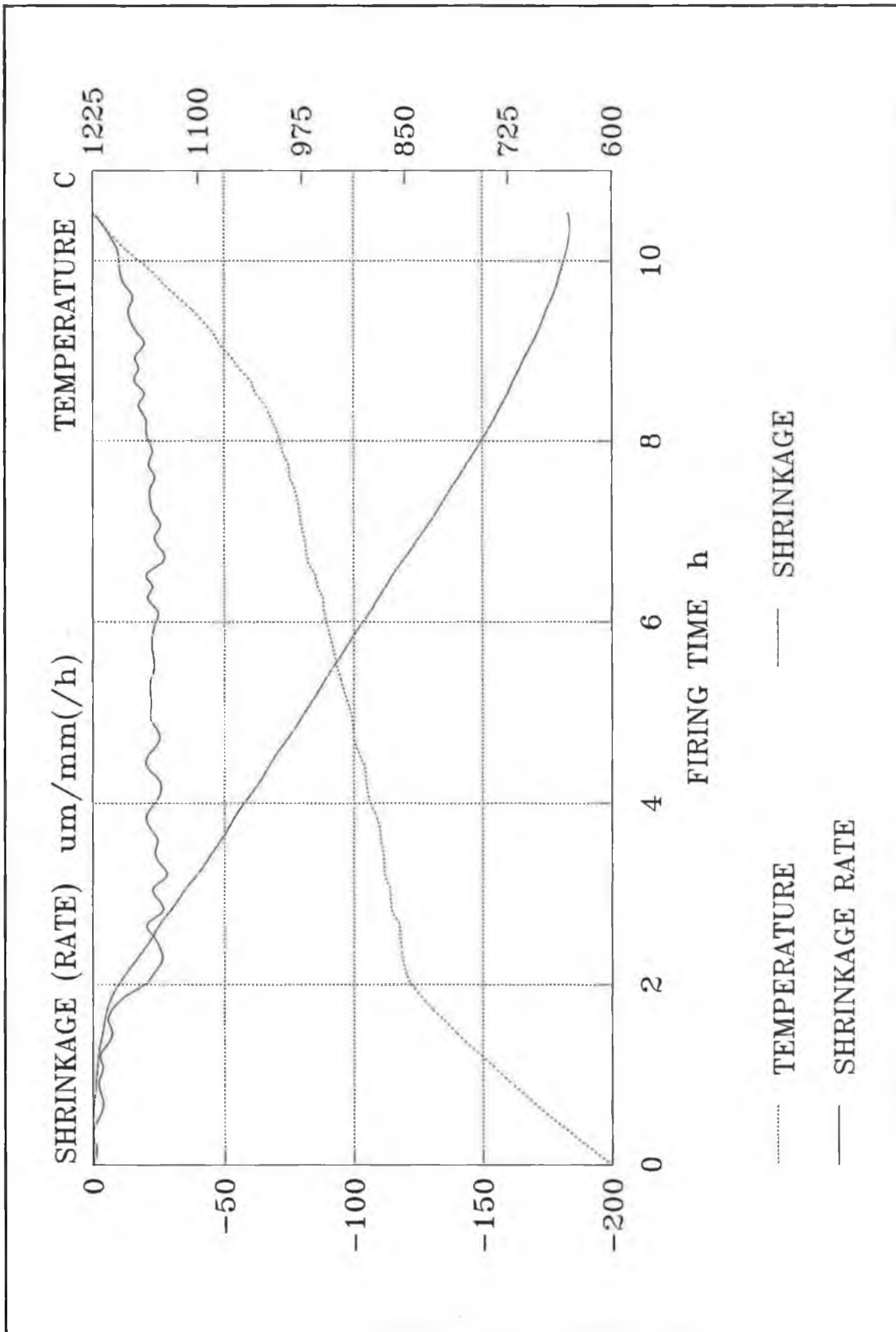


Figure 6.34 Shrinkage and shrinkage rate curves using two values for the slope m .

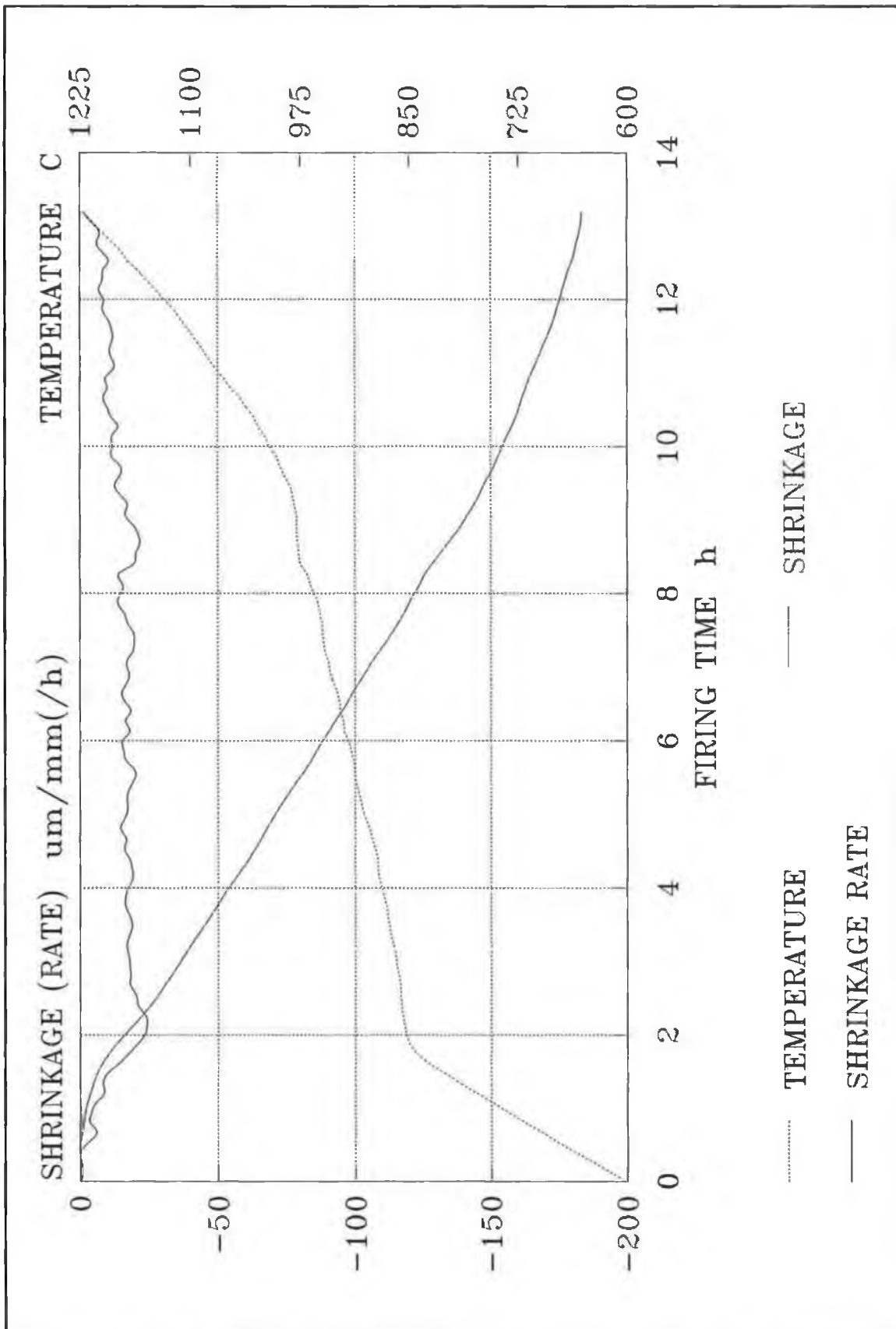


Figure 6.35 Shrinkage and shrinkage rate curves for shrinkage rate limit of 20 $\mu\text{m}/\text{mm}/\text{h}$.

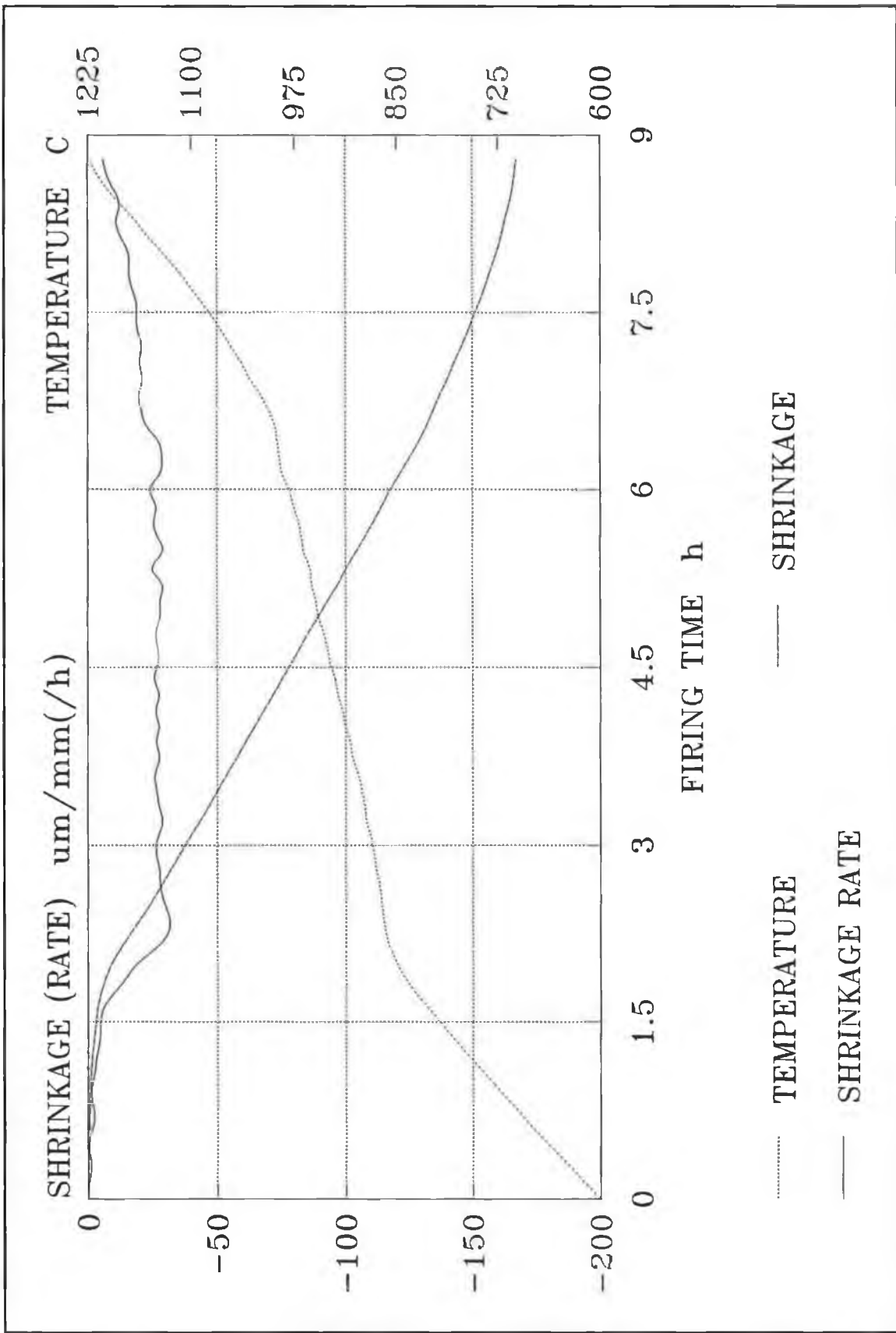


Figure 6.36 Shrinkage and shrinkage rate curves for shrinkage rate limit of 30 $\mu\text{m}/\text{mm}/\text{h}$.

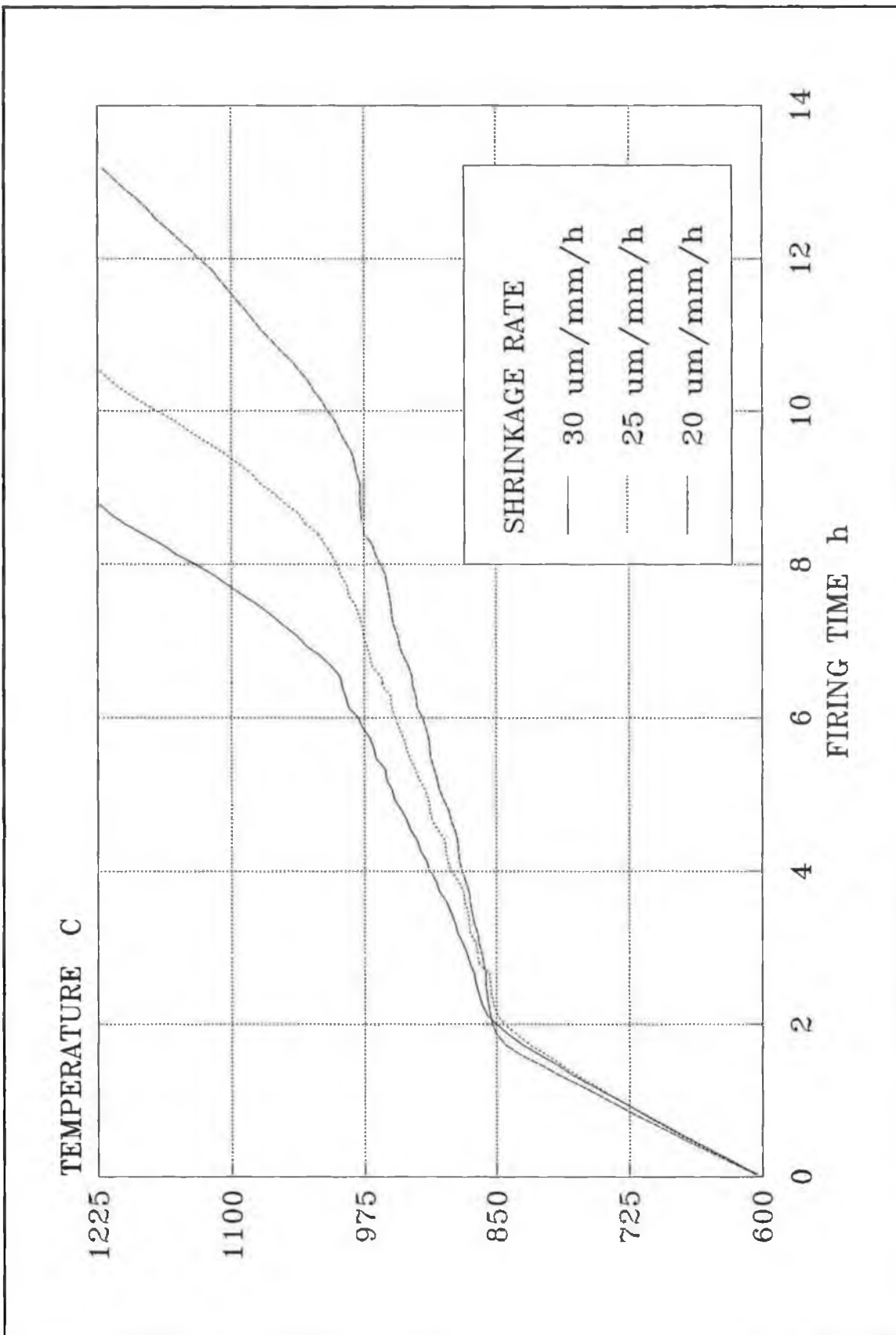


Figure 6.37 Different temperature profiles generated from the software for three shrinkage rate limits.

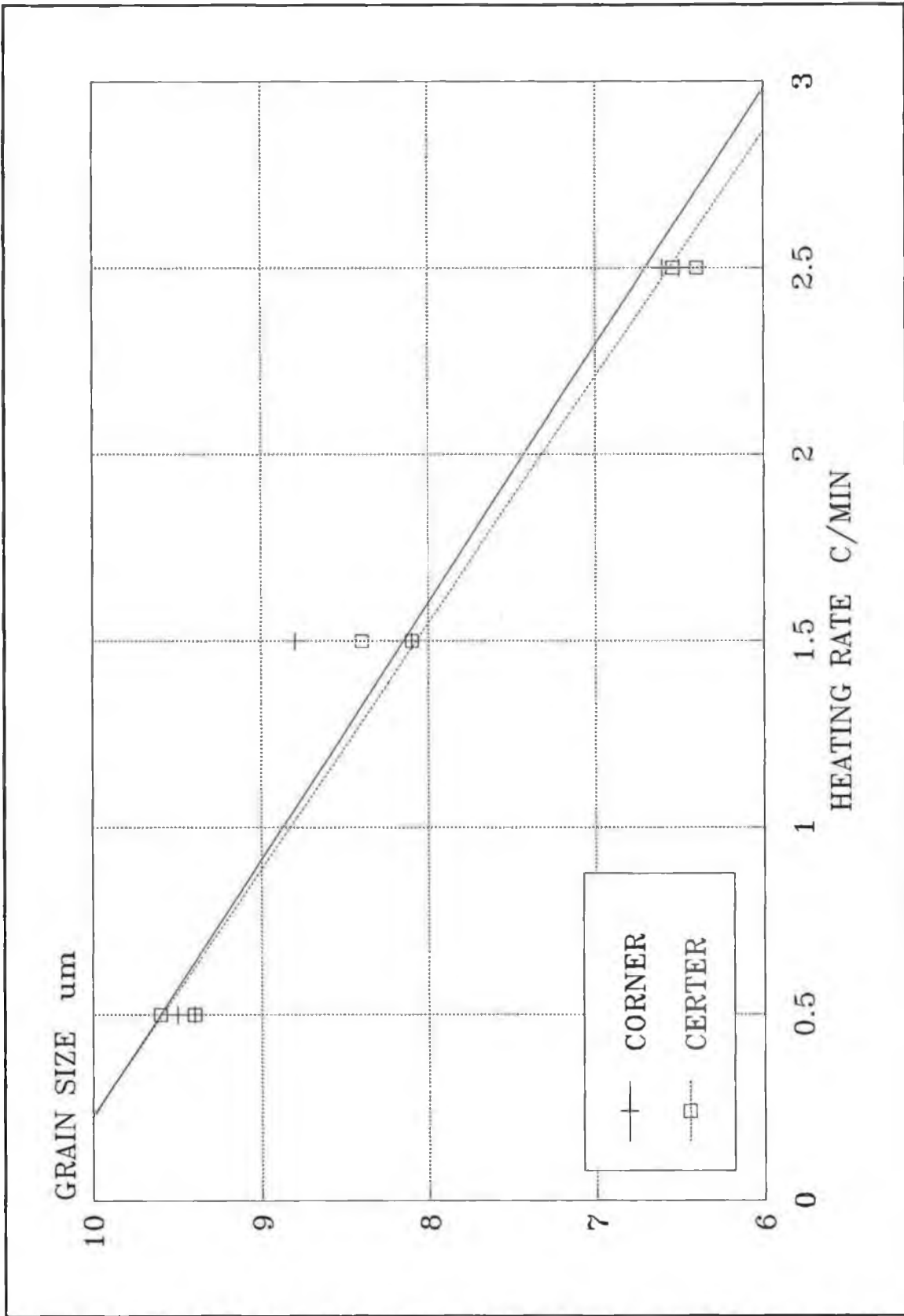


Figure 6.38 Effect of heating rate during shrinkage on the grain growth without any soaking period at the sintering temperature.

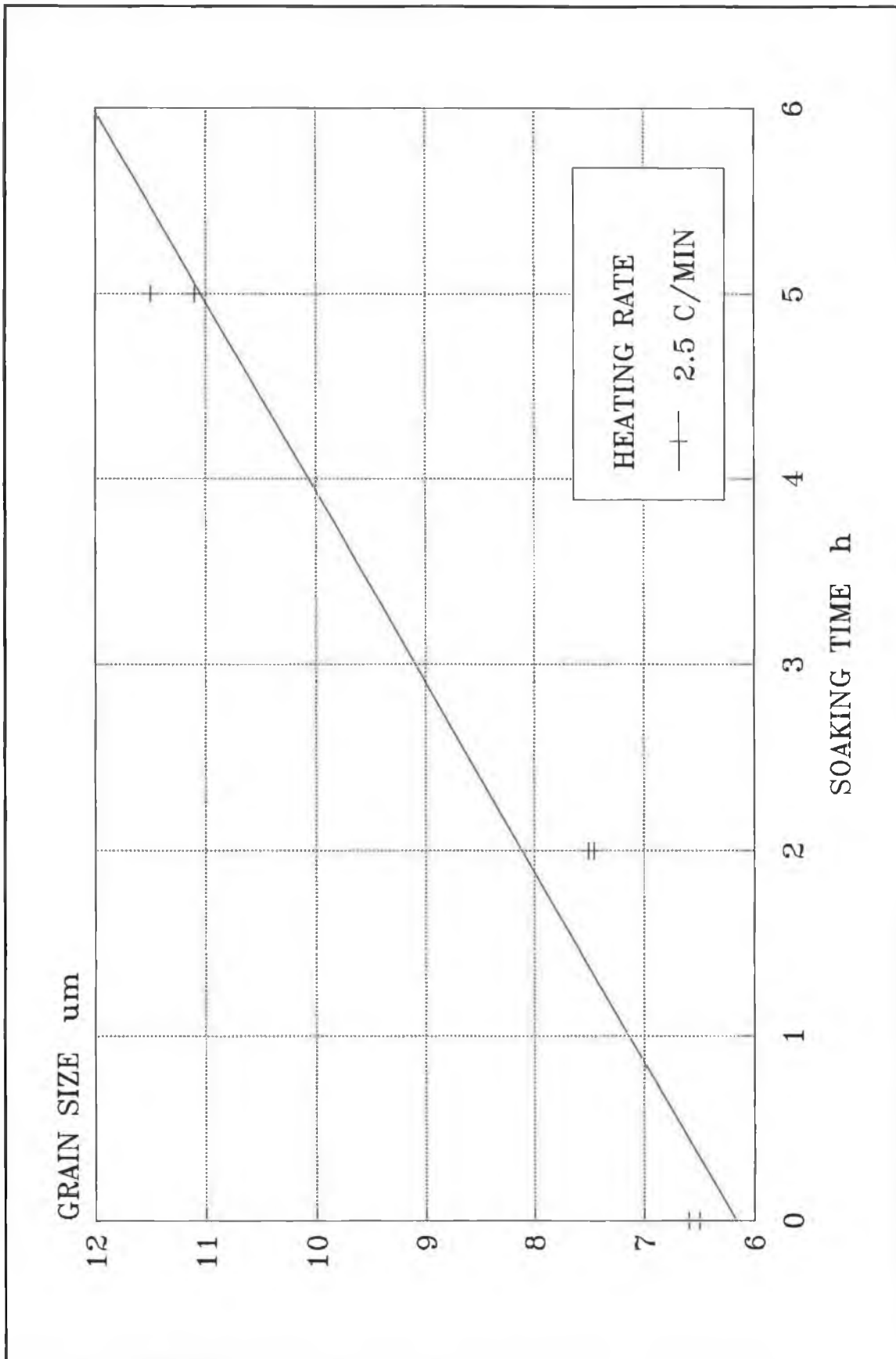


Figure 6.39 Effect of soaking time on the grain growth.

CHAPTER SEVEN

CONCLUSIONS AND RECOMMENDATIONS

7.1 CONCLUSIONS:

7.1.1 STAINLESS STEEL:

In this work, stainless steel powders have been studied in terms of compressibility and strength.

It can be concluded that the three stainless steel powders have different compressibility curves.

In terms of densification during sintering, it was found that for 900°C sintering temperature no shrinkage has been detected. As for the other sintering temperatures shrinkage has taken place. However, the amount of densification is affected by the sintering temperature where the higher the sintering temperature the bigger is the shrinkage.

Regarding the strength of the sintered compacts, it was found that the strength increases with the increase in sintering temperature. However, the compacts which were sintered at 900°C show different strength behaviour in terms of higher strain hardening slope in the plasticity region.

Densification also takes place during compression due to the existing pores in the sintered compacts. This densification behaviour due to straining was found to be linear. Moreover, the slope of the densification curves are found to be decreasing with the increase in the initial density of the sintered compacts.

In respect to the dynamic behaviour of sintered stainless steel, it can be concluded that the sintered compacts were found to be sensitive to the increase in strain rate. However, sintering temperature shows little effect on the compacts' strength at high strain rates.

Finally a constitutive equation for the dynamic behaviour has been established which takes into account the static behaviour of the material and the current density of the compact. This equation relates the dynamic strength of the material with the strain, strain rate, and density of the compact.

7.1.2 CERAMIC POWDERS:

Regarding ceramic powder compaction, it can be concluded that there are many parameters which affect the compressibility of powders. It was found that powders with smaller particle size improve the compressibility. However, the increase in binder content can adversely affect the compressibility. Powder compaction is also affected by the

binder type. As for the effect of lubricant additions, it can be concluded that the compressibility increases with the increase in Zinc stearate up to a ratio of 0.25%, then it starts to decrease.

These parameters also have a significant effect on the green strength of the compacts. It was found that the green strength decreases with smaller particle size powder. However, it was found that the green strength was improved with the increase in binder content. The sintered strength was not affected by the above mentioned parameters, since the binder had been eliminated during sintering and the particles have bonded together to form the same structure.

Two instruments have been built to control the sintering process more precisely on the basis of the evolution of material parameters. The first one was for controlling the weight loss due to the binder burn out. This instrument has been tested and used to successfully control the weight loss at a certain rate. However, the rate at which the binder should burn out has not been optimized. This is because several factors have to be taken into account such as sample size, surface to volume ratio, binder content and binder composition. The results from this instrument (temperature profile) were verified using two methods. The first method was to measure the weight loss during sintering using the resultant temperature profile, while the second method was to measure the temperature gradient inside the compact during

firing using the same resultant temperature profile. The second instrument was developed to control the shrinkage during sintering at a certain rate. It can be concluded that controlling the shrinkage was successfully carried out at a certain rate.

The grain growth was briefly studied and it can be concluded that both the heating rate and the soaking time at the sintering temperature play a significant role in the control of the grain size. However, it was found that the soaking time at the sintering temperature plays more dominant role in the grain growth.

7.2 RECOMMENDATIONS:

7.2.1 STAINLESS STEEL:

Regarding the high strain rate properties of sintered materials, it is recommended that the dynamic behaviour should be studied experimentally more in depth in terms of the wave propagation during impact and the effect of the initial density of the compact on its deformation. The forces which are developed as a result of the impact should be measured by means of developing the ballistic testing machine to incorporate a load cell in the anvil to measure the forces. These measured forces should then be compared with the theoretical results obtained from the numerical technique to see how close the two results are. A correction factor

might be introduced to the dynamic equation, which can be related to the material properties, to take into account any discrepancy between the two results.

7.2.2 CERAMIC:

Ceramic powders have been studied in terms of the compaction and sintering process.

Regarding the compaction process, it is recommended to study the effect of the grain size distribution on the compressibility of the agglomerated ceramic powders. The binding system in the powder consists of several binding elements. The ratios of these binding elements in the binding system could have a significant effect on the compressibility of these powders and this is worth looking into it.

As for the sintering process, the ultimate goal of this project is to develop an expert system to fully govern the thermal and atmosphere cycle in a closed-loop feedback mode. This will allow optimization of the sintering path (time, temperature, heating rate, cooling rate, atmosphere composition, .. etc.) for any material and component geometry. To achieve this, it is recommended as a first step to combine the two developed system together to control the weight loss and shrinkage. A further step would be to monitor and control the evolved gas composition using various gas analytical methods. Then, this new system could be combined

with the previous one.

The densification behaviour during sintering could also be studied using the second instrument which controls the shrinkage. However, the instrument has to be developed to measure the radial shrinkage of the disc to be able to calculate the current density during sintering. This can be accomplished by introducing a second displacement transducer to be used to measure the radial shrinkage. This also requires some modification in the software to take into account the second transducer.

The grain growth should be studied more in detail. The effect of shrinkage rate on the grain growth is worth looking into. These results could be included in the library of the developed system at a later stage.

The cooling rate or the cooling stage, in the firing cycle, should also be looked into to see its effect, if any, on the physical properties of the sintered disc.

REFERENCES

1 - R.M. GERMAN "Powder Metallurgy Science" MPIF Princeton, NJ 1984.

2 - J.S. BENJAMIN & T.E. VOLIN "The Mechanism of Mechanical Alloying" Met. Trans. 1974 vol 5 pp. 1929-1934.

3 - J.K. BEDDOW "The Production of Metal Powder by Atomization" Heyden & Son Ltd. London England 1978

4 - A. LAWLEY "An Overview of Powder Atomization Processes and Fundamentals" Inter. J. Powder Met. Powder Tech. 1977 vol 13 pp. 169-188.

5 - P.J. James "Fundamental Aspects of the Consilidation of Powders" Powder Metall. Int. 1972 vol 4 pp. 82-85

6 - H.S. Alkatib " Properties and Deformation Characteristics of Mechanically Worked Sintered Billets". CNA A Ph.D. Thesis SHEFFFIELD CITY POLYTECHNIC 1982.

7 - M.J. Donachie & M.F. Burr "Effects of pressing on Metal Powders" J. Met. 1963 vol 15 pp. 849-854.

8 - A. Kao & M.J. Koczak " Mixing and Compacting Behaviour of

Ferrous Powders". Inter. J. Powder Met. Powder Tech. 1980 vol 16 No. 2 pp. 105-121.

9 - J.M. Wheatley & G.C. Smith "The Fatigue Strength of Sintered Iron Compacts" Powder met. 1963 vol 6 pp. 141.

10 - S. Clyens & W. Johnson "The Dynamic Compaction of Powdered Materials" Mater. Sci. & Eng. 1977 vol 30 No. 2 pp. 121-139.

11 - N.W. Page & P.D. Killen " Powder Flow During Dynamic and Quasistatic Compaction" Powder Metallurgy 1987 vol 30 No. 4 pp. 233-239.

12 - R. M. German "Strength Dependence on Porosity for P/M Compacts" Int. J. Powder Met. Powder Tech. 1977 vol 13 No.4 pp. 259-271.

13 - T. Honda " Effect of sintering Temperature and Time on Fatigue Strength of Iron Compacts with Different Particle Sizes." J. Jpn. Soc. Powder Powder Metall. 1983 vol. 30 No. 9 Sep. pp. 273-277.

14 - A. Duffield & P. Grootenhuis
J. Inst. Metals 1958-1959 vol 87 pp. 33

15 - P. Wiest "Symposium sur la Metallurgie de Poudres" Saint Germain: Editions Metaux 1964 pp. 329

16 - S. Lal & G.S. Upadhyaya "Sintering of Stainless Steel and Their Based Composites" Rev. Powder Metall. & Physical Ceramics 1986 vol 3 No. 2 pp. 165-203

17 - D.H. Row & E. Klar " Modern Developments in Powder Metallurgy" Ed. H.H Haisner et al. 1980 MPIF Princeton N.J. pp. 247

18 - S.K. Mukherjee & G.S Upadhyaya Oxidation of Metals. vol 23 no 3/4 1985 pp. 177

19 - K.H. Moyer " The Burn-Off Characteristics of Common Lubricants in 316L Powder Compacts" Int. J. Powder Metall. Powder Tech. vol 7 no 3 1971 pp. 33-43.

20 - R.M. German " The Sintering of 304L Stainless Steel" Metallurgical Transactions A vol 7A Dec 1976 pp. 1879-1885.

21 - D.L. Dyke & H.D. Ambs "Stainless Steel Powder Metallurgy" Powder Metallurgy Applications, Advantages and Limitations. Ed. E. Klar ASM Ohio 1983.

22 - S. Lal & G.S. Upadhyaya "Effect of Phosphorus and Silicon Addition on the Sintered Properties of 316L Stainless Steel and its Composites Containing 4 vol% Yttria" J. Mater. Sci. vol 24 1989 pp. 3069-3075.

23 - A. Stosuy & R.R. Holmes "Sintered Type 316L Stainless

Steel ... Its Properties and Processing" Metal Progress vol 91 1969 pp. 81-85.

24 - A. Stosuy, Technical Bulletin Hoeganaes Corporation, 1969 Riverton N.J. pp. 13

25 - P.M. French & P.G. Mardon " The Mechanical Properties of Sintered 316L Stainless Steel" Int. J. Powder Metall. Powder Tech. vol 3 no 4 1967 pp. 65-81.

26 - "Shock waves and high strain rate phenomena in metals". Edited by: M.A.Meyers & L.E. Murr, 1981 Plenum Press New York.

27 - J. Hopkinson "On The Rupture of Iron Wire by a Blow", Proc. Manchester Lit. and Phil. Soc., II 40 (1872).

28 - J. Hopkinson "Further Experiments on The Rupture of Iron Wire", Proc. Manchester Lit. and Phil. Soc., II, 119, (1872).

29 - H. Hennecke, Warmstauchversuche mit Perlitischen Martensitischen und Austenitischen Stahlen, Dr-Dissertation, Aachen Technische Hochschule (1926).

30 - H.Ll.D. Pugh & M.T. Watkins Proc. Conf. Properties of Materials at High Rates of Strain, I. Mech. E., London, Session 3, Paper 5, 1957.

31 - J. Harding " The Effect of High Strain Rate on Material

Properties" in Materials at High Strain Rates, Edited by:
T.Z. Blazynski, Elsevier Applied Science 1987.

32 - T. Honda " The intergranular Fracture of Sintered Iron
Compacts on Tensile Test." J. Jpn. Soc. Powder Powder Metall.
vol 23 no. 2 Mar 1976 pp. 61-67.

33 - J.D. Campbell & W.G.Ferguson Phil. Mag., vol 21 1970 pp.
63.

34 - S. Clyens & W. Johnson " A Shear Cell for the
Determination of the Dynamic Shear Strength and Flow
Behaviour of Particulate Materials" Int. J. Mech. Soc. vol.19
pp. 745-752.

35 - A. Vose, D. Sims & R.M. German , Met Trans. 19A 1988 pp.
487-494.

36 - A. Al-Tounsi & M.S.J. Hashmi " Effect of Sintering
Temperature on the High Strain Rate Properties of Iron Powder
Compacts", 3rd International Conference on Mechanical and
Physical Behaviour of Materials Under Dynamic Loading Oct 14-
18 1991 Strasbourg- France.

37 - Transient Voltage Suppression Devices, Publ. Harris
Semiconductor 1990.

38 - J.S. Reed & R.B. Runk Ceramic Fabrication Process,
Treatise on Materials Science and Technology, vol. 9 ed.

F.F.Y. Wang Academic Press 1976.

39 - M. Takahashi & S. Suzuki " Compaction Behaviour and Mechanical Characteristics of Ceramic Powders", Handbook of Ceramics and Composites vol.1: Synthesis and Properties ed. by: N.P. Cheremisinoff, Marcel Dekker 1990.

40 - S. Levine "Organic (Temporary) Binders for Ceramic Systems" Ceramic Age Jan 1960 pp. 39-43.

41 - J. Van Der Zwan & C.A.M. Siskens " The Compaction and Mechanical Properties of Agglomerated Materials" Powder Technology 1982 vol. 33 pp. 43-54.

42 - F.W. Dynys & J.W. Halloran "Compaction of Aggregated Alumina Powder", J. Am. Ceram. Soc. vol.66 no. 9 1983 pp. 655-659.

43 - R.G. Frey & J.W. Halloran " Compaction Behaviour of Spray-Dried Alumina" J. of Am. Ceram. Soc. 1984 vol 67 no.3 pp. 199-203.

44 - R.A. Dimila & J.S. Reed " Stress Transmission During the Compaction of a Spray Dried Alumina Powder in a Steel Die" J. of Am. Ceram. Soc. vol 66 no.9 1983 pp. 667-672.

45 - S. Strijbos "Powder-Wall Friction: The Effects of Wall Grooves and Wall Lubricants" Powder Tech. vol.8 1977 pp. 209-214.

46 - A.R. Cooper, Jr. & L.E. Eaton " Compaction Behaviour of Several Ceramic Powders" J. Am. Ceram. Soc. vol.45 no.3 1962 pp. 97-101.

47 - C.W. Marchall & A. Rudnick " Conventional Strength Testing of Ceramics" in Fracture Mechanics of Ceramics Publ. Plenum Press.

48 - F.L.L.B. Carniero & G.J. Barcellos, Union of Testing and Research Laboratories for Materials and Structures, No. 13 (1953).

49 - O. Vardar & I. Finnie " An Analysis of the Brazilian Disk Fracture Test using Weibull Probabilistic Treatment of Brittle Strength" Int. J. Fracture vol. 11 no. 3 June 1975.

50 - C.W. Nies & G.L. Messing " Effect of Glass-Transition Temperature of Polyethylene Glycol-Plasticized Polyvinyl Alcohol on Granule Compaction" J. Am. Ceram. Soc. vol.67 no.4 1984 pp.301-304.

51 - J.W. Harvey & D.W. Johnson "Binder System in Ferrites" Ceram. Bull. vol.59 no. 6 1980 pp. 637-645.

52 - P. Stanley, H.Fessler & A.D. Sivill "An Engineer's Approach to the Prediction of Failure Probability of Brittle Components" Proc. Brit. Ceram. 1973 part 22 pp. 453-487.

53 - W. Weibull " A Statistical Theory of The Strength of

Materials" Publ. GENERALSTABENS LITOGRAFISKA ANSTALTS FORLAG
Stockholm 1939.

54 - D.G.S. Davies "Design in Brittle Materials with Special
Reference to Silicon Carbide" Fulmer Research Institute
Report R.275/5/March 1971.

55 - R.M. Williams & L.R. Swank " Use of Weibull Statistics
to Correlate MOR, Ball-on-Ring and Rotational Fast Fracture
Tests" J. Am. Ceram. Soc vol.66 no.11 1983 pp. 765-768.

56 - J.T. Strauss & R.M. German " Analytical Furnace and
Close-Loop Feedback Controlled Sintering" Physical Chemistry
of Powder Metals, Production and Processing ed. W. Murray
Small, The minerals Metals and Materials Society 1989

57 - C.Dong & H.K. Bowen " Hot Stage Study of Bubble
Formation During Binder Burnout" J. Am. Ceram. Soc. vol.72
no.2 1989 pp. 1082-1087.

58 - T. Tsurumi & H.K. Bowen " Binder Burnout" CPRL Report
#Q4 MIT Cambridge 1985 pp. 48-50.

59 - H. Verweij & W.H.M. Bruggink " Reaction Controlled
Binder Burnout of Ceramic Multilayer Capacitors" J. Am.
Ceram. Soc. 1990 vol. 73 no. 2 pp. 226-231.

60 - A. Johnsson, E. Carlstrom, L. Hermansson & R. Carlsson
"Rate-Controlled Thermal Extraction of Organic Binders from

Injection-Molded Bodies" Advances in Ceramics vol. 9 "Forming of Ceramics" Ed. J.A. Mangels & Y.L. Messing Publ. Am. Ceram. Soc. 1984.

61 - E. Carlstrom, M. Sjostedt, B. Mattsson & L. Hermansson "Binder Removal From Injection Moulded Ceramic Turbocharger Rotors" Science of Ceramics, Edt. D. Taylor, Publ. The Institute of Ceramics 1988 pp. 199-204.

62 - W.J. Lackey, P. Angelini, A.J. Caputo, C.E. Devore, J.C. McLaughlin, D.P. Stinton and R.E. Hutchens "Rate-Controlled Technique for Calcining and Drying" Communication Am. Ceram. Soc. June 1984 pp. C-102-C-104.

63 - M.J. Cima, J.A. Lewis & A.D. Devoe "Binder Distribution in Ceramic Greenware During Thermolysis" J. Am. Ceram. Soc. vol.72 no.7 1989 pp. 1192-1199.

64 - M. Trontelj & D. Kojar "Sintering and Grain Growth in Doped ZnO" J. Mater. Sci. 13 (1978) pp. 1832-1834.

65 - P.A. Marshall Jr., D.P. Enright & W.A. Weyl Proceedings of the International Symposium on the Reactivity of Solids, Gothenburg 1952 pp. 273.

66 - T. Asokan, G.N.K. Iyengar & G.R. Nagabhushana "Studies on Microstructure and Density of Sintered ZnO-Based Non-Linear Resistors" J. Mater. Sci. vol 22 (1987) pp. 2229-2236.

67 - M. Chu, M.N. Rahaman, L.C. De Jonghe "Effect of Heating Rate on Sintering and Coarsening" J. Am. Ceram. Soc. vol. 74 no. 6 (1991) pp. 1217-1225.

68 - F.F. Lange " Approach to Reliable Powder Processing" Ceramic Powder Science IIB Edited by: G.L. Messing, E.R. Fuller and H. Hausner Am. Ceram. Soc. Westerville, OH. (1989) pp. 1069-1083.

69 - M.L Huckabee & H. Palmour III "Rate Controlled Sintering of Fine Grained Al_2O_3 " American Ceramic Society Bulletin 51(7) (Jul 1972) pp. 574-576.

70 - W.A. Kaysser & A. Lenhart "Optimization of Densification of ZnO During Sintering" Powder Metall. Int. vol 13 no 3 (1981) pp.126-128.

71 - J.A. Varela & O.J. Whittemore "Pore Size Evolution During Sintering of Ceramic Oxides" Ceramics International 16 (1990) pp. 177-189.

72 - M.M. Haque "Stress-Strain Properties and Microstructural Change in Metal Deformed at Strain Rates of up to 10^{+5} per second." CNA A PhD. Thesis SHEFFIELD CITY POLYTECHNIC 1983.

73 - G.I. Taylor "The Use of Flat-Ended Projectiles for Determining Dynamic Yield Stress", Part (I) Theoretical Considerations, Proc. of Royal Soc. Ser. A194, London 1948, pp. 289-299.

74 - M.S.J. Hashmi & F.B. Klemz "The effect of Friction in Simple Upsetting of Cylindrical Billets of Elastic-Plastic and Elastic Strain Hardening Material: A Numerical Technique." Proc. 17th Int. MTDR Conf. 1976, pp. 597.

75 - M.S.J. Hashmi "A Numerical Technique for Analysing Simple Upsetting of Cylindrical Billets of Strain Rate Sensitive Material." Proc. 18th MTDR Conf. 1977, pp. 27.

76 - F.B. Klemz "Effect of Friction and Strain Rate in Simple Upsetting and Closed Die Forging." CNAA Ph.D Thesis, Sheffield City Polytechnique 1985.

77 - K. Kendall, N. McNalford & J.D. Birchall "The Strength of Green Bodies". Brit. Ceram. Proc. vol. 37 Oct.1986 pp. 255-265.

78 - F.V. Lenel Metals Handbook 9th edition vol. 7 Powder Metallurgy. ASM Ohio 1984 pp. 296-307.

79 - A.A. Griffith, Proceedings of the 1st International Congress for Applied Mechanics Edited by: C.B. Biezeno & J.M. Burgers. Waltman, Uitgeverij, Delft, The Netherlands. 1924 pp. 55-63.

80 - S.B. Batdorf & H.L. Heinisch, Jr. "Weakest Link Theory Reformulated for Arbitrary Fracture Criterion" J. Am. Ceram. Soc. vol 61 no 7-8, 1978. pp. 355-358.

81 - W. Weibull "The Phenomenon of Rupture in Solids"
INGVETENSK. AKAD. HANDL. 153 Publ. Royal Inst. Techn.,
Stockholm.

82 - R. Peltier "Theoretical Investigation of The Brazilian
Test." Union of Testing and Research Laboratories for
Materials and Structures, No. 19 1954.

83 - A. Rudnick, A.R. Hunter & F.C. Holden "An Analysis of
The Diametral-Compression Test." Materials Research and
Standards, Apr.1963, pp. 283-289.

84 - S.Timoshenko & J.N. Goodier "Theory of elasticity" 2nd
edition N.Y. McGraw-Hill Book Co. Inc. 1951.

85 - R. M. German, "Liquid Phase Sintering" Plenum Press New
York 1985.

86 - Quantitative Microscopy. Edt. R.T. DeHoff & F.N. Rhines,
McGraw-Hill Book Co. 1968.

APPENDIX A

**Technical Data for the Instron
Universal Testing Machine**

SPECIFICATIONS	MODEL 4204
Capacity	50 kN, or 5,000 kg, or 11,250 lb
Force Rating: (tension and compression below moving crosshead)	25 kN up to 500 mm/min 50 kN up to 100 mm/min
Load Range: (using interchangeable load cells)	0.1 N to 50 kN
Load Weighing System (accuracy at digital readout accessory or analog output)	±1% of reading to 1/50 of load cell capacity ±1 count of the display
Strain Measuring System (accuracy at digital readout accessory or analog output)	±0.6% of reading +- transducer linearity ±1 count of the display
Position measurement accuracy (no load)	±0.05 mm
Position measurement repeatability (no load)	±0.05 mm
Crosshead speed range	0.05 to 500 mm/min
Crosshead speed accuracy	±0.2% over 100 mm
Return speed	500 mm/min
Crosshead alignment	±0.20 mm over 25 mm travel ±0.51 mm over total travel
Axial stiffness	175 kN/mm
Testing (sample space Lateral: Front to back)	560 mm Unlimited
Power requirements Voltage: Frequency: Power:	110/120/220/240 VAC ±10%, single phase 47 to 63 Hz 2000 VA max.

APPENDIX B

PROGRAM TO CALCULATE THE DYNAMIC STRESS, STRAIN
AND STRAIN RATE DURING THE IMPACT OF AN IRON POWDER
COMPACT WITH A STEEL PROJECTILE USING FINITE
DIFFERENCE TECHNIQUE.

NAMES OF THE VARIABLES:

AFC AREA OF THE FRICTION CONE.....[m²]
AFL AREA OF EACH RING IN THE ELEMENT[m²]
ARR MEAN RADIUS OF EACH RING IN THE ELEMENT..[m]
ASFL AREA OF EACH SUBLAYER IN THE RING.....[m²]
BIGL INITIAL HEIGHT OF THE COMPACT.....[m]
BIGN FORCE IN EACH ELEMENT.....[N]
BIGR CURRENT RADIUS OF EACH ELEMENT.....[m]
BIGRO INITIAL RADIUS OF THE SPECIMEN.....[m]
C1 AUXILIARY VARIABLE.....[N/m³]
CINET THE CURRENT KINETIC ENERGY.....[N.m]
CINETO THE INITIAL KINETIC ENERGY.....[N.m]
DDS DIFFERENCE IN DISPLACEMENT
BETWEEN TWO ELEMENTS.....[m]
DELTAT TIME INTERVAL.....[sec]
DELTS CURRENT HEIGHT OF EACH ELEMENT.....[m]
DELTSO INITIAL HEIGHT OF EACH ELEMENT.....[m]
DENSO INITIAL DENSITY OF THE SPECIMEN.....[Kg/m³]
DV DISPLACEMENT OF EACH ELEMENT.....[m]
E DIFFERENT SLOPES OF THE STRESS-STRAIN
CURVE (YOUNG'S MODULUS).....[N/m²]
ELAST ENERGY CONSUMED ON ELASTIC DEFORMATION.[N.m]
EPSIL THE STRAIN OF THE MATERIAL
FMU FRICTION COEFFICIENT
FN AUXILIARY VARIABLE FOR THE FORCE.....[N]
J COUNTER
M TOTAL NUMBER OF CALCULATIONS
M1 FIRST NUMBER OF CALCULATIONS AFTER
WHICH THE RESULTS ARE PRINTED
M2 NUMBER OF CALCULATION AFTER WHICH
THE RESULTS ARE PRINTED
N NUMBER OF DIVISIONS OF THE COMPACT
NFL NUMBER OF DIVISIONS OF EACH ELEMENT
NSFL NUMBER OF DIVISIONS OF EACH RING
PI CONSTANT
PLAST ENERGY CONSUMED ON PLASTIC DEFORMATION.[N.m]
RCB CONSTANT FOR THE DENSITY-STRAIN EQUATION
RHO CURRENT DENSITY OF THE ELEMENT.....[Kg/m³]
SIGMA STATIC STRESS OF THE MATERIAL.....[N/m²]
SN STRESS IN EACH SUBLAYER.....[N/m²]
SNO FICTITIOUS STRESS.....[N/m²]
STR STRAIN FOR EACH ELEMENT
STRT STRAIN-RATE FOR EACH ELEMENT.....[1/sec]
T DISTANCE BETWEEN THE CENTRE AND THE
RADIUS OF THE LAYER.....[m]


```

C      TIME      CUMULATIVE TIME.....[sec]
C      V         POSITION OF EACH ELEMENT.....[m]
C      VDOTO     VELOCITY OF THE PROJECTILE.....[m/sec]
C      WE        MASS OF EACH ELEMENT.....[Kg]
C      WP        MASS OF THE PROJECTILE.....[Kg]
C      WS        MASS OF THE WHOLE COMPACT.....[Kg]
C
      IMPLICIT REAL * 8 (A-H , O-Z)
      COMMON AFL,ARR,ASFL,BIGN,BIGR,BIGRO,C1,CINETO,D,
1         DDS,DELTAT,DELTS,DELTSO,DENSO,DV,E,FMU,J,
2         N,N1,NFL,NSFL,P,PI,RCB,RHO,SN,SNO,STR,
3         STRT,T,V,WE,WP,I1
      DIMENSION AFL(5,13),ARR(5,13),ASFL(5,5,13),BIGR(13),
1         BIGN(13),C1(13),DDS(13),DELTS(13),DV(13),
2         E(5),EPSIL(5),RHO(13),SIGMA(5),SN(5,5,13),
3         SNO(5),STR(13),STRT(13),T(5,13),V(13)
      DO 1100 I2=70,90,10
      DO 1200 I3=4,6
      OPEN(UNIT=1,FILE='IMPACT.DAT',STATUS='OLD')
      READ(1,10) N,NFL,NSFL,M,M1,M2,BIGRO,BIGL,WS,WP,DENSO,
1         FMU,VDOTO,DELTAT,PI,D,P,RCB,
2         (SIGMA(L),EPSIL(L),L=1,NSFL)
10     FORMAT(6(10X,I10/),22(10X,D15.8/))
      CLOSE(UNIT=1,STATUS='KEEP')
      P=I3/10.D0
      D=I2*1.D+0
C
C      CALCULATE THE SLOPE FOR EACH PART OF THE
C      STRESS-STRAIN CURVE
C
      E(1)=SIGMA(1)/EPSIL(1)
      IF(NSFL .LT. 1) THEN
          WRITE(6,*)' * ERROR * THERE IS NO SUBLAYERS '
          WRITE(6,*)'          CHECK THE DATA FILE '
          STOP
      ELSE IF(NSFL .GT. 1) THEN
          DO 40 L=2,NSFL
              E(L)=(SIGMA(L)-SIGMA(L-1))/(EPSIL(L)-EPSIL(L-1))
40         CONTINUE
      END IF
      E(NSFL+1)=0.
      DO 510 I1=1,4
          M1=400
          M2=400
          VDOTO=VDOTO+10.D0
C
C      INTRODUCING SOME AUXILIARY VARIABLES
C
      N1=N+1
      WE=WS/FLOAT(N)
C
C      CALCULATE THE INITIAL PARAMETERS FOR THE ELEMENTS
C
      DELTSO=BIGL/FLOAT(N)
      DO 80 I=1,N1
          DDS(I)=0.0

```

```

STR(I)=0.0
STRT(I)=0.0
RHO(I)=DENSO
BIGR(I)=BIGRO
V(I)=DELTSO*FLOAT(2*I-1)/2.
DV(I)=0.
DELTS(I)=DELTSO
BIGN(I)=0.
DO 70 K=1,NFL
  T(K,I)=BIGR(I)/FLOAT(NFL)
  ARR(K,I)=FLOAT(2*K-1)*T(K,I)/2.
  AFL(K,I)=2.*PI*ARR(K,I)*T(K,I)
  DO 60 L=1,NSFL
    ASFL(L,K,I)=AFL(K,I)*(E(L)-E(L+1))/E(1)
    SNO(L)=E(1)*EPSIL(L)
    SN(L,K,I)=0.
60    CONTINUE
70    CONTINUE
80    CONTINUE
C
C    PRINT OUT OF THE MATERIAL SPECIFICATION AND THE
C    PARAMETERS OF THE EXPERIMENT.
C
WRITE(6,90) N,NFL,NSFL,BIGRO,BIGL,WS,DENSO,
1      (L,SIGMA(L),EPSIL(L),E(L),L=1,NSFL),
2      VDOTO,WP,FMU,DELTAT,DENSO,RCB,D,P
90    FORMAT(24H NUMBER OF ELEMENTS = ,I3/
1      24H NUMBER OF LAYERS = ,I3/24H NUMBER OF
2      SUBLAYERS = ,I3// 30H SPECIMEN
3      MEASUREMENTS// 12H RADIUS = ,E10.4,20H m.
4      HEIGHT = ,E10.4,4H m.,/12H MASS = ,E10.4,
5      19H Kg. DENSITY = ,E12.5,7H kg/m^3,//46H L
6      SIGMA EPSIL E /
7      44H [N/m^2] [N/m^2]/4
8      (I4,3E14.4/)/14H VELOCITY = ,E12.5,20H m/Sec
9      PROJ MASS = ,E10.4,6H Kg/14H FMU = ,F6.3,
0      T35,11HDELTAT = ,E12.5,5H Sec//46H THE CONSTANTS
1      IN THE DENSITY-STRAIN EQUATION//6H A = ,E10.5,T40,
2      4H B = ,E10.5//40H THE CONSTANTS IN THE PROPOSED
3      EQUATION//,6H D = ,E10.5,7H 1/Sec,T40,4HP = ,E10.5/)
J=0
DV(1)=DELTAT*VDOTO
C
C    PRINT OUT THE STATUS OF THE SPECIMEN
C    BEFORE THE IMPACT.
C
CALL PRINT
BIGN(1)=0.
130 J=J+1
C
C    PRINT OUT THE RESULTS WHEN THE PROJECTILE
C    STARTS TO REBOUND AND THEN STOP.
C
IF(BIGN(2) .GT. 0.0) THEN
  WRITE(6,*) ' FORCE BIGGER THAN 0 '
  CALL PRINT

```

```

      GOTO 500
    END IF
    IF((V(N1)-V(1)) .LT. (0.4*1.D-3)) THEN
      WRITE(6,*) ' HEIGHT IS TOO SMALL '
      CALL PRINT
      GOTO 500
    END IF

```

```

C
C
C      ASSIGNING BOUNDARY LIMITS

```

```

180    DDS(N1)=-2.*DV(N)
      V(N1)=V(N1)-DV(N)
      DDS(1)=0.0

```

```

C
C
C      CALCULATING THE STRAIN, STRESS AND THE
      FORCES IN EACH ELEMENT.

```

```

      CALL STRAIN
      CALL STRESS
      CALL EQUILI

```

```

C
C
C      PRINT OUT THE RESULTS AFTER THE SPECIFIED INTERVAL

```

```

      IF(J .LT. M1) GOTO 130
      M1=M1+M2
      IF (M .LT. M1) M1=M
      CALL PRINT
      IF (J .LT. M) GOTO 130
500    TRAIN=V(N1)-V(1)
      TRAIN=LOG(TRAIN/(N*DELTSO))
      WRITE(2,501)VDOTO,TRAIN,D,P
501    FORMAT(4E18.8)
510    CONTINUE
1200   CONTINUE
1100   CONTINUE
1000   END

```

SUBROUTINE EQUILI

```

  IMPLICIT REAL * 8 (A-H , O-Z)

```

```

1    COMMON AFL,ARR,ASFL,BIGN,BIGR,BIGRO,C1,CINETO,D,
2      DDS,DELTAT,DELTS,DELTSO,DENSO,DV,E,FMU,J,
3      N,N1,NFL,NSFL,P,PI,RCB,RHO,SN,SNO,STR,
      STRT,T,V,WE,WP,I1

```

```

1    DIMENSION AFL(5,13),ARR(5,13),ASFL(5,5,13),BIGR(13),
2      BIGN(13),C1(13),DDS(13),DELTS(13),DV(13),
3      E(5),EPSIL(5),RHO(13),SIGMA(5),SN(5,5,13),
      SNO(5),STR(13),STRT(13),T(5,13),V(13)

```

```

  DO 30 I=1,N

```

```

    IF (I .EQ. 1) THEN

```

```

      DV(I)=DV(I)+DELTAT**2*(BIGN(I+1)-BIGN(I))/(WE+WP)

```

```

    ELSE

```

```

      DV(I)=DV(I)+DELTAT**2*(BIGN(I+1)-BIGN(I))/WE

```

```

    END IF

```

```

30    CONTINUE

```

```

  RETURN

```

```

  END

```

SUBROUTINE STRESS

IMPLICIT REAL * 8 (A-H , O-Z)

COMMON AFL,ARR,ASFL,BIGN,BIGR,BIGRO,C1,CINETO,D,
1 DDS,DELTAT,DELTS,DELTSO,DENSO,DV,E,FMU,J,
2 N,N1,NFL,NSFL,P,PI,RCB,RHO,SN,SNO,STR,
3 STRT,T,V,WE,WP,I1
DIMENSION AFL(5,13),ARR(5,13),ASFL(5,5,13),BIGR(13),
1 BIGN(13),C1(13),DDS(13),DELTS(13),DV(13),
2 E(5),EPSIL(5),RHO(13),SIGMA(5),SN(5,5,13),
3 SNO(5),STR(13),STRT(13),T(5,13),V(13)

SUM=0.

DO 10 I=2,N1

SUM=SUM+DELTS(I)

10

CONTINUE

DO 20 I=2,N1

SNDS=C1(I)*DDS(I)

BIGN(I)=0.

DO 30 K=1,NFL

FN=0.

DO 40 L=1,NSFL

C
C
C
C

CALCULATING THE STRESS AND COMPARE IT WITH
THE PRESUMED EQUATION.

SN(L,K,I)=SN(L,K,I)+SNDS

IF(SN(L,K,I)-SNO(L))50,60,70

70

SNY=SNO(L)*(1.+ABS(DDS(I)/DELTAT/DELTS(I)/D)**P)

IF(SN(L,K,I)-SNY)60,60,80

80

SN(L,K,I)=SNY

GOTO 60

50

IF(SN(L,K,I)+SNO(L))90,60,60

90

SNY=SNO(L)*(1.+ABS(DDS(I)/DELTAT/DELTS(I)/D)**P)

IF(SN(L,K,I)+SNY)100,60,60

100

SN(L,K,I)=-SNY

C
C
C
C
C
C
C

CALCULATING THE FORCE FROM THE STRESS

FN=FN+SN(L,K,I)*ASFL(L,K,I)

60

CONTINUE

40

C
C
C

INCLUDING THE RADIAL INERTIA IN THE FORCE

RADF=3.*PI*ARR(K,I)*T(K,I)*RHO(I)*(DDS(I)/

1

DELTAT)**2*(BIGR(I)**2-ARR(K,I)**2-(T(K,I)**2

2

/4.))/4./DELTS(I)**2

RADF=DSIGN(RADF, FN)

FN=FN+FRI

C
C
C
C

INCLUDING THE FRICTION FORCE TAKING INTO ACCOUNT
THE FRICTION CONE.

IF(FMU)320,320,12

12

FFTOT=2.*FMU*(BIGR(I)-ARR(K,I)-(T(K,I)**2/

1

12./ARR(K,I)))/SUM

X=0.

DO 200 M=2,I

X=X+DELTS(M)

200

CONTINUE

X=X-DELTS(I)/2.

IF(BIGR(2)-(SUM/2.))210,210,220

210

IF(X-BIGR(2))230,230,240

```

230      II=2
        GOTO 270
220      IF(X-(SUM/2.))230,230,250
250      X=SUM-X
        GOTO 260
240      X=SUM-X
        IF(X-BIGR(N1))260,260,320
260      II=N1
270      RFC=BIGR(II)-X
        AFC=PI*RFC**2
        IF(RFC-(ARR(K,I)-T(K,I)/2.))320,320,280
280      IF(RFC-(ARR(K,I)+T(K,I)/2.))290,300,300
290      A=RFC**2-(ARR(K,I)-T(K,I)/2. )**2/2./ARR(K,I)/T(K,I)
        GOTO 310
300      A=1.
310      FF=RFC**2*FFTOT/BIGR(I)**2
        FN=A*FN*(1.+FF)
320      BIGN(I)=BIGN(I)+FN
30      CONTINUE
20      CONTINUE
        BIGN(1)=0.
        RETURN
        END

```

SUBROUTINE STRAIN

```

IMPLICIT REAL * 8 (A-H , O-Z)
COMMON AFL,ARR,ASFL,BIGN,BIGR,BIGRO,C1,CINETO,D,
1      DDS,DELTAT,DELTS,DELTSO,DENSO,DV,E,FMU,J,
2      N,N1,NFL,NSFL,P,PI,RCB,RHO,SN,SNO,STR,
3      STRT,T,V,WE,WP,I1
DIMENSION AFL(5,13),ARR(5,13),ASFL(5,5,13),BIGR(13),
1      BIGN(13),C1(13),DDS(13),DELTS(13),DV(13),
2      E(5),EPSIL(5),RHO(13),SIGMA(5),SN(5,5,13),
3      SNO(5),STR(13),STRT(13),T(5,13),V(13)
DO 10 I=2,N
    DDS(I)=DV(I)-DV(I-1)
10  CONTINUE
DO 20 I=1,N
    V(I)=V(I)+DV(I)
20  CONTINUE
DO 70 I=1,N1
    C1(I)=E(1)/DELTS(I)
    DELTS(I)=DELTS(I)+DDS(I)
    IF(DELTS(I) .LT. (.01*DELTSO)) THEN
        WRITE(6,*)I,DELTS(I),DDS(I),J
        DELTS(I)=.01*DELTSO
        WRITE(6,*)'ERROR * Height of element too small'
    END IF
    STR(I)=LOG(DELTS(I)/DELTSO)
    RHO(I)=DENSO+(ABS(STR(I))*RCB)
    BIGR(I)=(BIGRO**2*DELTSO*DENSO/DELTS(I)/RHO(I))**.5
DO 60 K=1,NFL
    T(K,I)=BIGR(I)/FLOAT(NFL)
    ARR(K,I)=FLOAT(2*K-1)*T(K,I)/2.
    AFL(K,I)=2.*PI*ARR(K,I)*T(K,I)
DO 50 L=1,NSFL
    ASFL(L,K,I)=AFL(K,I)*(E(L)-E(L+1))/E(1)
50  CONTINUE

```

```

60     CONTINUE
70     CONTINUE
      RETURN
      END

      SUBROUTINE PRINT
      IMPLICIT REAL * 8 (A-H , O-Z)
      COMMON AFL,ARR,ASFL,BIGN,BIGR,BIGRO,C1,CINETO,D,
1         DDS,DELTAT,DELTS,DELTSO,DENSO,DV,E,FMU,J,
2         N,N1,NFL,NSFL,P,PI,RCB,RHO,SN,SNO,STR,
3         STRT,T,V,WE,WP,I1
      DIMENSION AFL(5,13),ARR(5,13),ASFL(5,5,13),BIGR(13),
1         BIGN(13),C1(13),DDS(13),DELTS(13),DV(13),
2         E(5),EPSIL(5),RHO(13),SIGMA(5),SN(5,5,13),
3         SNO(5),STR(13),STRT(13),T(5,13),V(13)
      TIME=0.0
      TIME=DELTAT*FLOAT(J)

C
C     CALCULATING THE KINETIC ENERGY FOR THE SPECIMEN
C
      CINET=0.0
      DO 10 I=2,N
          CINET=CINET+DV(I)**2*WE/2./DELTAT**2
10     CONTINUE
      CINET=CINET+DV(1)**2*(WE+WP)/2./DELTAT**2
      ELAST=0.

C
C     THE KINETIC ENERGY IS THE INITIAL ONE AT THE
C     MOMENT OF IMPACT.
C
      IF(J .EQ. 0) THEN
          PLAST=0.
          CINETO=CINET
      ELSE

C
C     CALCULATION OF THE ELASTIC AND PLASTIC ENERGY
C
          DO 60 L=1,NSFL
              SUM=0.
              DO 50 I=1,N
                  DO 40 K=1,NFL
                      SUM=SUM+SN(L,K,I)**2*ASFL(L,K,I)*DELTS(I)
40                 CONTINUE
50                 CONTINUE
              ELAST=ELAST+SUM
60                 CONTINUE
              ELAST=ELAST/2./E(1)
              PLAST=CINETO-CINET-ELAST
          END IF

C
C     CALCULATION OF THE STRAIN RATE FOR EACH ELEMENT
C
          DO 80 I=1,N1
              STRT(I)=DDS(I)/DELTS(I)/DELTAT
80         CONTINUE
          WRITE(6,90) J,TIME,CINET,ELAST,PLAST,(I,DELTS(I),

```

```

1          BIGN(I),STR(I),RHO(I),BIGR(I),
2          STRT(I),I=1,N1)
90  FORMAT(/6H J = ,I5,9H TIME = ,E12.5,4H Sec, /
1  12H KINETIC = ,E11.4,4H N.m,
2  10H ELAST = ,E11.4,14H N.m PLAST = ,E11.4,4H N.m//
3  79H I      V      F      STRAIN      DENSITY
4  RADIUS    STRT    /25H    [m.]      [N.]
5  49H                                [Kg/m^3]    [m.]      [1/Sec]
6  /(I4,6E12.4))
RETURN
END

```

APPENDIX C

MAIN PROGRAM

Program for controlling the binder burn out.

```
DECLARE SUB PrintOut ()
DECLARE SUB InputData ()
DECLARE SUB WeightRead ()
DECLARE SUB WeightLoss ()
DECLARE SUB WeightLimit ()
DECLARE SUB FinalRecipe ()
DECLARE SUB StartProgram ()
DECLARE SUB FinalRampTemp ()
DECLARE SUB ProgramSetting ()
DECLARE SUB Initialization ()
DECLARE SUB ControllerInit. ()
DECLARE SUB PointSet (temp%)
DECLARE SUB Commands (a$, p$, decimal$, num%)
DECLARE SUB RampTime (temp2%, temp1%, time%)

COMMON SHARED weight0, weight1, weight2, wkg0
COMMON SHARED dwmin, wloss, wlr1, wlr2, wlrlim
COMMON SHARED i%, dt%, delay, hour, weighttime, hrmax
COMMON SHARED const1, const2, const3
COMMON SHARED dtmax%, setpoint%, setpoint0%, ramptemp%
COMMON SHARED deltatemp%
COMMON SHARED shrinktemp%, firingtemp%, firingtime%
COMMON SHARED outfile$

CALL InputData
OPEN outfile$ FOR OUTPUT AS #3
CLOSE #3
CLS
CALL ControllerInit.
CALL WeightRead
CALL Initialization
CALL WeightLoss
CALL PrintOut
CALL WeightLimit
DO
CALL FinalRampTemp
CALL ProgramSetting
CALL StartProgram
SLEEP delay
CALL WeightRead
CALL WeightLoss
CALL WeightLimit
CALL PointSet(ramptemp%)
CALL PrintOut
LOOP UNTIL ramptemp% >= shrinktemp%

CALL FinalRecipe
CALL PointSet(setpoint0%)
CALL StartProgram
END
```


SUB Commands (command3\$, command4\$)

Subroutine for communication with the furnace controller

Two commands are used for the communication. The first one gives the parameter and its new value and the second command is to make sure that the controller implement the changes in the first command.

For more information about these commands refer to the instruction manual of the controller. These commands are: Command 3 and Command 4

```
num$ = RIGHT$("0000" + LTRIM$(STR$(num%)), 4)
command3$ = a$ + "1" + p$ + "#" + num$ + decimal$ + "*"
command4$ = a$ + "1" + p$ + "I*"
OPEN "COM1:4800,E,7,1,RS,CS0,DS0,CD0,,,PE" FOR RANDOM AS #2
DO UNTIL a$ = "I"
    PRINT #2, command3$;
    reply3$ = INPUT$(10, #2)
    a$ = MID$(reply3$, 9, 1)
LOOP
FOR j = 1 TO 100: NEXT j
PRINT #2, command4$;
relpy4$ = INPUT$(10, #2)
CLOSE #2
END SUB
```

SUB ControllerInit.

```
CLS
PRINT
PRINT
PRINT
FOR module% = 1 TO 8
    PRINT "      Initializing module . . ."; module%
    a$ = "R"
    p$ = "S"
    decimal$ = "0"
    CALL Commands(a$, p$, decimal$, module%)
    FOR stage% = 1 TO 4
        p$ = "A"
        decimal$ = "0"
        CALL Commands(a$, p$, decimal$, stage%)
        p$ = "B"
        num% = 0
        CALL Commands(a$, p$, decimal$, num%)
        p$ = "C"
        decimal$ = "2"
        CALL Commands(a$, p$, decimal$, num%)
        p$ = "E"
        CALL Commands(a$, p$, decimal$, num%)
    NEXT stage%
NEXT module%
END SUB
```

SUB FinalRampTemp

Subroutine to calculate the final ramp temperature
which will be given to the controller

ramptemp% = ramptemp% + deltatemp%
END SUB

SUB FinalRecipe

Subroutine to make the necessary commands for the
controller to run the temperature profile for
firing after the binder burnout stage has been
completed.

Calling module No. 1

a\$ = "R"
p\$ = "S"
decimal\$ = "0"
module% = 1
CALL Commands(a\$, p\$, decimal\$, module%)

Calling stage No. 1

p\$ = "A"
stage% = 1
CALL Commands(a\$, p\$, decimal\$, stage%)

Setting the ramp time to zero to make the programmer
starts from the previous ramp temperature.

p\$ = "C"
decimal\$ = "2"
num% = 0
CALL Commands(a\$, p\$, decimal\$, num%)

Calling stage No. 2 for heating to
sintering temperature.

p\$ = "A"
decimal\$ = "0"
stage% = 2
CALL Commands(a\$, p\$, decimal\$, stage%)

Setting the ramp temperature

p\$ = "B"
CALL Commands(a\$, p\$, decimal\$, firingtemp%)

Calculating the ramp time from the end of the burn
off temperature to the firing temperature.

CALL RampTime(firingtemp%, ramptemp%, total.ramptime%)
p\$ = "C"
decimal\$ = "2"

```

CALL Commands(a$, p$, decimal$, total.ramptime%)
'
'   Setting the dwell time for the firing.
'
p$ = "E"
CALL Commands(a$, p$, decimal$, firingtime% * 100)
'
'   Calling stage 3 for cooling.
'
p$ = "A"
decimal$ = "0"
stage% = 3
CALL Commands(a$, p$, decimal$, stage%)
'
'   Setting the ramp temperature for cooling.
'
p$ = "B"
CALL Commands(a$, p$, decimal$, setpoint0%)
'
'   Setting the ramp time for cooling.
'
CALL RampTime(firingtemp%, setpoint0%, total.ramptime%)
p$ = "C"
decimal$ = "2"
CALL Commands(a$, p$, decimal$, total.ramptime%)
END SUB

```

SUB Initialization

```

weight0 = weight2
weight1 = weight2
i% = 0
delay = dt% * 60           ' Time interval in seconds.
wkg0 = weight0 / 1000     ' Initial weight in kg.
weighttime = 60 / dt% / wkg0
wlrmin.readout = dwmin * weighttime
deltatemp% = 0
setpoint0% = setpoint%
ramptemp% = setpoint%
const3 = 2 * wlrmin.readout
const1 = (2 * dtmax% * (const3 - wlrlim) + wlrlim) /
          (2 * const3 - wlrlim)
const2 = (2 * dtmax% - 2) / (2 * const3 - wlrlim)
END SUB

```

SUB InputData

```

INPUT "BALANCE MINIMUM READOUT"           "; dwmin
INPUT "INITIAL WEIGHT OF THE DISKS IN GRAMS" "; weight0
INPUT "TIME INTERVAL IN MINUTES"         "; dt%
INPUT "MAXIMUM TEMPERATURE INCREASE IN C" "; dtmax%
INPUT "WEIGHT LOSS RATE LIMIT IN g/kg/h" "; wlrlim
INPUT "INITIAL SET POINT IN C"           "; setpoint%
INPUT "TEMPERATURE WHEN WEIGHT LOSS ENDS IN C "; shrinktemp%
INPUT "FIRING TEMPERATURE IN C"         "; firingtemp%
INPUT "SOAKING TIME IN HOURS"           "; firingtime%
INPUT "MAXIMUM HEATING RATE IN C/MIN"    "; hrmax
INPUT "OUTPUT DATA FILE"               "; outfile$
END SUB

```

SUB PointSet (temp%)

' Subroutine to make the required command for
' the controller to change the setpoint.
'

```
a$ = "L"  
p$ = "S"  
decimal$ = "0"  
CALL Commands(a$, p$, decimal$, temp%)  
END SUB
```

SUB PrintOut

```
wlr1 = wlr2  
hour = i% * dt% / 60  
PRINT i%; ; hour, weight2, wloss, wlr2; ; ramptemp%  
OPEN outfile$ FOR APPEND AS #3  
PRINT #3, hour, weight2, wloss, wlr2, ramptemp%  
CLOSE #3  
i% = i% + 1  
END SUB
```

SUB ProgramSetting

' Subroutine to set the programmer parameters
' for temperature profile.
'

' Calling module No. 1
'

```
a$ = "R"  
p$ = "S"  
decimal$ = "0"  
module% = 1  
CALL Commands(a$, p$, decimal$, module%)
```

' Calling stage No. 1
'

```
p$ = "A"  
CALL Commands(a$, p$, decimal$, module%)
```

' Setting the ramp temperature.
'

```
p$ = "B" ' Parameter name. B for ramp temperature.  
CALL Commands(a$, p$, decimal$, ramptemp%)
```

' Setting the ramp time.
'

```
p$ = "C" ' Parameter name. C for ramp time.  
decimal$ = "2"  
CALL Commands(a$, p$, decimal$, dt%)
```

END SUB

SUB RampTime (temp2%, temp1%, time%)

Subroutine to calculate the time for ramping
to the sintering temperature in hh:mm

ramptime.in.minutes% = INT(ABS(temp2% - temp1%) / hrmax)
hours.ramptime% = INT(ramptime.in.minutes% / 60)
minutes.ramptime% = ramptime.in.minutes% MOD 60

minutes.ramptime\$ = "00" + LTRIM\$(STR\$(minutes.ramptime%))
minutes.ramptime\$ = RIGHT\$(minutes.ramptime\$, 2)
total.ramptime\$ = LTRIM\$(STR\$(hours.ramptime%)) +
minutes.ramptime\$

time% = VAL(total.ramptime\$)

END SUB

SUB StartProgram

Subroutine to run the program in the controller.

a\$ = "R"
p\$ = "K"
decimal\$ = "0"
num% = 21
CALL Commands(a\$, p\$, decimal\$, num%)

END SUB

SUB WeightLimit

This subroutine is to calculate the temperature
increase due to the resultant weight loss rate.
It takes into account the acceleration of weight
loss where it is found that the acceleration of
weight loss has an effect on the controlling process.

SELECT CASE ABS(wlr2)
CASE IS < (wlrlim / 2)
deltatemp% = dtmax%
CASE (wlrlim / 2) TO (wlrlim - const3)
deltatemp% = CINT(const1 + (const2 * ABS(wlr2)))
CASE (wlrlim - const3) TO wlrlim
deltatemp% = 1
CASE ELSE
deltatemp% = CINT(const1 + (const2 * ABS(wlr2)))

END SELECT

END SUB

SUB WeightLoss

Subroutine to calculate the weight loss and
weight loss rate.

wloss = (weight2 - weight0) / wkg0
wlr2 = (weight2 - weight1) * weighttime
weight1 = weight2

END SUB

SUB WeightRead

' Subroutine to read the value of the current
' weight of the fired samples.
'

```
OPEN "COM2:2400,E,7,1,CS,DS,LF" FOR RANDOM AS #1
PRINT #1, "S"
INPUT #1, W$
CLOSE #1
weight2 = VAL(MID$(W$, 3, 11))
END SUB
```

PUBLICATIONS

- "Effect of sintering temperature on the high strain rate properties of iron powder compacts"

Presented at the 3rd International Conference on Mechanical and Physical Behaviour of Materials under Dynamic Loading. Strasbourg- FRANCE, 14-18 October 1991.

- "Weight Loss Control during the Firing Process of Enhanced ZnO Varistors"

Presented at the 1992 Powder Metallurgy World Congress. San Francisco- USA, 21-26 June 1992.

- "Feedback Loop for Controlling the Binder Burn out During the Firing Process of Enhanced ZnO Varistors"

Accepted for presentation at the 8th International Symposium on Ceramic Processing. Rimini - ITALY, 11-13 November 1992.

- "Compaction of Agglomerated Zinc Oxide Powder"

Refereed and accepted for presentation at the Asia Pacific Conference on Materials Processing. Singapore, 23-25 February 1993. To be Published in the Journal of Materials Processing Technology.

- "Effect of Sintering Temperature on Densification, Shrinkage and Compression Strength of Stainless Steel 300 Series"

Refereed and accepted for presentation at the Asia Pacific Conference on Materials Processing. Singapore, 23-25 February 1993. To be Published in the Journal of Materials Processing Technology.